

2

CHORS

Center for Hydro-Optics & Remote Sensing

San Diego State University 6505 Alvarado Road, Suite 206 San Diego, CA 92120-5005 619/594-2272 or 594-2230

AD-A271 671



CHORS Technical Memorandum 001-93

OPTICAL CLIMATOLOGY OF THE NORTHEAST PACIFIC OCEAN

James L. Mueller

Final Report

NOARL Contract N00014-89-C-6007

3 March 1993

93-26217



127PR

This report has been prepared for the Naval Research Laboratory Tactical Oceanographic Warfare Support Program Office under the sponsorship of the Oceanographer of the Navy (NO96), under Program Element No. 0603704N, Project No. R0118.

Approved for public release; distribution is unlimited.

San Diego State University
Center for Hydro-Optics and Remote Sensing
6505 Alvarado Road, Suite 206
San Diego, CA 92120

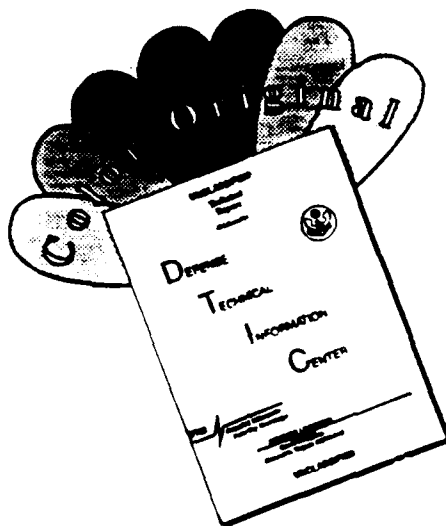
0 0 C 1

REPORT DOCUMENTATION PAGEForm Approved
OBM No. 0704-0188

Public reporting burden for this collection of information is estimated to average 1 hour per response, including the time for reviewing instructions, searching existing data sources, gathering and maintaining the data needed, and completing and reviewing the collection of information. Send comments regarding this burden or any other aspect of this collection of information, including suggestions for reducing this burden, to Washington Headquarters Services, Directorate for Information Operations and Reports, 1215 Jefferson Davis Highway, Suite 1204, Arlington, VA 22202-4302, and to the Office of Management and Budget, Paperwork Reduction Project (0704-0188), Washington, DC 20503.

1. Agency Use Only (Leave blank).		2. Report Date. March 3, 1993	3. Report Type and Dates Covered. Contractor Report	
4. Title and Subtitle. Optical Climatology of the Northeast Pacific Ocean			5. Funding Numbers. Contract N00014-87-C-6002 N00014-89-C-6007 Program Element No. 0603704N Project No. R1299 Task No. 300 Accession No. DN257005 Work Unit No. 113119B	
6. Author(s). James L. Mueller*				
7. Performing Organization Name(s) and Address(es). *CHORS Center for Hydro-Optics & Remote Sensing 6505 Alvarado Road, Suite 206 San Diego, CA 92120-5005			8. Performing Organization Report Number. 001-93	
9. Sponsoring/Monitoring Agency Name(s) and Address(es). Naval Research Laboratory Tactical Oceanographic Warfare Support Office Stennis Space Center, MS 39529-5004			10. Sponsoring/Monitoring Agency Report Number. NRL/CR/7410--93-0004	
11. Supplementary Notes.				
12a. Distribution/Availability Statement. Approved for public release; distribution is unlimited.			12b. Distribution Code.	
13. Abstract (Maximum 200 words). <p>This report describes the results of a climatological study of optical variability in the upper 200 m of the Northeast Pacific Ocean. This work was supported by the Oceanographer of the Navy under NORDA/NOARL contracts N00014-87-C-6002 (SIO Visibility Lab., UCSD, La Jolla, CA) and N00014-89-C-6007 (SDSU CHORS, San Diego, CA), and this document constitutes our Final Report under those contracts. The project addressed two primary objectives. The first objective was to describe the two-dimensional spatial distribution and temporal variability of near-surface bio-optical properties derived from satellite ocean color imagery, and to deliver the results in the form of a data base suitable for the developing new environmental products to support naval applications in the region. The second objective was to develop a model, with which the near-surface bio-optical properties derived from satellite data can be extrapolated downward to depths of interest for naval operations (i.e. 200 m).</p>				
14. Subject Terms. Physical oceanography, computers, optics			15. Number of Pages. 118	
			16. Price Code.	
17. Security Classification of Report. Unclassified	18. Security Classification of This Page. Unclassified	19. Security Classification of Abstract. Unclassified	20. Limitation of Abstract. SAR	

DISCLAIMER NOTICE



THIS DOCUMENT IS BEST QUALITY AVAILABLE. THE COPY FURNISHED TO DTIC CONTAINED A SIGNIFICANT NUMBER OF COLOR PAGES WHICH DO NOT REPRODUCE LEGIBLY ON BLACK AND WHITE MICROFICHE.

Table Of Contents

1.0	INTRODUCTION	1
2.0	DATA	6
2.1	CZCS Data	6
2.1.1	CZCS LEVEL-1 BINARY DATA FILES	6
2.1.2	LEVEL-1 CRTT CONTROL RECORDS	6
2.1.3	CZCS LEVEL-2 BINARY DATA FILES	7
2.1.4	CZCS LEVEL-2 NAVIGATION (NAV) FILES	8
2.1.5	CZCS LEVEL-3 DAILY COMPOSITE K(490) MAPS	9
2.1.6	CZCS LEVEL-3 MONTHLY COMPOSITE MEAN K(490) MAPS	10
2.1.7	CZCS LEVEL-3 K(490) TIME-SERIES at 5° LAT × 5° LON GRID POINTS	10
2.2	Ancillary Data	11
2.3	<i>In situ</i> Irradiance and Chlorophyll <i>a</i> Fluorescence Profiles	11
3.0	CZCS DATA PROCESSING AND ANALYSES	12
3.1	Methods	12
3.1.1	DATA BASE MANAGEMENT	14
3.1.2	LEVEL-1 SCREENING and PROCESSING	16
3.1.3	LEVEL-2 PROCESSING	17
3.1.4	LEVEL-3 ANALYSES	21
3.1.4.1	Mercator Grid Description	21
3.1.4.2	Daily Composite K(490) Maps	23
3.1.4.3	Monthly Composite Means K(490) Maps	24
3.1.4.4	K(490) Time Series at Selected Locations	24
3.2	CZCS Radiance Responsivity Calibration	25
3.2.1	PRE-LAUNCH CALIBRATION	25
3.2.2	PREVIOUS MODELS of POST-LAUNCH DEGRADATION	25
3.2.3	DATA and METHODS for REVISED RESPONSIVITY DEGRADATION ANALYSIS	26
3.2.4	RESULTS: REVISED CZCS RESPONSIVITY CORRECTIONS	27
3.2.5	DISCUSSION and CONCLUSIONS	28
3.3	Monthly Composite Means of CZCS K(490)	28
3.4	Time-Series of K(490) At Selected Locations	30
4.0	ERROR ANALYSIS of CZCS K(490) ESTIMATES	31
4.1	Methods	31
4.2	Results	32
4.3	Discussion and Conclusions	32
5.0	BIO-OPTICAL PROVINCE ANALYSES: VERTICAL PROFILE MODELS OF K(490) AND CHLOROPHYLL <i>a</i> FLUORESCENCE	33
5.1	Methods	34
5.2	Results	36
5.3	Discussion and Conclusions	38

Dist		Avail and for Special	
A-1			

Table Of Contents (con't.)

6.0	SUMMARY AND RECOMMENDATIONS	43
7.0	REFERENCES	44

Appendices

APPENDIX A	ATLAS OF K(490) IN THE NORTHEAST PACIFIC OCEAN NOVEMBER 1978-JUNE 1986
APPENDIX B	TEMPORAL TRENDS IN CZCS K(490) COMPARED WITH <i>IN SITU</i> MEASUREMENTS
APPENDIX C	DIGITAL DATA DIRECTORY
APPENDIX D	TIMES SERIES GRAPHS OF CZCS K(490) AT SELECTED LOCATIONS
APPENDIX E	"BIO-OPTICAL PROVINCES OF THE NORTHEAST PACIFIC OCEAN: A PROVISIONAL ANALYSIS "

List of Tables

Table 2.1	CZCS Level-2 Lookup Tables	5
Table 2.2	Latitude and Longitude Coordinates of CZCS K(490) Lines and Pixels in Mercator Grid Lines	9
Table 3.2.1	CZCS Pre-Launch Radiance Calibration Coefficients	19
Table 4.1	CZCS Trend Estimates $\hat{K}(490)$ Compared to <i>in situ</i> $\bar{K}(490, z)$	33
Table 5.1	Table of Coefficients for Models of Irradiance Attenuation at 490 nm	43

List of Figures

Fig. 1.1	Major Ocean Currents and Fronts in the Northeast Pacific Ocean	2
Fig. 2.1	Tracklines of Research Cruises	12
Fig. 3.1.1	CZCS Data Processing	14
Fig. 3.1.2	CZCS Level-1 Data Screening	16
Fig. 3.1.3	CZCS Level-2 Processing	18
Fig. 3.1.4	CZCS Level-3 Analyses	22
Fig. 3.1.5	Total Numbers of CZCS K(490) Observations at $5^\circ \times 5^\circ$ Grid Points	24
Fig. 3.2.1	CZCS Time Dependent Radiance Responsivity Adjustment Coefficients $g(\lambda, N)$	29
Fig. 4.1	Time Series of CZCS K(490) ... Compared with <i>in situ</i> K(490)	34
Fig. 4.2	Frequency Distribution of Relative Error ... of CZCS K(490)	34
Fig. 5.1	Schematic Example of the Relative Irradiance Profile Model	35
Fig. 5.2	Schematic Diagram Illustrating the Log-Linear Chlorophyll <i>a</i> Fluorescence Model	37
Fig. 5.3	Schematic Diagram ... Chlorophyll <i>a</i> Fluorescence Profile Model	38
Fig. 5.4	Geographic Locations of Optical Profile Stations on NAVOCEANO Cruise 260488	39
Fig. 5.5	Geographic Locations of Optical Profile Stations on NAVOCEANO Cruise 260189	40
Fig. 5.6	Covariability of ... $1/K(490)$ with ... z_n ... NAVOCEANO Cruise 260488, Jun. 1988	41
Fig. 5.7	Covariability of ... $1/K(490)$ with ... z_n ... NAVOCEANO Cruise 260189, Oct. 1988	42

AN OPTICAL CLIMATOLOGY OF THE NORTHEAST PACIFIC OCEAN:

K(490) from the Nimbus-7 Coastal Zone Color Scanner (1978-1986),
and

Statistical Models of Vertical Bio-Optical Profiles

James L. Mueller

1.0 INTRODUCTION

This report describes the results of a climatological study of optical variability in the upper 200 m of the Northeast Pacific Ocean. This work was supported by the Oceanographer of the Navy under NORDA/NOARL contracts N00014-87-C-6002 (SIO Visibility Lab., UCSD, La Jolla, CA) and N00014-89-C-6007 (SDSU CHORS, San Diego, CA), and this document constitutes our Final Report under those contracts. The project addressed two primary objectives. The first objective was to describe the two-dimensional spatial distribution and temporal variability of near-surface bio-optical properties derived from satellite ocean color imagery, and to deliver the results in the form of a data base suitable for developing new environmental products to support naval applications in the region. The second objective was to develop a model, with which the near-surface bio-optical properties derived from satellite data can be extrapolated downward to depths of interest for naval operations (*i.e.* 200 m). Potential applications of remotely sensed ocean color products to naval warfare planning and operational decision aids are discussed in Hickman (1992) and in Arnone *et al.* (1992), and we will not discuss them here. Indeed, many of the motivations for Navy interest in ocean color apparently stem from classified programs which cannot be discussed in an open forum.

We addressed the first objective through analyses of time series of ocean color image data measured, between October 1978 and June 1986, by the Nimbus-7 Coastal Zone Color Scanner (CZCS). From the raw CZCS data, we calculated distributions and averages of the diffuse attenuation coefficient K(490) at 490 nm (Austin and

Petzold, 1981), which is the optical variable of primary focus in this study. The primary end product of that analysis is a consistently processed time series of Monthly Composite Mean K(490) map arrays, presented here in color atlas form (Appendix A) and delivered also as a digital data base (Appendix C) suitable for use in further analyses and/or development of secondary environmental products. A second end product from our CZCS analysis is a set of Time Series of CZCS K(490) observations from individual days at grid points spaced at intervals of 5° latitude and 5° longitude. These time series are illustrated here in Appendix D, and they are also delivered as digital ASCII files on 9-track magnetic tape (Appendix C). This report describes the format and data conversion algorithms/tables needed to access and use the digital products, and briefly discusses the oceanographic information content of the optical climatology. We also describe the algorithms, software, and procedures implemented, developed and used at CHORS to derive these products from the CZCS data base. In the context of describing the heritage of the CZCS optical climate products, we also describe the content and structure of large intermediate CZCS Level-2 and Level-3 data bases, which are not deliverables under this contract, but which will be retained at CHORS for possible future use.

We addressed the second project objective by developing a set of statistical models which convert remotely sensed K(490) values to predicted vertical profiles of relative irradiance [or alternatively, of K(490,z)] and chlorophyll *a* fluorescence extending to 200 m (Sect. 5.0 and Appendix E). Separate sets of model coefficients, which are derived from profiles of irradiance $E_d(\lambda, z)$

measured *in situ*, apply within geographically distinct bio-optical provinces, and in different seasons and/or years within provinces. A "bio-optical province" is a geographically defined region, throughout which variations in the near-surface and deep segments of bio-optical profiles are systematically coupled in a statistical sense.

The area selected for study under this contract spans the northeastern portion of the North Pacific Ocean, extending from 30°N to 62°N latitude and 115°W to 165°W longitude. The principal well-known features of large-scale ocean circulation in the region are illustrated schematically in Fig. 1.1.

The eastward flowing extension of the Kuroshio Current bifurcates as it approaches the west coast of North America at latitudes near 45°N, feeding the southward flowing California Current System (CCS) and the Alaskan Gyre (AG) circulation in the Gulf of Alaska. At scales

> 450 km, the circulation in this region has been shown to maintain a local, time-dependent Sverdrup vorticity balance between the curl of the wind stress and torque associated with strong features in the topography of bottom depth H (e.g. the Mendocino escarpment and large-scale seamount chains extending into the Gulf of Alaska), expressed as the gradient of f/H , where f is the local Coriolis parameter (Niiler and Koblenz 1985).

Seasonal variations in the climatological wind stress patterns of this region also directly force the surface layer in ways which affect the bio-optical characteristics of these ocean circulation features. The climatological pattern of Ekman convergence between 42°N and 30°N is an important factor in the creation and maintenance of the Sub-Arctic Front (SAF) near 42°N and Sub-Tropical Front (STF) near 32°N (Roden 1975, 1977 and 1980). Vertical circulation and mixing of nutrients in these fronts

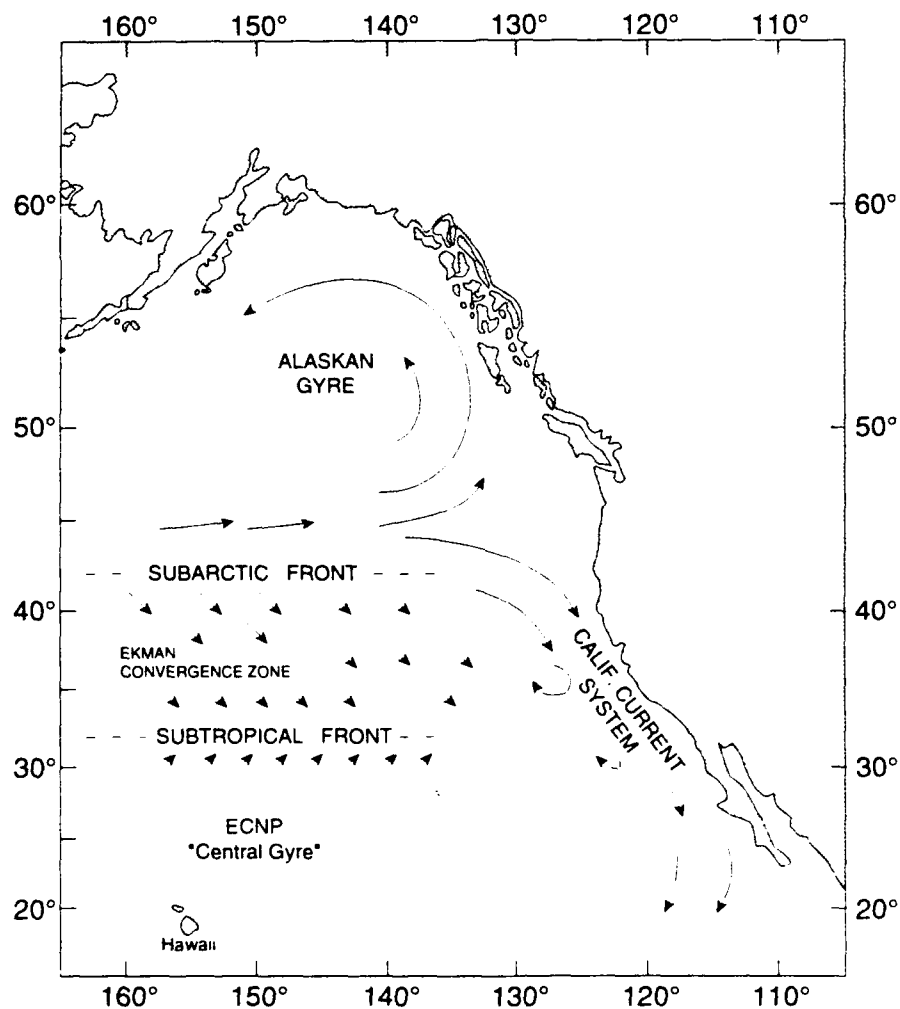


Fig. 1.1. Major ocean currents and fronts in the Northeast Pacific Ocean.

are important factors affecting primary productivity and resulting bio-optical profile characteristics. In the STF (in winter) for example, convergence extends from the surface to depths as great as 300 m (Niiler and Reynolds 1984), whereas the nutricline is typically found near 100 m in these water masses (Pak *et al.* 1988).

The CCS is characterized by slow southward mean surface flow of low salinity sub-arctic water masses along the United States West Coast and Baja California, but with a narrow jet which carries high salinity water (of tropical origin) northward over the inner continental shelf as an undercurrent, which surfaces in winter as the Davidson Inshore Current (Hickey 1979). The CCS extends up to 1000 km offshore, where its cool, low-salinity sub-Arctic water masses transition to the higher salinity ECNP water masses of the oligotrophic central gyre. Productivity is generally greatest near the coast, especially in late spring and summer months when prevailing northerly winds drive intense coastal upwelling over the inner continental shelf (*e.g.* Hickey 1979; Huyer 1983). We typically expect to find a relatively narrow band of high K(490) and phytoplankton pigment concentrations within 50 to 100 km of the coast, therefore, and indeed that has been observed in many published analyses of CZCS imagery of the CCS (*e.g.* Abbott and Barksdale 1991, and other references cited there). Over the continental slope, the CCS is characterized by a rich field of persistent and recurrent eddies, many of which appear to be closely associated with major headlands and related bathymetric features along the coast (*e.g.* Simpson *et al.*, 1984). Many of these eddies are frequently visualized in both infrared and ocean color satellite images (Simpson *et al.*, 1986; Abbott and Barksdale, 1991). The outer shelf and slope regime in the CCS is also characterized by cross-slope jet-like features (Mooers and Robinson, 1984), which entrain cold, turbid water from the inshore upwelling zone and transport it across the shelf and slope in narrow "streamers", which are often present in both thermal and ocean color satellite images (Flament, Armi and Washburn, 1985; Strub *et al.*, 1991).

The bio-optical characteristics associated with these ocean circulation features are obvious in even a cursory perusal of the CZCS K(490) products (Appendix A), and we briefly discuss the appearance and significance of several of the features in Sect. 3.3. We also found that our partition of the region into bio-optical provinces largely followed the geographic patterns and boundaries associated with the large-scale features illustrated in Fig. 1.1 (Sect. 5 and Appendix E).

The Nimbus-7 CZCS was a 6-channel radiometer

which measured images of ocean color in four 20 nm bands at wavelengths of 443, 520, 550 and 670 nm; CZCS channel 5 was a broad-band channel centered at approximately 750 nm, and channel 6 was a thermal infrared channel which failed less than a year after Nimbus-7 was launched in October 1978. The CZCS scan mirror was designed to tilt up to 20° forward or back to scan the ocean surface away from sunglint (an essential feature for an ocean color instrument). The scan-mirror tilt was implemented in such a way that the scan pixel geometry was distorted, and in the 20° forward (northward) tilt mode, the spacing between individual pixels increased to approximately 2 km near the outer edges of the swath. Therefore, a 2 km grid spacing is the smallest resolution to which CZCS data may be resampled without introducing spatial aliasing. In the present study, we have resampled the data onto a Mercator grid at approximately 5 km resolution (Sect. 3.1.4.1) so the possibility of aliasing does not arise. These and other technical characteristics of the CZCS are described in Hovis *et al.* (1980), and in more detail in the manufacturer's final report (Ball Brothers, 1979). CZCS data formats are described below in Sect. 2.1. Algorithms, software and procedures used to process CZCS data to Level-2 and 3 are described in Sect. 3.1.

The CZCS Level-1 data base used for this study was drawn from the archive assembled at the former Visibility Laboratory (VISLAB) at Scripps Institution of Oceanography (SIO) in La Jolla, CA. By the time this project was initiated at the VISLAB in 1987, the laboratory had assembled a virtually complete archive of the global CZCS Level-1 data. These data were stored on 9-track magnetic tape (1600 bpi), with each tape containing 3 CZCS "scenes" in NASA's standard Calibrated Radiance and Temperature Tape (CRTT) format (Wolford, 1980). Each CRTT file contains raw digital counts recorded from the CZCS system over a 2 minute (or less) orbital period, together with housekeeping annotation (gain, tilt-angle, etc.) and approximate image navigation records. A black-and-white photographic transparency, depicting the data content of the 6 CZCS channels, accompanied each CRTT file; these transparencies and catalog records of CRTT file attributes were organized and assembled into a "CZCS Browse Library" by the VISLAB.

The Director of SIO closed down the VISLAB in 1987 (without advance warning) shortly after this project was initiated. SIO management had further determined to retain the CZCS archive, and to transfer its custody to the SIO Satellite Remote Sensing Facility, but they made no immediate specific arrangements to do so in a way that

would preserve the archive's integrity. The present Principal Investigator (Mueller) was at that time the sole major user of the CZCS archive and was dependent on free-of-charge access to carry out the work on this project. It, therefore, fell on this project to organize the physical transfer of the full tape archive to suitable storage facilities on the SIO main campus in La Jolla (albeit with financial support from SIO for transport and facilities), and to extract from that archive the approximately 7000 CRTT files covering the Northeast Pacific study area (Fig. 1.1).

Computer resources needed for this project were also disrupted by the VISLAB shutdown. We dealt with this problem by rebudgeting resources to purchase a used HP-9000/550 workstation and peripherals, and VHS tape drives and controllers. SIO transferred to our custody the 9-track tape drives which had been part of the VISLAB's Prime computer system. And finally, the sponsor (then called NORDA) furnished us with an additional HP-9000/520 workstation on long term loan as Government Furnished Equipment (GFE). This assemblage of equipment gave us the computer tools necessary to pursue the project.

Over the next several months, after the VISLAB was dismantled, we extracted the NE Pacific CRTT scenes, and transferred the files to VHS cassettes. Each VHS cassette is capable of storing up to 150 CRTT files.

The Principal Investigator's appointment as a Visiting Research Oceanographer at SIO expired in April 1988. Because it proved impossible for him to negotiate an acceptable continuing appointment at SIO, he arranged with the San Diego State University Foundation (SDSUF) to establish the new Center for Hydro-Optics and Remote Sensing (CHORS) under the College of Sciences at San Diego State University (SDSU). This and other contracts and grants were transferred from SIO to SDSUF, along with the associated computer equipment.

The project continued at CHORS, by first developing new software to process and analyse the CZCS data base. Functional FORTRAN source code and data processing procedures existed from the earlier work we had done at the VISLAB, but the code was not structured efficiently for handling and processing the data base in the HP-UX (UNIX) operating environment. The principal fault with these FORTRAN codes was that efficient input/output (I/O) of CRTT files could only be handled in HP-UX through C, and efficient I/O is a major factor controlling execution time for this type of data processing. Furthermore, the code structure was not designed to efficiently manipulate and process large numbers of CZCS Level-1

CRTT files when they are stored sequentially on VHS cassettes. The VHS storage media provided a compact and inexpensive archive, but one not well suited for arbitrary random access to selected files. We therefore developed new codes in C to screen the Level-1 VHS cassettes, to batch process Level-1 and Level-2 data and store the Level-2 files on new VHS cassettes, and to resample the Level-2 K(490) data to create Level-3 map products on the Mercator grid we established as the framework for this study. This system of software and procedures, its application to the CZCS Level-1 data base, and the resulting products, analyses and conclusions are covered in Section 3 below.

With the delivery of this Final Report, together with the accompany data base on magnetic tape, we have fulfilled both primary objectives of this project.

The results of our climatological analyses of near-surface ocean optical properties from satellite ocean color imagery are embodied primarily in the time series of CZCS monthly composite mean K(490) maps illustrated in Appendix A, and delivered in digital form in the data base. The information content of the monthly means K(490) distributions is briefly summarized in Sect. 3.3. The time series of CZCS K(490) observations on individual days (but at irregular time intervals), which are also included in the digital data base, are displayed graphically in Appendix D and are briefly discussed in Sect. 3.4. A directory of data files in the delivered data base is contained in Appendix C. The data formats of the Monthly Mean K(490) Map files are described in Sect. 2.1.5, the recipe needed to convert 8-bit byte-encoded values at each map grid point into K(490) in m^{-1} is given in Table 2.1, and conversion of lines and pixel coordinates (in the map arrays) to geographic latitude and longitude is explained in Sect. 2.1.5 and Table 2.2. The storage format of the ASCII files containing each K(490) Time Series is described in Sect. 2.1.7.

The algorithms, procedures and software used to prepare these CZCS data products are described in detail in Sect. 3.1. Sect. 3.2 presents the results of our independent analyses of time dependent change in CZCS radiance responsivity, and the resulting correction model we used in preparing the final version of this CZCS data base. The content and structure of the intermediate CZCS Levels-1, 2 and 3 data bases leading to final production of this climatology are described in detail in Sect. 2.1.1 through 2.1.5. Even though these data sets were not scheduled for delivery, their description fills in many details documenting the overall quality and internal consistency of the end product. Moreover, these working data bases will all be

TABLE 2.1

CZCS LEVEL-2 LOOKUP TABLES
For Converting Byte Indices D_n (0 To 255 Counts)
In CHORS CZCS LEVEL-2 Files To Geophysical Units

i	Variable	D_n	Gain	Conversion	Units
1	$L_w(443, D_{n1})$	0 to 254	1	(float) $D_{n1} \times 0.044$	$\mu W \text{ cm}^{-2} \text{ sr}^{-1} \text{ nm}^{-1}$
		"	2	(float) $D_{n1} \times 0.036$	$\mu W \text{ cm}^{-2} \text{ sr}^{-1} \text{ nm}^{-1}$
		"	3	(float) $D_{n1} \times 0.030$	$\mu W \text{ cm}^{-2} \text{ sr}^{-1} \text{ nm}^{-1}$
		"	4	(float) $D_{n1} \times 0.021$	$\mu W \text{ cm}^{-2} \text{ sr}^{-1} \text{ nm}^{-1}$
		255	-	Bad Data Flag	
2	$L_w(520, D_{n2})$	0 to 254	1	(float) $D_{n2} \times 0.031$	$\mu W \text{ cm}^{-2} \text{ sr}^{-1} \text{ nm}^{-1}$
		"	2	(float) $D_{n2} \times 0.025$	$\mu W \text{ cm}^{-2} \text{ sr}^{-1} \text{ nm}^{-1}$
		"	3	(float) $D_{n2} \times 0.020$	$\mu W \text{ cm}^{-2} \text{ sr}^{-1} \text{ nm}^{-1}$
		"	4	(float) $D_{n2} \times 0.015$	$\mu W \text{ cm}^{-2} \text{ sr}^{-1} \text{ nm}^{-1}$
		255	-	Bad Data Flag	
3	$L_w(550, D_{n3})$	0 to 254	1	(float) $D_{n3} \times 0.25$	$\mu W \text{ cm}^{-2} \text{ sr}^{-1} \text{ nm}^{-1}$
		"	2	(float) $D_{n3} \times 0.020$	$\mu W \text{ cm}^{-2} \text{ sr}^{-1} \text{ nm}^{-1}$
		"	3	(float) $D_{n3} \times 0.016$	$\mu W \text{ cm}^{-2} \text{ sr}^{-1} \text{ nm}^{-1}$
		"	4	(float) $D_{n3} \times 0.012$	$\mu W \text{ cm}^{-2} \text{ sr}^{-1} \text{ nm}^{-1}$
		255	-	Bad Data Flag	
4	$L_w(670, D_{n4})$	0 to 254	1	(float) $D_{n4} \times 0.011$	$\mu W \text{ cm}^{-2} \text{ sr}^{-1} \text{ nm}^{-1}$
		"	2	(float) $D_{n4} \times 0.009$	$\mu W \text{ cm}^{-2} \text{ sr}^{-1} \text{ nm}^{-1}$
		"	3	(float) $D_{n4} \times 0.007$	$\mu W \text{ cm}^{-2} \text{ sr}^{-1} \text{ nm}^{-1}$
		"	4	(float) $D_{n4} \times 0.005$	$\mu W \text{ cm}^{-2} \text{ sr}^{-1} \text{ nm}^{-1}$
		255	-	Bad Data Flag	
5	$L_a(670, D_{n5})$	0 to 254	1	(float) $D_{n5} \times 0.011$	$\mu W \text{ cm}^{-2} \text{ sr}^{-1} \text{ nm}^{-1}$
		"	2	(float) $D_{n5} \times 0.009$	$\mu W \text{ cm}^{-2} \text{ sr}^{-1} \text{ nm}^{-1}$
		"	3	(float) $D_{n5} \times 0.007$	$\mu W \text{ cm}^{-2} \text{ sr}^{-1} \text{ nm}^{-1}$
		"	4	(float) $D_{n5} \times 0.005$	$\mu W \text{ cm}^{-2} \text{ sr}^{-1} \text{ nm}^{-1}$
		255	-	Bad Data Flag	
6	$L_t(750, D_{n6})$	0 to 254	-	(float) $D_{n6}/10.0$	$\mu W \text{ cm}^{-2} \text{ sr}^{-1} \text{ nm}^{-1}$
		255	-	Bad Pixel Flag	
7	Phyto. Pigment Conc. $C(D_{n7})$	0 to 150	-	(float) $D_{n7}/100.0$	mg m^{-3}
		151 to 180	-	(float) $C(D_{n7}-1) + 0.05$	mg m^{-3}
		181 to 254	-	(float) $C(D_{n7}-1) + 0.10$	mg m^{-3}
		255	-	Bad Pixel Flag	
8	$K(490, D_{n8})$	0	-	Missing Data Flag	-
		1	-	0.0220	m^{-1}
		2 to 57	-	$K(490, D_{n8}-1) + 0.0005$	m^{-1}
		58 to 107	-	$K(490, D_{n8}-1) + 0.001$	m^{-1}
		108 to 147	-	$K(490, D_{n8}-1) + 0.005$	m^{-1}
		148 to 192	-	$K(490, D_{n8}-1) + 0.01$	m^{-1}
		193 to 227	-	$K(490, D_{n8}-1) + 0.05$	m^{-1}
		228 to 254	-	$K(490, D_{n8}-1) + 0.1$	m^{-1}
		255	-	Bad Pixel Flag	-
9	$K(520, D_{n9})$	0	-	Missing Data Flag	-
		1	-	0.044	m^{-1}
		2 to 57	-	$K(520, D_{n9}-1) + 0.001$	m^{-1}
		58 to 97	-	$K(520, D_{n9}-1) + 0.005$	m^{-1}
		98 to 142	-	$K(520, D_{n9}-1) + 0.01$	m^{-1}
		143 to 177	-	$K(520, D_{n9}-1) + 0.05$	m^{-1}
		178 to 254	-	$K(520, D_{n9}-1) + 0.1$	m^{-1}
		255	-	Bad Data Flag	-

maintained at CHORS and will be available for future access; we have far from exhausted the information content of this overall CZCS data base in the analyses carried out under the scope of the present project.

The accuracy of daily CZCS K(490) estimates is analysed, in Sect. 4, through direct comparisons with *in situ* ship measurements; they are generally accurate to within 20% (at least during the limited period when ship data were available to us). The CZCS-Ship K(490) comparisons are illustrated graphically in Appendix B.

The second objective of this project was to develop models predicting vertical bio-optical profiles extending to 200 m, from CZCS K(490). This was accomplished through the statistical models giving K(490,z) and chlorophyll *a* fluorescence $F^*(z)$ as functions of CZCS K(490) in specific bio-optical provinces of the Northeast Pacific Ocean. We present these models in Sect. 5 and Appendix E.

2.0 DATA

2.1 CZCS Data

CZCS data used for this study are organized into 3 major levels. Level-1 data consist of NASA's CZCS Level-1 binary CRTT files (Sect. 2.1.1), plus CRTT control records (Sect. 2.1.2) generated locally at CHORS during our initial interactive Level-1 data screening (Sect. 3.1.1). Level-2 data consist of a binary file of radiometric and geophysical parameters (Sect. 2.1.3), together with an associated image navigation file (Sect. 2.1.4), both of which are calculated during Level-2 processing (Sect. 3.1.3). Level-3 data products were also produced locally at CHORS by resampling the Level-2 K(490) values from scan coordinates, at 1 to 2 km resolution, onto a geographically fixed Mercator grid, with approximately 5 km resolution (Sect. 3.1.4); the principal Level-3 products are a time series of Daily Composite K(490) Maps (Sect. 2.1.5), Monthly Composite Mean K(490) Maps (Sects. 2.1.6 and 3.4, and Appendix A), and Time Series of K(490) extracted from the Daily Composite Map series at selected geographic locations (5° latitude \times 5° longitude) (Sects. 2.1.7, 3.5 and Appendix D).

Of these CZCS data products, only the Monthly Composite Mean K(490) Maps and the $5^\circ \times 5^\circ$ K(490) Time Series climatology products are delivered with this report. The other CZCS data products simply represent essential intermediate steps in preparing the end product. The voluminous intermediate CZCS Level-1, Level-2 and daily Level-3 working archives will be maintained at CHORS, and will be available for access in the future (should that be requested).

2.1.1 CZCS LEVEL-1 BINARY DATA FILES

Binary Level-1 data consist of 8-bit digital counts for each of the 6 CZCS channels (as received from the spacecraft), repackaged by NASA into a standardized CRTT format (Wolford, 1980) to add housekeeping data (time, gain, tilt, instrument, temperature, reference lamp readings, etc.) and navigation data (latitudes and longitudes of anchor points distributed across the scan) for each CZCS scan. There are 1968 earth-view pixels recorded for every scan line, and an internal reference lamp was viewed and recorded during the back-scan of every 16th scan. The detailed sequence of CZCS measurements (and associated geometry) during each scan cycle is described in Ball Brothers (1979) final report. The CZCS completed 972 scans per each 2 minute period, and generated approximately 12.4 Mbytes of 8-bit binary data. After pre-screening quick-look images to eliminate orbital image segments which contained no usable CZCS ocean data (i.e. scenes containing only land, or clouds), each usable data segment was broken into orbital segments of up to 2 minutes duration each. Each such 2-minute segment was stored as a single binary CRTT file (together with a short, ASCII header file identifying the scene time and geographic location) on 9-track magnetic tape at 1600 bpi density. NASA stacked 3 CRTT files per tape for distribution and Level-1 archival. A virtually complete archive set of Level-1 CRTT tapes had been delivered to the SIO VISLAB by the time it was disestablished in mid-1987. For the present work, we copied approximately 7000 CRTT files onto digital VHS tape cassettes. The data were organized on the VHS cassettes by month and catalogued in external files; NASA's ASCII CRTT Header Files were not transferred to the CHORS VHS library.

2.1.2 LEVEL-1 CRTT CONTROL RECORDS

During the interactive Level-1 screening of each VHS CRTT image file (Sect. 3.1.2), a control record was generated to preserve all information needed for subsequent Level-2 and Level-3 processing. The information stored in each CRTT control record includes:

- a. Date and time (GMT) when the first scan line was observed, and cumulative numbers of days and orbits since Nimbus-7 launch.
- b. Numbers of scan line records in the file and number of missing lines.
- c. CZCS gain and gain threshold settings.
- d. Nimbus-7 spacecraft attitude (roll, pitch and yaw).
- e. Latitudes and Longitudes of the four corner pixels of the scene.

- f. Lines MINLIN and MAXLIN, and Pixels MINPIX and MAXPIX which delineate the sub-area of the scene containing potentially useful views of ocean areas (as opposed to cloud-covered, or sun-glint contaminated areas).
- g. Flags set to control Level-2 processing, including overall scene rejection/acceptance, the cloud threshold for channel-5, and settings for various other Level-2 processing options.
- h. Nimbus-7 orbital parameters, calculated from the NORAD/NAVSPASUR Nimbus-7 orbit element history, as derived from NORAD radar tracking data.
- i. Greenwich Hour Angle (GHA) and declination of the sun at the GMT of the first scan line.
- j. Identification of the VHS cassette, and sequential file number where the CRTT file is stored.
- k. A flag indicating whether sun-glint was detected in the scene.

The control records for all CRTT files on a single VHS cassette were recorded in a separate control file. The associated control file was then used to control the Level-2 processing of all of the CRTT files (up to approximately 150) on each Level-1 VHS cassette in a single unattended batch run. The control record for an individual CRTT file is also written as the first header record of the new Level-2 file.

2.1.3 CZCS LEVEL-2 BINARY DATA FILES

Level-2 processing (Sect. 3.1.3) first applies radiometric calibration coefficients to the Level-1 CZCS digital counts for each pixel and channel, corrects for time dependent change in the instrument's radiance responsivity (see also Sect. 3.2), and corrects for atmospheric transmission and path radiance contributions to compute water-leaving radiances $L_w(\lambda)$ ($\lambda = 443, 520, 550, \text{ and } 670 \text{ nm}$) and aerosol radiance $L_a(670)$ at 670 nm. The ratios $L_w(443)/L_w(550)$ and $L_w(520)/L_w(550)$ are then used with in-water algorithms to calculate phytoplankton pigment concentrations $C(\text{mg m}^{-3})$ and diffuse attenuation coefficients $K(\lambda) (\text{m}^{-1})$ for $\lambda = 490$ and 520 nm. These calculations are performed for each pixel between the limits MINPIX and MAXPIX for every scan line between MINLIN and MAXLIN. The limits MINLIN, MAXLIN, MINPIX and MAXPIX are selected during the Level-1 Interactive Image Screening process (Sect. 3.1.2) and are passed to the Level-2 processing program as part of the CRTT Control Record (Sect. 2.1.2).

Nine Level-2 variables are computed and saved for each pixel between MINPIX and MAXPIX, for every scan line between MINLIN and MAXLIN. These 9

Level-2 parameters are, in the order stored, $L_w(443)$, $L_w(520)$, $L_w(550)$, $L_w(670)$, $L_a(670)$, $L_t(750)$, C , $K(490)$ and $K(520)$. To compress the data files, each Level-2 parameter is encoded as an unsigned 8-bit integer D_{ni} (ranging from 0 to 255) according to the lookup table recipes given in Table 2.1. In perusing Table 2.1, note that the recipes for C , $K(490)$ and $K(520)$ are recursion relations, which are used to generate floating point conversion arrays (e.g. $C[0]$, $C[1]$, ..., $C[D_{ni}]$, ..., $C[255]$).

The first record saved in a CHORS CZCS Level-2 Data File is the CRTT Control Record (Sect. 2.1.2), which serves as a documentation header for the new file. This record is always 180 bytes in length.

Records 2 through 9 are Lookup-Table arrays LT_i ($i = 1, 2, \dots, 9$) containing values of the 9 Level-2 variables in scaled geophysical units. The integer $LT_i[D_{ni}]$ ($D_{ni} = 0, 1, \dots, 255$) arrays provide an alternative to Table 2.1 for converting the byte-encoded Level-2 variables to geophysical units. The variables and geophysical units associated with these arrays are

$LT_i[D_{ni}]$ ($i = 1, 2, \dots, 5$) are arrays of 4-byte integers corresponding to $L_w(\lambda)$ ($\lambda = 443, 520, 550, 670 \text{ nm}$) and $L_a(670)$, respectively, in $(\mu\text{W cm}^{-2} \text{ sr}^{-1} \text{ nm}^{-1}) \times 1000.0$, for $D_{ni} = 0, 1, \dots, 254$ ($LT_i[255] = 255000$, a bad data flag).

$LT_6[D_{n6}]$ are 4-byte integers corresponding to aperture radiance $L_t(750)$ in $(\mu\text{W cm}^{-2} \text{ sr}^{-1} \text{ nm}^{-1}) \times 10.0$, for $D_{n6} = 0, 1, \dots, 254$ ($LT_6[255] = 2550$, a bad data flag).

$LT_7[D_{n7}]$ are 4-byte integers corresponding to phytoplankton pigment concentrations in $(\text{mg m}^{-3}) \times 1000.0$, for $D_{n7} = 0, 1, \dots, 254$ ($LT_7[255] = 25500$, a bad data flag).

$LT_8[D_{n8}]$ and $LT_9[D_{n9}]$ are arrays of 4-byte integers corresponding to $K(490)$ and $K(520)$, respectively, in $(\text{m}^{-1}) \times 10000.0$, for D_{n8} or $D_{n9} = 0, 1, \dots, 254$ ($LT_8[255] = LT_9[255] = 2550000$, a bad data flag).

The nine Level-2 parameters are each saved, in byte-encoded form (as per the Lookup Table arrays LT_i and/or Table 2.1), for all pixels in a single scan line as a record (array) of bytes

$$D_{ni}[\text{pixel}],$$

where pixel = MINPIX, MINPIX + 1, ..., MAXPIX,
and $i = 1, 2, \dots, 9$.

A composite data record, containing 9 arrays of Level-2 parameters for a single scan line, is $L = 9 \cdot (\text{MAXPIX} - \text{MINPIX} + 1)$ bytes in length. The header record is a fixed size of 180 bytes, and the Lookup Table records are each

1024 bytes in length, for a total of $180 + 9 \times 1024 = 9396$ bytes. The total size of a CHORS CZCS Level-2 file is, therefore, $9396 + L \times (\text{MAXLIN} - \text{MINLIN} + 1)$ bytes. The maximum Level-2 file size, *i.e.* for a full 1968 pixel \times 972 line two minute scene, would therefore be $9396 + 9 \times 1968 \times 972 = 17,225,460$ bytes.

The information needed to determine the geographic position, and solar and view-axis geometries, associated with each pixel in a CZCS Level-2 image file are stored in a separate CHORS CZCS Level-2 Navigation File (Sect. 2.1.4).

The CHORS CZCS Level-2 archive is a very large, intermediate working data base which is not delivered as part of this final report, and therefore, detailed header formats are not given here. This Level-2 archive will be maintained at CHORS, and will be available for future access.

The principal differences between the CHORS CZCS Level-2 archive products and NASA CZCS Level-2 products are:

- The CHORS Level-2 data are produced at full CZCS resolution, whereas the equivalent NASA products are subsampled to 1/4 resolution (every other pixel of every other scan line).
- Different algorithmic models of time dependent degradation of the CZCS radiance responsivities were used in the two Level-2 algorithms (Sect. 3.2).
- K(490) was calculated directly in the CHORS Level-2 products, whereas it was derived indirectly from phytoplankton pigment concentration in the GSFC Level-3 product.
- Pigment concentrations C and K(490) are recorded at finer resolution in the CHORS byte encoding scheme (Table 2.1) than they are in the GSFC version.
- There are differences between NASA and the CHORS implementations of image navigation, cloud overshoot screening, ozone transmittance corrections, K(490) algorithms, aerosol wavelength dependence determination, and $L_w(670)$ algorithms (Sects. 3.1.2 and 3.1.3).

2.1.4 CZCS LEVEL-2 NAVIGATION (NAV) FILES

A separate CHORS CZCS Level-2 NAV file contains the information needed to calculate the geographic latitude and longitude, solar azimuth and zenith angles, and CZCS azimuth and zenith angles at each pixel for which Level-2 parameters are saved in a companion CHORS CZCS Level-2 Data File (Sect. 2.1.3). These six variables are computed for reference pixels spaced at 16 line \times 16

pixel intervals. During CZCS Level-2 and 3 processing (Sects. 3.1.3 and 3.1.4), geographic and geometric data for these reference pixel locations are used for bilinear interpolation of latitude and longitude over 16 line \times 16 pixel grid cells, and of modeled radiometric terms (Rayleigh radiance, diffuse atmospheric transmittance, etc.) over 32 line \times 32 pixel grid blocks.

The navigation record for each reference pixel contains latitude (radians), longitude (radians), the cosine of the CZCS view-axis zenith angle μ , the CZCS view-axis azimuth angle θ (radians), the cosine of the solar zenith angle μ_0 , and the solar azimuth angle θ_0 (radians). All angles are measured at the pixel location, with reference to the local vertical and true North. These six variables are stored in the 4-byte floating point format used by the HP9000/500 series workstations under the HP-UX operating system; the Level-2 NAV files may not, therefore, be directly readable on other manufacturer's computer systems.

In each reference scan line, navigation records are saved at 16-pixel intervals over the extent from pixel MINPIX - 1 to $(\text{MINPIX} - 1) + 32 \times \text{NPIX_BLKS}$, where NPIX_BLKS is the smallest integer such that

$$32 \times \text{NPIX_BLKS} \geq \text{MAXPIX} - \text{MINPIX} + 1.$$

Similarly, the range of navigation reference lines extends from $(\text{MINLIN} - 1)$ to $(\text{MINLIN} - 1) + 32 \times \text{NLIN_BLKS}$, where NLIN_BLKS is the smallest integer such that

$$32 \times \text{NLIN_BLKS} \geq \text{MAXLIN} - \text{MINLIN} + 1.$$

Therefore, a 24 byte NAV record is saved for $(2 \times \text{NPIX_BLKS} + 1)$ pixels in each of $(2 \times \text{NLIN_BLKS} + 1)$ scan lines, so that a CHORS CZCS Level-2 NAV file will be $24 \times (2 \times \text{NPIX_BLKS} + 1) \times (2 \times \text{NLIN_BLKS} + 1)$ bytes in overall size.

For example, consider the Level-2 processing of a full 972 line by 1968 pixel two-minute CZCS CRTT file. We would set NPIX_BLKS = 62 and NLIN_BLKS = 31, and we would compute and save NAV records for 125 pixels 0(16)1984 on each of 63 scan lines 0(16)992. The total size of the NAV file for this full-size Level-2 scene would be $24 \times 125 \times 63 = 189\text{K}$ bytes.

The CHORS Level-2 NAV file and binary data file archives were not created as deliverable products. Therefore, we have not had occasion (or resources) to convert our Level-2 NAV files from their HP9000/500 series binary floating point representation into a more portable format. This archive will be maintained at CHORS, and it will be available for future access.

2.1.5 CZCS LEVEL-3 DAILY COMPOSITE K(490) MAPS

The primary CZCS Level-3 working data base created for this study consists of a time series of digital K(490) map files, with each map retaining data for a single day. For each day between November 1978 and June 1986 on which usable CZCS observations exist for the study area, all Level-2 K(490) data were resampled

onto a Mercator grid (Sect. 3.1.4). This grid covers the Northeast Pacific Ocean with 962 lines of 1002 pixels (or grid cells); lines of pixels are oriented zonally. The latitude and longitude limits of the grid, and recipes to convert grid cell (line, pixel) indices to geographic (latitude, longitude) coordinates are recorded in Table 2.2. The detailed parameters and algorithms used to generate the conformal Mercator projection are described in Sect.

Table 2.2

Latitude and Longitude Coordinates of CZCS K(490) Lines and Pixels in Mercator Grid Files

Upper Left-Hand Corner: Line = 0, Pixel = 0
Lat. = 62.890°N, Long. = 165.000°W

Lower Right-Hand Corner: Line 961, Pixel = 1001
Lat. = 30.000°N, Long. = 114.95°W

Longitude = 165.000° - Δ Lon. * Pixel
Δ Lon. = 0.050° (3.0 arc minutes)

Grid Line	N. Lat. (dec. degrees)	Grid Line	N. Lat. (dec. degrees)
0	62.890°	520	48.453°
20	62.431°	540	47.785°
40	61.966°	560	47.109°
60	61.493°	580	46.424°
80	61.013°	600	45.731°
100	60.525°	620	45.028°
120	60.030°	640	44.317°
140	59.528°	660	43.597°
160	59.018°	680	42.869°
180	58.500°	700	42.131°
200	57.974°	720	41.385°
220	57.441°	740	40.630°
240	56.899°	760	39.866°
260	56.350°	780	39.094°
280	55.793°	800	38.313°
300	55.227°	820	37.523°
320	54.653°	840	36.725°
340	54.071°	860	35.919°
360	53.481°	880	35.104°
380	52.882°	900	34.281°
400	52.275°	920	33.449°
420	51.659°	940	32.610°
440	51.035°	960	31.762°
460	50.40°	980	30.907°
480	49.761°	1000	30.043°
500	49.111°	1001	30.000°

3.1.4.1 below. The procedures used to resample Level-2 K(490) data to fill in the Mercator grid cells are described in Sect. 3.1.4.2.

All Level-2 K(490) records for a given day were resampled to fill in the observed ocean cells of a single 962×1002 byte digital Daily Composite K(490) Map file. Observed CZCS K(490) data are written, in byte-encoded form (Table 2.1), into the cells at appropriate grid locations following a "nearest-neighbor" selection criterion (Sect. 3.1.4.2). Grid cells without a valid CZCS K(490) observation on that day retain their initial value of "zero". The data in a Daily Composite K(490) Map comprise a 2-dimensional array of type unsigned characters (*i.e.* binary byte) K490[962][1002]; following the data storage convention of the C language, the first 1002 bytes in the file represent the pixels of line 0, the next 1002 bytes represent the pixels of line 1, and so forth. Each Daily Composite K(490) Map file is approximately 964K bytes in size, and all such files for a given month are stored on a VHS cassette as a CPIO tape archive file of a single UNIX directory.

The Level-3 Daily Composite K(490) Maps comprise a very large data base (containing mostly zero's). It was created as a necessary intermediate step in creating the final Monthly Composite Mean K(490) Map climatology (Sects. 2.1.5, 3.1.4 and 3.3, and Appendix A), and the task of reformatting and copying it onto a portable media is beyond the scope of the present project. As with the other intermediate CZCS data bases, it will be maintained at CHORS, should access be requested in the future.

2.1.6 CZCS LEVEL-3 MONTHLY COMPOSITE MEAN K(490) MAPS

For each month, the Daily Composite K(490) values at each grid cell were averaged and stored in Monthly Composite Mean K(490) maps, on the same Mercator grid described in Sects. 2.1.5 and 3.1.4.1. The number of observations contributing to the composite mean K(490) in each grid cell were retained in a separate file. Mean K(490) values in these files are byte-encoded, following the recipe in Table 2.1. Numbers of observations in each cell are also recorded and filed as binary unsigned 8-bit integers (0, 1, ..., 255).

Each Monthly Composite Mean K(490) Map array is stored in a 962×1002 byte binary file, named according to the format MMYYY.m.K490, where "MMM" is the month (Jan, Feb, Mar, Apr, May, Jun, Jul, Aug, Sep, Oct, Nov, or Dec), "YY" are the last two digits of the year, and "m" denotes the mean files. The associated 962×1002 byte Sample Size file for each month is named, following

a similar convention, in format MMYYY.n.K490, where "n" denotes a Sample Size file and the other characters are the same as described above for the mean file names.

The up to 12 Monthly Composite Mean K(490) files and 12 Monthly sample size files for a given year are delivered as a separate TAR (tape archive) file on 9-track magnetic tape (6250 bpi, blocksize = 10,240; see also Appendix C). The size of each year's TAR file is approximately 23.15 Mbytes (1978 and 1986, being only partial years of CZCS operation, are smaller). To convert the byte-encoded K(490) values to m^{-1} , use Table 2.1. To convert grid line and pixel indices (0 to 961 and 0 to 1001) to latitude and longitude respectively, interpolate using the data from Table 2.2 and ancillary grid descriptions in Sect. 2.1.5.

Color encoded images of the Monthly Mean K(490) Maps were annotated and displayed on the color video screen of our HP9000/550 computer (Sect. 3.1.4.2). Due to equipment limitations, the displayed images were sub-sampled to 1/4 resolution (481 lines \times 510 pixels). Color photographs were taken of each Monthly Composite Mean K(490) Map display, using a 35 mm camera. Color xerographic copies of these photographs were then made to assemble the Atlas of Monthly Mean CZCS K(490) Maps included here as Appendix A.

2.1.7 CZCS LEVEL-3 K(490) TIME-SERIES AT 5° LATITUDE \times 5° LONGITUDE GRID POINTS

Time series of CZCS K(490) estimates were extracted from the Daily Composite K(490) Map series (Sect. 2.1.5) at a few selected grid points. The purpose of this data product is to illustrate examples of CZCS K(490) sampling frequency and temporal variability in various sub-regions of the Northeast Pacific Ocean study area (Fig. 3.1.5 and Sects. 3.1.4.4 and 3.4). Examples of CZCS K(490) time series are displayed graphically in Appendix D for several locations distributed at 5° latitude \times 5° longitude grid intervals (Fig. 3.1.5).

The time series of K(490) at each 5° latitude \times 5° longitude grid point is recorded in a separate file, which is named according to the convention "LL_III.Ks", where LL are integer degrees of North Latitude and III are integer degrees of West Longitude. The suffix ".Ks" denotes the ASCII version of each file, which is delivered along with this Final Report (a separate binary version is retained also at CHORS and is denoted with suffix "*.ks"). Each ASCII "K-series" file contains a brief header identifying the variable formats and location of the K(490) time series; the end of the header information is marked by the

character '@'. The time series data follow in 3 columns of tab delimited data:

- Col. 1: Days elapsed since 31 Dec. 1978, in ASCII integer format (FORTRAN I4).
- Col. 2: Median $K(490) \text{ m}^{-1}$ in the $5 \text{ line} \times 5 \text{ pixel}$ grid box centered at the nominal location (Sect. 3.1.4.4), in ASCII floating point (FORTRAN F8.4) format.
- Col. 3: Estimated standard deviation of $K(490) \text{ m}^{-1}$ in the 5×5 grid box at the site (Sect. 3.1.4.4), in ASCII floating point (FORTRAN F8.4) format.

Each data record [day, median $K(490)$, and standard deviation] is terminated by an ASCII newline character. We have not included "zero" records, for days when the CZCS did not observe a given site, so that file size varies widely at the various grid locations (Sect. 3.4 and Fig. 3.1.5).

All $5^\circ \text{ Latitude} \times 5^\circ \text{ Longitude } K(490) \text{ Time Series}$ files were collected in a single directory and are delivered as a single TAR (Tape Archive) file on 9-track magnetic tape (6250 bpi, blocksize = 10,240; see also Appendix C).

2.2 Ancillary Data

The orbital elements calculated by the U.S. Navy's NAVSPASUR Center in Dahlgren, VA., using radar tracking data from the North American Radar Air Defense (NORAD) system, are generally regarded as being the most accurate record of the Nimbus-7 orbit history. The NAVSPASUR Nimbus-7 ephemeris history was used for all Nimbus-7 orbit and CZCS pixel geolocation computations (Sects. 3.1.2 and 3.1.3).

The Nimbus-7 Gridded TOMS Ozone Concentration time series were obtained from NASA GSFC. The TOMS ozone analysis was produced by the Nimbus Observation Processing System (NOPS) at GSFC (NOPS, 1986; Bowman and Krueger, 1985). For each Level-1 CRTT file, we extracted a 9×17 array of ozone concentrations in Dobson Units (DU). The 9×17 ozone grid locations are spaced at line and pixel intervals of 128 each, corresponding to lines 0(128)1024 and pixels 0(128)2048 in the associated Level-1 CZCS CRTT. These extended grid limits easily cover the largest possible CRTT file. Each ozone record is a data structure containing three 16-bit integers identifying: 1) the sequential file number, on a particular VHS cassette, of the Level-1 CRTT file to which the ozone data is to be applied, 2) the sequential day of the year, and 3) the year, followed by the 9×17 array of ozone concentrations in DU, each of which is recorded

as a 16-bit integer. A separate auxiliary file of ozone records was assembled for each CZCS Level-1 VHS cassette in the CHORS archive. The total size of a CRTT's ozone record is $2 \times (3 + 9 \times 17) = 312$ bytes. An ozone auxiliary file for a Level-1 VHS cassette containing 150 CRTT files, for example, would be 46.8 Kbytes in overall size.

In preparing our final version of the CZCS Level-2 data base (Sect. 2.1.3), Rayleigh radiances $L_R(\lambda)$ in $(\mu\text{W cm}^{-2} \text{ sr}^{-1} \text{ nm}^{-1})$, were generated using the multiple scattering model of Gordon, Brown and Evans (1988). Their model results were implemented at CHORS using numerical lookup tables of polynomial coefficients provided by the University of Miami (R.H. Evans, personal communication, 1989). These coefficients were determined, by Gordon, Brown and Evans (1988), to provide a means to economically interpolate their radiative transfer solutions for normalized Rayleigh radiance $I_R(\lambda)$ to arbitrary combinations of solar zenith and azimuth angles, and view axis zenith and azimuth angles. Our application of the University of Miami's Rayleigh radiance coefficient tables is described in Sect. 3.1.3.

The Word Data Bank II (WDB-II) digital representation of coastlines and islands was used to overlay these features on the map displays prepared for this study (e.g. Appendix A). WDB II was prepared by the U.S. Central Intelligence Agency and is distributed to the general public through NTIS (Anderson *et al.*, unpublished internal WDB-II documentation, *ca.* 1980).

2.3 In Situ Irradiance and Chlorophyll *a* Fluorescence Profiles

Measured vertical profiles of downwelling spectral irradiance $E_d(490, z)$ at a wavelength of approximately 490 nm, and the derived profiles of attenuation coefficients $K(490, z)$, were essential for two aspects of this study. First, they were used to estimate the accuracy of remote sensing $K(490)$, as estimated using Nimbus-7 CZCS data (Sect. 4.0 and Appendix B below). Second, these profiles were the basis for statistical models relating remote sensing $K(490)$ to the vertical profiles of $K(490, z)$ and chlorophyll fluorescence $F(z)$ (Mueller and Lange, 1989: reproduced here as Appendix E, and see Sect. 5.0 below).

In situ vertical profiles of $E_d(\lambda, z)$, $K_d(\lambda, z)$ and $F(z)$ were available at CHORS from four separate cruises in the Northeast Pacific Ocean. These were the ODEX cruise of the R/V Acania in Oct./Nov. 1982, (Scripps Inst. of Oceanogr., SIO Ref. 87-23), the ODEX/VISLAB cruise of the USNS DeSteiguer in Oct./Nov. 1982 (Scripps Inst.

Oceanogr., SIO, TM: DL-001-83t), the Oregon State University cruise aboard the R/V Discoverer in Jun./Jul. 1985 (Oregon State University, OSU Opt. Oceanogr. Group Cruise Data Rep., and Pak *et al.*, 1988), and the VISLAB cruise, aboard the USNS DeSteiguer in the Northeast Pacific and Bering Sea Jun./Jul. 1985 (Scripps Inst. Oceanogr., SIO VISLAB TM: EN-009-85t).

The geographic tracklines followed during these four cruises are illustrated in Fig. 2.1 [and in Fig. 1 of Mueller and Lange (1989: copy included here as Appendix E)]. $E_d(\lambda, z)$ and $F(z)$ profiles were both measured simultaneously at stations during the Acania (1989) and Discoverer (1985) cruises, but only $E_d(\lambda, z)$ profiles were measured at stations during the two DeSteiguer cruises (1982 and 1985). These data were available as digital tables of depth z , downwelling spectral irradiances $E_d(490, z)$ (μW

$\text{cm}^{-2}\text{nm}^{-1}$) and chlorophyll a fluorescence $F(z)$ (recorded as fluorometer response in volts). The data were tabulated at depth intervals of 1 m.

Data from all four of the above cruises were used for bio-optical province model analyses (Sect. 5.0, and Appendix E). Only the station data from the two Oct./Nov. 1982 cruises were useful for CZCS K(490, z) accuracy assessment (Sect. 4.0 and Appendix B), because very sparse CZCS coverage of the region in the summer of 1985 did not include any of the station locations from either the Discoverer or DeSteiguer cruises in that year.

3.0 CZCS DATA PROCESSING AND ANALYSES

3.1 Methods

The computer software and procedures used at CHORS, to prepare the CZCS data products reported

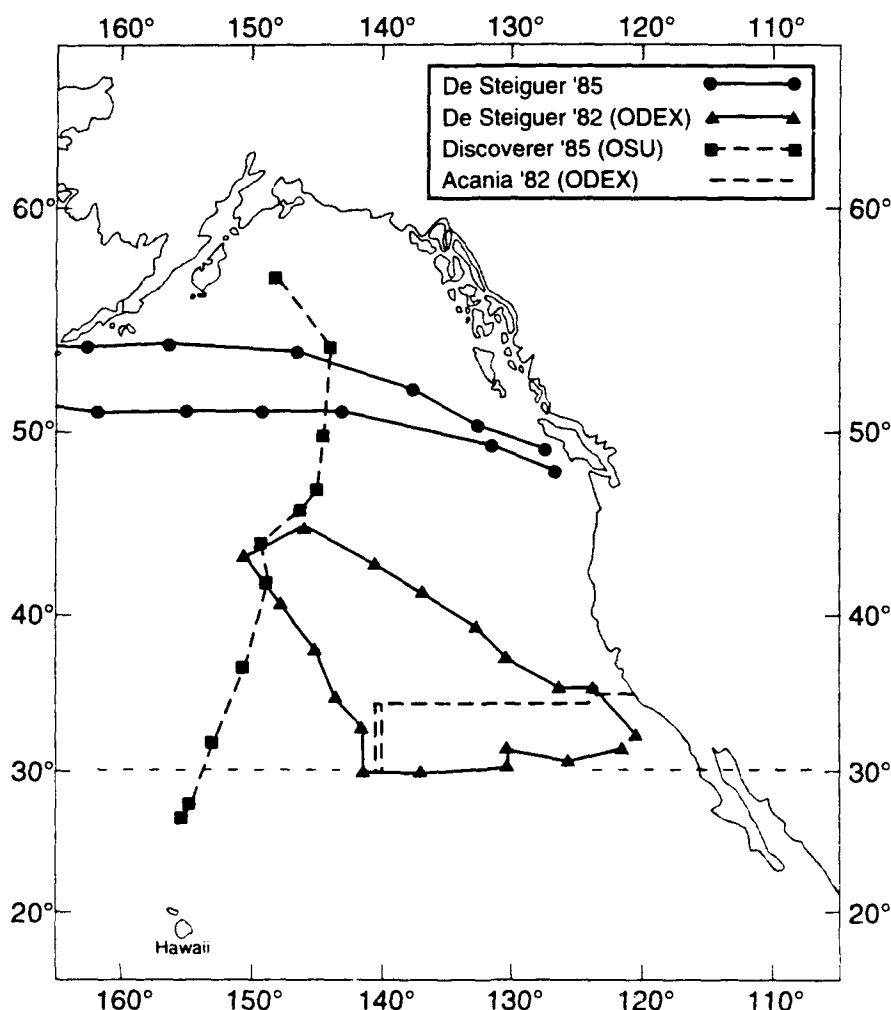


Fig. 2.1. Tracklines of research vessel cruises, during which were measured the *in situ* profiles of spectral irradiance $E_d(\lambda, z)$ and chlorophyll a fluorescence $F(z)$ used in this study to develop bio-optical profile models and to estimate the accuracy of CZCS K(490) determinations.

here, were implemented independently from those used in preparing the NASA GSFC CZCS products, and other well known counterparts. The algorithms and ancillary data sets underlying the present analyses are, for the most part however, identical to those used in the other products, with the following significant exceptions:

1. The histories of temporal change in the radiance responsivities of CZCS channels 1, 2 and 3 were analysed and modeled independently in the course of the present project (Sect. 3.2). This is the most significant quantitative distinction between this and CZCS data products produced elsewhere.
2. The CHORS intermediate CZCS Level-2 data base (Sect. 2.1.3 and 2.1.4) retains the full resolution of the CZCS Level-1 data files. This stands in contrast to the NASA GSFC 1/4 resolution Level-2 product, but other CZCS Level-2 and 3 data products have been produced previously at full resolution (e.g. the "West Coast CZCS Time Series" at NASA's Jet Propulsion Laboratory in Pasadena, CA).
3. CZCS data from areas possibly affected by the cloud overshoot effect (Mueller, 1988) have been rigorously and conservatively screened out of the present Levels-2 and 3 data products. We are uncertain of the extent to which this filter has been imposed on CZCS data products created elsewhere.

The three levels of CZCS data, and the principal data sets in each level, were introduced under Sect. 2.1. There are three corresponding levels of CZCS data processing and analysis which will be introduced and described below. The relationship of each external data set (subsections of 2.1) to the 3 separate sets of CZCS data processing modules is outlined schematically in Fig. 3.1.1. The Levels 1, 2 and 3 Processing Modules and Procedures are described in Sects. 3.1.2, 3.1.3 and 3.1.4, respectively.

As was explained briefly in the Introduction (Sect. 1.0), and alluded to in Sect. 2.1, all of the external CZCS data sets used and/or generated in this project (Fig. 3.1.1 and Sect. 2.1) were archived and accessed as digital files on VHS cassettes. The organization and management of this overall data base is described below in Sect. 3.1.1.

The CZCS data base was processed completely in three separate (and sequential) end-to-end passes (Fig. 3.1.1). These 3 complete versions of CZCS Level-2 and Level-3 products are denoted "Provisional Series 1", "Provisional Series 2", and "Final".

The Provisional Series 1 data set was produced using a linearized single-scattering Rayleigh radiance model

(Gordon *et al.*, 1983b), a fixed set of nominal ozone optical depths, early estimates of extraterrestrial solar spectral flux (Neckel and Labs, 1981), the K(490) algorithm of Austin and Petzold (1981) (exclusively in all cases), and corrections for time dependent variations in radiance responsivities of the CZCS channels made using locally developed extensions of Mueller (1985) through Nimbus-7 orbit number 30,000. This first series of end-to-end CZCS products provided a framework for developing and diagnostically examining the new, locally-developed software comprising the Levels-1, 2 and 3 process modules (Fig. 3.1.1). Provisional Series 1 also provided a baseline against which we could compare previously published CZCS products, assess the impact of improved or modified algorithms, and develop internal quality control procedures for verifying the Level-2 and 3 CZCS data products. The Provisional Series 1 data base was also used to provide a framework for our initial bio-optical province model analyses and development (Mueller and Lange, 1989), an important result of which was that this version of CZCS K(490) estimates were chronically and significantly higher than *in situ* measurements throughout the study area.

The "Provisional Series 2" CZCS data set was calculated following the implementation, at CHORS, of several improved algorithms. The multiple-scattering Rayleigh radiance model of Gordon, Brown and Evans (1988) was implemented using tables provided courtesy of R.H. Evans (University of Miami). The revised spectral solar flux values of Neckel and Labs (1984) were substituted for the less accurate values used previously (Neckel and Labs, 1981). The CZCS responsivity correction models were adjusted following the recommendations of Gordon, Brown and Evans (1988). Finally, the revised K(490) algorithm of Mueller, Trees and Arnone (1990) was inserted to augment the Austin and Petzold (1981) algorithm in turbid water areas. The Provisional Series 2 data products were carefully compared to their corresponding Provisional Series 1 counterparts to understand the (often subtle) relative effects of the new algorithms, and to verify that they were implemented correctly in the revised Level-1 screening and Level-2 software modules. Level-3 modules were not affected.

Finally, the Provisional Series 2 products were examined critically to determine whether the multiple-scattering Rayleigh radiance model (Gordon, Brown and Evans, 1988), and other algorithm changes, had sufficiently improved the agreement between *in situ* measurements and CZCS estimates of K(490). Despite some notable improvements at pixel locations where solar zenith angles

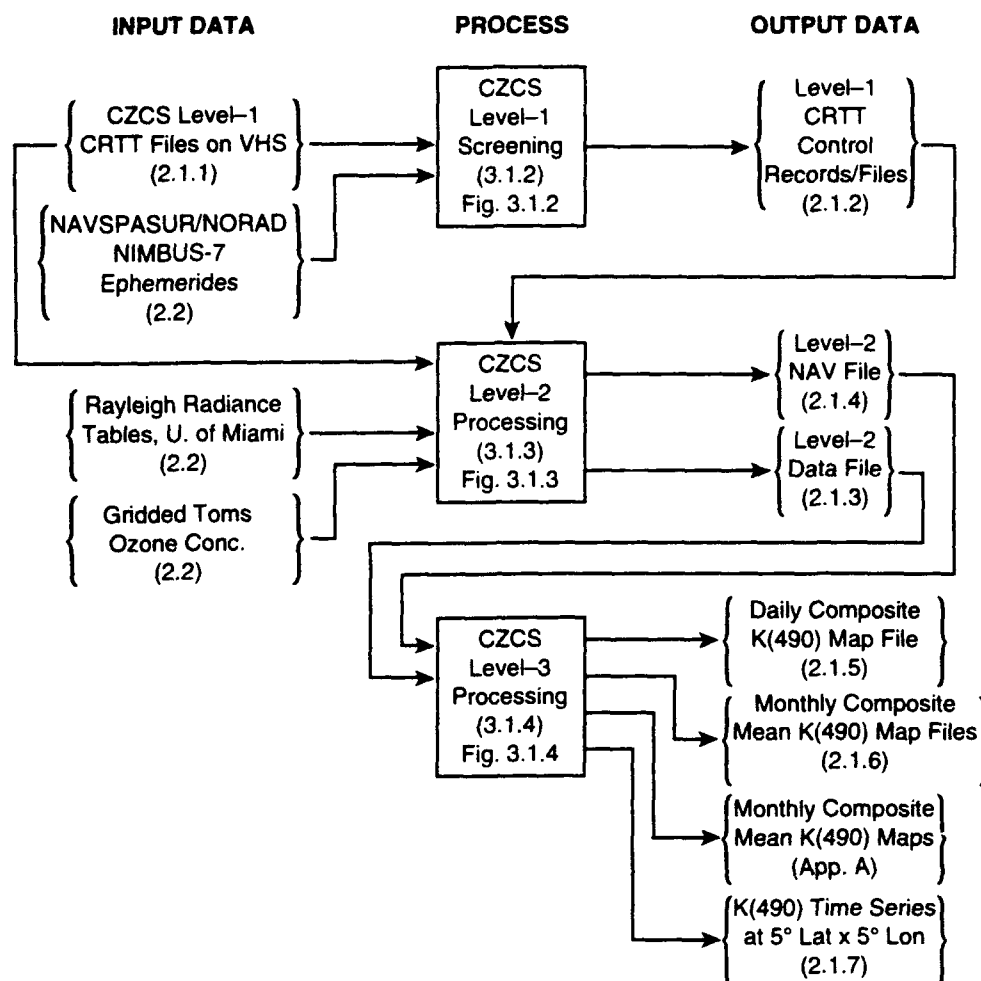


Fig. 3.1.1. CZCS Data Processing: Top level process design and data flow schematic for CZCS data processing and analysis software and procedures. Data sets are enclosed in { } brackets, process steps are enclosed in rectangular boxes, and arrows denote data flow. Numbers in parenthesis indicate the section of this report where a data set or process is described. Fig. numbers refer to the design and data flow schematics which illustrate the individual process steps in more detail.

exceed 30°, the Provisional Series 2 CZCS K(490)'s obviously continued to chronically overestimate *in situ* observations. We therefore undertook the analyses described below in Sect. 3.2, to develop a revised set of models to correct for time-dependent variabilities in radiance responsivities of the CZCS channels.

Finally, we implemented our improved model of CZCS responsivity decay [equations (3.2.6)] into the processing software. At this stage we also implemented an improved ozone transmittance model using the Nimbus-7 Gridded TOMS Ozone Concentration data base produced and distributed by the Nimbus Observing Processing System (NOPS) at NASA's GSFC (NOPS, 1983; Bowman and Krueger, 1985). With these upgrades installed and verified, we repeated the Level-2 and Level-

3 process steps for the third time to produce the full Final Series of CZCS Level-2 and Level-3 external data sets outlined in Fig. 3.1.1. The accuracies of the CZCS K(490) estimates in this final product, which are much improved over our two earlier versions, are analysed in Sect. 4.

3.1.1 DATA BASE MANAGEMENT

To economically handle the extremely large CZCS data base (Sect. 2.1), we configured our HP-9000/500 workstations with three Gigastore VHS cassette drives, (manufactured by Digi-Data Corp., Jessup, Md.), and three standard 9-track computer tape drives, salvaged from the SIO VISLAB computer system when it was shut down (Sect. 1.0). We selected the VHS cassette drives, because they used the same Pertec Standard interface used by the 9-track drives. This commonality allowed us

to control both types of tape drives over each HP-9000/500 workstation's built-in HP-IB interface, via two Dylon Model 1015 Tape Controllers (manufactured by Liken Industries Inc., of Irvine, CA.), one of which was already available to us as surplus VISLAB equipment.

All of the CZCS data sets (Sect. 2.1) used in this study are archived on VHS cassettes, which were also used to backup the operating systems, software, and other miscellaneous data sets used on the HP9000/500 workstations. In addition, the Level-1 CRTT files and all Level-2 and 3 data files were accessed from, and/or saved to, VHS cassettes during batch execution of the process modules (Fig. 3.1.1); this procedure was dictated by the severe disk space limitations of our workstations (135 Mbytes on the HP-9000/550 and 70 Mbytes on the HP-9000/520).

At the outset of the project, the VISLAB CZCS Browse Notebooks were searched to identify all CZCS Level-1 CRTT images which could possibly provide usable data segments within the geographic limits of the study area. These CRTT files were then located, on 9-track tapes (1600 bpi), in the VISLAB CZCS Archive (which by then had been relocated to temporary storage on campus at SIO) and copied to VHS cassettes. We attempted to order the CRTT's sequentially on the VHS cassettes by date (to the extent possible), but the 3 files on a given CRTT tape were often not stored in time sequence. Again to the extent possible, the CRTT files for a single month were stored together on one VHS cassette. Altogether, approximately 7000 CRTT files were copied from more than 2500 9-track tapes and stored on approximately 95 VHS cassettes.

The contents of each VHS cassette were initially catalogued in text files by the computer operators. A more accurate and comprehensive catalogue of the contents of each CRTT VHS cassette was generated automatically, and recorded in its Level-1 VHS CRTT Control File (Sect. 2.1.2), during interactive Level-1 data screening (Sect. 3.1.2). The Level-1 VHS CRTT Control Files are maintained on-line, but were periodically backed up to CPIO directory archive files on VHS cassettes during the progress of the work.

During Level-2 processing, the Level-1 VHS CRTT Control File for a single cassette was used to control the batch processing of all usable CRTT files on that cassette. A control script was used to first search to each CRTT file scheduled for processing, and to read that file into temporary storage on disk. The resulting Level-2 NAV (Sect. 2.1.4) and Data (Sect. 2.1.3) files were first written to temporary disk storage, and then both were transferred to

an output Level-2 VHS cassette on a second VHS drive. The control script automatically maintained a catalog of Level-2 file pairs stored on a given Level-2 VHS cassette. The Level-1 CRTT file and Level-2 NAV and Data files were then all erased from disk storage, and the procedure was repeated for the next input CRTT, and so forth.

During Level-3 processing (Sect. 3.1.4) to create the Daily Composite K(490) Map products (Sect. 2.1.5), each pair of Level-2 NAV and Data files in a given month was read from Level-2 VHS cassette to temporary disk storage. The CZCS K(490) data from all pixels which were "nearest neighbors" of a Mercator grid cell's geographic location were copied into the corresponding line and pixel index of the appropriate Daily Composite K(490) Map file array (Sect. 2.1.5). After all K(490) values were so copied, that pair of Level-2 files was erased from disk, and the next scheduled pair of Level-2 NAV and Data files was read onto disk to repeat the process. All Daily Composite K(490) Map files for a given month were maintained on-line in disk storage until all Level-2 files for that month had been accessed from the VHS Level-2 archive and resampled onto the appropriate day's map file. Level-2 VHS catalog files created during Level-2 processing were used to schedule files for resampling during a given run.

After all the Level-3 Daily composite K(490) Maps for a given month were completely assembled on disk, each map was color-encoded and displayed for visual inspection and quality control. After any data anomalies were dealt with, the Daily Composite K(490) Maps for the month were averaged to create the Monthly Composite Mean K(490) Map file, and its associated sample size file, for the month (Sect. 3.1.4.3). Finally, each Daily Composite K(490) and Monthly Composite Mean K(490) was color-encoded, annotated, displayed on the computer screen, with grid and coastline overlays, and photographed; a color 35-mm slide of each map is maintained in a set of browse notebooks at CHORS. The entire set of Daily Composite K(490) Map files and Monthly Composite Mean K(490) Map files for that month was then transferred to VHS cassette as a CPIO archive directory file. All Level-3 files for that month were then erased from disk storage and the process was repeated for the next month, and so forth.

The K(490) 5° Latitude × 5° Longitude Time Series (2.1.7) was extracted by reading each month's Daily Mean K(490) Map directory from the VHS Level-3 archive to temporary disk storage, extracting non-zero K(490) data from the selected grid locations, erasing the

map files from disk, and proceeding to the next month. The resulting K(490) Time Series data set is relatively small and is maintained on-line in disk storage.

3.1.2 LEVEL-1 SCREENING and PROCESSING

This module is a semi-automated, interactive procedure designed to extract essential process control and data file identification parameters from the internal documentation records of each CRTT file, to visually examine the CRTT image and reject scenes (or sub-areas) which

contain no usable data, to calculate and record orbit parameters and solar ephemeris data, to determine and record aerosol Angstrom coefficients, and to catalog the file number and VHS cassette identification where the CRTT is located in the Level-1 VHS archive. The sequence of major process steps in this module is outlined schematically in Fig. 3.1.2.

The operator sequentially processes each CRTT file on a VHS cassette. Each CRTT file is first read to temporary disk storage.

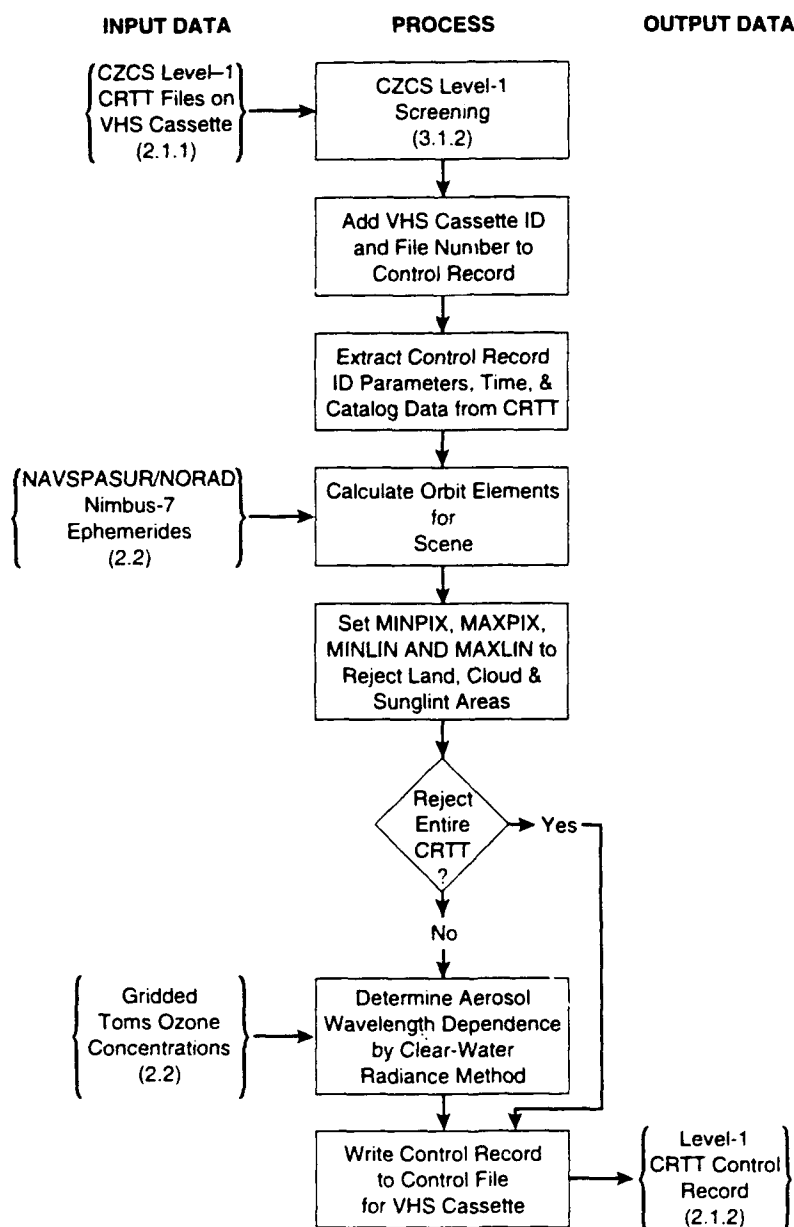


Fig. 3.1.2. CZCS Level-1 Data Screening: Process design and data flow schematic following the conventions described for Fig. 3.1.1.

A new CRTT control record is initialized by first cataloging the Level-1 VHS cassette Identification Index and File Number where the CRTT is stored, and then extracting the following information from the CRTT file's internal documentation:

- a. Date and time (GMT; corrected for a 124 msec clock error) when the first scan line of the file was recorded.
- b. The cumulative numbers of days and orbits since Nimbus-7 was launched.
- c. Missing line data.
- d. Gain and gain threshold settings.
- e. Instrument tilt, and spacecraft roll, pitch and yaw angles.
- f. Approximate latitudes and longitudes of the four corners of the scene image.

The NAVSPASUR/NORAD Nimbus-7 orbit ephemeris data (Sect. 2.2) are next used to calculate the ascending node time (GMT) and longitude, argument of perigee, eccentricity, inclination, orbit rotation rate, semi-diameter and effective period of the Nimbus-7 orbit during which the CZCS CRTT data were obtained. These variables are recorded in the CRTT control record (Sect. 2.1.2).

The solar Greenwich Hour Angle (GHA) and declination, which define the geographical position of the sun at the time (GMT) of the first line, are calculated using an abbreviated version of the solar almanac algorithm developed by Wilson (1980).

The geographic coordinates of the four corners of the image are then listed on the screen. If all four corners fall outside the limits of the study area, the operator has the option to skip the CRTT file. If the entire scene is rejected, the default CRTT control record is so annotated and written to the control file in its proper sequential location.

If the scene is accepted to this point, CZCS channel 5 of the image is masked for "electronic overshoot" and displayed on the console as a gray-shade image.

The "electronic overshoot mask" eliminates data in each scan line for some distance to the right of the edges of bright clouds. When the CZCS views bright clouds, the detector signal level exceeds its designed full-scale range, and in effect, "overdrives" the analog amplifiers in each channel. It takes each amplifier some time to recover normal operations after the scan proceeds over water past the edge of a cloud bank, a phenomenon called "electronic overshoot". To avoid artifacts in areas affected by electronic overshoot, we used the model reported by Mueller (1988) to predict the suspect area to the right of each cloud edge and overwrote that data segment with saturation values ($D_n = 255$) to mask them as apparently cloud covered.

At this point, the operator uses the cursor to extract MINPIX, MAXPIX, MINLIN and MAXLIN indices, which limit the area of the CRTT to be processed to create Level-2 and 3 data. These limits are set to exclude areas of the scene which are wholly covered by clouds or land, as well as open water areas of the image where sunglint contamination is apparent.

Finally, the operator uses the cursor to select several open-water pixels in offshore areas where low-chlorophyll, clear water conditions are likely to be found which may be suitable for aerosol Angstrom exponent determinations. The CZCS raw digital count data for channels 1 through 4 are extracted from the CRTT file for the 5×5 pixel array centered on each selected pixel. The full set of Level-2 computations (Sect. 3.1.3) are carried out on this small data sample, and used to calculate Angstrom exponents from aerosol radiance $L_a(\lambda)$ estimates computed using the "clear-water radiance model" of Gordon and Clark (1981). The results of these computations are then displayed and examined. The results are accepted only if pigment concentration $C \leq 0.30 \text{ mg m}^{-3}$ and aerosol radiance $L_a(670) \geq 0.5 (\mu\text{W cm}^{-2} \text{ sr}^{-1} \text{ nm}^{-1})$. If one, or more, acceptable clear-water radiance sites are found by this procedure, the operator selects an aerosol Angstrom coefficient for the scene that is representative of these results, otherwise the coefficient defaults to 0.0 (wavelength-independent aerosol radiance).

The completed CRTT Control record is then written to the Level-1 CRTT Control File (Sect. 2.1.2) and the operator repeats the entire procedure for the next CRTT file on the VHS cassette.

3.1.3 LEVEL-2 PROCESSING

The CRTT files (Sect. 2.1.1) on each Level-1 VHS cassette were batch processed, using information from the associated file of CRTT Control Records (Sects. 2.1.2 and 3.1.2), to produce a corresponding set of Level-2 NAV and DATA files (Sects. 2.1.4 and 2.1.3). The overall Level-2 process, and its relationship to external CZCS and ancillary data sets, is outlined schematically in Fig. 3.1.3.

The shell command script first examines each CRTT Control Record (Sects. 2.1.2 and 3.1.2) to determine whether or not the next CRTT file on the Level-1 VHS cassette has been accepted or rejected for processing. If the file has been rejected, the script skips that file on the VHS and proceeds to the next. When a CRTT file is accepted, the command script reads the CRTT file from VHS cassette into temporary disk storage in preparation for processing. The CZCS Level-2 processing program is then executed.

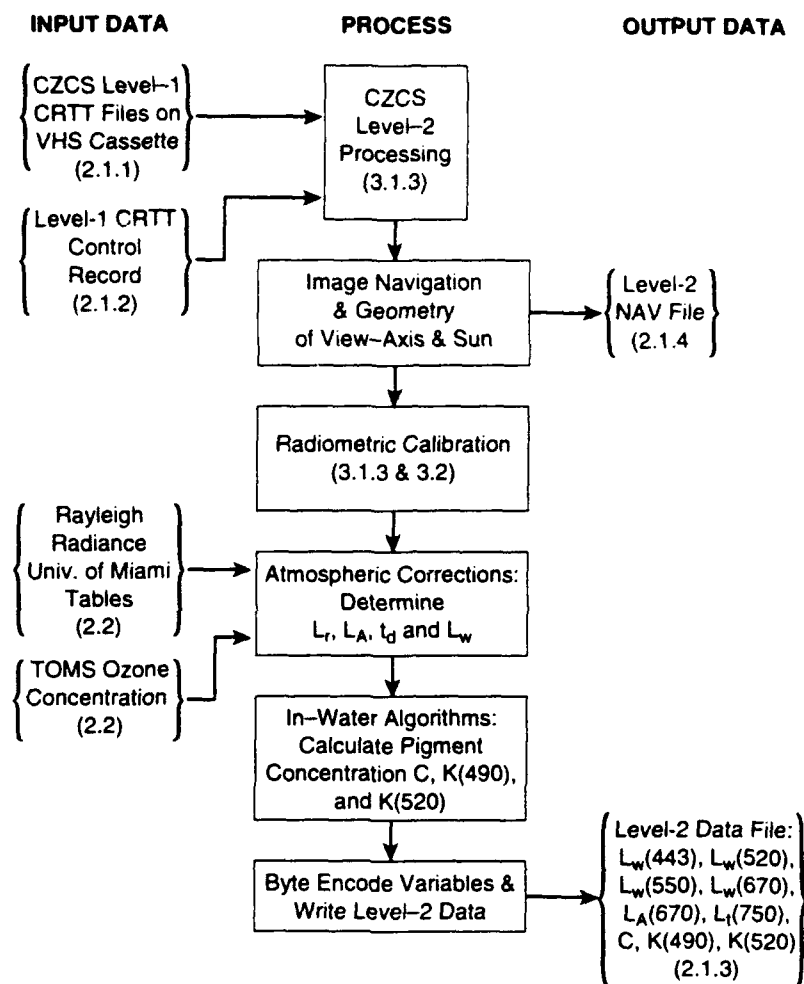


Fig. 3.1.3. CZCS Level-2 Processing: Process design and data flow schematic following the conventions described for Fig. 3.1.1.

The CRTT Control Record is read first, and after quality control checks (e.g. to verify file size, and exact matches between date, orbit, etc. in the CRTT Control Record and CRTT file internal documentation), the orbit parameters and solar GHA and declination are used to compute the navigation, solar geometry, and CZCS view-axis geometry data for the first three lines of NAV records (Sect. 2.1.4) at 16 line \times 16 pixel intervals, beginning at MINLIN-1 and MIPIX-1. These records are written to the newly opened Level-2 NAV File (Sect. 2.1.4), and are used subsequently to calculate matrices for two-dimensional interpolation of latitude, longitude and various atmospheric corrections terms, which will be described subsequently.

The next step is to initialize several Lookup Table arrays which facilitate computational processing of the scene.

- a. A floating point Lookup Table (array) $L_t[i][D_n]$ is created to convert digital counts D_n to radiance in ($\mu\text{W cm}^{-2} \text{sr}^{-1} \text{nm}^{-1}$), for each CZCS channel i , as

$$L_t[i][D_n] = g_n[i] * \{a[i][G] + b[i][G] * D_n\},$$

$$D_n = 0, 1, \dots, 255, i = 1, 2, 3, 4, 5,$$

where G is CZCS gain (1, 2, 3, 4) (from the CRTT Control Record), N is Nimbus-7 Orbit (from the CRTT Control Record), $g_n[i]$ is the CZCS responsivity correction for orbit N [computed using equations (3.2.6) for $i = 1, 2, 3$, and $g_n[i] \equiv 1$ for $i = 4$ and 5] (Sect. 3.2), and $a[i][G]$ and $b[i][G]$ are pre-launch CZCS radiance calibration coefficients for channel i and gain G (Table 3.2.1).

- b. The Rayleigh optical depth $\tau_R(\lambda)$ and extraterrestrial solar flux $F(\lambda)$ for each channel are set to be consistent with the date of the CRTT. The wavelength scaling

Table 3.2.1: CZCS Pre-Launch Radiance Calibration Coefficients

$L'(n, \text{Gain}) = a(n, \text{Gain}) + b(n, \text{Gain}) * D_n$,
where D_n are digital counts (0,1,...,255) recorded for channel n .

Channel	Wavelength	Gain	a(Chan,Gain)	b(Chan,Gain)
1	443.0	1	0.0396	0.0445
		2	0.0528	0.0359
		3	0.0288	0.0297
		4	0.0336	0.0211
2	520.0	1	0.0636	0.0310
		2	0.0883	0.0249
		3	0.0975	0.0203
		4	0.0565	0.0149
3	550.0	1	0.0799	0.0247
		2	0.0625	0.0202
		3	0.0657	0.0164
		4	0.0472	0.0118
4	670.0	1	0.0114	0.0114
		2	0.0359	0.0090
		3	0.0296	0.0074
		4	0.0160	0.0053
5	750.0	—	-0.0282	0.0942

factors for aerosol radiance $\epsilon(443, 670)$, $\epsilon(520, 670)$ and $\epsilon(550, 670)$ are calculated as

$$\epsilon(\lambda, 670) = (\lambda/670)^n,$$

where n is the aerosol Angstrom exponent (from the CRTT Control Record) (Sects. 2.1.2 and 3.1.2). Nominal ozone optical depths $\tau_{oz}(\lambda)$ are calculated for a default ozone concentration of 325 Dobson Units (DU). Nominal $\tau_{oz}(\lambda) = \kappa(\lambda) \times 325$, where $\kappa(\lambda) = 0.0040, 0.0898, 0.1097$, and 0.0580 (base-e "optical depths" per DU) for $\lambda = 443, 520, 550, 670$ nm. $\kappa(\lambda)$ at each wavelength was calculated from the ozone specific absorption data of Inn and Tanaka (1953).

Ozone optical depths are scaled, at a later point in the processing, to be consistent with actual ozone concentrations estimated from the Nimbus-7 TOMS data base (Sect. 2.2). An array of ozone concentrations O_3 (DU), for the CRTT date and covering the CRTT image location at 128 line \times 128 pixel intervals, is read from the Ancillary CRTT Ozone File prepared for this Level-1 VHS cassette (Sect. 2.2). These concentrations O_3 were extracted from the Nimbus-7 Gridded TOMS data base (NOPS, 1986; Bowman and Krueger, 1985). When each ozone transmittance

$$t_{oz}(\lambda, \theta) = e^{\tau_{oz}(\lambda) \sec \theta}$$

is calculated for an atmospheric path at zenith angle θ , nominal ozone optical depth is multiplied by $O_3/325$, where O_3 is ozone concentration in DU and 325 DU is the default ozone concentration used to compute nominal $\tau_{oz}(\lambda)$.

c. The in-water algorithm we used to compute pigment concentration is (Gordon *et al.* 1983b)

$$C1 = 1.129 \left[\frac{L_w(550)}{L_w(443)} \right]^{1.711},$$

$$C2 = 3.326 \left[\frac{L_w(550)}{L_w(443)} \right]^{2.439}$$

$$C = \begin{cases} C1, & \text{if } C1 \leq 1.5 \text{ mg m}^{-3}, \\ C2, & \text{otherwise.} \end{cases}$$

The in-water algorithm used for diffuse attenuation coefficient $K(490)$ is (Mueller, Trees and Arnone 1990; Austin and Petzold 1981)

$$K1 = 0.022 + 0.0883 \left[\frac{L_w(550)}{L_w(443)} \right]^{1.491},$$

$$K2 = 0.022 + 0.1773 \left[\frac{L_w(550)}{L_w(520)} \right]^{2.914}$$

$$K(490) = \begin{cases} K1, & \text{if } K1 \leq 0.15 \text{ m}^{-1}, \\ K2, & \text{otherwise.} \end{cases}$$

During the processing of an individual CRTT, these exponential functions will typically be evaluated between 5 and 10 million times. To speed processing, therefore, an internal floating point lookup table was created for each of these exponential functions. Floating point counterparts to array indices i (ranging from 0 to 511) are computed as

$$\left[\frac{L_w(\lambda_1)}{L_w(\lambda_2)} \right] * \text{SCALE},$$

where SCALE = 100.0 for C, SCALE = 50.0 for K(490) and K(520), and SCALE = 10.0 for the inverse C2 correction algorithm (used in the iterative atmospheric correction algorithm of Mueller, 1984). To save execution time during Level-2 processing, the code linearly interpolates in the appropriate lookup table [*i.e.* between floating-point values of the table for the two integer indices bracketing $(L_w[\lambda_1]/L_w[\lambda_2]) \times \text{SCALE}$] to determine C, K(490), or K(520), and thus avoids several million explicit exponential evaluations.

d. The tables of polynomial coefficients used to calculate normalized Rayleigh radiance $I_R(\lambda)$ are read into memory (Gordon, Brown and Evans, 1988; table and algorithm courtesy of R. Evans, University of Miami, 1989) from on-line disk storage.

The CZCS atmospheric correction algorithm, which is applied to each pixel, obtains water-leaving radiance $L_w(\lambda)$ as (Gordon *et al.*, 1983b; Gordon, Brown and Evans, 1988)

$$L_w(\lambda) = t_d(\lambda)^{-1} \{ L_t(\lambda) - L_R(\lambda) - \epsilon(\lambda, 670) S_a(\lambda, 670) L_a(670) \}$$

where $t_d(\lambda)$ is diffuse transmittance of the atmosphere, $L_t(\lambda)$ is calibrated CZCS aperture radiance (Sect. 3.2), $L_R(\lambda)$ is Rayleigh radiance, $\epsilon(\lambda, 670) = (\lambda/670)^n$ are the

aerosol wavelength dependence constants determined for the scene (see above), $S_a(\lambda, 670)$ are geometry and data dependent aerosol radiance scaling coefficients, and $L_a(670)$ is aerosol radiance at 670 nm.

Rayleigh radiance $L_R(\lambda)$ at a pixel is calculated as

$$L_R(\lambda) = I_R(\lambda) t_{oz}(\lambda) F(\lambda),$$

where normalized Rayleigh radiance $I_R(\lambda)$ is calculated using the polynomial fit to the multiple-scattering model of Gordon, Brown and Evans (1988; with coefficient tables provided by the University of Miami, R. Evans, Personal Communication, 1989), $t_{oz}(\lambda)$ is two-way ozone transmittance of the atmosphere

$$t_{oz}(\lambda) = \exp[-\tau_{oz}(\lambda) / (\mu + \mu_0)]$$

for cosines of solar and view-axis zenith angles μ_0 and μ [with $\tau_{oz}(\lambda)$ adjusted for local ozone concentration (see above)], and $F(\lambda)$ is extraterrestrial spectral solar flux (Neckels and Labs, 1984) adjusted for earth-sun distance on the CRTT date.

Diffuse transmittance $t_d(\lambda)$ at a pixel is calculated as

$$t_d(\lambda) = \exp\{-[0.5 \tau_R(\lambda) + \tau_{oz}(\lambda)] / \mu\}$$

for cosine of the view-axis zenith angle μ , and τ_{oz} adjusted for local ozone concentration.

Aerosol radiance scaling $S_a(\lambda, 670)$ at a pixel is calculated as

$$S_a(\lambda, 670) = \frac{F(\lambda) t_{oz}(\lambda)}{F(670) t_{oz}(670)}$$

where $t_{oz}(\lambda)$ and $F(\lambda)$ are defined the same as for $L_R(\lambda)$ above.

$L_R(\lambda)$, $t_d(\lambda)$ and $S_a(\lambda, 670)$ are explicitly calculated only at the locations of 5 NAV reference locations in each 32 line \times 32 pixel block formed by the 3 NAV record lines (Sects. 2.1.4 and 3.1.2) containing the current scan line and pixel. In each block, origin values are taken from the NAV pixel at the center pixel and line of the block, values from NAV pixels 16 pixels to the right and left on the center NAV line are used to calculate pixel-gradients [$\Delta L_R(\lambda) / \Delta \text{pixel}$, $\Delta t_d(\lambda) / \Delta \text{pixel}$, and $\Delta S_a(\lambda, 670) / \Delta \text{pixel}$], and values from the block-center NAV pixels on the top and bottom scan lines are used to calculate the equivalent line-gradients. $L_R(\lambda)$, $t_d(\lambda)$ and $S_a(\lambda, 670)$ at individual pixels falling within a 32 line \times 32 pixel NAV block are then calculated using bilinear interpolation. The error in this approximation is much less than the digital resolution of the CZCS measurements at all gain settings.

For most oceanic Case I water masses, $L_a(670)$ may be determined at each pixel by assuming that $L_w(670) \equiv 0.0$ (Gordon *et al.*, 1983b). With this assumption, aerosol radiance may be calculated as

$$L_a(670) = L_t(670) - L_R(670).$$

In Case II water masses, and in some turbid coastal Case I water masses, $L_w(670) > 0.0$. In the present implementation, this condition is tested by first computing $L_w(\lambda)$, C1 and C2 under the assumption the $L_w(670) = 0$. The assumption is accepted if $L_w(443)$ exceeds the radiance level corresponding to one digital count at the current gain setting, and if $(|C1 - C2| < 0.5$ or $C1 < 2.1)$. If either condition is not satisfied, the iterative algorithm of Mueller (1984) is applied to simultaneously adjust $L_w(670)$ and $L_a(670)$ until either internal consistency is achieved, or the algorithm fails and the pixel is flagged as containing bad data.

At each step in the iteration, the in-water algorithm interpolation tables are used to calculate C, K(490) and K(520) from ratios $L_w(550)/L_w(443)$ and $L_w(550)/L_w(520)$ (see sub-paragraph c above).

The code processes the data for pixels MINPIX to MAXPIX one line at a time, beginning with line MINLIN (limits taken from the header CRTT Control Record; Sects. 2.1.2 and 3.1.2). When each line is finished, the nine Level-2 parameters are byte-encoded according to Table 2.1 and written to the Level-2 DATA file (Sect. 2.1.3). After the next scan line is read in from the CRTT file (on disk), it is first tested to determine whether it falls within the current 32-line NAV block; if it does not, the current top line of NAV pixels becomes the bottom line of the next 32-line block, NAV records are computed for the middle and top lines of the new block and written to the NAV file, and new sets of interpolation coefficients are calculated for $L_R(\lambda)$, $t_d(\lambda)$ and $S_a(\lambda)$. Processing then resumes. This procedure continues until MAXLIN has been processed and written to the Level-2 DATA file, at which time the Level-2 program exits to the batch processing command script.

The new Level-2 NAV and DATA files are copied from disk storage to the Level-2 VHS cassette, their file names are entered in the catalogue for that cassette, and the Level-1 CRTT and Level-2 disk files are erased to make space for processing the next CRTT file.

The overall Level-2 process is repeated, unattended, until all CRTT files on the current Level-1 VHS cassette have been processed and saved in the Level-2 VHS archive.

3.1.4 LEVEL-3 ANALYSES

The overall process of Level-3 analyses, and the relationship of each process module to external CZCS and ancillary data sets, are outlined schematically in Fig. 3.1.4.

To form the CZCS K(490) optical climatology, which represents the primary objective of this project, the Level-2 K(490) data (Sects. 2.1.3, 2.1.4 and 3.1.3) were first organized spatially on a Mercator grid (Sects. 3.1.4.1 and 2.1.5) on a daily basis (Sects. 2.1.5 and 3.1.4.2). The Daily Composite K(490) Map digital data set for each grid point was averaged on a monthly basis to produce the time series of Monthly Composite Mean K(490) Maps [reported here in Sect. 3.3 and Appendix A, and delivered in digital form on 9-track magnetic tape at 6250 bpi (Sects. 3.1.4.3, 2.1.6 and Appendix C)]. The hard-copy Atlas of Monthly Composite Mean K(490) Maps (Appendix A) was produced by binning and color-coding the Monthly Composite Mean K(490) Map files and photographing the computer screen for subsequent color-xerographic reproduction (Sect. 3.1.4.3). K(490) Time Series were also extracted from the Daily Composite K(490) Map data base at a selected subset of grid locations (Sects. 3.1.4.4 and 3.4, and Appendix B) and copies are delivered with this report as digital files on 9-track magnetic tape (Sect. 2.1.7 and Appendix C).

3.1.4.1 Mercator Grid Description

For the purposes of most users of this data base, the Mercator grid on which we have assembled the CZCS K(490) climatology of the Northeast Pacific Ocean is described in sufficient detail in Sect. 2.1.5, and Table 2.2 provides an efficient means of converting line and pixel indices in the digital Level-3 map arrays to geographic latitude and longitude. The purpose of this section is to document the geodetic parameters of the Mercator grid projection, and the method by which geographic latitude and longitude were transformed to Mercator Coordinates.

We adopted the 2-step strategy of first mapping geodetic latitude and longitude to latitude and longitude on the conformal sphere (Richardus and Adler, 1972; Snyder, 1982). In this intermediate transformation, the elliptical distortions of geodetic latitude and longitude are projected into spherical coordinates on a sphere which intersects the reference ellipsoid. Simple spherical trigonometry can then be used to transform latitude and longitude on the conformal sphere into X and Y (respectively) coordinates of the Mercator projection.

Following the coordinate and sign conventions of Richardus and Adler (1972), the equations transforming

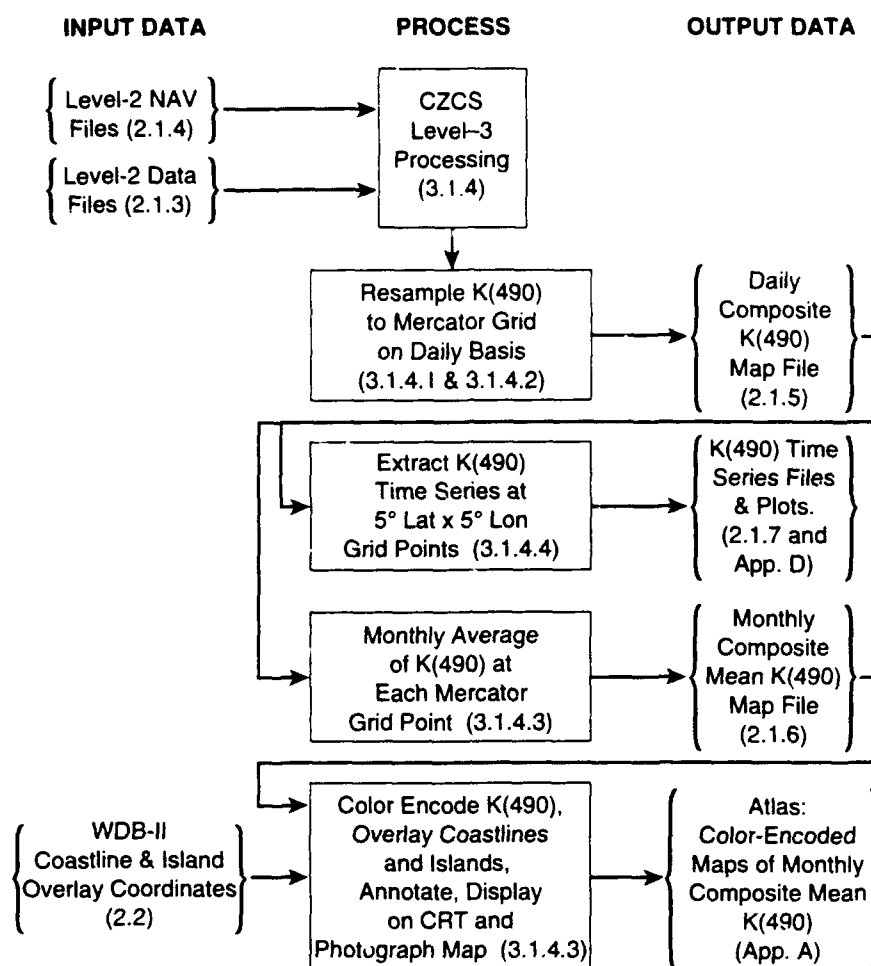


Fig. 3.1.4. CZCS Level-3 Analyses: Process design and data flow schematic following the conventions described for Fig. 3.1.1.

geodetic latitude (Lat) and longitude (Lon) to latitude (ψ) and longitude (Λ) on the conformal sphere of radius R are

$$\psi = 2 \left\{ \tan^{-1} \left[\left(\frac{1 - \xi \sin(\text{Lat})}{1 + \xi \sin(\text{Lat})} \right)^{\frac{\xi}{2}} \tan \left(\frac{\pi}{4} + \frac{\text{Lat}}{2} \right) \right]^C - \frac{\pi}{4} \right\}, \text{ and}$$

$$\Lambda = \text{Lon}.$$

where $\xi = 8.2271853e-2$ is the eccentricity of the reference ellipsoid, and $C = 1.0034017$ is a constant of the reference ellipsoid (Richardus and Adler, 1973). The subsequent transformation from (ψ, Λ) to Mercator (X, Y) is then easily accomplished with the equations

$$X = R \ln \left[\tan \left(\frac{\pi}{4} + \frac{\psi}{2} \right) \right], \text{ and}$$

$$Y = -R\Lambda$$

where the radius of the conformal sphere $R = 6367.386$ km.

To establish local X, Y coordinates corresponding to line and pixel indices in the CZCS Level-3 Map arrays (Sects. 2.1.5 and 2.1.6), we set the origin of the Mercator projection at geodetic (Lat, Lon) = (30,000°, -165,000°) corresponding to (line, pixel) = (961, 1001); map grid points are spaced relative to this origin at fixed intervals $DX = DY = 5.5565925$ units in Mercator projection space.

This 2-stage transformation is both algebraically easier, and computationally much faster, than direct

mathematical transformations from (Lat, Lon) to Mercator (X,Y). Furthermore, the accuracy of the simple 2-stage method far exceeds that required for the present application of satellite remote sensing image data.

The inverse transformation from X-to- Ψ -to-Lat is neither algebraically simple, nor computationally efficient. It is far simpler, and more efficient, to approximate the inverse transformation from X-to-Lat by linear interpolation in tables generated through the forward Lat-to- Ψ -to-X transformation at fixed Lat increments (Table 2.2 was prepared in this way).

3.1.4.2 Daily Composite K(490) Maps

To provide a working Level-3 archive, all Level-2 CZCS K(490) data for a given day were assembled into map arrays on the Mercator grid described in Sect. 3.1.4.1, in the digital array format described in Sect. 2.1.5.

To begin this process, a blank array KMAP [962] [1002] of type unsigned char (byte) was created, initialized to 0 at all indices, and written to disk storage (array notation and conventions are those of ANSI C) on a file named in the form "ddmmmyy.K490", where dd is day of the month, mmm is the month (abbreviated as Jan, Feb, ..., Dec), and yy are the last 2 digits of the year.

After the first Level-2 NAV and DATA file pairs for that day are loaded from the VHS archive into disk storage and opened for read-only mode, the *.K490 map file is opened for direct-access read-write. To begin resampling, the first two lines of NAV records (Sect. 2.1.4) are read into disk to form the first set of 16 line 16 pixel NAV blocks (Sect. 3.1.3). For each pixel from MINPIX to MAXPIX on line MINLIN, (latitude, longitude) are calculated by bilinear interpolation in the appropriate NAV block, and converted to Mercator (X,Y) (Sect. 3.1.4.1). Using the fixed $DX = DY = 5.5565925$ grid interval (Sect. 3.1.4.1), the line and pixel coordinates of the Mercator grid point closest to the current pixel are calculated. Then, a local search is conducted to determine whether, of all the pixels in this Level-2 file, this pixel is the closest one to that grid point. If it is not, the process moves on to the next pixel without further action. If the current pixel is the grid point's "nearest neighbor" in that scene, then the byte-encoded K(490) values corresponding to that pixel, and the two pixels adjacent to it, are extracted from the Level-2 data file; the actual "nearest neighbor" K(490) value which will be assigned to the *.K490 grid point is the median of these three values. The "median nearest neighbor" K(490) is then written directly to the *.K490 map file at the byte offset corresponding to that grid points

line and pixel indices in the map grid array. The process then moves to the next Level-2 pixel on the current line by incrementing the CZCS pixel index, and so forth until the CZCS pixel index exceeds MAXPIX.

When all pixel indices for a line have been processed, the CZCS line index is incremented and tested to determine whether the new line remains within the current 16-line row of NAV interpolation blocks. If it does not, the current top line of NAV pixels becomes the bottom line of the next set of NAV blocks, and a new top line of NAV records is read from the Level-2 NAV file.

The resampling process continues in this way until the line index exceeds MAXLIN. The K(490) resampling for that Level-2 NAV and DATA file pair is then complete, so those input files are erased from the disk. The next pair of Level-2 files for that day are staged to disk, and its "nearest neighbor" K(490) measurements are added to the daily *.K490 map file, and so forth, until all Level-2 files for that day have been processed.

All *.K490 daily map files for a given month are retained on disk until the entire month's set of Level-2 files have been extracted from the VHS archive and processed. Then, each map array is binned, color-encoded, displayed on the monitor, and examined for data quality. If obvious navigational errors are present in a CRTT file image, that file is removed from the sample. Some radiometric anomalies, which may result from undetected sun glint contamination, were also treated by simply removing the offending CRTT data from the sample. Other anomalies, detected during our analyses of the Provisional Series 1 and/or 2 products, were treated more selectively. For example, chronic anomalies near the right-hand side of the CZCS scan at full tilt were treated by eliminating the rightmost 100 pixels during the Level-1 screening phase (Sect. 3.1.2) of the Provisional Series 2 and Final Series processing.

The "median filter" K(490) assignment scheme described above was not implemented in the Provisional Series 1 and 2 version of the Level-2 process; in those implementations, the K(490) actual "nearest-neighbor" CZCS pixel was assigned directly to each Mercator grid point in the daily maps. During quality-control screening of the Provisional Series 1 and 2 Daily Composite K(490) maps, however, large spikes of single-pixel noise were observed to occur sporadically in some months. We do not understand the source of this noise phenomenon, but at times it could severely contaminate the monthly composite means. We therefore implemented the "3-pixel, median filter" K(490) assignment described above for

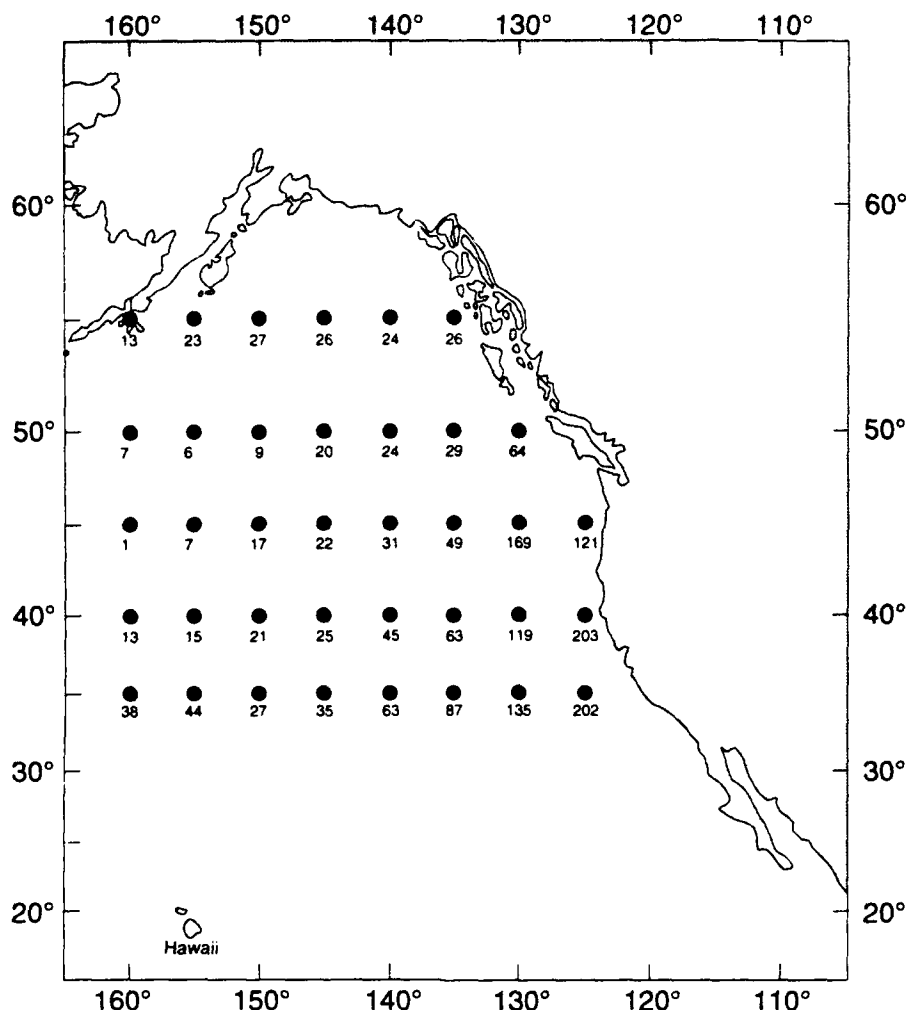


Fig. 3.1.5. Total numbers of valid CZCS K(490) measurements over the period from Jan 1979 through Jun 1986 at selected geographic locations (5° Lat. x 5° Lon. intervals).

Time series of CZCS K(490) at these locations are illustrated in Appendix D.

processing the Final Series of Level-3 products, having first verified that this filter was effective in eliminating this noise source from the resampled maps.

The final set of color-encoded Daily Composite K(490) Map displays were photographed on 35-mm slides for the Level-3 CZCS Browse Notebooks.

3.1.4.3 Monthly Composite Mean K(490) Maps

Each month's sample of Daily Composite K(490) Map files was averaged, at each grid location, to produce a Composite Mean K(490) Map, and an associated Sample Size Map containing the number of observations in that month at each grid cell.

The mean maps were produced by accumulating an array of floating point sums, dividing by the sample size

array, and then byte encoding the final result (Table 2.1). The entire set of daily, monthly mean and sample size map files was then written on Level-3 VHS cassettes in a standard UNIX CPIO directory archive file.

The Monthly Composite Mean K(490) Maps were color-encoded, annotated and displayed for visual inspection. Each map was photographed twice, once on 35-mm slides for the CHORS Level-3 CZCS Browse Notebooks, and once on 35-mm color print film. The color prints were used to create the ATLAS OF MONTHLY COMPOSITE MEAN CZCS K(490) delivered here as Appendix A.

3.1.4.4 K(490) Time Series at Selected Locations

The CZCS Daily Composite K(490) time series (Sects. 2.1.5 and 3.1.4.2) contain a wealth of information on

temporal variability in K(490), as well as on its spatial variability. To obtain examples of the temporal characteristics of K(490) variability in different subareas of the study region, we elected to extract K(490) Time Series from the Daily Composite K(490) Map series at grid points spaced at 5° latitude × 5° longitude intervals (locations illustrated as solid dots in Fig. 3.1.5). The number of valid CZCS K(490) observations acquired over the entire 7.5 year period (Jan. 1979-Jun. 1986) is annotated at each location in Fig. 3.1.5.

Each Daily Composite K(490) Map file (Sect. 2.1.5) was searched to extract all sets of non-zero K(490) values (byte-encoded) in the 5 line × 5 pixel grid boxes centered on the time series locations (Fig. 3.1.5). The median K(490) is taken as the estimator of the mean for each box (assuming a log-normal distribution), and the standard deviation is estimated as

$$0.25 \times |\max[K(490)] - \min[K(490)]|.$$

The day (cumulative days elapsed since 31 Dec. 1978), median K(490), and estimated standard deviation were then appended to the separate K(490) Time Series file (Sect. 2.1.7) assembled for that grid point during this process.

After the extraction process was completed, the binary Time K(490) Series file for each grid point was sorted, to order the records sequentially by day (in increasing order), and converted to an ASCII formatted file, which is delivered with this report (Sect. 2.1.7 and Appendix C). The time series for each grid point was also graphed, showing for each day with valid data, the median K(490) (solid dot) and standard deviation (error bar); these graphs are presented in Appendix D.

3.2 CZCS Radiance Responsivity Calibration

3.2.1 Pre-Launch Calibration

Prior to its installation on Nimbus-7 and launch in 1978, each of the 5 CZCS channels was characterized to determine its relative spectral response (to determine the wavelength bandpass), and absolute responsivity, to spectral radiance received at its entrance aperture. A separate set of radiance responsivities and dark offsets were determined for each of 4 commandable gain settings (Channels 1-4 only). The results of the pre-launch characterization are summarized below in Table 3.2.1 (page 19).

Using the coefficients $a(n,G)$ and $b(n,G)$ in Table 3.2.1, total apparent radiance measured in CZCS channel n , with gain setting G , is calculated as

$$L'_i(\lambda_n) = a(n,G) + b(n,G)D_n, \quad (3.2.1)$$

where D_n are digital counts recorded for channel n at a given pixel.

3.2.2 PREVIOUS MODELS of POST-LAUNCH DEGRADATION

Approximately 18 months following launch, attempts to remove atmospheric effects from CZCS Channel 1 (443 nm) radiances began to regularly produce negative anomalies of magnitudes too great to be ascribed to algorithm errors (R.W. Austin, Visibility Lab, Scripps Inst. of Oceanogr., San Diego, CA, Personal Communication, ca. 1980). Subsequent investigations confirmed and began to quantify a temporally progressive degradation of CZCS radiance responsivities, most prominently in Channel 1, but with significant trends also in Channels 2 and 3. In each case, sensitivity decay models were developed to correct CZCS radiances according to

$$L_i(\lambda) = g(\lambda, N) L'_i(\lambda) \quad (3.2.2)$$

where $L'_i(\lambda)$ is computed using equation (3.2.1) with pre-launch coefficients from Table 3.2.1, and N is time measured in Nimbus-7 orbits (~13.8173 orbits per day, counted from launch on 23 Oct. 1978).

Gordon *et al.* (1983) first published a set of correction models by fitting CZCS data from areas in the North Atlantic Ocean which are known to have persistently very low pigment concentrations. Based on CZCS data from orbits in the range $0 < N \leq 3200$, Gordon *et al.* (1983) published models which may be expressed [in compatible form with equation (3.2.2)] as

$$g(443, N) = \frac{1.069}{1.086 - 2.46 \times 10^{-5} N + 5.05 \times 10^{-10} N^2}, \quad (3.2.3a)$$

$$g(443, N) = \frac{0.993}{1.024 - 5.9 \times 10^{-6} N}, \quad (3.2.3b)$$

$$g(550, N) = \frac{0.995}{1.007 - 2.8 \times 10^{-6} N}, \quad (3.2.3c)$$

$$g(670) = 1.0 \quad (3.2.3d)$$

Mueller (1985) used similar methods, with data from a region of the Northeast Pacific Ocean where K(490) was known to be low and very homogeneous, to confirm the basic tendencies found by Gordon *et al.* (1983) and extend

the fit to orbits near 20,000 with the linear models

$$g(443, N) = 0.9947 + 1.788 \times 10^{-5} N, \quad (3.2.4a)$$

$$g(520, N) = 0.9642 + 6.97 \times 10^{-6} N, \quad (3.2.4b)$$

$$g(520, N) = 0.9406 + 4.28 \times 10^{-6} N, \quad (3.2.4c)$$

$$g(670) = 1.0. \quad (3.2.4d)$$

Gordon *et al.* (1988) published multiple scattering models for calculating Rayleigh radiance (3.1.3 above) which were significantly more accurate than the single scattering approximations in common use up to that time. Because the determinations of $g(\lambda, N)$ are intimately intertwined with the atmospheric correction model (and especially with the Rayleigh radiance computation), the implementation of their new multiple scattering model required modifications to the $g(\lambda, N)$ models as well. Gordon *et al.* (1988) recommended linear multiplicative scaling of their previous correction model (Gordon *et al.*, 1983b). When this scaling was applied to a locally revised model, previously developed at CHORS to include orbit 30,000 (Mueller, 1988, unpublished), we obtained the following responsivity correction models

$$g(443, N) = 1.038 + 1.667 \times 10^{-5} N, \quad (3.2.5a)$$

$$g(520, N) = 0.986 + 7.36 \times 10^{-6} N, \quad (3.2.5b)$$

$$g(550, N) = 0.986 + 4.52 \times 10^{-6} N, \quad (3.2.5c)$$

$$g(670) = 1.026. \quad (3.2.5d)$$

In models 3.2.3 and 3.2.4, it was assumed that any degradation of responsivity in CZCS Channel 4 is negligible; Gordon *et al.* (1988) recommended a constant adjustment to retain consistency with their new model, but they did not propose any time dependent variation in $g(670)$. None of the three models represent an analysis of CZCS data from the complete range of Nimbus-7 orbits $0 < N \leq 40000$ (between late 1978 and mid 1986).

Unpublished work at the University of Miami (R.H. Evans, RSMAS, University of Miami, Personal Communications ca. 1984 to 1988) provided the basis for $g(\lambda, N)$ corrections used in producing NASA's CZCS Level-2 and Level-3 data base at Goddard Space Flight Center. This algorithm was apparently developed following principles similar to those leading to equations (3.2.3) through (3.2.5), but using much larger data sets and allowing

higher frequency and step-like adjustments in $g(\lambda, N)$ at many times through the 7 year operational history. The University of Miami (Evans) model also reportedly includes time variability in $g(670, N)$. Unfortunately, the details of this unpublished analysis by Evans (Univ. of Miami) were not available to us for either critical review and assessment, or for implementation. Therefore, we revisited the problem and independently determined a new set of $g(\lambda, N)$ models which apply to the full range of Nimbus-7 orbits $0 < N \leq 40000$ and are consistent with our final implementation of the CZCS atmospheric correction algorithm (3.1.3 above).

3.2.3 DATA and METHODS for REVISED RESPONSIVITY DEGRADATION ANALYSIS

The approach and assumptions adopted here follow those described in Mueller (1985), much of which was adapted, in turn, from Gordon *et al.* (1983b). The analysis hinges on the equation

$$g(\lambda, N)L'_t(\lambda) = L_R(\lambda) + t_d(\lambda)L_w(\lambda)$$

$$+ S(\lambda, 670)[L_t(670) - L_R(670) - t_d(670)L_w(670)], \quad (3.2.6)$$

where $L'_t(\lambda)$ is calculated with (3.2.1), $L_R(\lambda)$ is calculated using the multiple scattering model of Gordon *et al.* (1988), and the other terms are described in Section 3.1.3 above. We assume in clear water pixels (pigment conc. < 0.20), that $L_w(670) \equiv 0$, and that $L_w(520)$ and $L_w(550)$ may be calculated using the "clear water normalized radiance" model of Gordon and Clark (1981).

The wavelength dependence of aerosol radiance is assumed to follow

$$S(\lambda, 670) = \left(\frac{\lambda}{670} \right)^n,$$

and for this study we have assumed that $n = 0$ and was constant; this choice is consistent with the approach used to produce NASA's CZCS products at GSFC. To minimize dependence on the assumption that $S(\lambda, 670)$ is constant, data used in this analysis were limited to very clean atmosphere cases where $L_a(670) < 0.35 \mu W cm^{-2} nm^{-1} sr^{-1}$. Following Mueller (1985), we further limited data selection for this study to the geographic area $30^\circ N < Lat < 32^\circ N$ and $130^\circ W < Lon < 145^\circ W$, where *in situ* observations in 1982, 1983 and 1985 indicate that $K(490) \sim 0.034 \pm 0.0025 m^{-1}$.

When we first began this analysis, we attempted a modified approach. Consider a case where CZCS data are acquired from a given geographic location on two successive days. The instrument will view the pixel with two different viewing and solar illumination angles. If pigment concentration is very low and constant over the two day period, then $L_w(\lambda)$ should vary in direct proportion to the cosine of the solar zenith angle, and the principle residual variation between the two observations should result from differences in $L_R(\lambda)$ and $t_d(\lambda)$ over the two different atmospheric pathlengths. In principle, we could then write two independent equations (3.2.6) and solve for $g(\lambda, N)$ without accurately modeling $L_w(\lambda)$.

To explore this very different approach, we first searched the entire Level-3 gridded Daily Composite K(490) data base to identify all occurrences where geographic locations were observed on successive days. The Level-1 data base was then searched to extract the raw data records for each such two-day pair of observations. For each two-day pair of CZCS radiance measurements, we calculated $L'_i(\lambda)$, $L_R(\lambda)$ and $t_d(\lambda)$ and substituted them in (3.2.6). We assumed that $S(\lambda, 670) \approx 1.0$, and that $L_w(670) \approx 0.0$. We further assumed that normalized water leaving radiance (Gordon, 1988) remains constant over the two days, so that

$$L'_w(\lambda, \text{day } 2) \equiv \frac{t(\lambda, \mu_{02})(1 - \rho(\mu_{02}))\mu_{02}}{t(\lambda, \mu_{01})(1 - \rho(\mu_{01}))\mu_{01}} \cdot L_w(\lambda, \text{day } 1),$$

where μ_{0i} is the cosine of the solar zenith angle on day i ($i = 1, 2$), $t(\lambda, \mu_{0i})$ is direct transmittance of the sun through the atmosphere on each day i , and $\rho(\mu_{0i})$ is the Fresnel reflectance of the sea surface on each day i .

With the above assumptions, a pair of equations (3.2.6) were solved for $g(\lambda, \bar{N})$ for each data pair, where \bar{N} is the average of the two orbit numbers on which the CZCS data were measured. Unfortunately, the solutions for $g(\lambda, \bar{N})$ ($\lambda = 443, 520$ and 550) obtained using this conceptionally elegant approach were neither stable, nor consistent within individual orbit pairs. The probable source of the apparent lack of robustness in those solutions is that systematic and known variability in $L_R(\lambda)$ and $t_d(\lambda)$ was not large enough, in most cases, to make errors in the assumed aerosol radiance and $L_w(\lambda)$ terms negligible, with the result that the equation pairs were not well conditioned.

We were, therefore, forced to return to the methodology and assumptions described in Mueller (1985). Only the subset of the two-day pairs of CZCS data falling within the above latitude and longitude limits (and other

data acceptance criteria outlined above) were used for the analysis. For each day, $L_w(520)$ and $L_w(550)$ were calculated using the "clear water radiance model" of Gordon and Clark (1981), and $L_w(443)$ was estimated by inverting the K(490) algorithm (Austin and Petzold, 1981). Ozone transmittances were computed using the Nimbus-7 TOMS results as explained under 3.1 above. Rayleigh radiances were those of Gordon *et al.* (1988), using tables furnished to us by the University of Miami (R.H. Evans, personal communication, 1989). Solar flux values were those of Neckel and Labs (1984), and since the $g(\lambda, N)$ models were based on these inputs, in combination with the multiple scattering Rayleigh radiance model of Gordon *et al.* (1988), we assumed that $g(670) = 1.0$. The solutions for $g(520, N)$ and $g(550, N)$ were computed first, and the new regression fits were used to estimate $L_w(443)$ and $g(443, N)$. As a further data quality filter at each wavelength, the two $g(\lambda, N)$ solutions for each two-day data pair were retained only if

$$|g(\lambda, N_1) - g(\lambda, N_2)| \leq \begin{cases} 0.02, \lambda = 443 \text{ nm} \\ 0.015, \lambda = 520, 550 \text{ nm} \end{cases}$$

3.2.4 RESULTS: REVISED CZCS RESPONSIVITY CORRECTIONS

The CZCS two-day pairs sample was processed to produce time series of $g(520, N)$ and $g(550, N)$ using the method described in 3.2.3 above. The scatter plots for these results are illustrated in Fig. 3.2.1 (panels b and c). Based on visual inspection of these scattergrams, it was apparent that the rates of change in responsivity of these two channels slowed significantly sometime between orbits 10,000 and 20,000. We therefore fit the $g(\lambda, N)$ data for each of these channels in two piecewise segments (eqs. 3.2.7b and 3.2.7c below, and solid lines in panels b and c of Fig. 3.2.1).

In calculating the $g(443, N)$ time sequence, we used the new eqs. 3.2.7b, 3.2.7c and 3.2.7d to correct $L_t(520, N)$, $L_t(550, N)$ and $L_t(670, N)$ prior to estimating $L_w(443, N)$ from the inverse K(490) algorithm (Mueller, 1985; Austin and Petzold, 1981). The scatter plot for $g(443, N)$ versus N is illustrated in Fig. 3.2.1 (panel a). Unlike the $g(\lambda, N)$ data for the other two wavelengths, the $g(443, N)$ scattergram shows no obvious break in slope between orbits 10,000 and 20,000. Furthermore, regression fits to data segments $N \leq 15000$ and $N > 15000$ did not yield statistically different coefficients. Therefore, we fit this data to one regression model over the entire orbit range $0 < N \leq 40000$ (equation 3.2.6a and the solid line in panel

a of Fig. 3.2.1).

Also illustrated as dashed lines in Fig. 3.2.1 are the regression lines of the previous models given here in eqs. 3.2.3 (Gordon *et al.*, 1983), 3.2.4 (Mueller, 1985), and 3.2.5 (Gordon *et al.*, 1988 applied to unpublished regression coefficients determined by Mueller in 1988).

The revised regression equations from the above analysis are:

$$g(443) = 1.054 + 1.678 \times 10^{-5} N, \quad (3.2.6a)$$

$$g(520) = \begin{cases} 0.927 + 1.094 \times 10^{-5} N, & N < 15470, \\ 1.015 + 5.270 \times 10^{-6} N, & N \geq 15470, \end{cases} \quad (3.2.6b)$$

$$g(550) = \begin{cases} 0.919 + 6.592 \times 10^{-6} N, & N < 12821, \\ 0.947 + 4.415 \times 10^{-6} N, & N \geq 12821, \end{cases} \quad (3.2.6c)$$

$$g(670) = 1.0. \quad (3.2.6d)$$

3.2.5 DISCUSSION and CONCLUSIONS

The $g(\lambda, N)$ models in equations (3.2.4) were used in this project for the first end-to-end processing of the CZCS data, to create "Provisional Series 1" (Sect. 3.1 above). Equations (3.2.5) were used to process "Provisional Series 2", which incorporated the results of Gordon *et al.* (1988). The revised fit, represented in the model equations (3.2.6), was used to prepare the final optical climatology products, which are delivered with this Final Report.

The most important changes represented by equations (3.2.6), relative to the previous models of equations (3.2.3), (3.2.4) and (3.2.5), are associated with the decrease in $g(550, N)$ relative to those calculated using equation (3.2.5c) (compare regression lines in Fig. 3.2.1c). By comparison, $g(443, N)$ varies only slightly between equations (3.2.5a) and (3.2.6a). The net effect of these changes is that the computed ratios $L_w(443)/L_w(550)$ are more than 5% higher, when they are computed using $g(\lambda, N)$ from equations (3.2.6), than they would be if computed using equations (3.2.5). This has the effect of significantly reducing the Final Series CZCS K(490) estimates (Sect. 3.1.3 above), which at least partially explains why the "Provisional Series 1" product was found by Mueller and Lange (1989) to significantly overestimate K(490) when compared to *in situ* profiles. The revised, final K(490) is shown in Sect. 4 to be in excellent agreement with *in situ* results, at least during the Oct./Nov. 1982 period.

3.3 Monthly Composite Means of CZCS (K(490))

The primary CZCS Optical Climatology resulting from this study consists of set of Monthly Composite Mean K(490) Maps (Sects. 2.1.6 and 3.1.4.1). A color-encoded xerographic print of each month's map is included here in the *Atlas of CZCS K(490) in the Northeast Pacific Ocean* (Appendix A). The digital, byte-encoded version of each month's map is included on the 9-track magnetic tape (2 copies) delivered with the original copy of this Final Report (Sect. 2.1.6 and Appendix C).

The spatial patterns of K(490) revealed in these maps visualize the geographic domains of many of the major, well-known features of the ocean circulation in the Northeast Pacific Ocean (Sect. 1.0 and Fig. 1.1). Distinctive surface bio-optical characteristics can be seen to distinguish the extents, large and mesoscale spatial structures, and temporal cycles of variability associated with the California Current System (CCS) (U.S. West Coast south of approximately 45°N and extending offshore approximately 500 km), the Alaskan Gyre (AG) (Gulf of Alaska, north of approximately 45°N), the oligotrophic central Gyre of the East Central North Pacific (ECNP), and the zonal Sub-Arctic Front (SAF) (near 42°N) and Sub-Tropical Front (STF) (near 30°N) (Fig. 1.1). The apparent associations between seasonally varying, organized spatial patterns of CZCS K(490) and these well known ocean circulation features guided our partition of the region into "bio-optical provinces" and provided a framework for developing statistical models which relate remote sensing K(490) to the underlying profiles of $K(490, z)$ and chlorophyll fluorescence $F(z)$ (Sect. 5 and Appendix E).

In the CCS, there is a distinctive cycle of annually recurring characteristic variability in K(490) patterns. K(490) values in the region reach a minimum each year sometime in January and February. Coastal upwelling, beginning sometime in March or April of each year, is manifested by the appearance of nearshore organized front and eddy features in the K(490) distribution, with maxima in the range 0.1 to 0.15 m^{-1} . Upwelling is associated with higher K(490) near the coast, decreasing with distance offshore through the zone of transition to the oligotrophic ECNP central gyre water masses. Initially, the band of elevated K(490) appears to grow in the offshore direction, with a relatively diffuse appearance. Then, in mid-summer (late June through August), the offshore waters appear to clear up somewhat [$K(490) < 0.05 m^{-1}$], and mesoscale structure in fronts, eddies and coastal upwelling centers become much more sharply

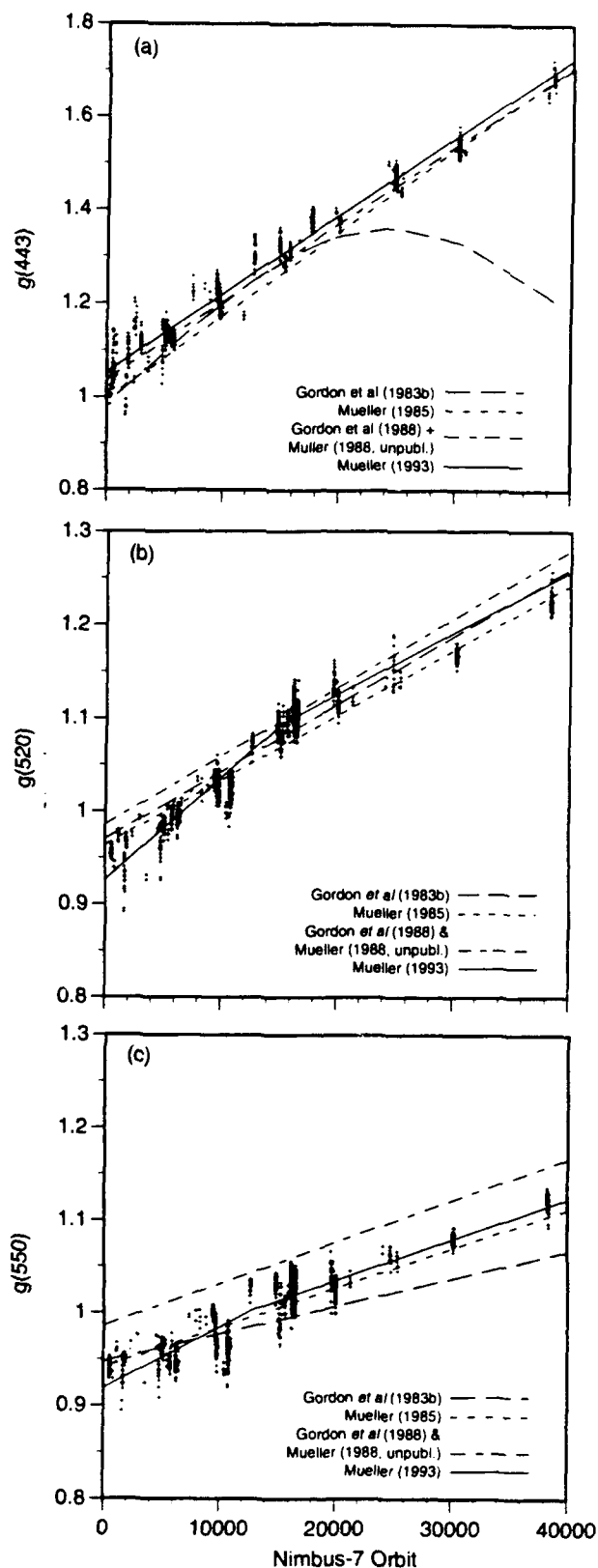


Fig. 3.2.1. CZCS time dependent radiance responsivity adjustment coefficients $g(\lambda, N)$ for CZCS channels at 443, 520, and 550 nm (panels a, b and c, respectively). Time N is measured in sequential Nimbus-7 orbits following launch on 23 Oct. 1978. Solid lines represent the present regression fit to these data, and dash lines refer to other $g(\lambda, N)$ models as indicated in the panel legends (also see main text).

defined in the patterns of $K(490)$. At this time of year, the coastal band of elevated $K(490)$ is confined to the first 50 km, with offshore water masses characterized by low $K(490)$ (0.04 to 0.05 m^{-1}) broken by filaments of high $K(490)$ streaming from the coastal upwelling zone in cross-shelf jets, possibly entrained in the boundaries of large mesoscale eddies which are recurring features of the CCS over the continental slope. In the fall, $K(490)$ begins to increase diffusely throughout the outer reaches of the CCS and its zone of transition to the ECNP central gyre. Turbidity, in CCS surface water masses over the continental slope, peaks sometime in November or early December, and then declines rapidly to a minimum throughout the CCS in January or February.

The oligotrophic ECNP Central Gyre (the region south of $\sim 32^\circ\text{N}$, and between 135°W and 150°W) is characterized by very low $K(490)$ (0.025 to 0.04 m^{-1}) at all times, but $K(490)$ increases slightly (into the range 0.04 to 0.05 m^{-1}) in mid-to-late winter. This is the province where data were selected to model the ratio of change in radiance responsivities of the CZCS (Sect. 3.2). In latitudes 30°N to 32°N between 150°W and 165°W , mesoscale features with localized maximum $K(490)$ values as high as 0.05 – 0.2 m^{-1} appear between October and March in years when the area was observed. These features may be associated with the eastward flow of the Kuroshio extension north of Hawaii and downstream from the Emperor Seamount chain.

The northern segment of the ECNP province lies between the Sub-Arctic Front (SAF) near 42°N and the Sub-Tropical Front (STF) near 32°N (Fig. 1.1). In summer and early fall (June – September, the SAF is manifested bio-optically in CZCS data as a ridge of elevated $K(490)$ with maxima near 0.1 m^{-1} , decreasing gradually northward to merge into the patchy structure of the AG, and decreasing sharply to the south to the $K(490) < 0.04\text{ m}^{-1}$ typical of ECNP. The summer "ridge" pattern is most clearly visualized in the Monthly Mean $K(490)$ for August 1980 (Appendix A), and is viewed in only a fragmentary way in the CZCS data for the other summer months and years. During winter and early spring (December through March) the ridgelike nature of the SAF disappears as winter productivity elevates biological productivity in the southern reaches of the AG; during this period the sharp bio-optical front bounding oligotrophic ECNP water masses propagates southward through the climatological Ekman convergence zone (Fig. 1.1; Sect. 1.0; Roden, 1977), and eventually delineates the mesoscale eddy features along the STF near 32°N . The Mean $K(490)$ map for January 1983 (Appendix A) gives an

especially clear visualization of the STF in mid-winter. Following the open ocean spring transition (typically in April), when the surface mixed layer shallows abruptly over a period of a week or two, the bio-optical front retreats northward rapidly to the SAF, and summer conditions are established by June.

The AG is characterized by patchy patterns of high and low $K(490)$ throughout the year, but with higher $K(490)$ patches being more prevalent in winter through spring months. Many of the elevated $K(490)$ patches appear to be associated with the chain of large seamounts which occupy the central Gulf of Alaska (an interesting potential association which we have not had resources or opportunity to explore systematically).

In reviewing the map series for 1979, $K(490)$ values in the CCS and AG seem anomalously low throughout the year, especially when compared to the data from later years. This could be an artifact, possibly resulting from overcorrection of CZCS responsivity by the linear degradation model (Sect. 3.2) during the first few months after launch. However, we have no independent information on which to make further adjustments to the model. We will comment further on this phenomenon in conjunction with the Time Series data (Sect. 3.4).

3.4 Time-Series of $K(490)$ at Selected Locations

Complete time series of CZCS $K(490)$ have been extracted from the Daily Composite $K(490)$ Map data base at grid points spaced at intervals of 5° latitude \times 5° longitude (Sects. 2.1.7 and 3.1.4.1), and are each graphed in a separate figure of Appendix D.

The time series illustrate the gappy and irregular nature of CZCS sampling frequency in the time domain at any fixed location. Coverage density is relatively good at latitudes 35° , 40° and 45°N in the California Current, and is sufficient to detect the presence of seasonal, annual and interannual cycles at grid points as far west as 140°W in these latitudes. Sampling frequency is too sparse to clearly discern these cycles in the far western and northern portions of the study region (figures of Appendix D and Fig. 3.1.5). Sampling was most complete at grid points within the CCS (35° , 40° and 45°N at 125°W), and the presence of strong annual and interannual variability is apparent in these time series plots (Appendix D), but it is partially masked by strong variability on shorter time and space scales in this dynamic region. At times when the annual cycle is near its maximum, local spatial variability, as evidenced by error bars indicating standard deviations in the $25\text{ km} \times 25\text{ km}$ area surrounding each grid point, is

approximately 20% of the amplitude of the apparent annual cycle. Indeed, at 40°N, 125°W, local spatial and high-frequency variance is large enough in amplitude to almost totally mask the presence of seasonal and annual signals. On the other hand, local variance is much smaller near periods of the annual minimum, and therefore, the annual periodicity is easier to detect in the spacing of minima than in maxima. Local variance is also significantly smaller at offshore locations where sampling frequency is sufficient to discern seasonal and longer scale cycles.

As noted in our descriptive scrutiny of the Monthly Composite Mean K(490) Map series (Sect. 3.3), CZCS K(490) estimates seem anomalously low throughout 1979. At 35°N, 125°W, for example, the apparent peak in the 1979 annual cycle (near day 110) is only approximately 0.045 m⁻¹, compared to maxima exceeding 0.06 m⁻¹ in the cycles straddling the 1982–83 El Niño event. The linear CZCS responsivity adjustment model (Sect. 3.2) may be overcorrecting aperture radiances during the first several months to year of operation on-orbit. Based on our experience with the sensitivity of CZCS Level-2 algorithms to this correction, we could probably adjust the model to increase the magnitude and variability amplitudes of CZCS K(490) during this first year, but absent any independent data for that year, any such adjustment would be purely arbitrary.

4.0 ERROR ANALYSIS OF CZCS K(490) ESTIMATES

The accuracy of K(490) estimates calculated from CZCS data was evaluated through direct comparisons with *in situ* K(490,z) profiles. *In situ* data for these comparisons was limited to profiles measured during Oct. and Nov. 1982 aboard the R/V Acania and USNS DeSteiguer (Sect. 2.3); CZCS coverage was inadequate during the one other period (Jun.–Jul. 1985) when *in situ* K(490,z) profiles exist in the data base which was available at CHORS.

4.1 Methods

The accuracy of K(490) products calculated from CZCS data (3.3 and 3.4 above) was estimated by direct comparisons with $\bar{K}(490,z)$ calculated from *in situ* profiles of downwelling spectral irradiance $E_d(490,z)$. Remote sensing K(490) is defined as the average value

$$\bar{K}(490, z_{37}) = \frac{1}{z_{37}} \int_0^{z_{37}} K(490, z) dz, \quad (4.1)$$

where

$$z_{37} = \frac{1}{\bar{K}(490, z_{37})} \text{ m}. \quad (4.2)$$

At first glance, this may seem a circular definition. To illuminate the point, we are given that by definition

$$E(\lambda, z_n) = E(\lambda, 0) e^{-\int_0^{z_n} K(\lambda, z) dz},$$

or

$$E(\lambda, z_n) = E(\lambda, 0) e^{-\bar{K}(\lambda, z) z_n},$$

and it follows that

$$E(490, z_{37}) = E(\lambda, 0) e^{-\bar{K}(490, z_{37}) z_{37}},$$

or from (4.1)

$$E(490, z_{37}) = E(\lambda, 0) e^{-1}.$$

Since $e^{-1} = 0.37$, the variable z_{37} (m) represents the e-folding depth at which $E_d(490, z_{37})$ has fallen to 37% of surface irradiance.

For each irradiance profile $E_d(490, z)$, z_{37} was determined by inspection as the depth at which

$$\frac{E_d(490, z_{37})}{E_d(490, 0)} = 0.37,$$

and the *in situ* estimate of remote sensing K(490) was calculated directly as

$$\bar{K}(490, z_{37}) = \frac{1}{z_{37}} \text{ m}^{-1}.$$

It rarely occurred that an $E_d(490, z)$ profile measurement and a CZCS observation were made on the same day at any given ship station location. Therefore, the set of CZCS K(490) values for the 3 × 3 pixel block centered on each station's geographic coordinates were extracted from all daily composite maps (3.3 above) in which that location was observed between 1 Oct. and 30 Nov. 1982. The minimum, maximum and median CZCS K(490) were recorded for each pixel block, and the resulting time series is plotted in one of the graphs of Appendix B, an example of which is reproduced below as Fig. 4.1. The least-squares linear trend in the median of CZCS (K490) at each station location was computed over the 2-month time period, and the estimated value $\hat{K}_n(490)$ on the day of a

shipboard observation at station n was calculated as

$$\hat{K}_n(490) = a_n + b_n t_n, \quad (4.3)$$

where t_n is time of station n in days since 30 September 1982, and a_n and b_n are the linear regression coefficients for that CZCS data sequence. Error δ_{kn} in the CZCS $\hat{K}_n(490)$ estimate at station n was then determined as

$$\delta_{kn} = \bar{K}_n(490, z_{37}) - \hat{K}_n(490), \text{ m}^{-1}. \quad (4.4)$$

The results of this approximate error analysis are described in 4.2 below.

4.2 Results

CZCS coverage was sufficient during Oct. and Nov. 1982 for comparisons to be made between *in situ* and CZCS $K(490)$ estimates at the locations of 10 DeSteiguer (1982) stations and 20 Acania (1982) stations (Sect. 2.3 and Fig. 2.1). Three additional stations (DeSteiguer stations 8, 15 and 16) had enough CZCS observations to estimate a trend, but the data were poorly distributed in time relative to the day of the *in situ* observations and were rejected from the error analysis. The station numbers, dates and geographic locations of these stations are listed in Table 4.1.

The CZCS $K(490)$ daily composite data base for the period between 1 Oct. and 30 Nov. 1982 was searched to extract the minimum, median and maximum $K(490)$ from each 3×3 pixel block centered on a comparison station (the effective spatial resolution, therefore, is approximately $15 \times 15 \text{ km}^2$). This time sequence has been plotted for each station location in the format illustrated in Fig. 4.1. The median is taken as an estimator of the mean of each observed pixel-block, and the standard deviation is estimated by $1/4$ of the range (maximum–minimum). For each comparison station, the CZCS $K(490)$ medians have been plotted in Fig. 4.1 (and in the graphs of Appendix B) as solid dots, with error bars estimated from pixel-block standard deviations.

The temporal trends in CZCS $K(490)$ medians were determined for all stations by linear least-squares regressions (solid lines in Fig 4.1 and graphs of Appendix B). The trend regression coefficients were used with equation (4.3) to estimate CZCS $\hat{K}(490)$ on the day of the corresponding *in situ* $\bar{K}(490, z_{37})$ measurement at each station (plotted as open circles in Fig. 4.1 and Appendix B), and error estimates were calculated using equation (4.4). The values of CZCS $\hat{K}(490)$, *in situ* $\bar{K}_n(490, z_{34})$, and relative error $\delta_{Kn} / \bar{K}_n(490, z_{37})$ are also listed in Table 4.1.

The sample mean and standard deviation of relative error $\delta_{Kn} / \bar{K}_n(490)$ are -0.0374 and 0.1774 , respectively. The frequency distribution of $\delta_{Kn} / \bar{K}_n(490)$, illustrated in Fig. 4.2, appears to be skewed towards negative values, suggesting qualitatively that the CZCS data tend to overestimate $K(490)$. Using a t -statistic test, however, the 90% confidence limits on the median $\delta_{Kn} / \bar{K}_n(490)$ are ± 0.0425 indicating that the present sample does not provide statistically significant evidence (at that confidence level) to reject a hypothesis that CZCS $K(490)$ estimates are unbiased. [The 75% confidence limits (± 0.0221) would exclude 0, but this level of statistical significance would comprise a weak basis for rejecting that hypothesis.]

4.3 Discussion and Conclusions

The largest errors, both positive and negative, occur in geographic areas where large spatial gradients in $K(490)$ are associated with major ocean fronts and eddies. In these areas, apparent errors in a 2-month trend estimate of CZCS $\hat{K}(490)$ may be as large as 30% to 50% when compared to data from an individual ship station. Much of this increased "error", relative to errors in regions of lesser mesoscale variability, is very likely to be associated with advection of gradient features during the period. This situation makes meaningful comparisons between the CZCS trend and individual ship measurements somewhat problematic. In other words, a single *in situ* irradiance profile provides a very poor statistical estimate of $\bar{K}(490, z_{37})$ at any given location in a gradient-rich front and eddy field. A reliable error estimate in such an oceanic environment would require far more intensive shipboard sampling than is represented in the data base which was available for this study. Perusal of the CZCS $K(490)$ composite mean maps from Oct. and Nov. 1982 (Appendix A) suggests that maximum gradient features occur in the transition from $0.05 < K < 0.1 \text{ m}^{-1}$. Acania stations 14, 181 and 182, and DeSteiguer stations 18 and 19 meet this criteria. Were we to exclude those stations from the foregoing analysis, the means and standard deviation of relative error $\delta_{Kn} / \bar{K}_n(490, z_{37})$ would be -0.0110 and 0.1284 , respectively. In this case, even the 75% confidence limits would indicate that the CZCS $\hat{K}(490)$ trend estimate is unbiased.

In sum, these results suggest that CZCS $K(490)$ climatologies of the type prepared for this study can generally be regarded as accurate within $< 20\%$, with the caveat that "errors" may be as large as 50% near major fronts and in areas rich in mesoscale eddies. This conclusion is consistent with those resulting from the indepen-

TABLE 4.1

CZCS Trend Estimates $\hat{K}(490)$ compared to *in situ* $\bar{K}(490, z)$ calculated from irradiance profiles $E_d(490, z)$ measured aboard the USNS DeSteiguer (stations "Dnn") and R/V Acania (stations "Ann") in October and November 1982.

Station	Date	Lat (°N)	Lon (°W)	$\hat{K}(490)$	$\bar{K}(490, z_{37})$	$\delta_{kn} / \bar{K}(490, z_{37})$
D2	10/28/82	31.008	-125.558	0.0356	0.0304	-0.1711
D3	10/29/82	30.255	-129.370	0.0285	0.0321	0.1121
D4	10/30/82	30.027	-133.308	0.0279	0.0330	0.1545
D5	10/31/82	30.015	-137.413	0.0292	0.0340	0.1412
D6	11/01/82	30.027	-141.357	0.0289	0.0300	0.0367
D7	11/02/82	33.078	-141.782	0.0317	0.0300	-0.0567
D8	11/03/82	35.600	-143.140	0.0335	0.0330	-0.0152
D10	11/05/82	40.830	-146.800	0.0713	0.0592	-0.2044
D15	11/10/82	39.833	-133.220	0.0706	0.0400	-0.7650
D16	11/11/82	37.840	-129.758	0.0662	0.0490	-0.3510
D17	11/12/82	35.837	-126.472	0.0444	0.0469	0.0533
D18	11/13/82	33.973	-123.698	0.0706	0.0559	-0.2630
D19	11/14/82	32.653	-120.085	0.0824	0.0893	0.0773
A13	10/14/82	34.993	-121.084	0.0866	0.1236	0.2994
A14	10/14/82	34.990	-121.217	0.0850	0.0610	-0.3934
A20	10/15/82	34.999	-123.003	0.0696	0.0658	-0.0578
A24	10/16/82	35.164	-124.866	0.0423	0.0392	-0.0791
A25	10/16/82	35.164	-124.708	0.0434	0.0382	-0.1361
A31	10/17/82	34.484	-123.827	0.0448	0.0439	-0.0205
A30	10/17/82	34.496	-123.667	0.0482	0.0520	0.0731
A47	10/22/82	34.205	-134.373	0.0269	0.0321	0.1620
A58	10/27/82	33.635	-142.105	0.0304	0.0295	-0.0305
A62	10/28/82	33.770	-141.454	0.0286	0.0247	-0.1579
A73	10/31/82	31.043	-141.582	0.0315	0.0298	-0.0570
A80	11/02/82	31.383	-140.848	0.0312	0.0279	-0.1183
A84	11/03/82	32.991	-140.797	0.0287	0.0289	0.0069
A94	11/04/82	33.883	-140.959	0.0274	0.0298	0.0805
A95	11/04/82	33.825	-141.250	0.0300	0.0283	-0.0601
A106	11/05/82	32.775	-141.532	0.0256	0.0279	0.0824
A123	11/07/82	33.462	-142.088	0.0301	0.0255	-0.1804
A155	11/10/82	32.878	-141.768	0.0274	0.0239	-0.1464
A181	11/17/82	35.889	-121.735	0.0956	0.0720	-0.3278
A182	11/17/82	35.887	-121.652	0.1063	0.0724	-0.4682

dent CZCS error estimates of Arnone *et al.* (1992). There is a qualitative suggestion in the data that CZCS $\hat{K}(490)$ calculations may tend to slightly overestimate *in situ* $\bar{K}(490, z_{37})$ determinations, but that apparent bias is not statistically significant at the 90% confidence level.

5.0 BIO-OPTICAL PROVINCE ANALYSES: VERTICAL PROFILES MODELS OF $K(490)$ and CHLOROPHYLL *a* FLUORESCENCE

The second principal objective of this project is to predict profiles of bio-optical properties over the upper 200 m of the water column, which is much deeper than the depth observed with ocean color sensors

$$\left(z - \frac{1}{K(490)} < 40\text{m} \right).$$

We approached this prediction by partitioning the study region into geographically distinct "bio-optical provinces" associated with several known features of the regional ocean circulation, specifically the California Current System (CCS), Alaskan Gyre (AG), East Central North Pacific central gyre water masses (ECNP), and the Sub-Arctic Front (SAF) (Sects. 1.0 and 3.3); we initially reported the results of this statistical model development in Mueller and Lange (1989), which we will henceforth

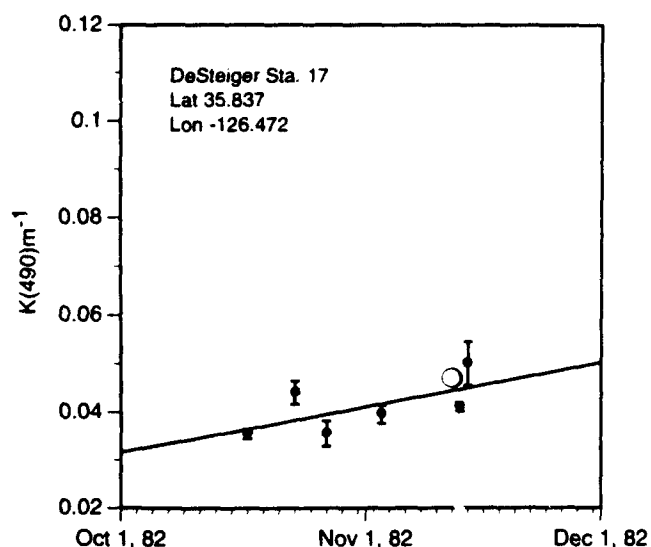


Fig. 4.1. Time series of CZCS median $K(490)$ (solid dots) at $35.83^{\circ}N$, $126.472^{\circ}W$, and estimated standard deviations (error bars) between 1 Oct. and 30 Nov. 1982, compared with the *in situ* $K(490)$ (open circle) measured aboard the USNS Desteiguer on 12 Nov. 1982. The solid line is the least-squares regression trend in CZCS $K(490)$ over the two-month period.

refer to as ML89, and which is included here as Appendix E. In ML89, we showed that, in each province in a given 2-month period (Jun.–Jul. 1985 and Oct.–Nov. 1982), a family of regression equations was found to accurately predict the vertical profiles of $K(490, z)$ and normalized chlorophyll *a* fluorescence $F^*(z)$ from remotely sensed $K(490)$. The reader should refer to ML89 (Appendix E) for a complete description of our approach, assumptions and the resulting model equations. In this section, we will briefly outline the method and its application, and then we will compare the ML89 results to new $K(490, z)$ regression models derived from irradiance profiles measured by the Naval Oceanographic Office in the ECNP, SAF and AG provinces during Jun. 1988 and Oct. 1988.

5.1 Methods

The statistical methods and assumptions used to derive the bio-optical province profile models are described in ML89 (Appendix E), which should be read before proceeding here. This section further illustrates the method by which the model may be applied through a specific example.

Figure 5.1 schematically outlines an example of how the regression model equations given in Table 1 and Fig. 3 of ML89 can be used to convert a remotely sensed $K(490) = 0.0667 \text{ m}^{-1}$ (e.g. as might be extracted from a

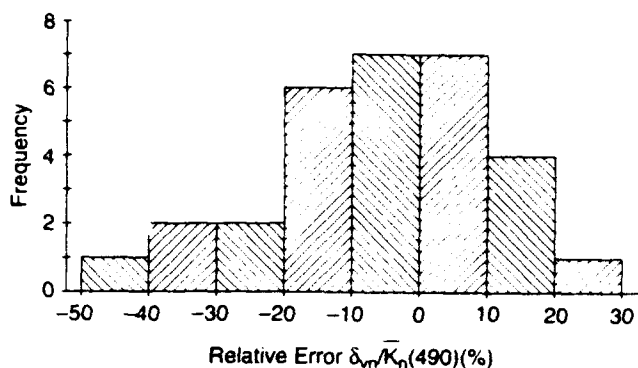


Fig. 4.2. Frequency distribution (counts) of relative error $\delta_{Kn}/K(490, z_{37}) \times 100\%$ of CZCS $K(490)$ two-month trend estimates, compared to *in situ* $K(490)$ measurements.

Monthly Mean $K(490)$ Map in Appendix A; and see Sect. 3.3 above) into vertical profiles of relative irradiance and/or $K(490, z)$ in the Gulf of Alaska (Jun. 1985). The remote sensing depth

$$z_{37} = \frac{1}{K(490)} = 15.0 \text{ m}$$

is used to enter the regression models (ML89, Table 1 and Fig. 1) and to compute the 5 depths z_n where

$$\frac{E(z, 490, z_n)}{E(490, 0)}$$

= 0.37, 0.03, 0.01, 0.003 and 0.001 [in the upper-right panel of Fig. 5.1, z_n correspond to the intersections of the vertical dashed line with the 5 AG regression lines], which can then be used to plot the optical attenuation profile illustrated in the table and figure in the bottom panels of Fig. 5.1. The irradiance attenuation profile is illustrated as either optical attenuation in decibels (lower axis), or \log_{10} relative irradiance (upper axis). The segment of the profiles between 121.2 m (the 0.1% light level) and 200 m was obtained by linear extrapolation of the slope in the segment between the 0.3% light level at 95.7 m and the 0.1% level.

The base-10 logarithmic representation of Fig. 5.1 is presented to illustrate how the ML89 model might be used to predict irradiance attenuation in an optical communication context (e.g. submarine LASER communications). The attenuation depths z_n are, of course, also directly related to the base-*e* (natural) logarithmic representations used elsewhere throughout this report (e.g. Sect. 4.1). In this representation, it is useful to introduce "optical depth" $\tau(490, z)$, defined as

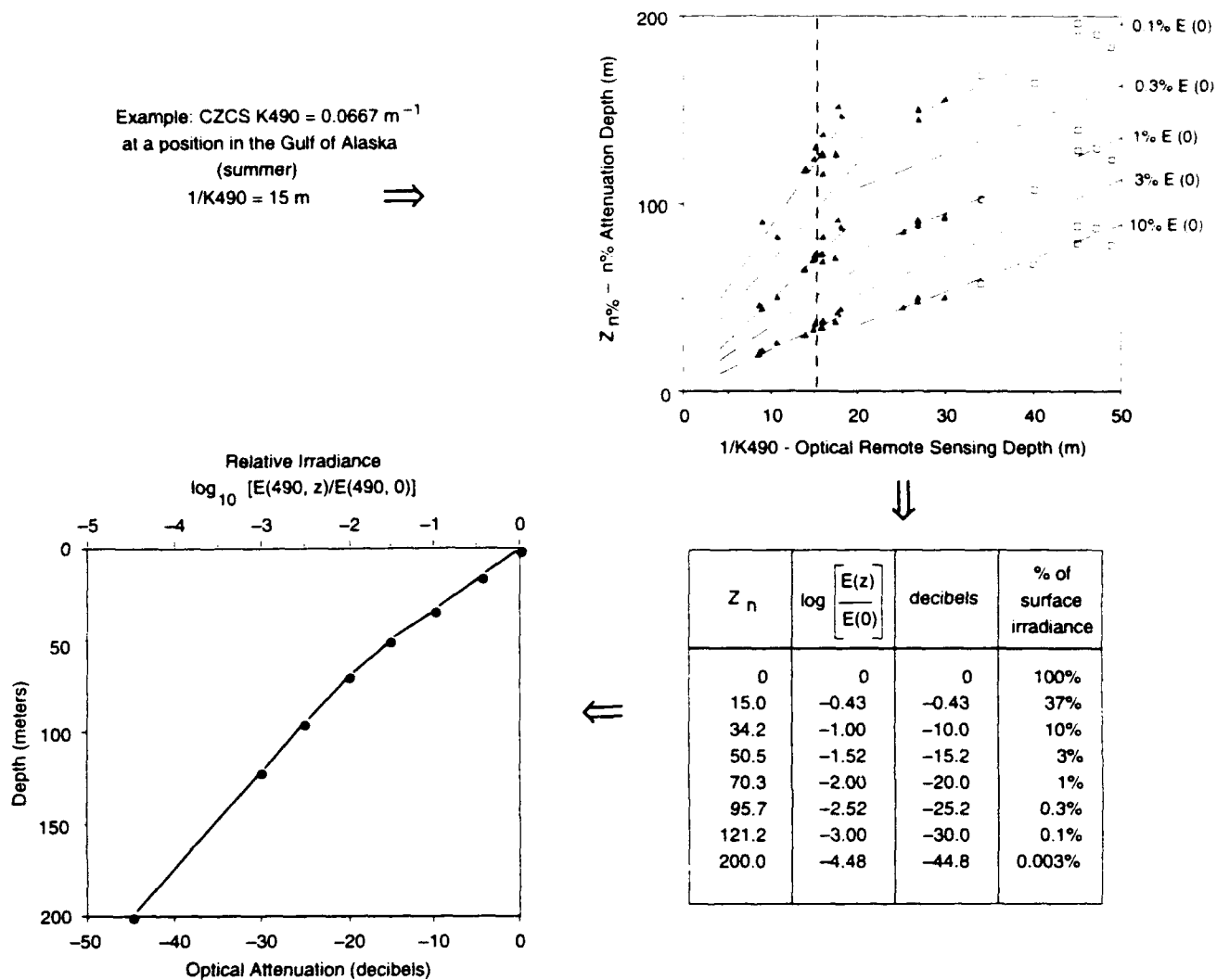


Fig. 5.1. Schematic example illustrating the method for generating an irradiance attenuation profile from remotely sensed K(490) and the Gulf of Alaska Bio-optical Province model of Mueller and Lange (1989).

$$\tau(490, z) = \overline{K}(\lambda, z)z = \int_0^z K(\lambda, z') dz',$$

so that

$$E(490, z) = E(490, 0)e^{-\tau(490, z)},$$

and

$$\tau(490, z) = \ln \frac{E(490, 0)}{E(490, z)}$$

(see also Sect. 4.1 and ML89). For the 6 depths $z_n = z_{37}$, z_{10} , z_3 , z_1 , $z_{0.3}$, and $z_{0.1}$, where $E(490, z)$ are respectively 37%, 10%, 3%, 1%, 0.3% and 0.1% of surface irradiance $E(490, 0)$, the corresponding optical depths are $\tau(490, z_n) = 1.0, 2.3026, 3.5066, 4.6052, 5.8091$ and 6.9078 . Using

the depths z_n from the table in the lower right-hand corner of Fig. 5.1 with these $\tau(490, z_n)$ values, we obtain [for this example, $1/K(490)=15$ m in the AG in June 1985] the optical depth profile illustrated in the lower-right panel of Fig. 5.2; again, the profile below $z_{0.1}$ is linearly extrapolated from the segment between $z_{0.3}$ and $z_{0.1}$ to 200m.

The optical depth profile $\tau(490, z_n)$ produced with this model can, if desired, be converted directly to a 6-layer model of $K(490, z)$:

$$K(490, z) = \frac{1}{z_{37}} = K(490), \quad z \leq z_{37},$$

i.e. remote sensing K(490) in the top layer,

$$K(490, z) = \frac{\tau(490, z_{10}) - \tau(490, z_{37})}{z_{10} - z_{37}}, \quad z_{37} < z \leq z_{10}$$

in the second layer,

$$K(490, z) = \frac{\tau(490, z_3) - \tau(490, z_{10})}{z_3 - z_{10}}, \quad z_{10} < z \leq z_3$$

in the third, and so forth down to

$$K(490, z) = \frac{\tau(490, z_{0.1}) - \tau(490, z_{0.3})}{z_{0.1} - z_{0.3}}, \quad z > z_{0.3},$$

for the entire water column below $z_{0.3}$ meters.

Fig. 5.2 illustrates schematically how the optical depth profile $\tau(490, z)$ generated for the example of Fig. 5.1, together with the counterpart fluorescence model equations of ML89, may be used to generate the companion profile of "log-linear photo-adaptive fluorescence" $F^*(z)$ vs $\tau(490, z)$ (ML89, Appendix E). The 4 panels at the left side of Fig. 5.2 illustrate the ML89 regression equations predicting the 4 parameters z_{\max} (depth of the chlorophyll fluorescence maximum in m), $\tau(z_{\min})$ (the optical depth where the log of normalized fluorescence reaches zero, and remains constant with increasing depth), and the coefficients A_f and B_f giving the surface intercept and slope of the profile between the surface and the optical depth $\tau(z_{\max})$ of the fluorescence maximum. These panels correspond to the regression models illustrated in Figs. 6 through 9 of ML89. Each of these 4 regression models is entered with an argument calculated from remote sensing $K(490)$. The depth of the chlorophyll maximum, z_{\max} , is then entered into the previously modeled $\tau(490, z)$ profile (lower-right panel) to estimate $\tau(z_{\max})$. These 4 model parameters are then used to directly generate the "log-linear photo-adaptive profile" of chlorophyll a fluorescence in the manner illustrated in the dashed arrows leading to the upper-right panel of Fig. 5.2.

Finally, the non-linear profile of $F^*(z)$ vs depth $z(m)$ may be generated by combining the modeled profiles of $\tau(490, z)$ and $\ln[F^*(\tau)]$ (the 2 panels on the right-hand side of Fig. 5.2) in the manner illustrated in Fig. 5.3. $\tau(490, z)$ is sequentially incremented at some small depth increment $\Delta\tau$ to step from the surface [$\tau(490, 0) = 0.00$] to as deep as is desired. At each step $\tau(490, z)$ is used, as shown in Fig. 5.3 to enter both the $\tau(490, z)$ model profile, to determine z in m, and the $\ln[F^*(\tau)]$ profile to determine FL^* , with the resulting profile $FL^*(z)$ illustrated in the lower-right panel of Fig. 5.3.

In most naval warfare applications, the optical depth model giving $\tau(490, z)$ [or equivalently $K(490, z)$] (Fig. 5.1 above and accompanying explanation) will be sufficient alone. Nevertheless, the associated chlorophyll a fluorescence profile model may be indirectly valuable as an input to process-based forecast models, which may eventually be developed to predict optical profile attenuation in the absence of satellite data, or for future operations. Therefore, both bio-optical models were developed and analysed for this project.

5.2 Results

The results of the initial ML89 bio-optical province modeling are given in Appendix E. In this section we report three new models of optical attenuation profiles for the AG, SAF and ECNP provinces, based on irradiance profiles $E_d(\lambda, z)$ measured by the Naval Oceanographic Office during two cruises in Jun. and Oct. 1988. These data were made available to us through the courtesy of Ms. Kimberley Davis of the Naval Oceanographic Office.

The location of the stations at which $E_d(490, z)$ were measured by NAVOCEANO are illustrated in Figs. 5.4 and 5.5, respectively, for Jun. and Oct. 1988. We have categorized the stations by bio-optical province (using latitude) according to the following rule:

AG: Lat > 40.000°N

SAF: 38.000°N < Lat ≤ 42.000°N, or

ECNP: Lat ≤ 38.000°N.

Using the methods of ML89 (Appendix E), we computed $K(490)$ and depths z_{10} , z_3 , z_1 , $z_{0.3}$, and $z_{0.1}$ for each profile $E_d(\lambda, z)$; the data for z_{10} , z_1 , $z_{0.1}$, are illustrated in Fig. 5.6 for Jun. 1988 and in Fig. 5.7 for Oct. 1988. The province in which each set of data was measured is indicated, in Figs. 5.6 and 5.7, as "o" for ECNP, "+" for SAF, and "x" for AG.

The levels and trends of ECNP and SAF attenuation depths z_n vs $K(490)$ relationships are not readily separable in Jun. and Oct. 1988 (Fig. 5.7). We therefore combined these samples to generate an overall SAF/ECNP regression model for $1/K(490) \geq 17.5$ m (Table 5.1). This regression fit is shown as a family of solid lines in the range $1/K(490) \geq 17.5$ m in both Figs. 5.6 and 5.7.

The SAF data in Jun. 1988 (Fig. 5.6) were all in the range $1/K(490) < 17.5$ m and follow a completely unique trend with $1/K(490)$. The one SAF data point measured at $1/K(490) < 17.5$ m in October 1988 also falls well within the scatter of the June 1988 data. Therefore, we pooled the data from the June and October 1988 SAF

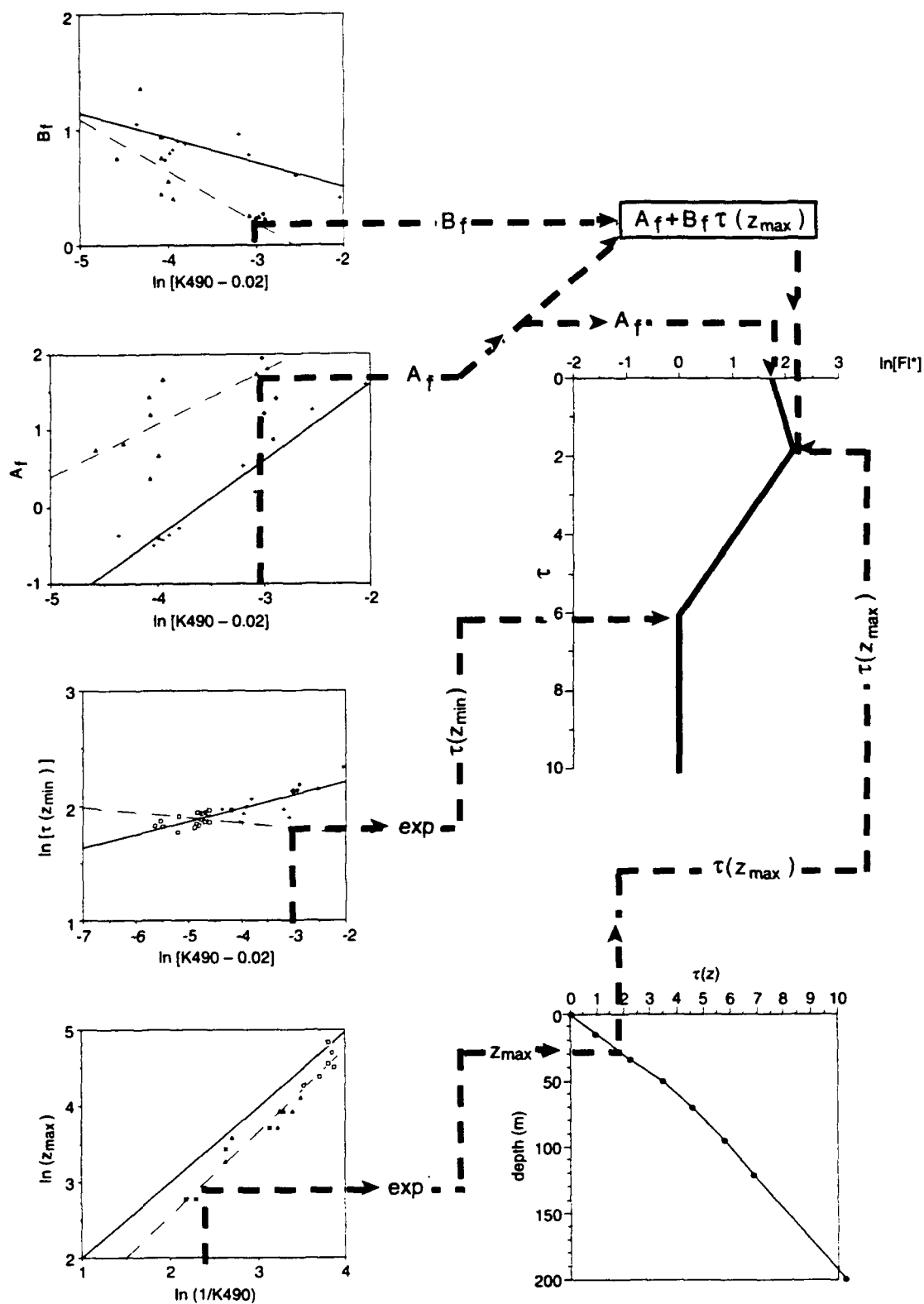


Fig. 5.2. Schematic diagram illustrating the log-linear chlorophyll *a* fluorescence model, using the example, and resulting optical depth profile from Fig. 5.1, and the regression models of Mueller and Lange (1989).

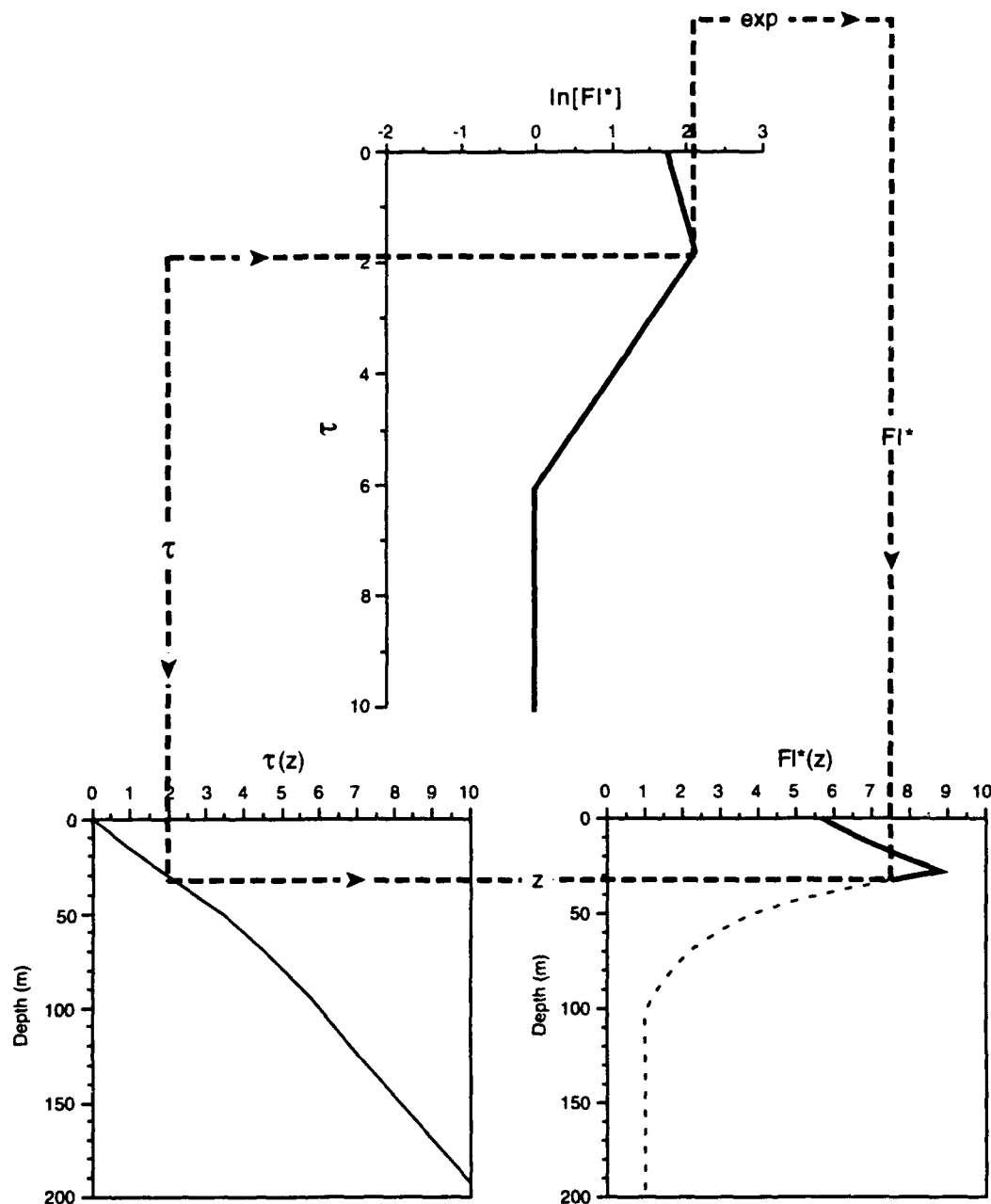


Fig. 5.3. Schematic diagram illustrating the method for generating a chlorophyll *a* fluorescence profile by combining the optical depth profile of Fig. 5.1 with the log-linear fluorescence profile of Fig. 5.2.

$[1/K(490) < 17.5 \text{ m}]$ samples to calculate that regression model (Table 5.1); the regression models for the SAF $[1/K(490) < 17.5 \text{ m}]$ are plotted as a family of double-dash lines in Figs. 5.6 and 5.7.

Finally, we also combined the AG stations from both periods to obtain a common regression model (Table 5.1), which are plotted as sets of dashed lines in Figs. 5.6 and 5.7.

5.3 Discussion and Conclusions

The results obtained above for June and October 1988, strongly support the primary conclusions of ML 89. Both analyses confirm that remote sensing $K(490)$ is closely related to the underlying profile of $K(490, z)$ to depths as great as 200 m, and that $K(490)$ can be used to statistically predict the $K(490, z)$ profile within geo-

graphically distinct bio-optical provinces. Furthermore, the bio-optical province models appear to persist for at least several months.

The present results for the SAF province (Figs. 5.6 and 5.7 and Table 5.1) are qualitatively similar to the more limited set of observations presented in ML 89 (Fig. 5), and support their supposition that the SAF is a separate province with bio-optical characteristics that are strongly distinct from those in adjacent waters of ECNP and AG provinces. However, the present results give the first quantitative characterization of the SAF province and show that while its turbid surface water masses ($1/K(490)$)

< 17.5 m) are associated with a very distinctive $K(490,z)$ profile, the SAF profiles with more transparent surface layers ($1/K(490) \geq 17.4$ m) are not distinguishable from those in ECNP. The distinguishing characteristic of turbid-surface SAF profiles is that the deep portion of the $K(490,z)$ profile is much cleaner than is the case for similar remote sensing $K(490)$ values in other provinces. This may manifest a thin layer of productive water in the SAF spread over much more transparent layers of ECNP intermediate water masses.

Contrary to the results of ML89, the families of z_n vs $K(490)$ relationships observed here (Figs. 5.6 and 5.7)

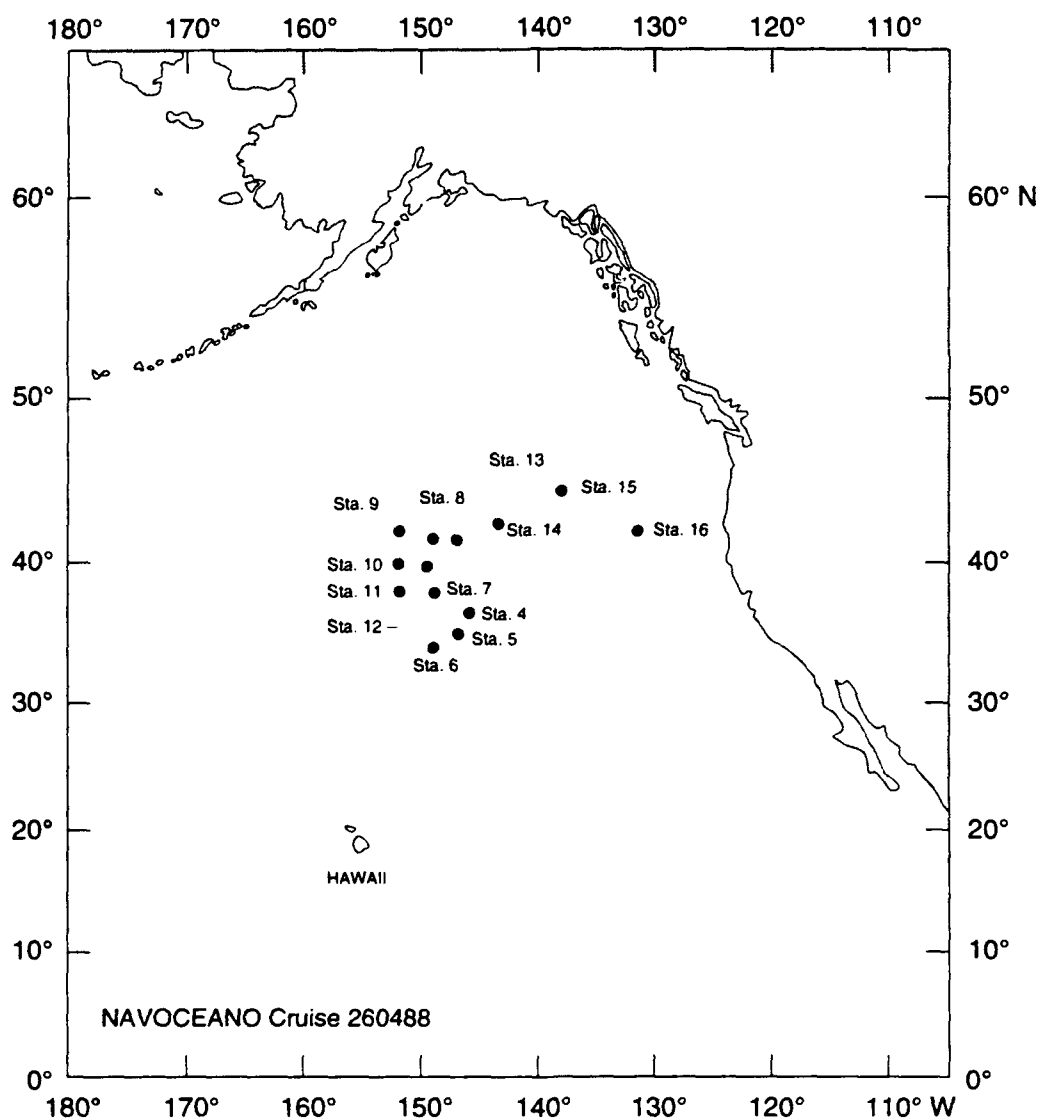


Fig. 5.4. Geographic locations of optical profile stations on NAVOCEANO Cruise 260488, 16 through 29 June 1988.

appear to have persisted unchanged through the period from Jun. through Oct. 1988. ML89 found significantly different relationships in ECNP in Jun.–Jul. 1985, compared to their results for Oct.–Nov. 1982. They suggest that the difference may be a manifestation of seasonal change. The present lack of any significant change between these two seasons in one year, however, would suggest that the differences observed by ML89 may have been interannual in nature.

The ECNP model coefficients are statistically different (at the 90% confidence level) for all depths z_n in both sets of models for that province in ML89 (Table 1). The

present AG [$1/K(490) < 25$ m] model coefficients fall within the 90% confidence limits of the counterpart ML89 June/July $1/K(490) < 20$ m models only at the 10% and 1% depths, and they are otherwise statistically different from the ML89 (Table 1) models. The lack of statistically significant quantitative agreement between the present results and those in ML89 further strengthens the suggestion that inter-annual variability is critically important, especially at depths below the 10% light levels.

Taken together, the results in ML89 and Sect. 5.2 demonstrate that profiles of $K(490, z)$ can be estimated

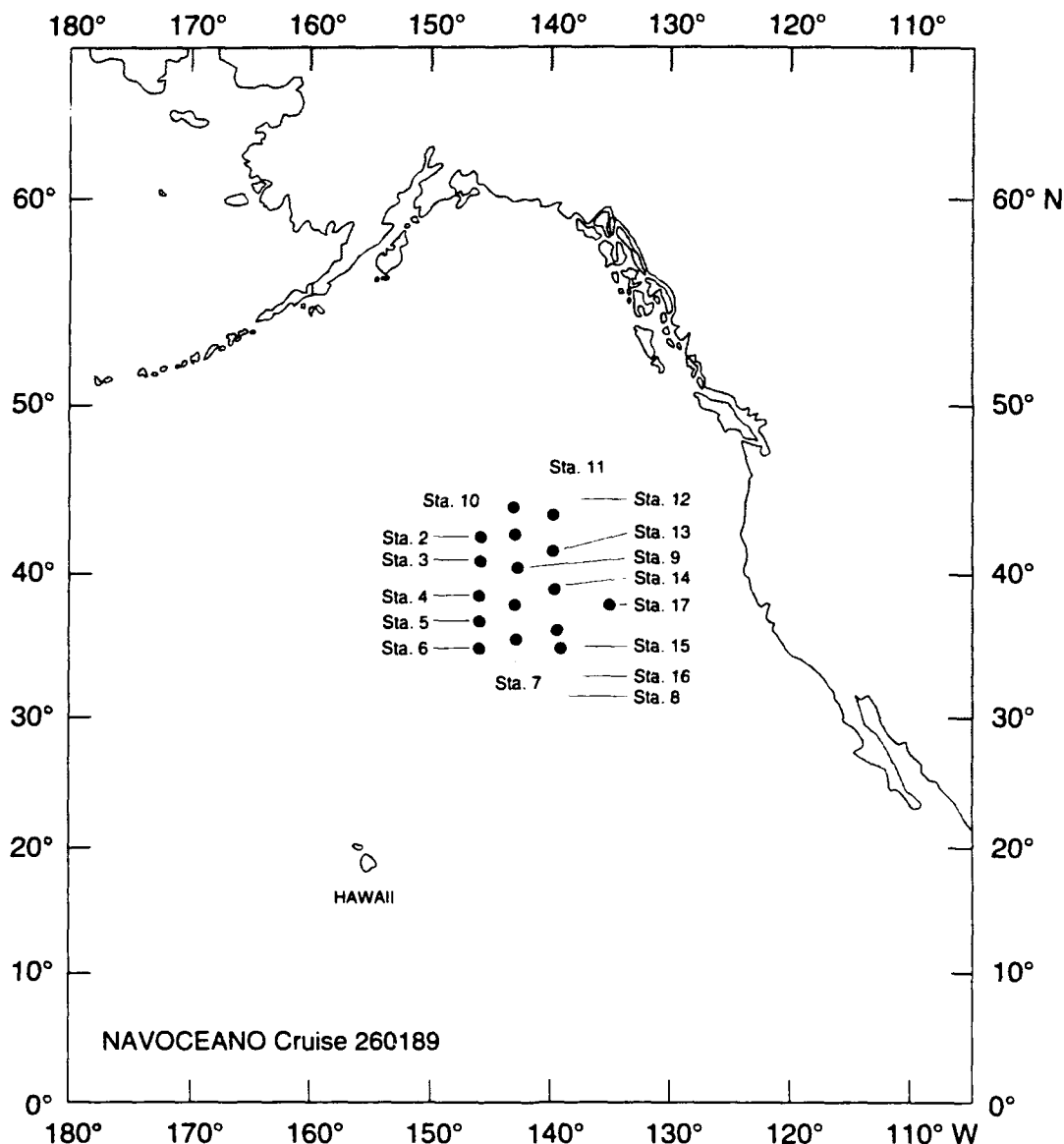


Fig. 5.5. Geographic locations of optical profile stations on NAVOCEANO Cruise 260189, 17 Oct through 1 Nov 1988.

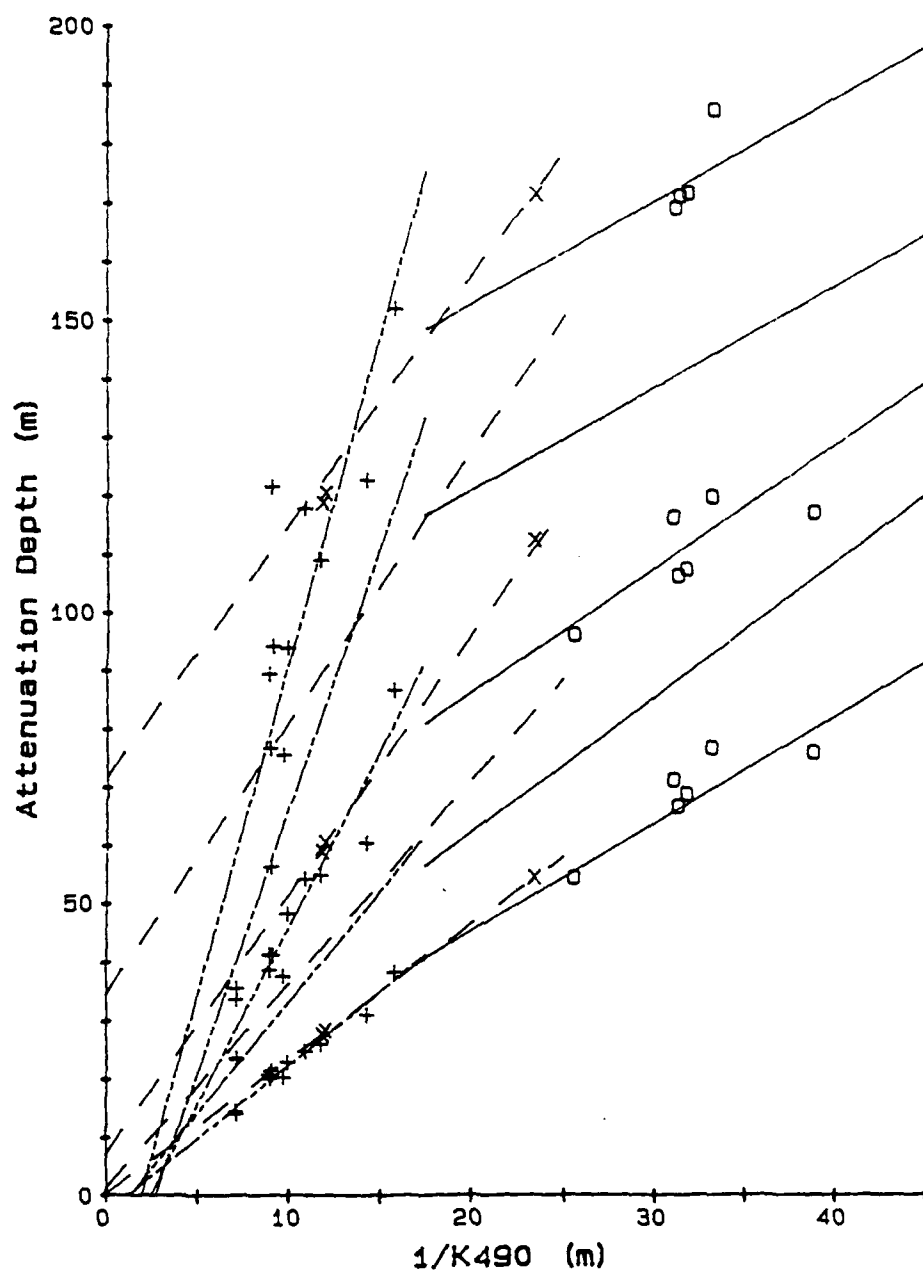


Fig. 5.6. Covariability of remote sensing optical depth $1/K(490)$ (m) with attenuation depths z_n (m), where irradiances $E_d(\lambda, z_n)$ are 10%, 3%, 1% and 0.1% of $E_d(\lambda, 0)$. The data points illustrated for the 10%, 1% and 0.1% levels were measured in the ECNP ("o"), SAF("+") and AG("x") provinces by the Naval Oceanographic Office in Jun. 1988 (Cruise 260488). The lines indicate the three families of regression lines relating the 5 attenuation depths z_n to $1/K(490)$ in the AG (— — —), SAF [$1/K(490) < 17.5$ m] (· · · · ·) and ECNP + SAF [$1/K(490) \geq 17.5$ m] (————); the regressions in each province combine the data shown here with that from Naval Oceanographic Office Cruise 260488 in Oct. 1988 (Fig. 5.7).

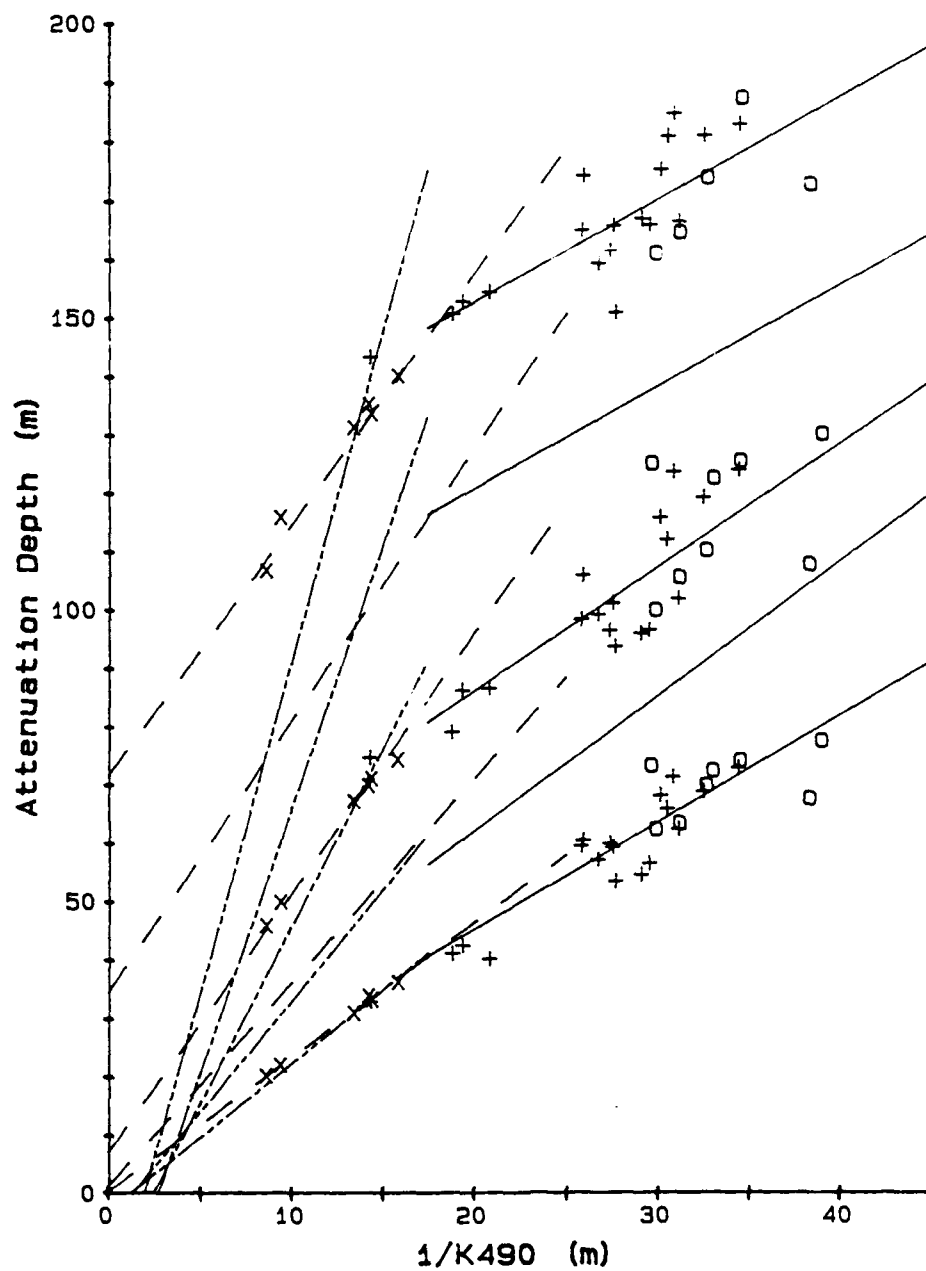


Fig. 5.7. Same as Fig. 5.6 for Naval Oceanographic Office Cruise 260189 in October 1988.

Table 5.1

Table of coefficients for models of irradiance attenuation at 490 nm, expressed in terms of depths z_n (m) where $E_d(490, z_n)$ are 10%, 3%, 1%, 0.3% and 0.1% of surface irradiance $E_d(490, 0)$. z_n are calculated according to the equation

$$z_n = A_n + B_n/K(490),$$

where $K(490)$ is the diffuse attenuation coefficient obtained from remotely sensed ocean color data, and A_n and B_n are sets of regression coefficients calculated from irradiance profiles $E_d(\lambda, z)$ measured by the Naval Oceanographic Office (Cruises 260488 and 260189) in the ECNP, SAF and AG bio-optical provinces.

Alaskan Gyre: Jun. and Oct. 1988
 $1/K(490) < 25$ m

n%	$\tau(z_n)$	A_n	B_n	r^2	S_{xy}
10*	2.30	0.1614	2.3095	0.998	0.44
3	3.51	1.1774	3.4845	0.99	1.21
1*	4.61	6.9291	4.4362	0.99	1.45
0.3	5.81	34.4146	4.6402	0.98	2.75
0.1	6.91	71.5425	4.2875	0.98	2.71

Sub-Arctic Front: Jun. and Oct. 1988
 $1/K(490) < 17.5$ m

n%	$\tau(z_n)$	A_n	B_n	r^2	S_{xy}
10	2.30	-3.1463	2.5297	0.97	1.216
3	3.51	-5.0938	3.7966	0.89	3.66
1	4.61	-14.8810	6.0456	0.84	7.34
0.3	5.81	-24.3646	8.9808	0.79	12.80
0.1	6.91	-22.0674	11.2638	0.71	19.708

Sub-Arctic Front and ECNP: Jun. and Oct. 1988
 $1/K(490) \geq 17.5$ m

n%	$\tau(z_n)$	A_n	B_n	r^2	S_{xy}
10	2.30	8.4958	1.8325	0.79	4.75
3	3.51	15.9886	2.3036	0.71	7.30
1	4.61	43.5587	2.1194	0.63	8.09
0.3	5.81	85.6198	1.7492	0.57	7.62
0.1	6.91	117.2540	1.7631	0.55	7.40

from remotely sensed $K(490)$ using statistical models based on *in situ* measurements of $E_d(\lambda, z)$ distributed within a geographically distinct bio-optical province. The coefficients of models persist for at least a few months, but they may vary seasonally, and certainly appear to do so annually. We therefore conclude that at least seasonal survey cruises of $E_d(\lambda, z)$ at a grid of station locations will be necessary to update bio-optical province profile models in a region of interest. Once updated, the models may then be used with satellite ocean color image data alone for periods of a few months. This approach is

a logistically feasible one, although it entails a more costly burden of field work than might be hoped for. Bio-optical moorings, similar to those proposed by various investigators for use during the JGOFS and NASA SeaWiFS programs, may offer a more economical alternative for acquiring the necessary *in situ* observations in the future.

6.0 SUMMARY AND RECOMMENDATIONS

With this Final Report, we deliver a digital climatology of monthly mean $K(490)$ distributions in the North-

east Pacific Ocean. This data base is the end result of an exhaustive and internally consistent effort to process and analyse the complete series of ocean color images which were measured in this area using the Nimbus-7 CZCS, and its production and delivery successfully completes one of the two primary objectives of this project. The daily K(490) estimates underlying this climatology are shown, by comparisons to *in situ* ship measurements, to be accurate within 20%, except in areas of strong spatial gradients, where discrepancies may be as large as 50% (Sect. 4 and Appendix B). The large discrepancies in ocean front regimes are due to the difficulty in comparing pointwise ship observations with satellite observations that are not strictly concurrent, and which represent a larger spatial scale. Therefore, these discrepancies in fronts are not a useful, direct measure of the error in K(490) derived from ocean color measurements.

The set of K(490,z) and chlorophyll fluorescence $f(z)$ profile models, which are presented as regression coefficients in Table 5.1 and Table 1 of Appendix E, provide an easily applied method for extrapolating the near-surface CZCS K(490) values to depths up to 200 m. These models fulfill the second major objective of this contract. At present, however, we can only be assured that these models will be reasonably accurate within each province, and within a few months of the observation dates of the *in situ* bio-optical profiles used to calculate the model coefficients. Interannual variability appears to be too large a signal to expect these models to be accurately applied to satellite data from other years. Therefore, any direct operational application of this method should include provisions for periodic surveys of irradiance profiles $E_d(\lambda, z)$ in regions where it is to be employed. The methods described in Appendix E may be used to analyse these new survey data and update the model coefficients for each included bio-optical province of the operating area.

The Monthly Composite Mean K(490) climatology, and the accompanying analyses under the scope of this contract (as reported in this Final Report), have not fully exploited the potential information content of the CZCS Levels 2 and 3 data bases described in Sects. 2.1 and 3.1. For example, the $5^\circ \times 5^\circ$ K(490) Time Series (Sects. 2.1.7, 3.1.4.4 and 3.4; Appendix D) are in ideal form for applying the method of Chelton and Schlax (1991) to optimally estimate two-week and monthly means. Sample sizes and data distributions in time are adequate for this analysis throughout most of the CCS and the region of transition into the oligotrophic water masses of the ECNP central

gyre, and it would not be difficult to extract time series at additional grid points from the Daily Composite K(490) Map series (Sects. 2.1.5 and 3.1.4.2). The Daily K(490) Map series would also directly support spatial analyses using EOF techniques similar to those employed by Abbott and Barksdale (1991), at 5 Km resolution. It would also be straightforward to resample K(490) (and chlorophyll also, if desired) from the CZCS Level-2 data base (Sects. 2.1.3 and 3.1.2) onto a Transverse Mercator Grid at 2 Km resolution (the approximate Nyquist spacing for CZCS data) for time/space analyses in selected coastal sub-areas. These additional analyses, and perhaps others, could be carried out in a cost-effective way under ongoing or future work, should the resulting analyses and products be considered appropriate to the Navy's needs.

7.0 REFERENCES

- Abbott, M.R. and B. Barksdale, 1991. Phytoplankton pigment patterns and wind forcing off Central California. *J. Geophys. Res.*, **96**(C8): 14,649-14,667.
- Anderson, D.E., J.L. Angel and A.J. Gorny, (ca.) 1980. *World Data Bank II: Content, Structure and Application*. Unpublished documentation. Central Intelligence Agency, Washington, DC. 16pp.
- Arnone, R.A., G. Terrie, L. Estep, and R.A. Oriol, 1992. *Ocean Optical Data Base*. NOARL Tech. Note 254. Naval Oceanog. and Atmos. Res. Lab., Stennis Space Center, MS 36 pp.
- Austin, R.W. and T.J. Petzold, 1981. The determination of diffuse attenuation coefficient of seawater using the Coastal Zone Color Scanner. In: *J.F.R. Gower (ed) Oceanography from Space*. Plenum Press, New York. pp 239-256.
- Ball Aerospace Systems Div., 1979. *Development of the Coastal Zone Color Scanner for Nimbus 7: Vol. 2 - Test and Performance Data*. Final Report F78-11, Rev. A., Boulder CO. pp. 2-22.
- Bowman, K.P. and A.J. Krueger, 1985. A global climatology of total ozone from the Nimbus-7 Total Ozone Mapping Spectrometer. *J. Geophys. Res.*, **90**: 7967-7976.
- Chelton, D.B. and M.G. Schlax, 1991. Estimation of time averages from irregularly spaced observations, with application to Coastal Zone Color Scanner estimates of chlorophyll concentration. *J. Geophys. Res.*, **96**: 14,669-14,692.
- Gordon, H.R., 1988. Ocean color remote sensing systems: radiometric requirements. In: P.N. Slater (ed)

- Recent Advances in Sensors, Radiometry and Data Processing for Remote Sensing*. SPIE, **924**: 151-167.
- Gordon, H.R., J.W. Brown and R.H. Evans, 1988. Exact Rayleigh scattering calculations for use with the Nimbus-7 Coastal Zone Color Scanner. *Appl. Opt.*, **27**: 862.
- Gordon, H.R., J.W. Brown, R.H. Evans and D.K. Clark, 1983a. Nimbus-7 CZCS: reductions of its radiometric sensitivity with time. *Appl. Opt.*, **22**: 3929.
- Gordon, H.R. and D.K. Clark, 1981. Clear water radiances for atmospheric correction of Coastal Zone Color Scanner imagery. *Appl. Opt.*, **20**: 4175.
- Gordon, H.R., D.K. Clark, J.W. Brown, O.B. Brown, R.H. Evans and W.W. Broenkow, 1983b. Phytoplankton pigment concentrations in the Middle Atlantic Bight: comparisons of ship determinations and CZCS estimates. *Appl. Opt.*, **22**: 20.
- Flament, P., L. Armi and L. Washburn, 1985. The evolving structure of an upwelling filament. *J. Geophys. Res.*, **90**(11): 11765-11778.
- Hickey, B.M., 1979. The California Current system—hypotheses and facts. *Prog. Oceanogr.*, **8**: 191-279.
- Hickman, G.D. (Ed.), 1991. *Applications of Ocean Color to Naval Warfare*. Report Nr. BC 009:91:321, NOARL, Stennis Space Center, MS. 43 pp.
- Hovis, W.A., D.K. Clark, F. Anderson, R.W. Austin, W.H. Wilson, E.T. Baker, D. Ball, H.R. Gordon, J.L. Mueller, S.Z. El-Sayed, B. Sturm, R.C. Wrigley, and C.S. Yentsch. Nimbus-7 Coastal Zone Color Scanner: system description and initial imagery. *Science*, **210**: 60-63.
- Huyer, A.E., 1983. Coastal upwelling in the California Current system. *Prog. Oceanogr.*, **12**: 259-284.
- Mooers, C.N.K. and A.R. Robinson, 1984. Turbulent jets and eddies in the California Current and inferred cross-shore transports. *Science*, **223**: 51-53.
- Mueller, J.L., 1984. Effects of water reflectance at 670 nm on Coastal Zone Color Scanner (CZCS) aerosol radiance estimates off the coast of California. *Ocean Optics*, SPIE, Vol. 489, SPIE, Bellingham, WA. pp 179-186.
- Mueller, J.L., 1985. Nimbus-7 CZCS: confirmation of its radiometric sensitivity decay rate through 1982. *Appl. Opt.*, **24**: 1043.
- Mueller, J.L. 1988. Nimbus-7 CZCS: Electronic overshoot due to cloud reflectance. *Appl. Opt.*, **27**: 438-440.
- Mueller, J.L. and R.W. Lange, 1989. Bio-optical provinces of the Northeast Pacific Ocean: a provisional analysis. *Limnol. Oceanogr.*, **34**(8): 1572-1586.
- Mueller, J.L., C.C. Trees and R.A. Arnone, 1990. Evaluation of Coastal Zone Color Scanner diffuse attenuation coefficient algorithms for application to coastal water. *Ocean Optics X*, Vol. 1032, SPIE, Bellingham, Wa. pp. 72-78.
- Neckel, H. and D. Labs, 1981. Improved data of solar spectral irradiance from 0.33 to 1.25 μ . *Solar Physics*, **74**: 231-249.
- Neckel, H. and D. Labs, 1984. The solar radiation between 3300 and 12500 Å. *Solar Phys.*, **90**: 205.
- Niiler, P.P. and C.J. Koblinsky, 1985. A local time-dependent sverdrup balance in the eastern North Pacific Ocean. *Science*, **229**: 754-756.
- Niiler, P.P. and R.W. Reynolds, 1984. The three-dimensional circulation near the eastern North Pacific Subtropic
- NOPS, 1986. *Nimbus-7 Solar Backscattered Ultraviolet and Total Ozone Mapping Spectrometer (SBOV/TOMS): GRIDTOMS Tape specifications*. NASA GSFC, Greenbelt, MD 17pp.
- Pak, H. and D.A. Kiefer, and J.C. Kitchen, 1988. Meridional variations in the concentration of chlorophyll and microparticles in the North Pacific Ocean. *Deep-Sea Res.*, **35**: 1151-1171.
- Rattray, M. Jr., 1982. A simple exact treatment of the baroclinicity-bathymetry interaction in a frictional, iterative, diagnostic ocean model. *J. Phys. Oceanogr.*, **12**: 997-1003.
- Richardus, P. and R.K. Adler, 1972. *Map Projections for Geodesists, Cartographers and Geographers*. American Elsevier, New York. 174 pp.
- Roden, G.I., 1975. On North Pacific temperature, salinity, sound velocity and density fronts and their relation to the wind and energy flux fields. *J. Phys. Oceanogr.*, **5**(4): 557-571.
- Roden, G.I., 1977. Oceanic subarctic fronts of the Central Pacific: structure of and response to atmospheric forcing. *J. Phys. Oceanogr.*, **7**(6): 761-778.
- Roden, G.I., 1980. On the subtropical frontal zone north of Hawaii during winter. *J. Phys. Oceanogr.*, **10**: 342-362.
- Simpson, J.J., C.J. Koblinsky, L.R. Haury and T.D. Dickey, 1984. An offshore eddy in the California Current System. *Prog. Oceanogr.*, **13**: 1-111.
- Simpson, J.J., C.J. Koblinsky, J. Peláez, L.R. Haury and D. Wiesenhahn, 1986. Temperature-plant pigment-optical relations in a recurrent offshore mesoscale eddy near Point Conception California. *J. Geophys. Res.*, **91**: 12919-12936.

- Snyder, J.P. 1982. *Map Projections Used by the U.S. Geological Survey*. Geological Survey Bulletin 1532, U.S. Government Printing Office, Washington, DC 313 pp.
- Strub, P.T., P.M. Kosro and A. Huyer, 1991. The nature of cold filaments in the California Current system. *J. Geophys. Res.*, **96**: 14743-14768.
- Wilson, W.H., 1980. *Solar Ephemeris Algorithm*. SIO Ref. 80-13, Visibility Laboratory, Scripps Institute of Oceanography, La Jolla, CA 70pp.
- Wolford, G.N., 1980. *Nimbus-GCZSCRT Tape*. Tape Specification T744041 (Rev. 5/5/80), Nimbus Observation Processing Systems (NOPS), NASA Goddard Space Flight Center, Greenbelt, MD. 31pp.

**OPTICAL CLIMATOLOGY OF THE NORTHEAST
PACIFIC OCEAN**

APPENDIX A

**ATLAS OF K(490) IN THE NORTHEAST PACIFIC OCEAN
NOVEMBER 1978 – JUNE 1986**

Monthly Composite Means of Diffuse Attenuation
Coefficients K(490) Derived from Nimbus-7 CZCS Data

James L. Mueller

Center for Hydro-Optics & Remote Sensing
San Diego State University
6505 Alvarado Road, Suite 206
San Diego, CA 92120-5005

CHORS Technical Memorandum 001-93

Prepared for the Naval Research Laboratory
(Stennis Space Center) Code 311
as part of the Final Report, NOARL Contract N00014-89-C-6007

APPENDIX A

ATLAS OF K(490) IN THE NORTHEAST PACIFIC OCEAN NOVEMBER 1978-JUNE 1986

The ocean optical climate in the NE Pacific Ocean is presented here as a map sequence, extending from November 1978 through June 1986, of monthly composite means of K(490), the diffuse attenuation coefficient at 490 nm. The maps are color-coded images of composite mean K(490) values on a 962×1002 (N-S \times E-W) Mercator grid extending from 30°N to 62°N in latitude and 115°W to 165°W in longitude; the spatial dimensions of each grid cell are 3' of longitude and the appropriate Mercator distance at each latitude, and both are ≤ 5 Km everywhere in the grid. The color scale with which values of K(490) in m^{-1} are coded in the map displays is illustrated on each page of this atlas.

The values of K(490) from all CZCS images on a given day were resampled onto the Mercator grid to form the digital version of a daily composite map of K(490). For each month, the number of daily composite maps having usable CZCS K(490) data within the grid area is listed in Table A1. All daily composite maps from a given month were combined by averaging the K(490) values at each grid cell to form the monthly composite mean. Refer to the main text of CHORS TM001-92 for a complete description of methods used in averaging and regridding the data, and to Appendix C for a description of the content and format of the digital data files.

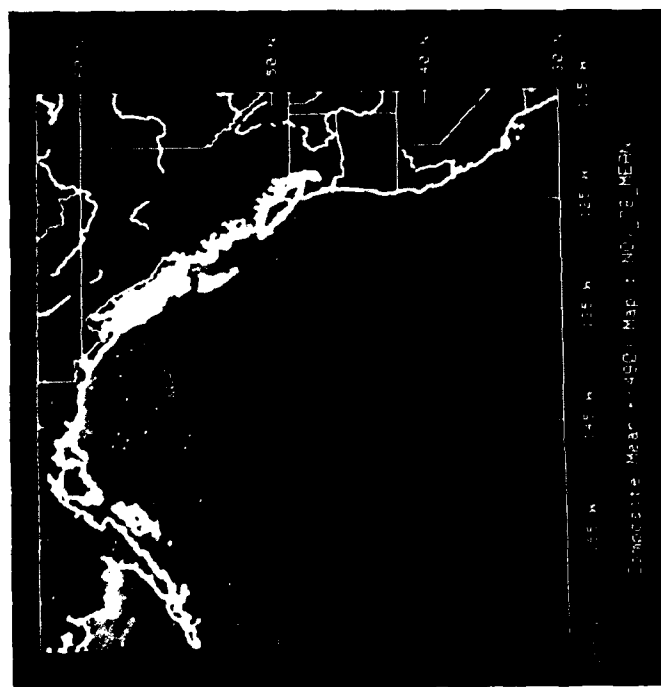
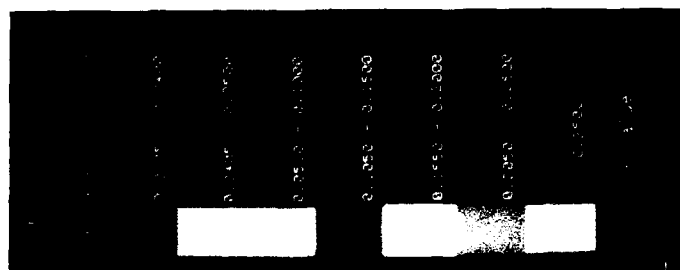
For each digital file, the monthly mean K(490) at each grid cell grid was coded to match the color scale illustrated on the following pages. A map overlay showing coastlines, islands, rivers and political boundaries was extracted from the CIA geographic data base and mapped to the 962×1002 Mercator projection grid. Finally, the overlay and color coded K(490) grid were merged to form a single image file, which was displayed on a color monitor and photographed to produce the map shown here.

Table A1
Monthly Mean K(490) Map Directory

Year	Month	Days with CZCS Data	Page
1978	Nov	17	4
	Dec	19	4
1979	Jan	15	5
	Feb	16	5
	Mar	26	5
	Apr	25	5
	May	20	6
	Jun	20	6
	Jul	17	6
	Aug	22	6
	Sep	27	7
	Oct	30	7
	Nov	28	7
	Dec	24	7
1980	Jan	21	8
	Feb	23	8
	Mar	30	8
	Apr	25	8
	May	25	9
	Jun	28	9
	Jul	29	9
	Aug	24	9
	Sep	30	10
	Oct	24	10
	Nov	21	10
	Dec	22	10
1981	Jan	18	11
	Feb	21	11
	Mar	22	11
	Apr	20	11
	May	19	12
	Jun	16	12
	Jul	16	12
	Aug	17	12
	Sep	15	13
	Oct	26	13
	Nov	20	13
	Dec	19	13
1982	Jan	17	14
	Feb	12	14
	Mar	17	14
	Apr	19	14
	May	17	15
	Jun	7	15
	Jul	14	15
	Aug	14	15
	Sep	22	16
	Oct	23	16
	Nov	14	16
	Dec	10	16

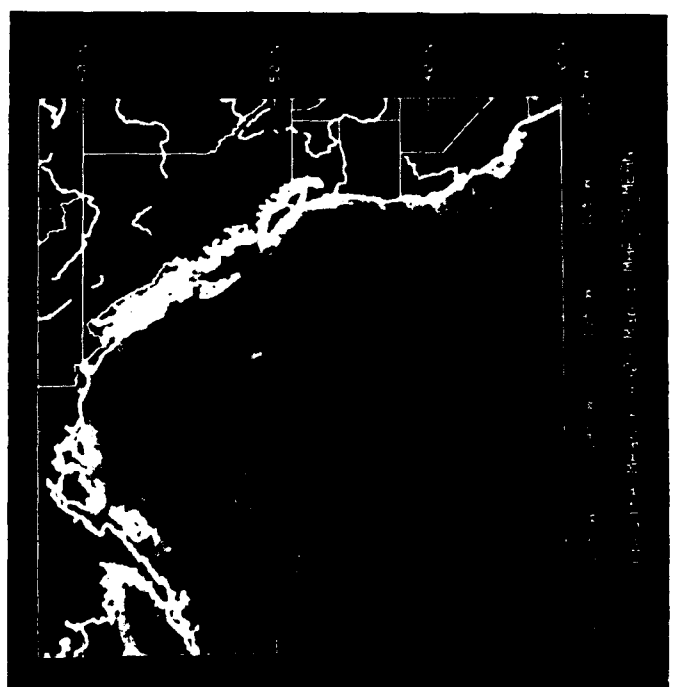
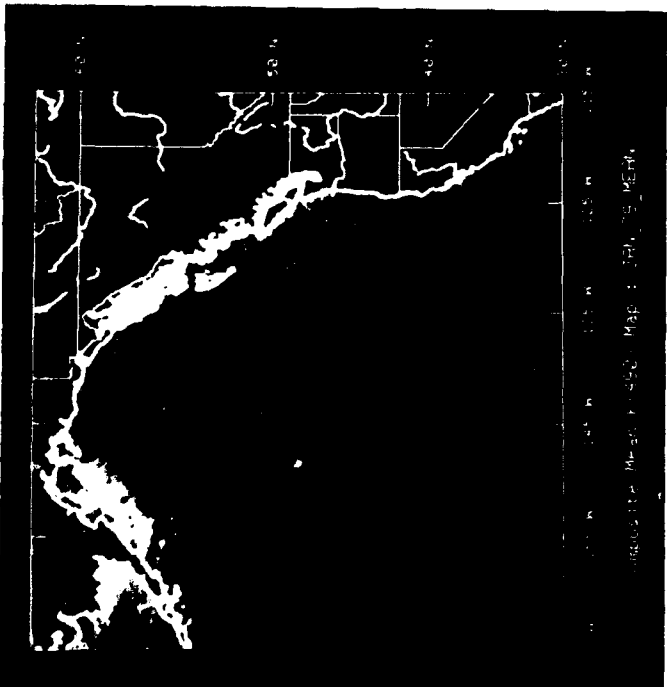
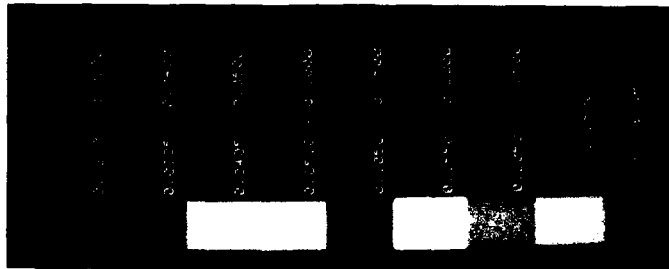
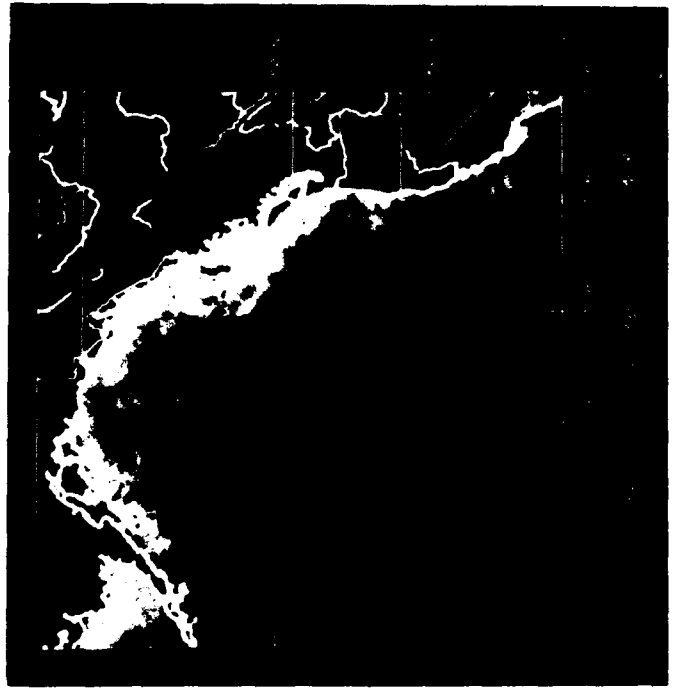
Table A1 (cont'd.)

Year	Month	Days with CZCS Data	Page
1983	Jan	19	17
	Feb	9	17
	Mar	10	17
	Apr	12	17
	May	10	18
	Jun	11	18
	Jul	13	18
	Aug	19	18
	Sep	18	19
	Oct	13	19
	Nov	8	19
	Dec	3	19
1984	Jan	7	20
	Feb	8	20
	Mar	8	20
	Apr	6	20
	May	5	21
	Jun	2	21
	Jul	2	21
	Aug	3	21
	Sep	8	22
	Oct	12	22
	Nov	11	22
	Dec	2	22
1985	Jan	7	23
	Feb	4	23
	Mar	16	23
	Apr	15	23
	May	9	24
	Jun	6	24
	Jul	6	24
	Aug	12	24
	Sep	13	25
	Oct	12	25
	Nov	15	25
	Dec	15	25
1986	Jan	9	26
	Feb	9	26
	Mar	13	26
	Apr	23	26
	May	24	27
	Jun	11	27

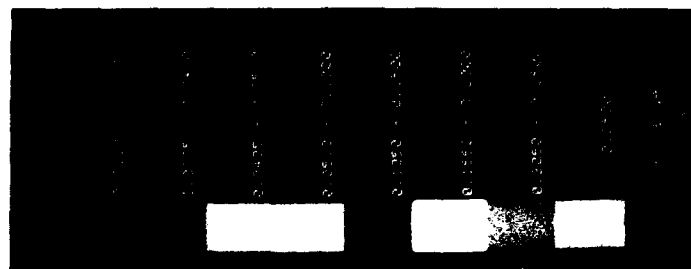
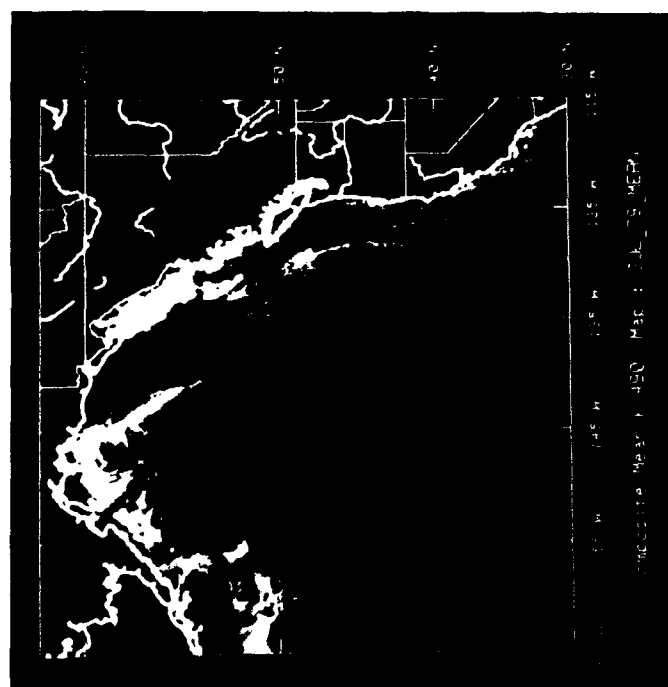
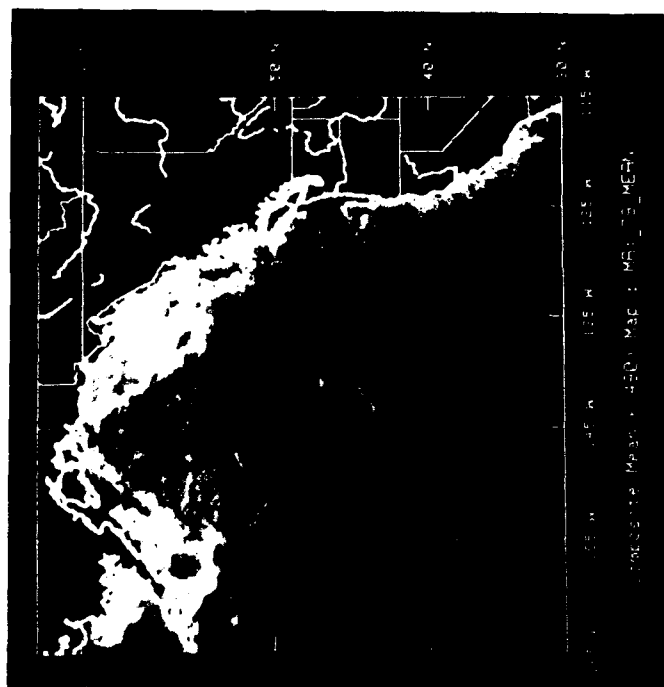


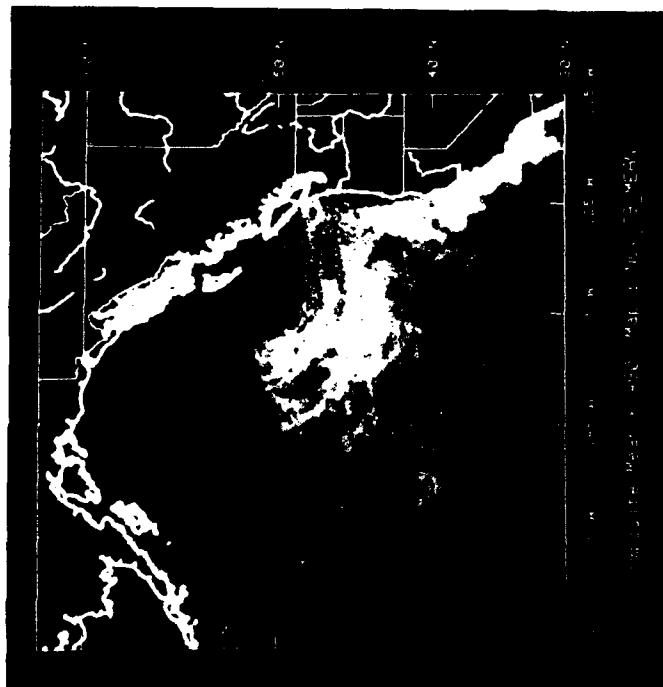
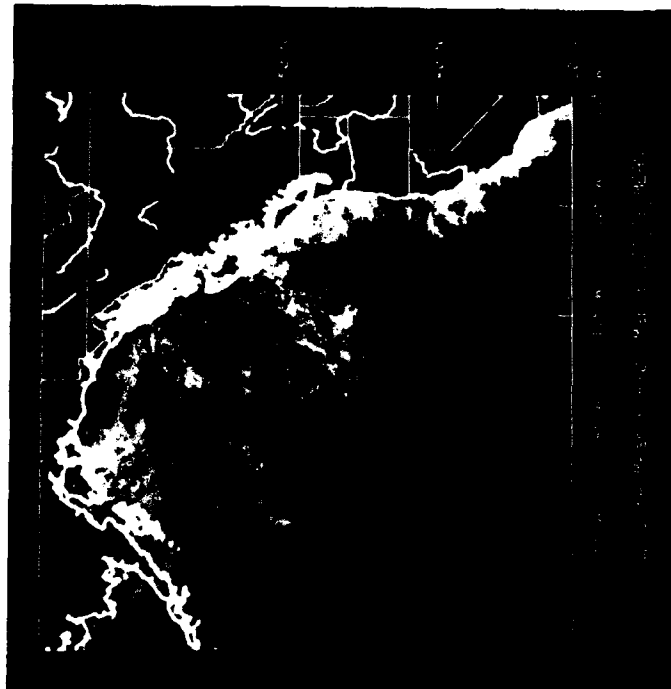
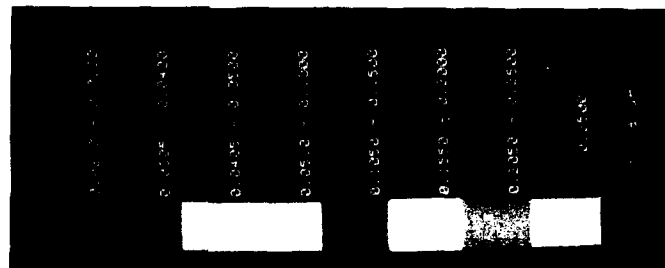
-4-

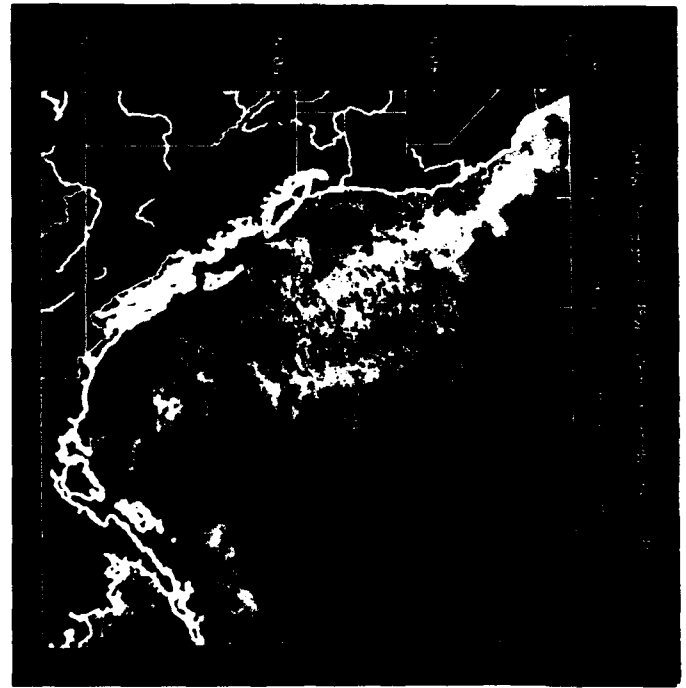
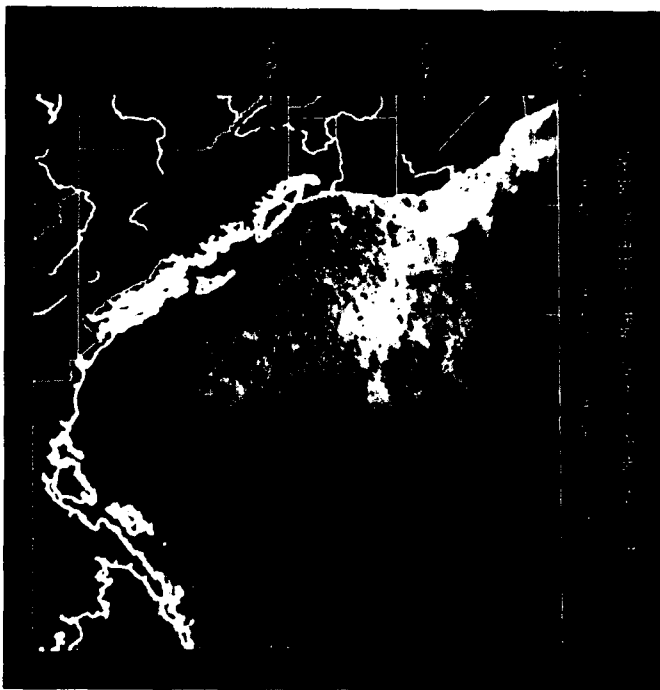
K(490)
Composite
Mean
Jan-Apr 1979



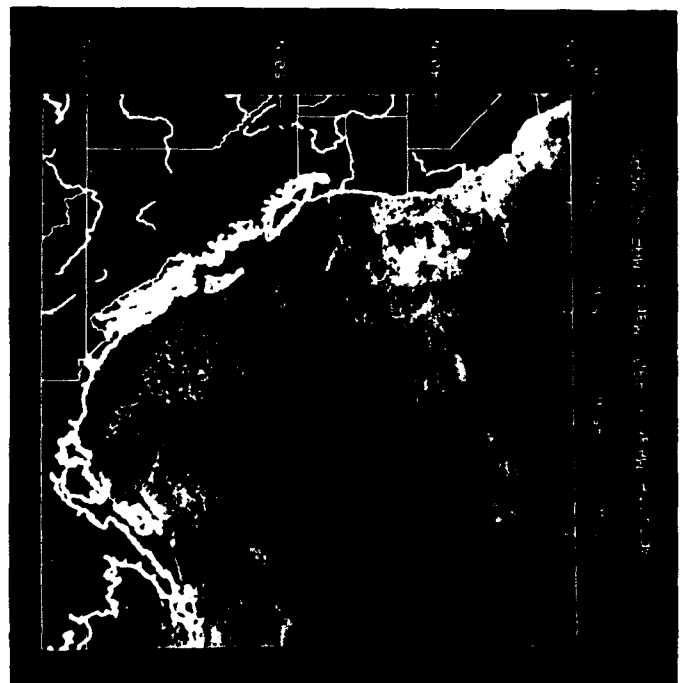
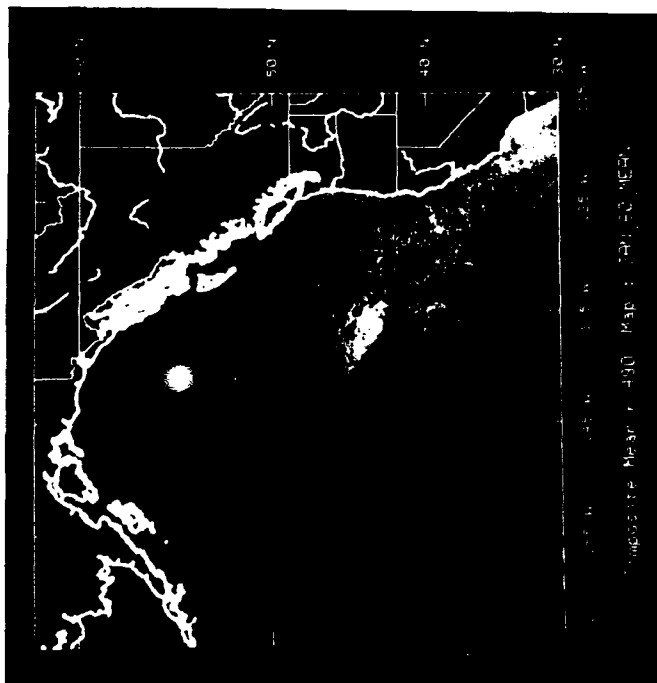
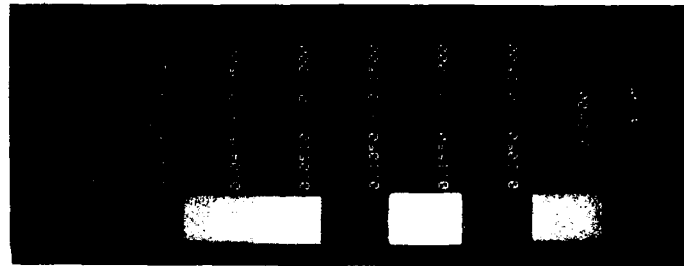
K(490)
Composite
Mean
May-Aug 1979

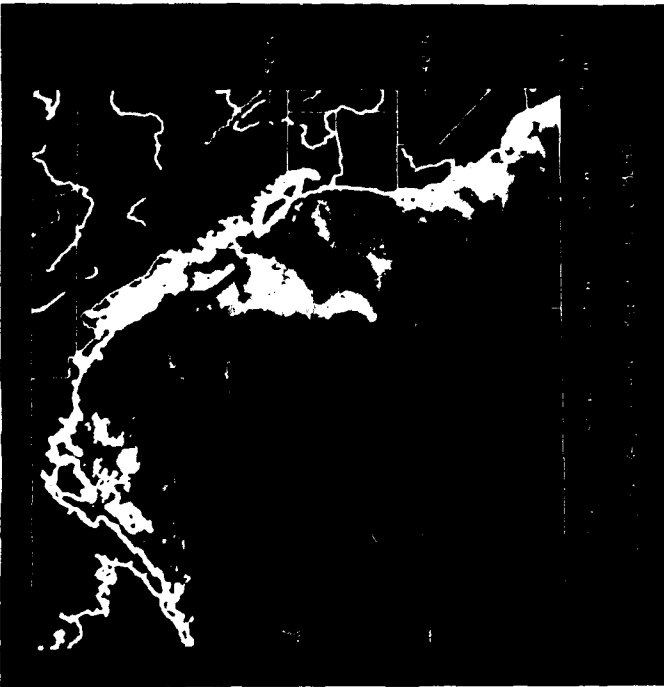




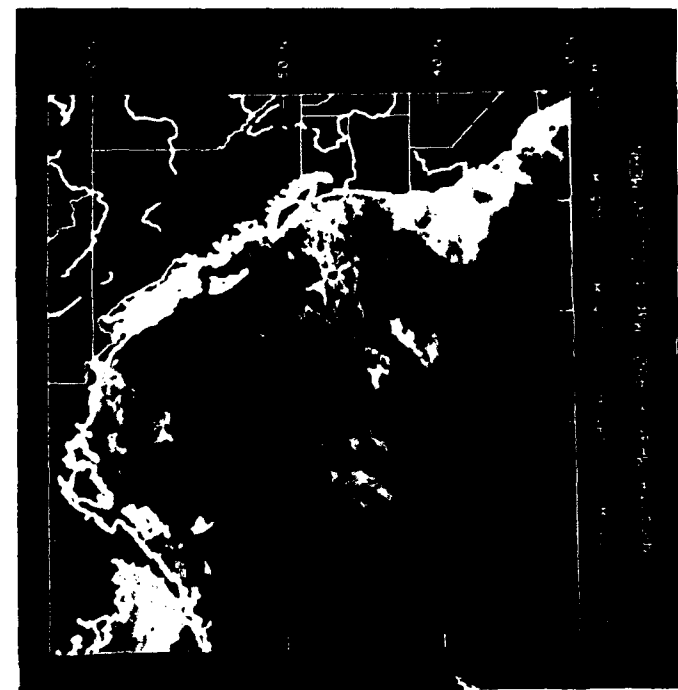
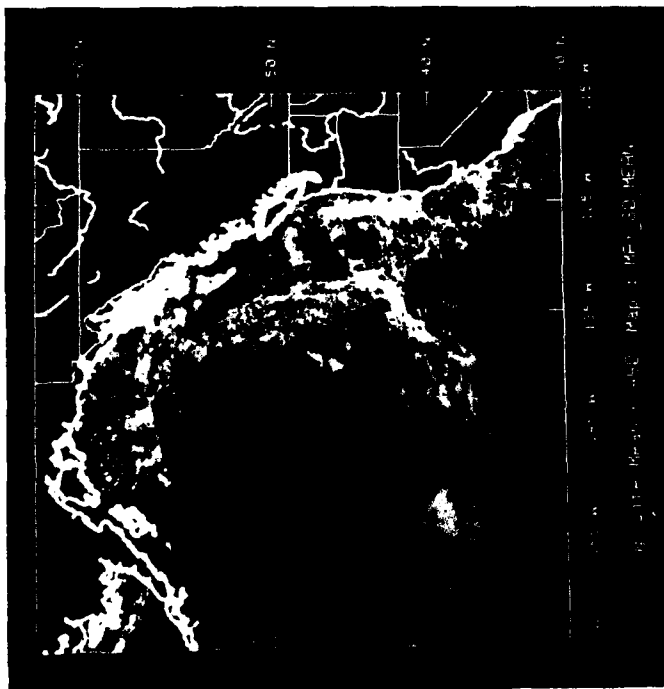
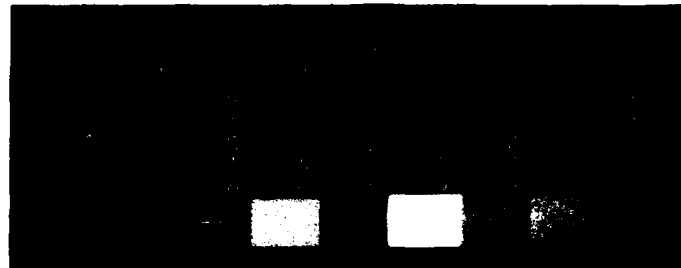


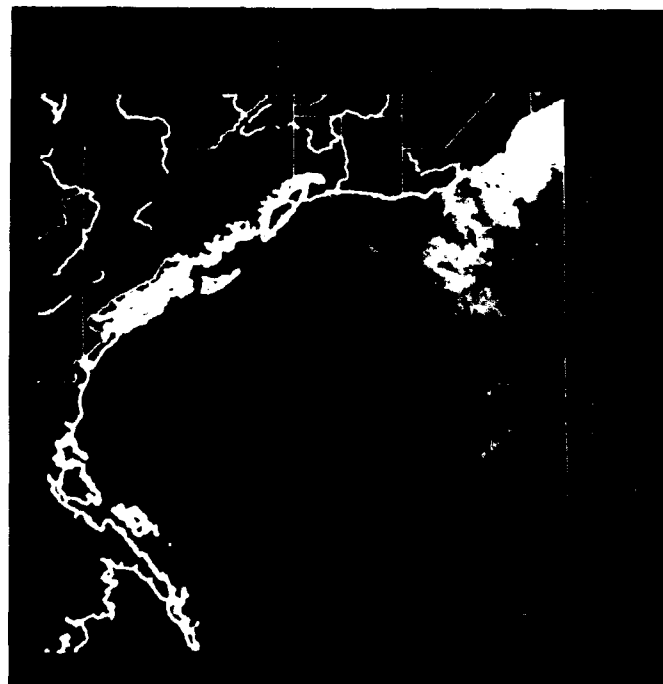
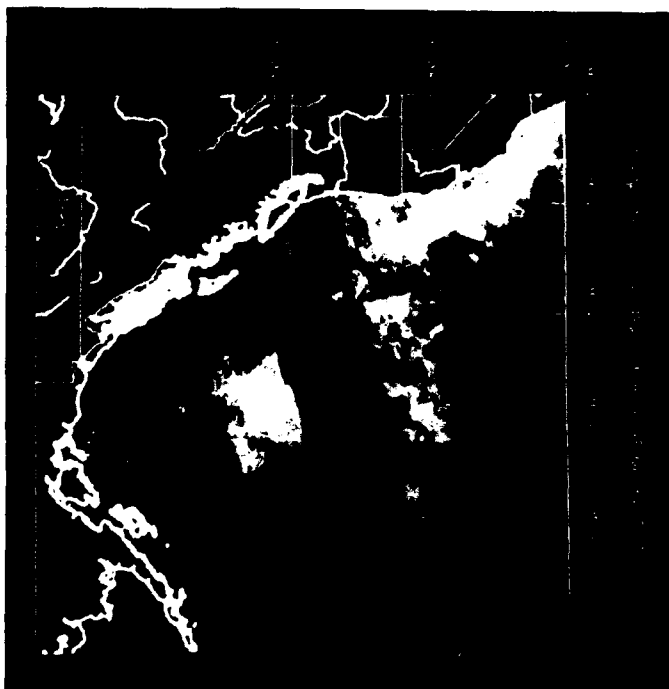
K(490)
Composite
Mean
Jan-Apr 1980



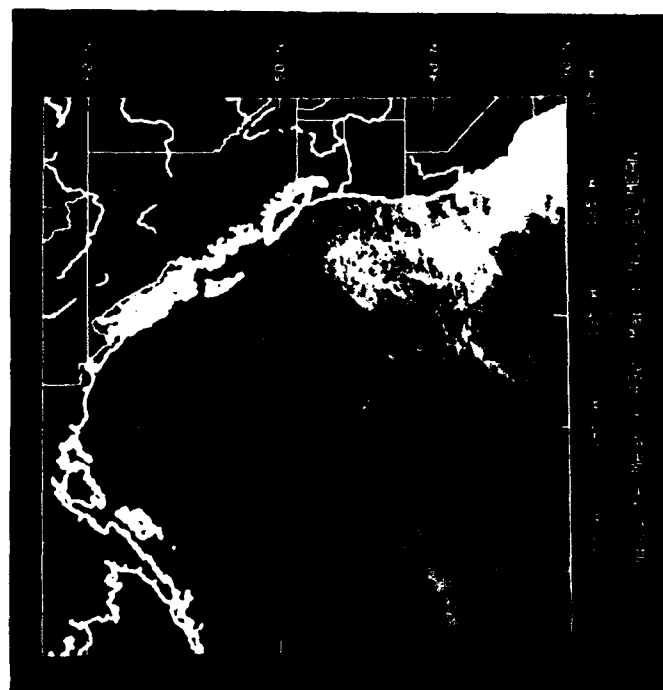
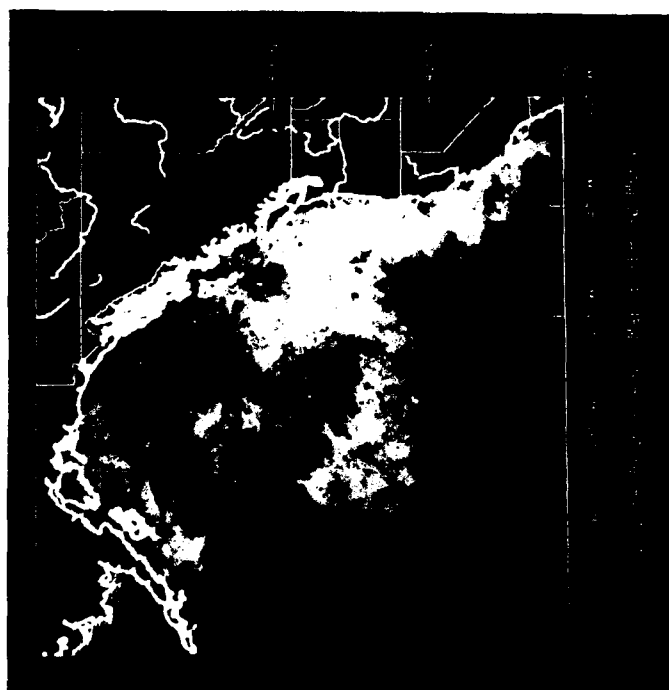
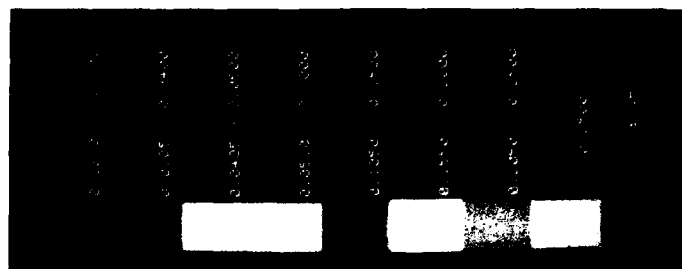


K(490)
Composite
Mean
May-Aug 1980

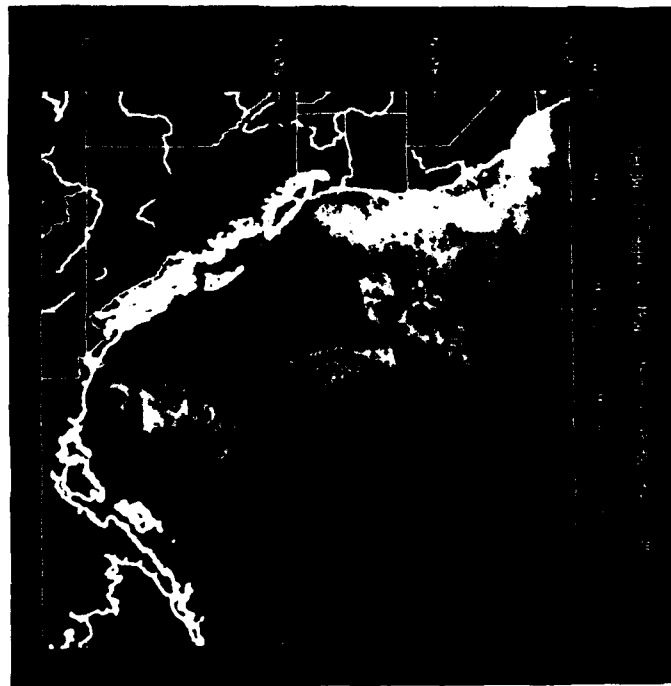
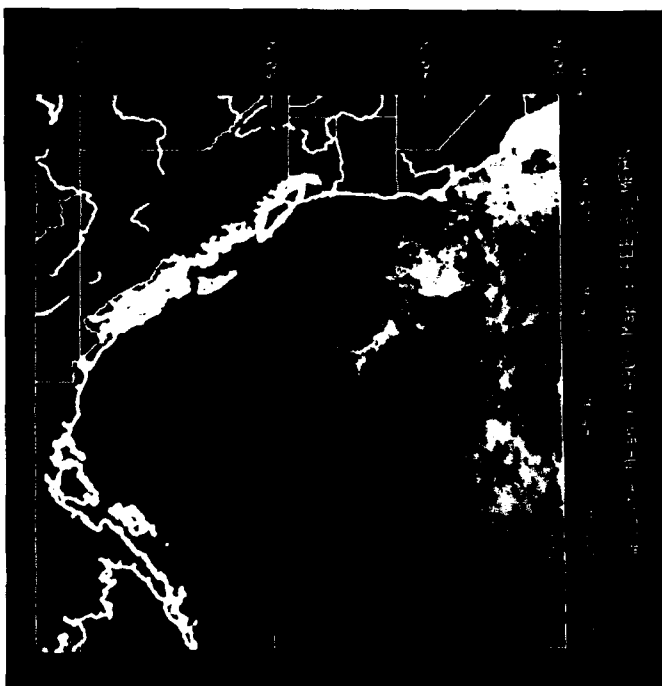
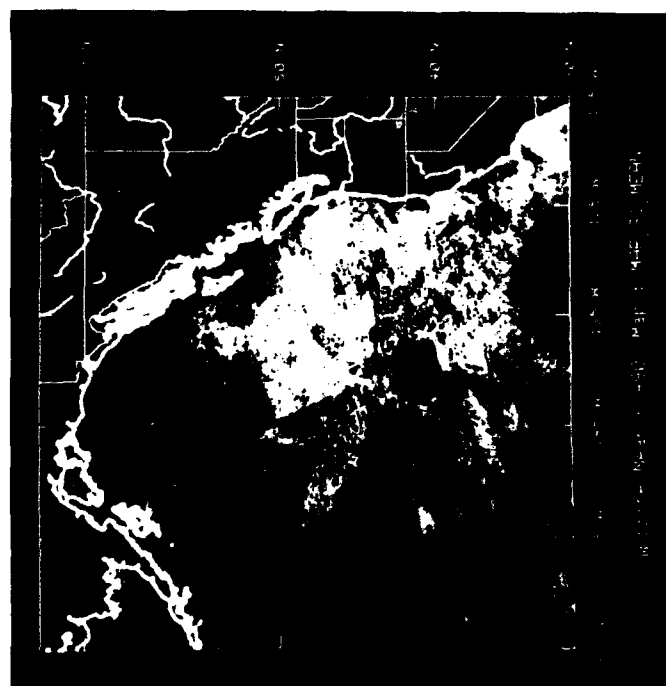
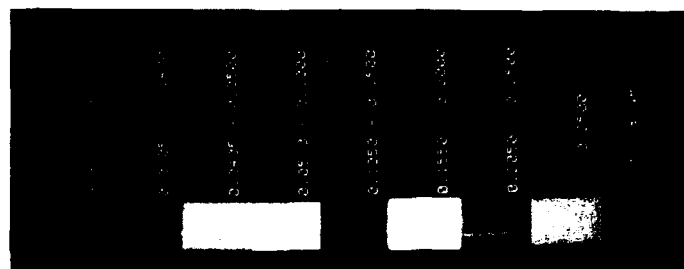
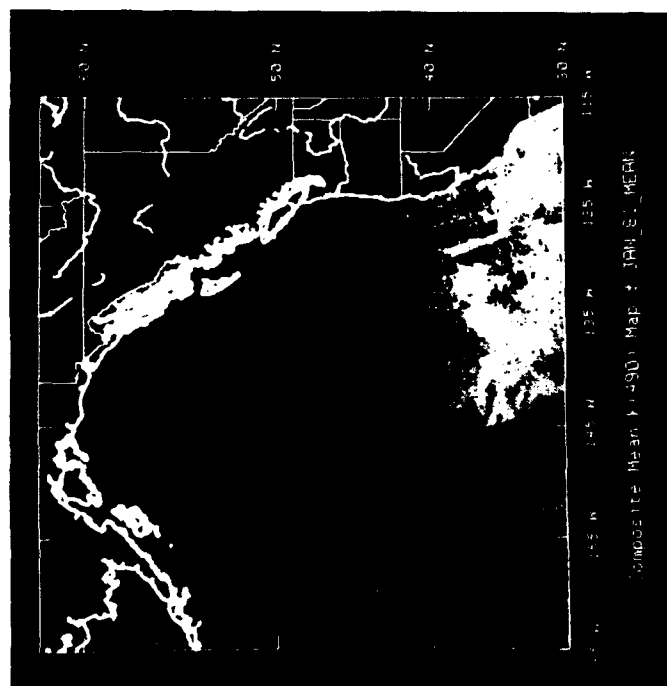


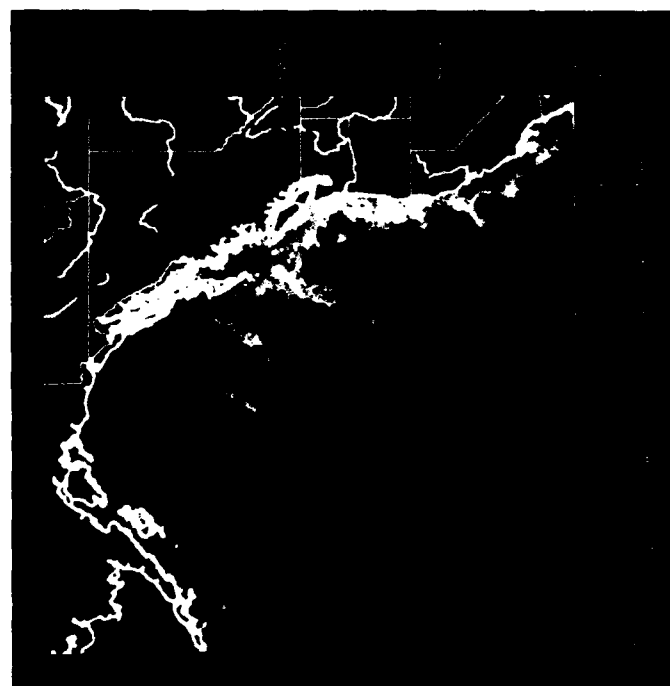
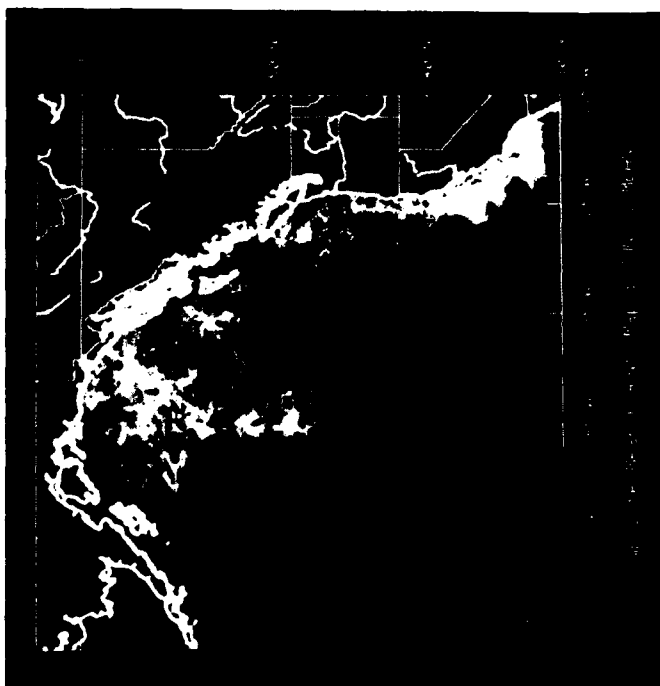


K(490)
Composite
Mean
Sep-Dec 1980

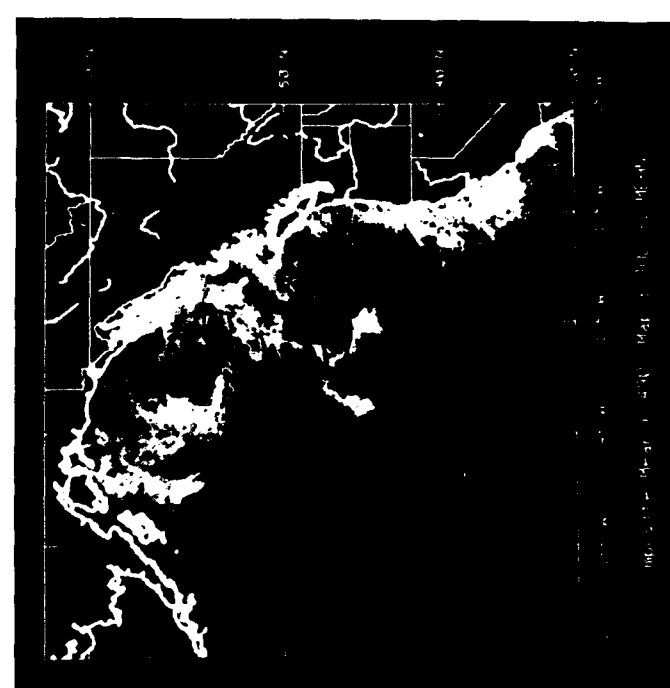
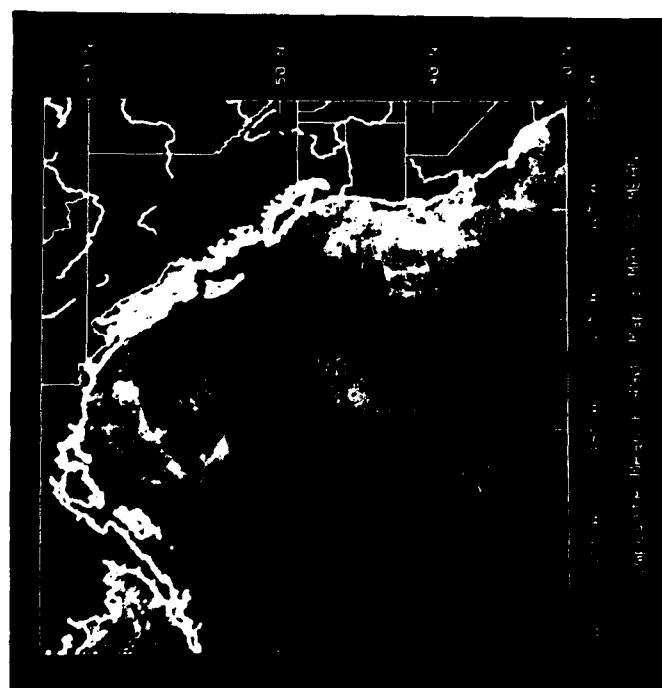
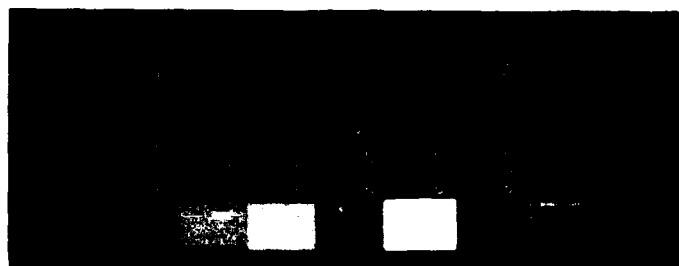


K(490)
Composite
Mean
Jan-Apr 1981

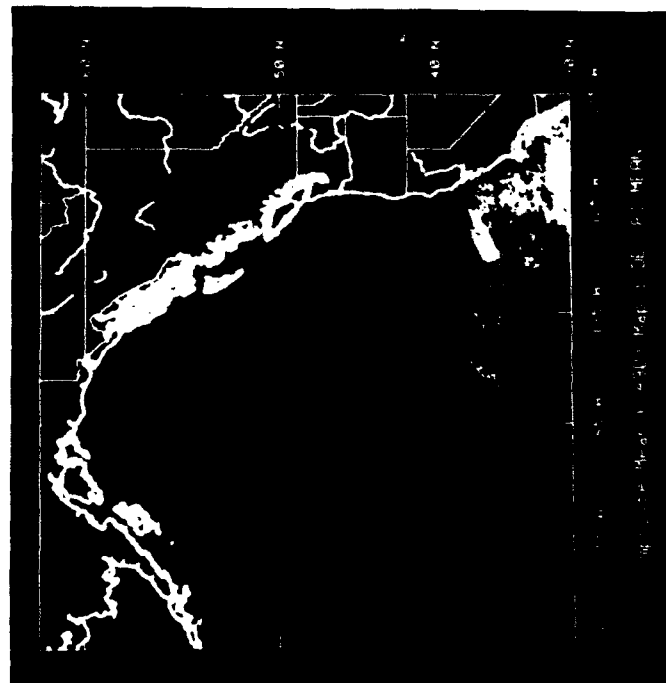
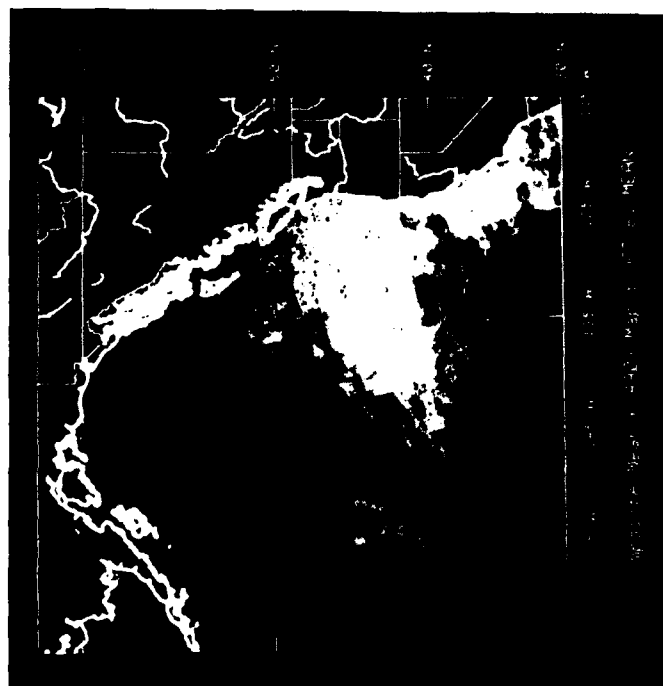
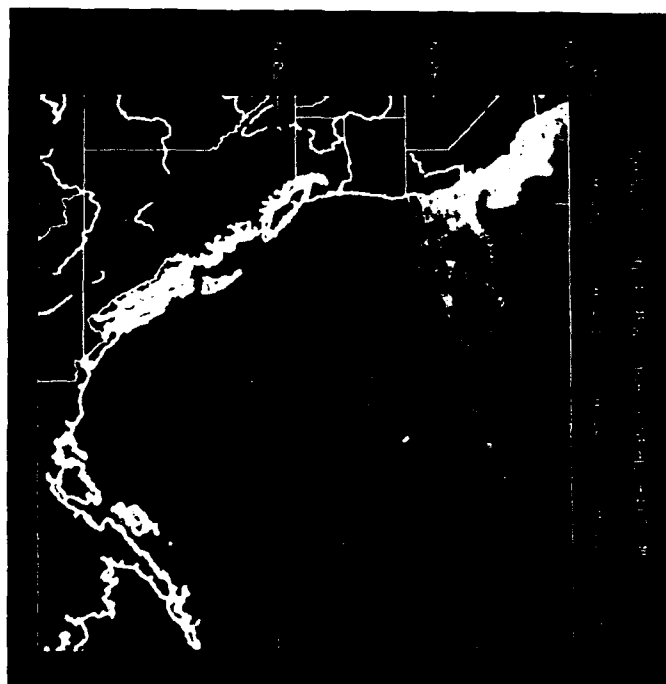
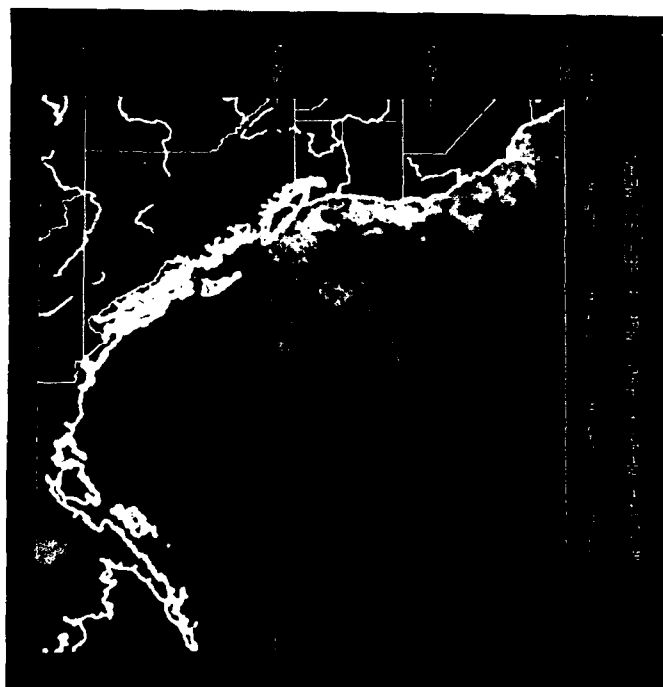
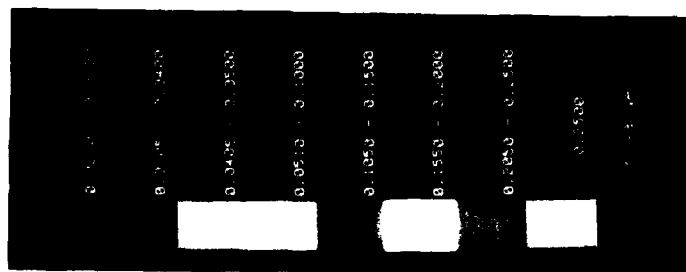


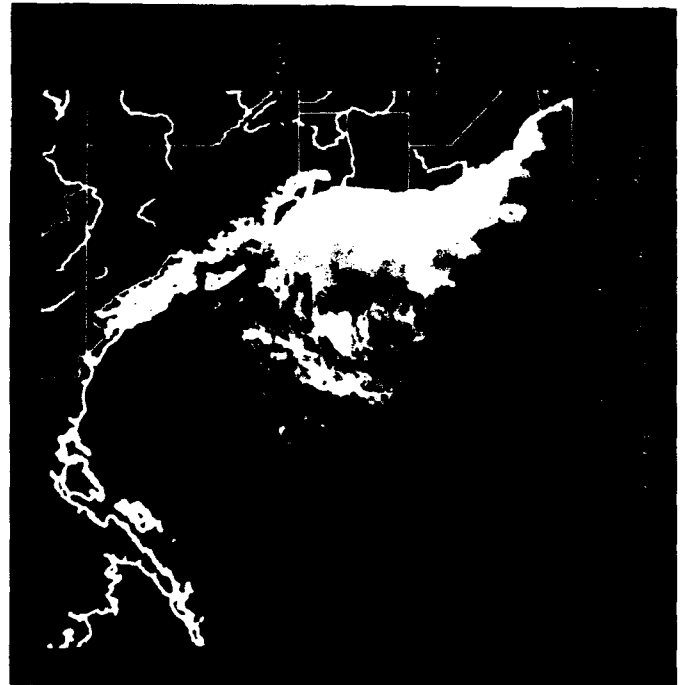
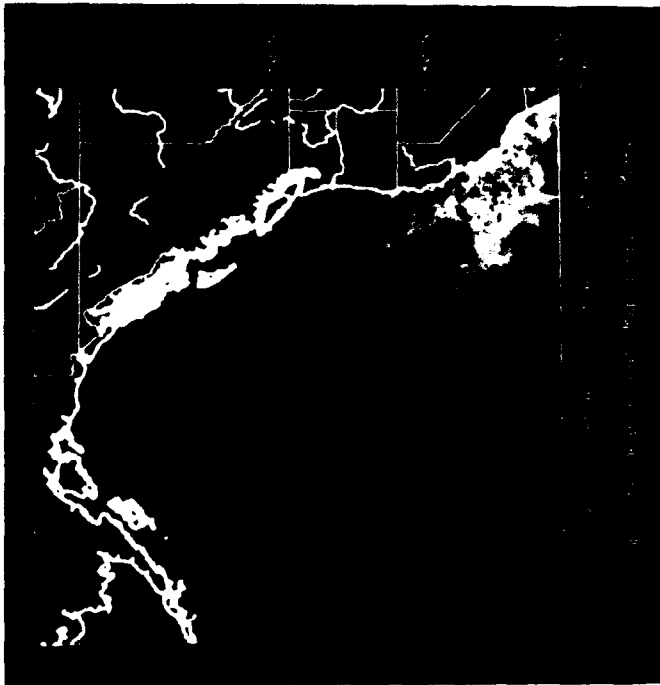


K(490)
Composite
Mean
May-Aug 1981

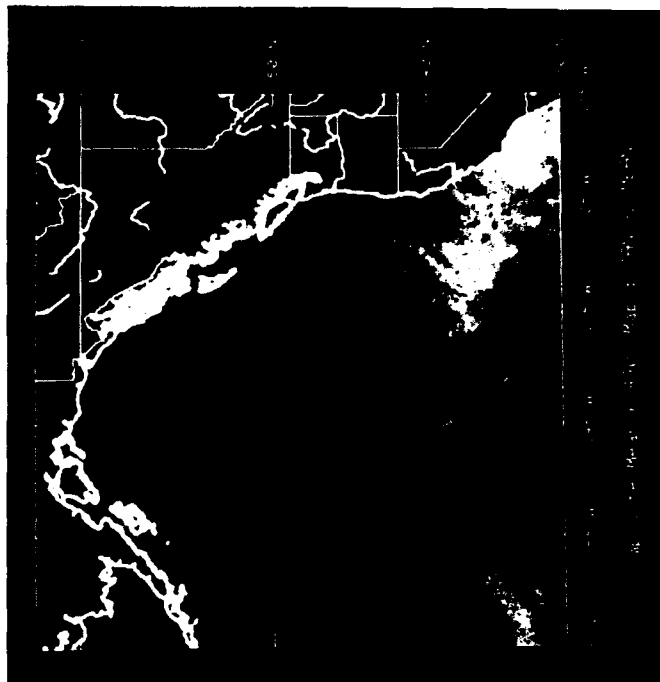
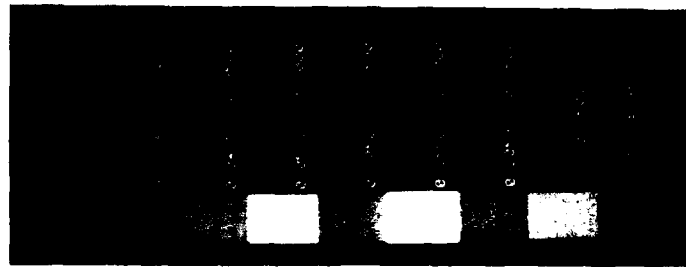


K(490)
Composite
Mean
Sep-Dec 1981

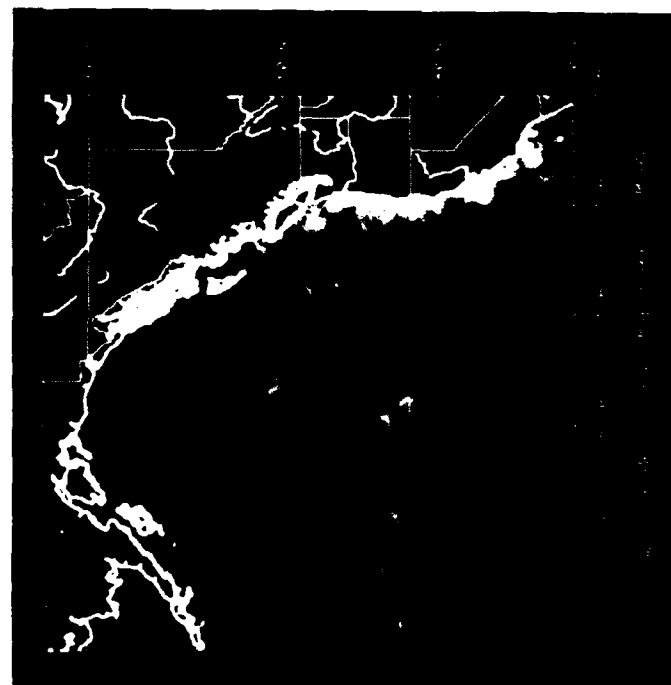
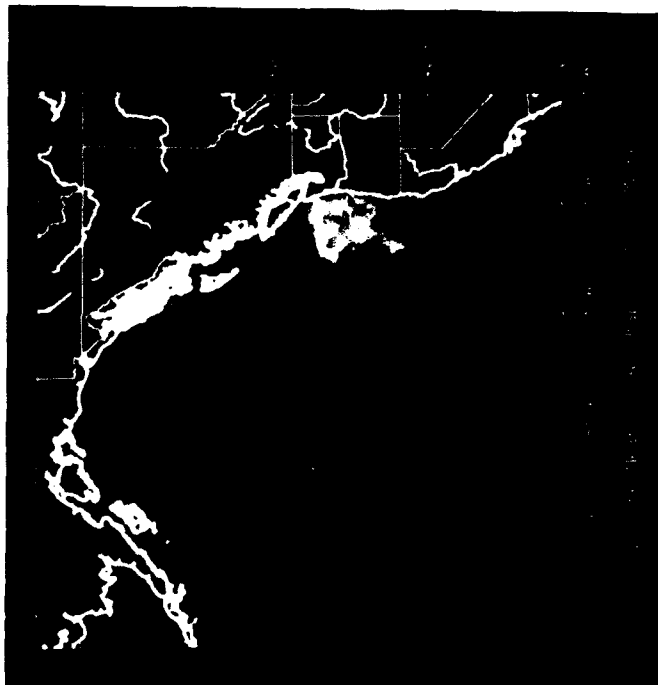
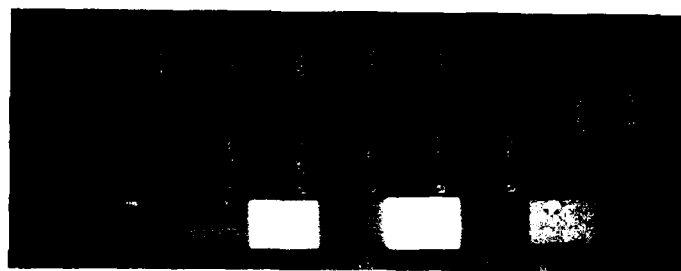
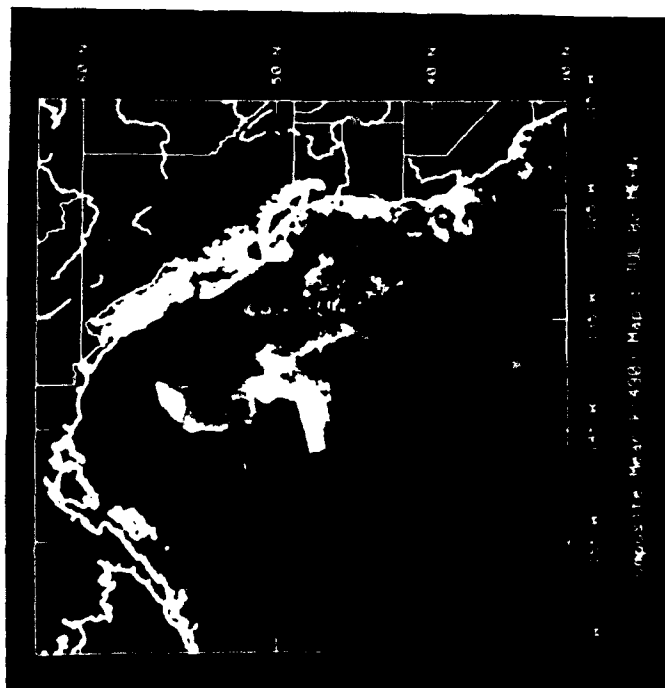
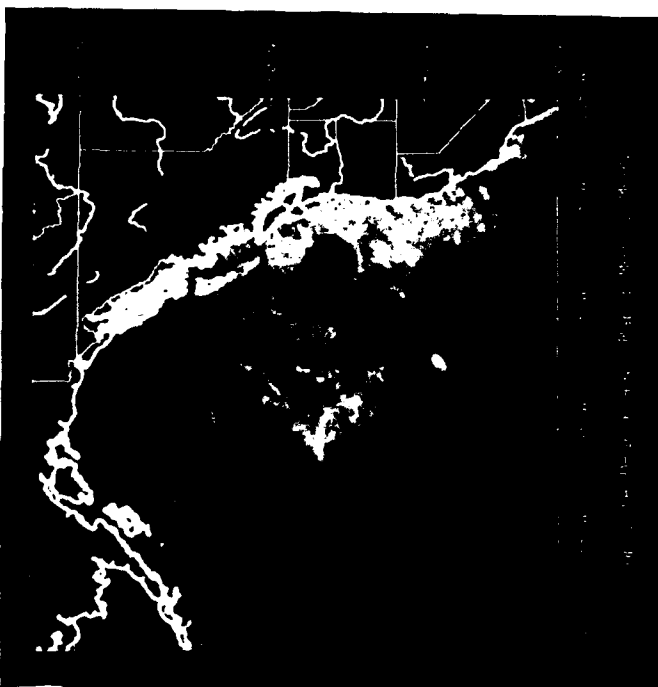


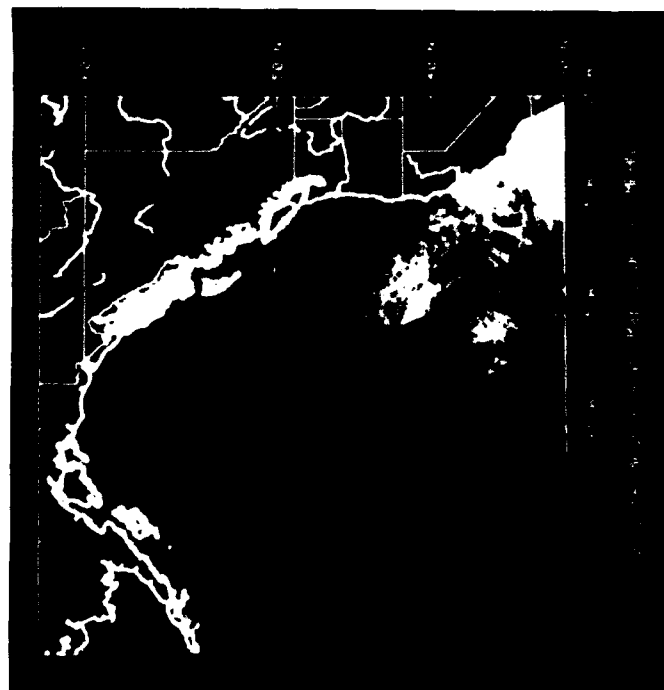
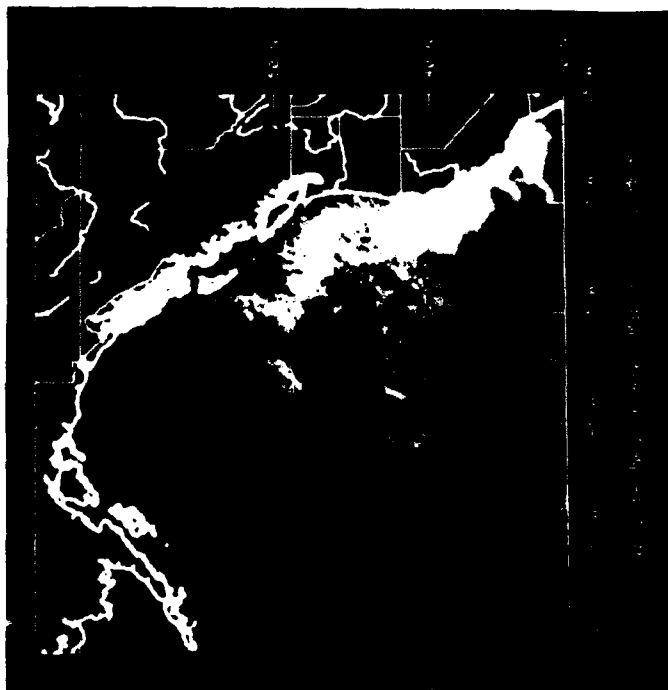


K(490)
Composite
Mean
Jan-Apr 1982

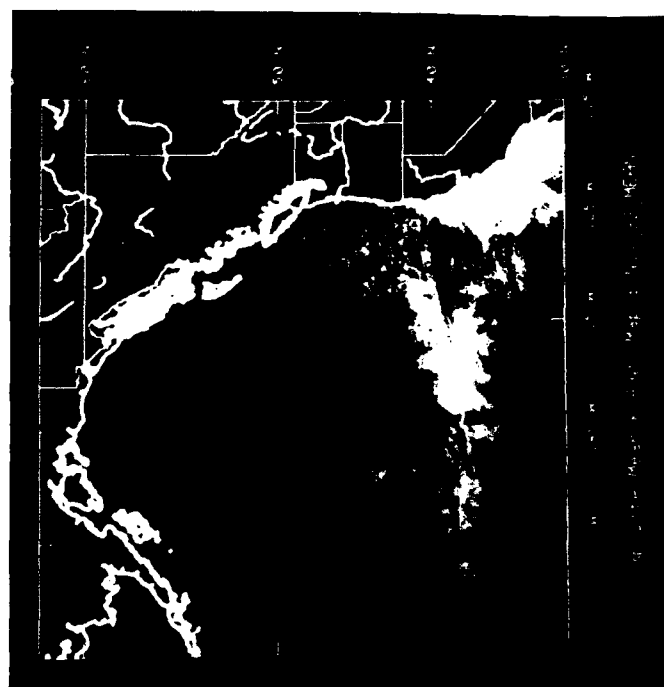
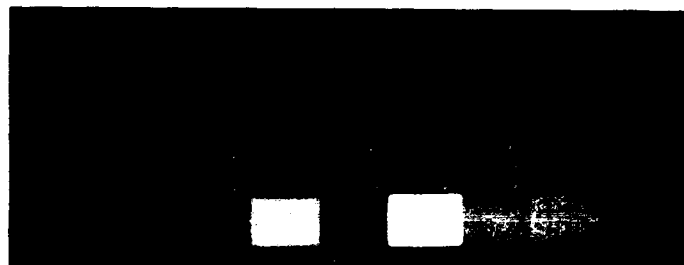


K(490)
Composite
Mean
May-Aug 1982

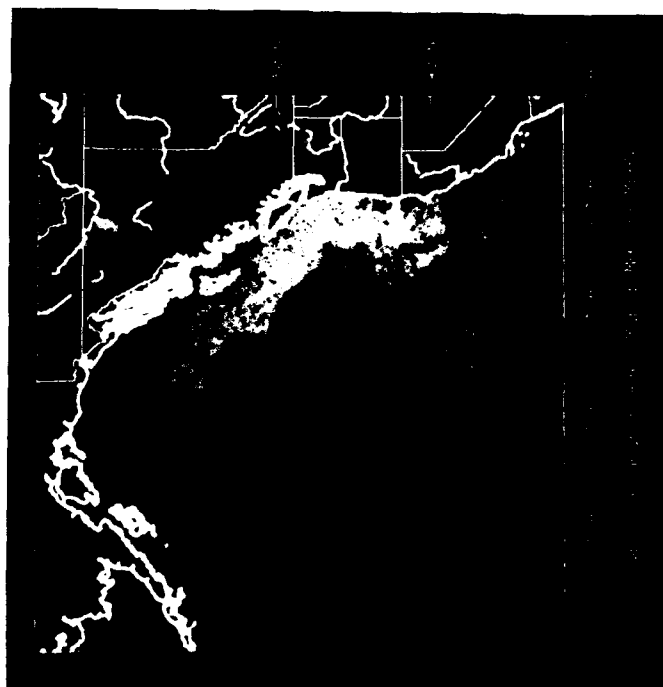
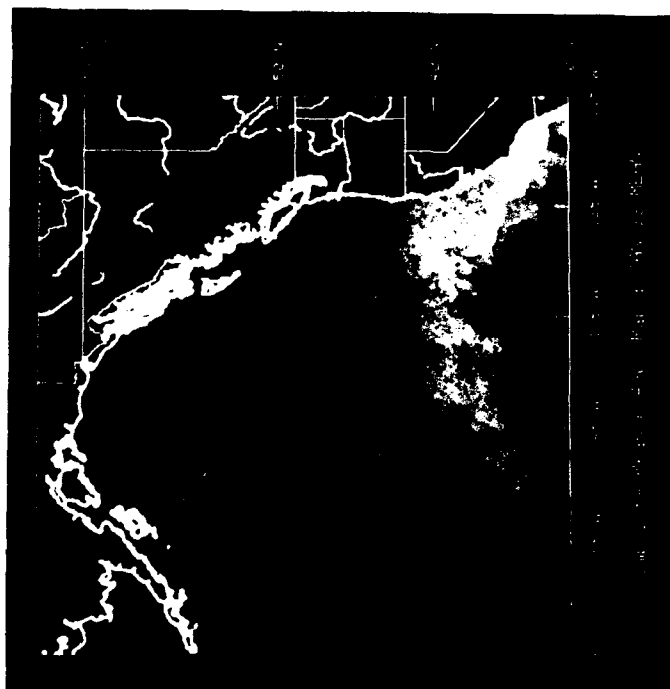
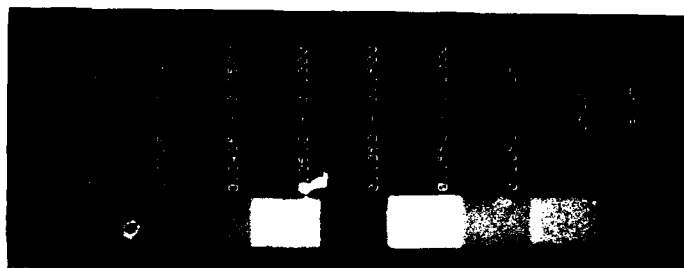
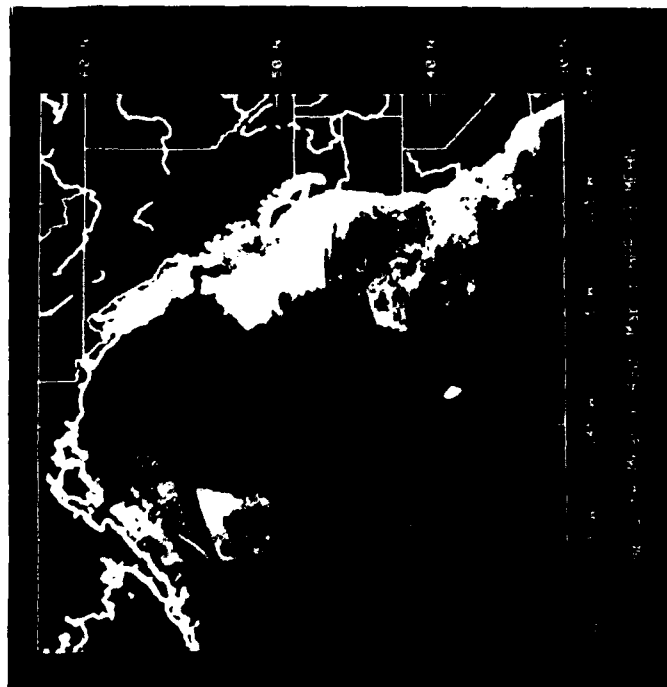
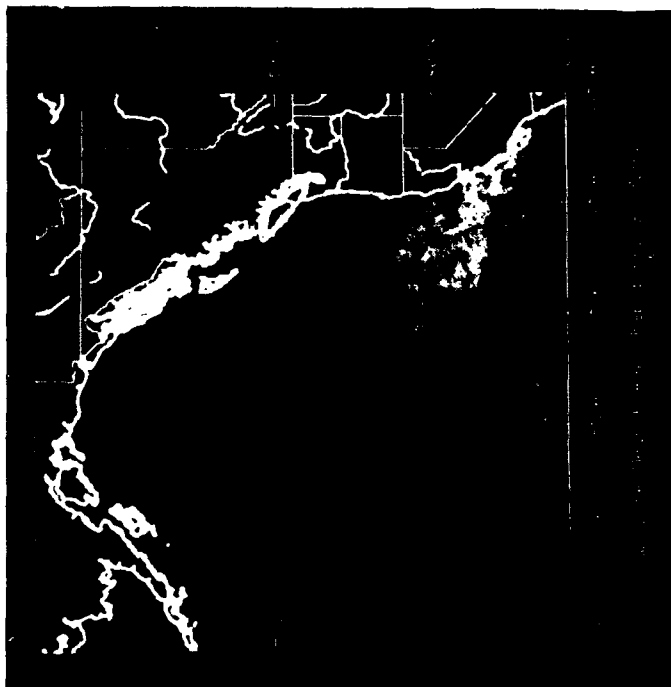




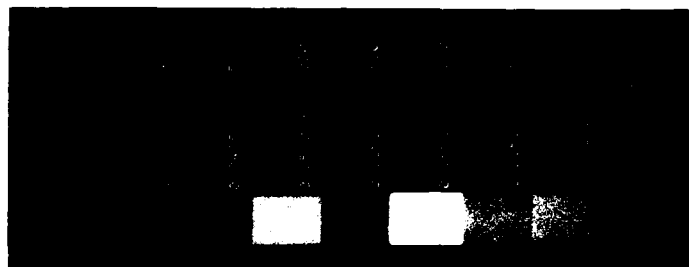
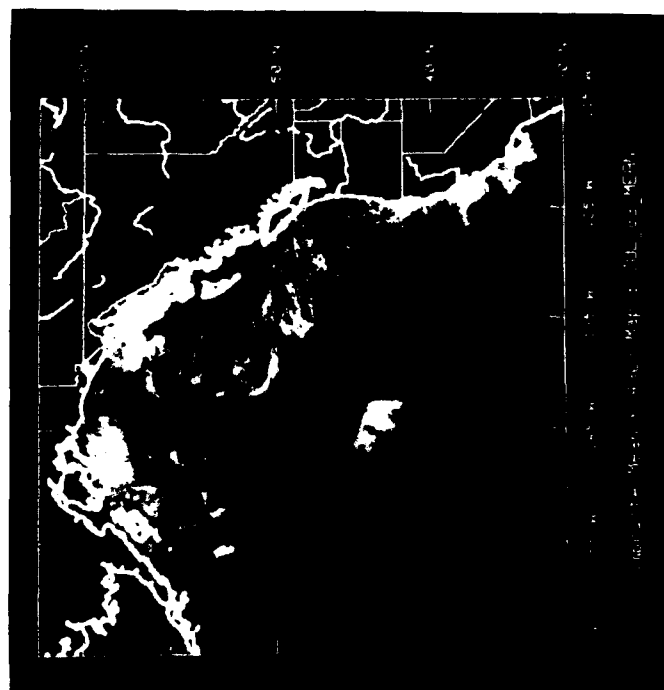
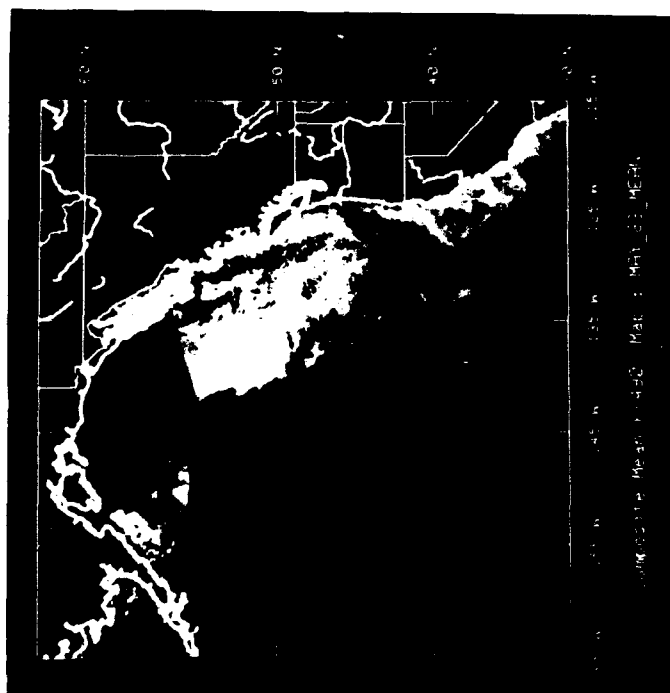
K(490)
Composite
Mean
Sep-Dec 1982

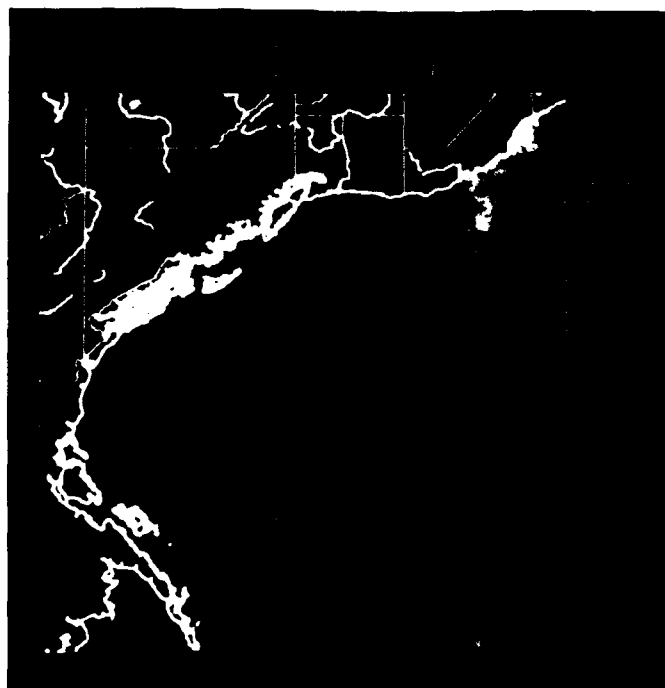
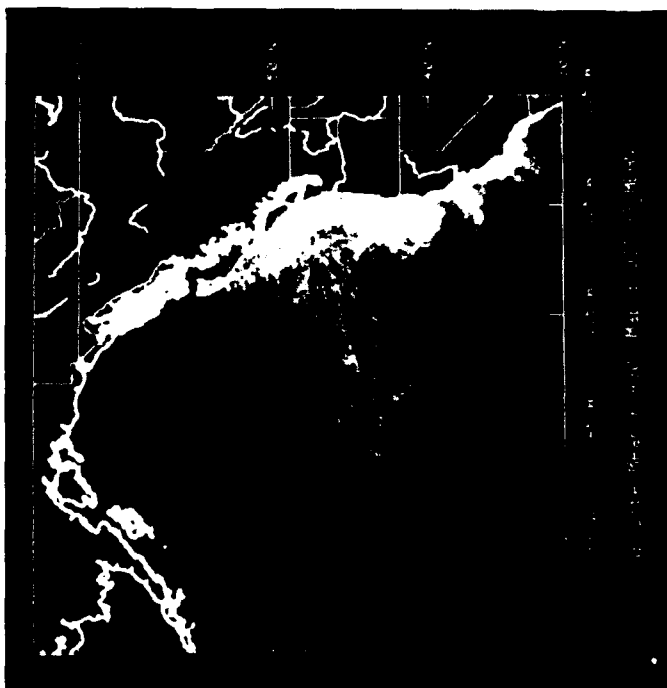


K(490)
Composite
Mean
Jan-Apr 1983

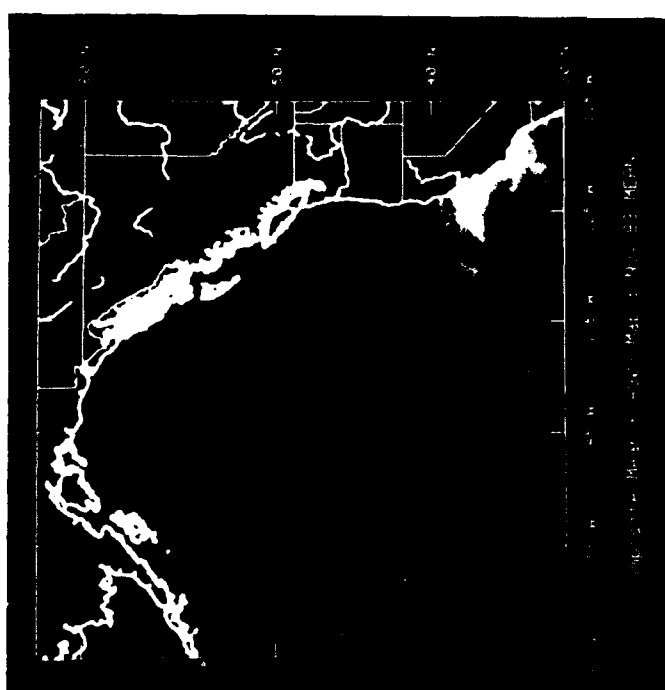
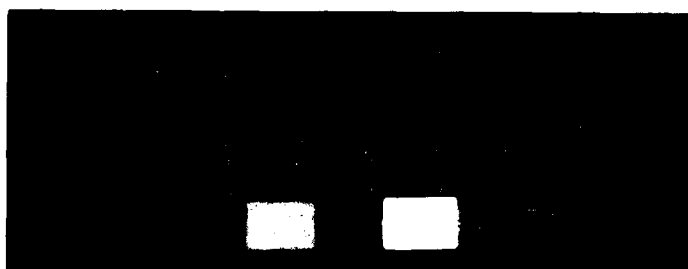


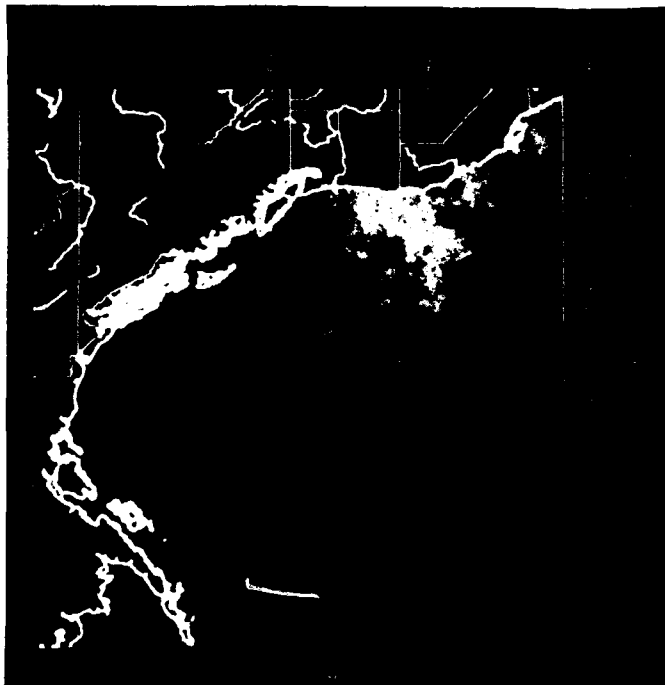
K(490)
Composite
Mean
May-Aug 1983



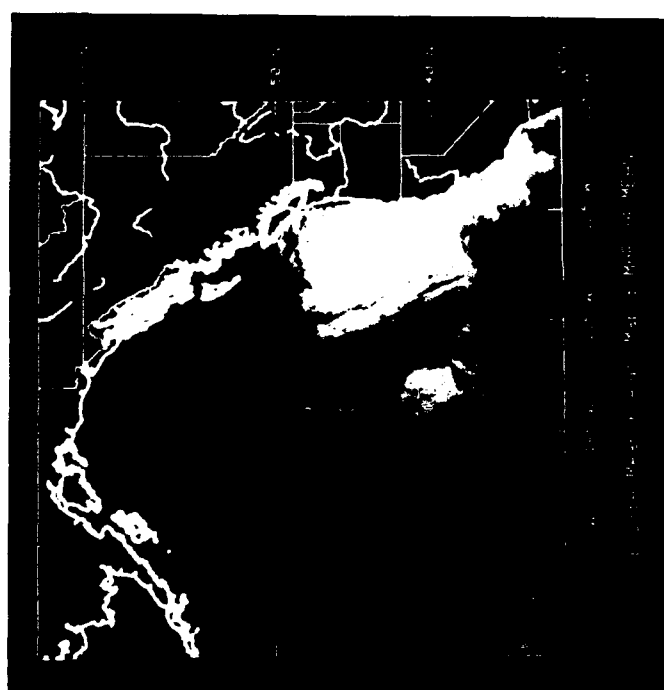
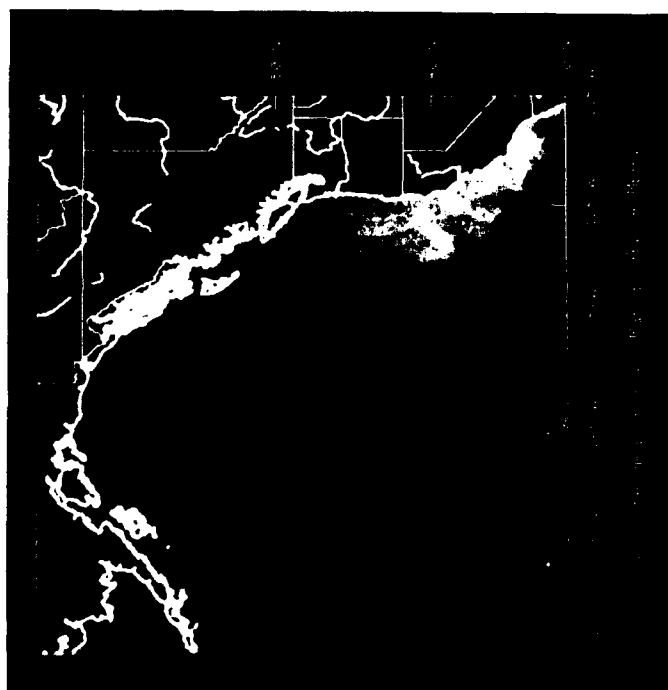
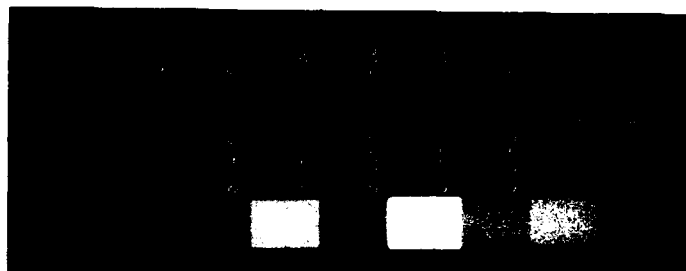


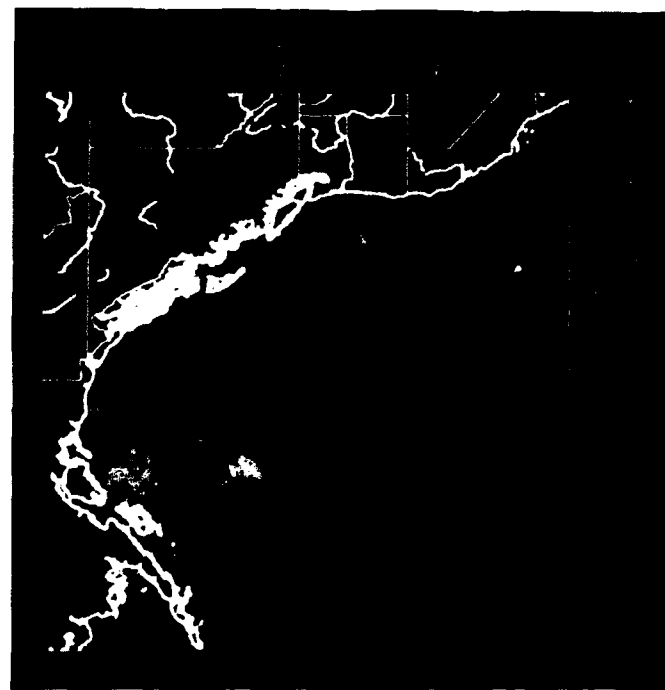
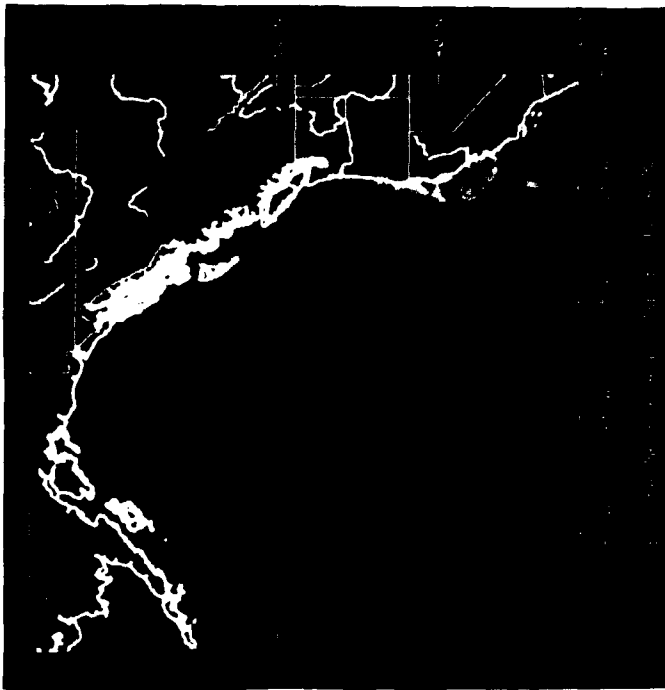
K(490)
Composite
Mean
Sep-Dec 1983



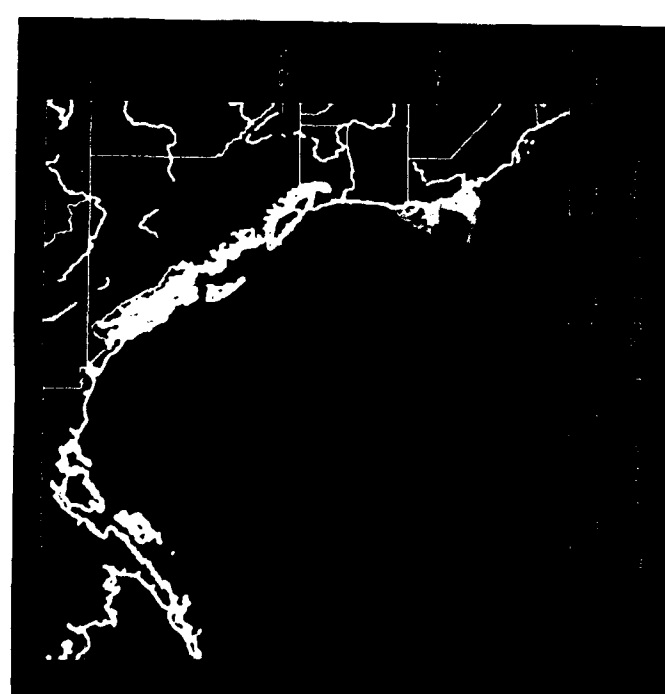
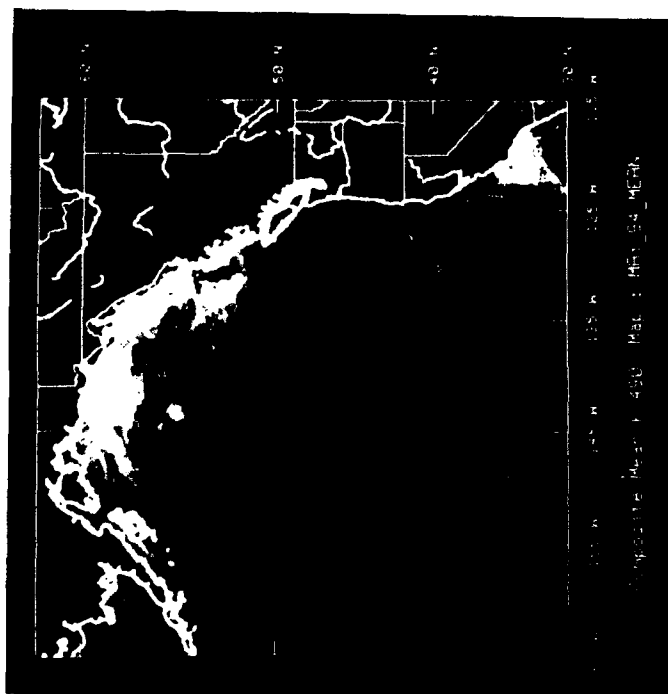
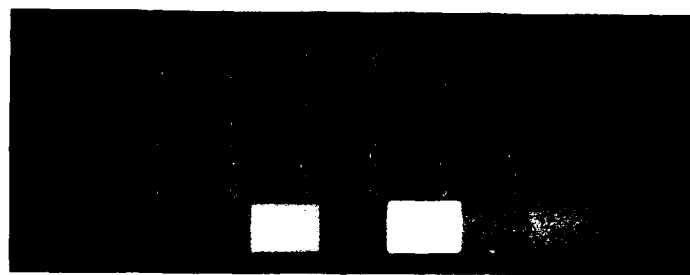


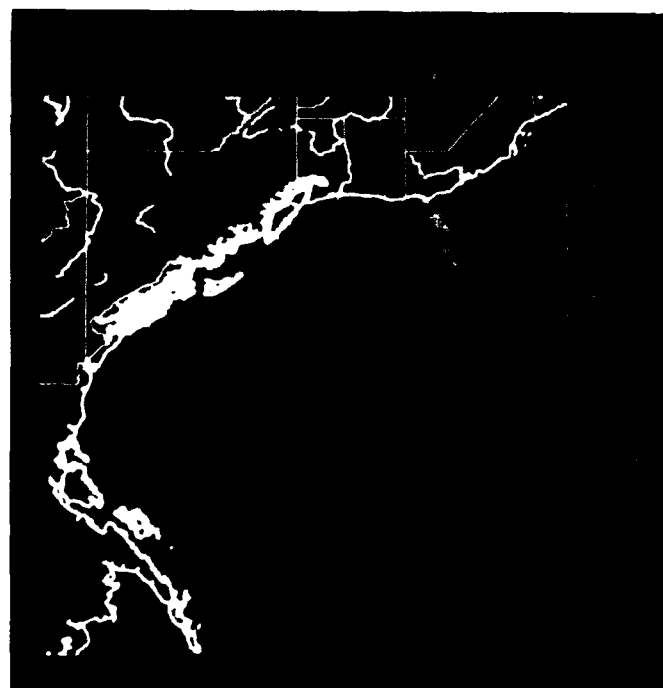
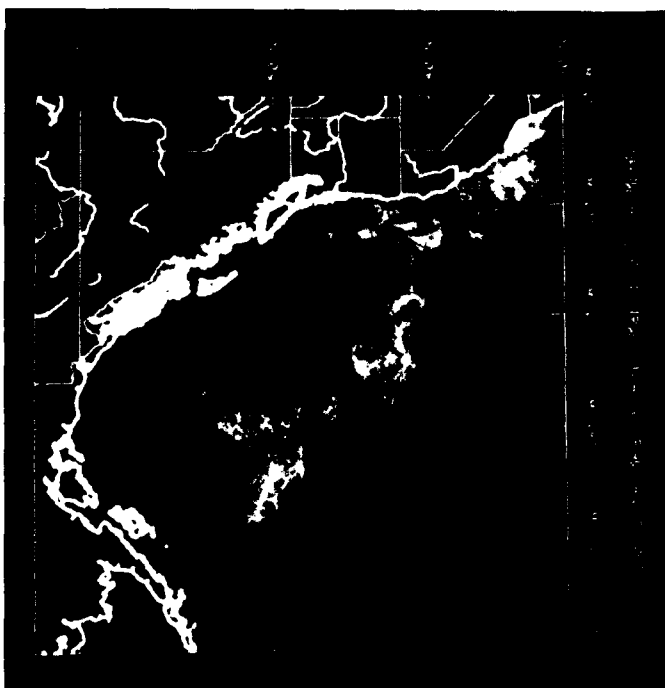
K(490)
Composite
Mean
Jan-Apr 1984



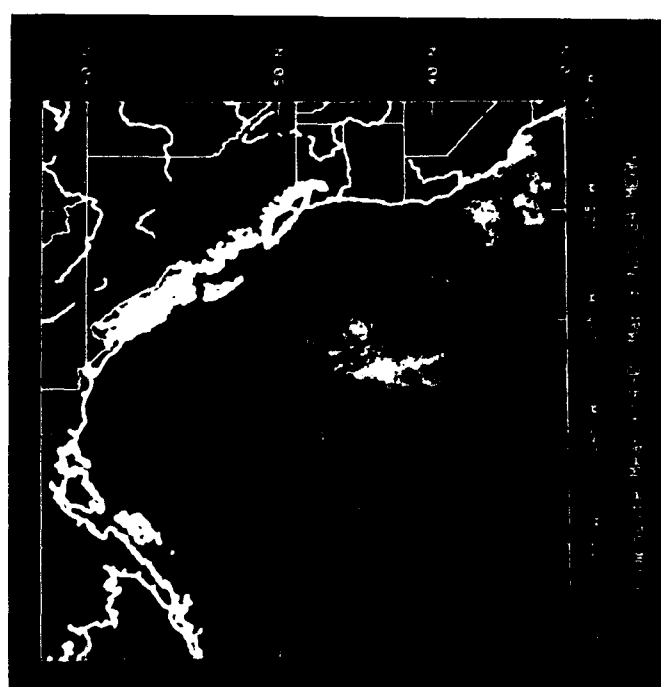
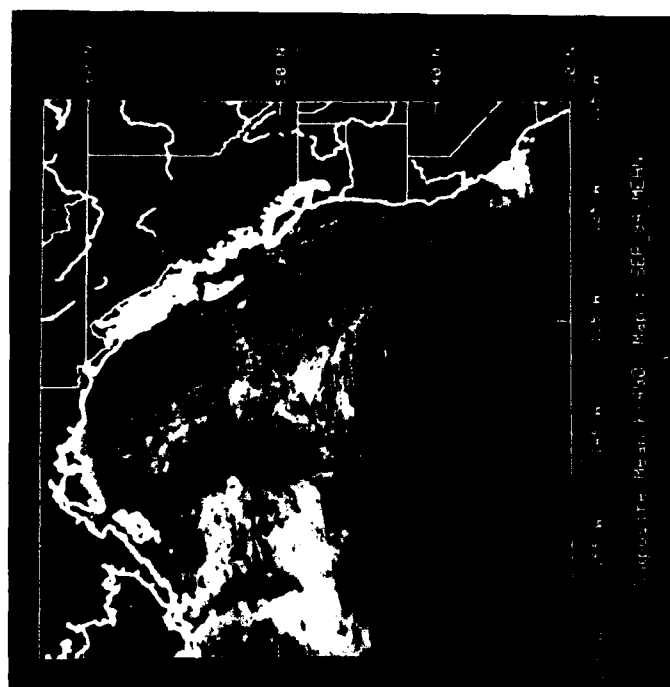
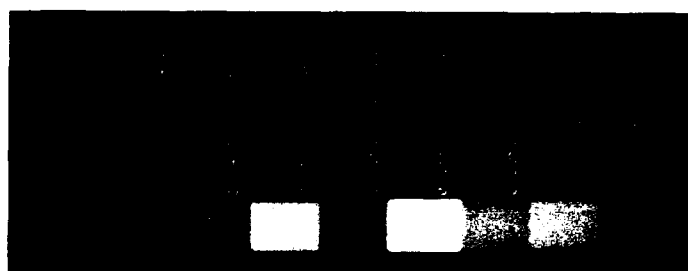


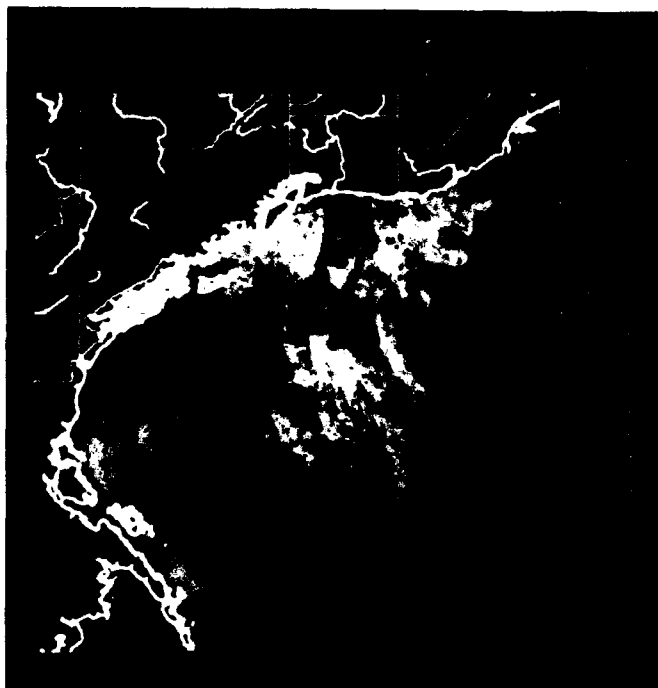
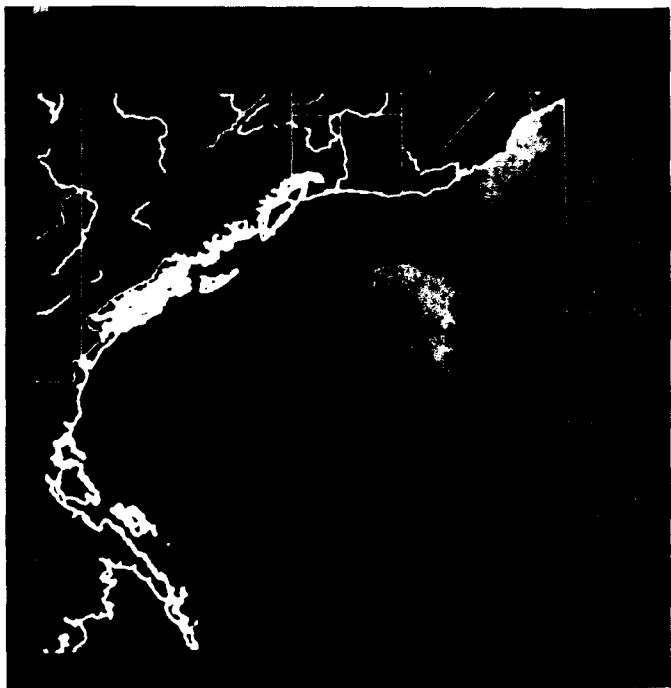
K(490)
Composite
Mean
May-Aug 1984



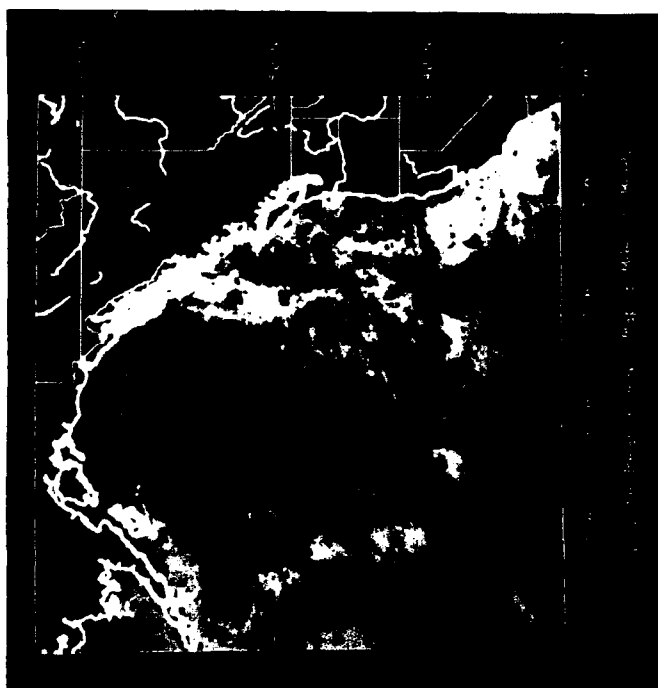
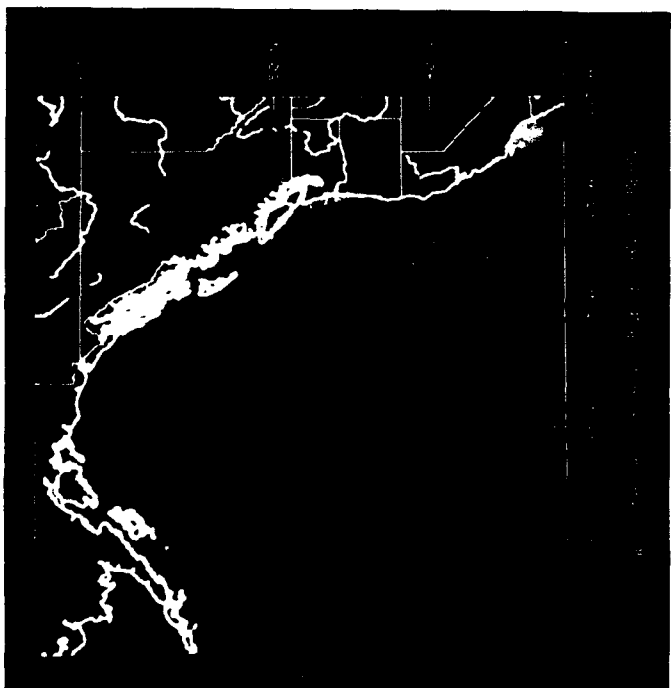
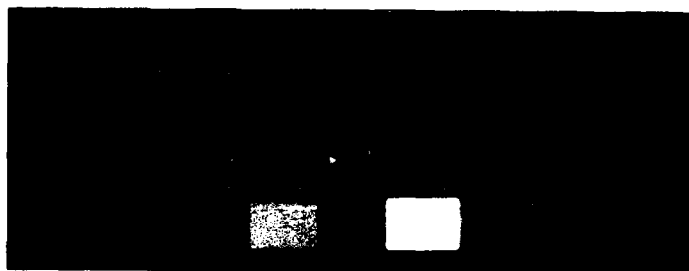


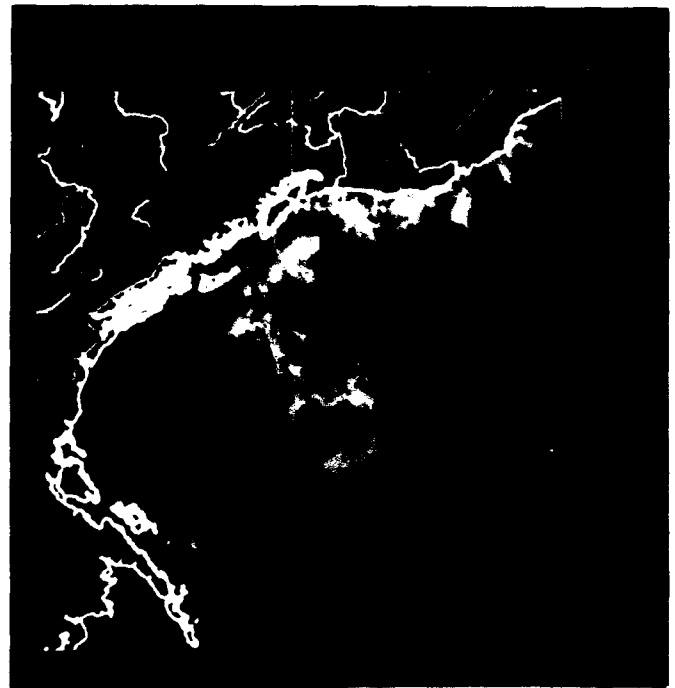
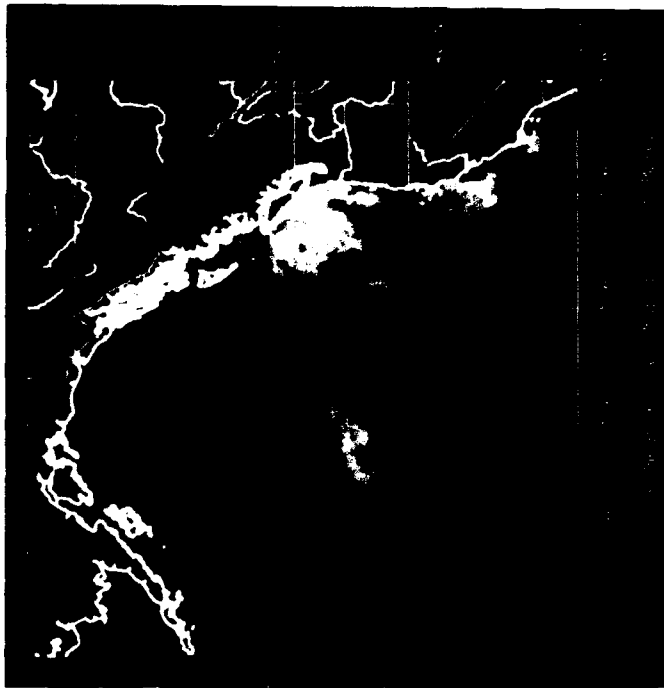
K(490)
Composite
Mean
Sep-Dec 1984



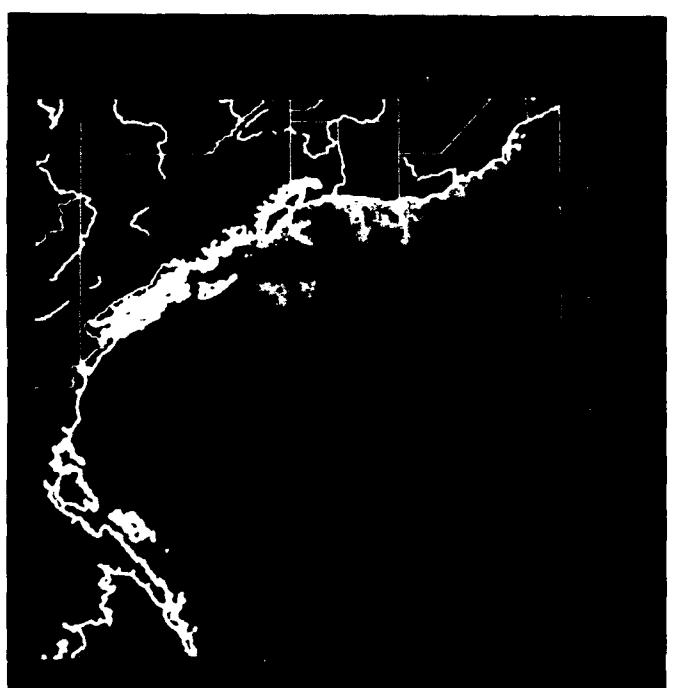
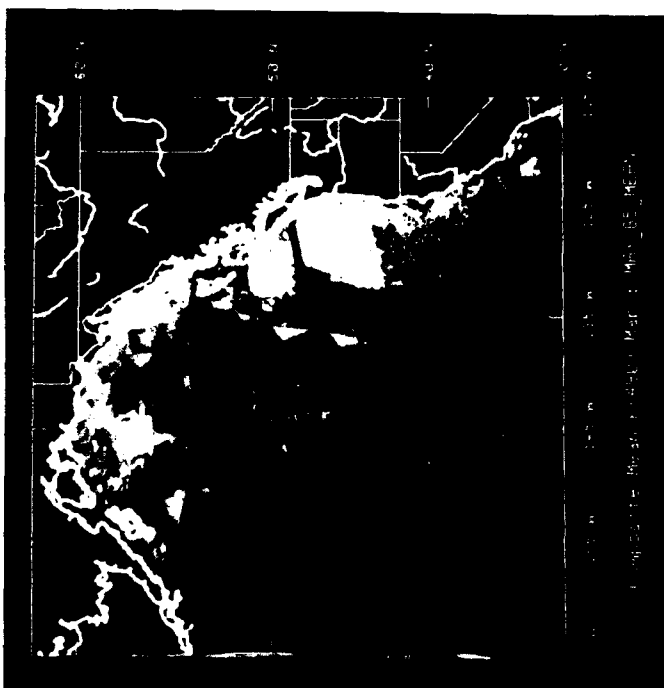
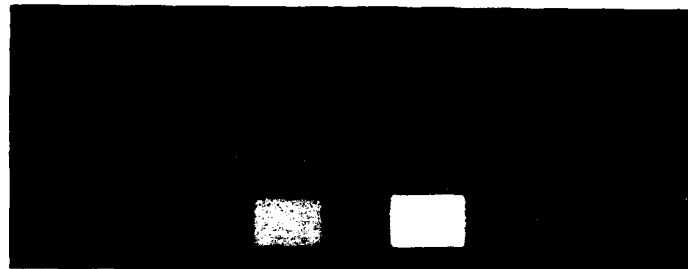


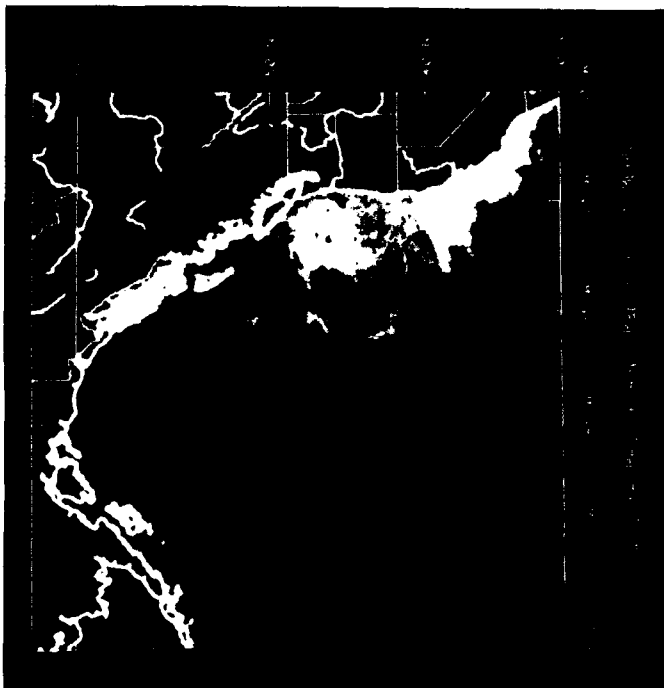
K(490)
Composite
Mean
Jan-Apr 1985



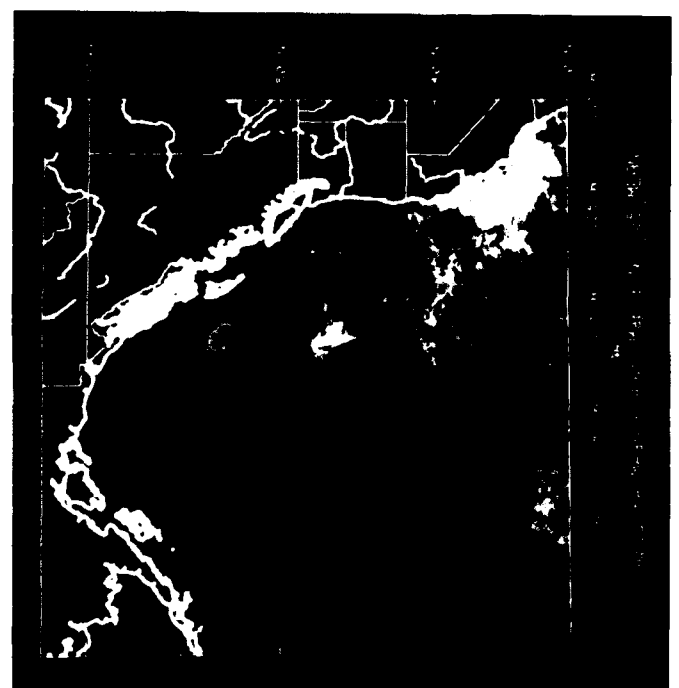
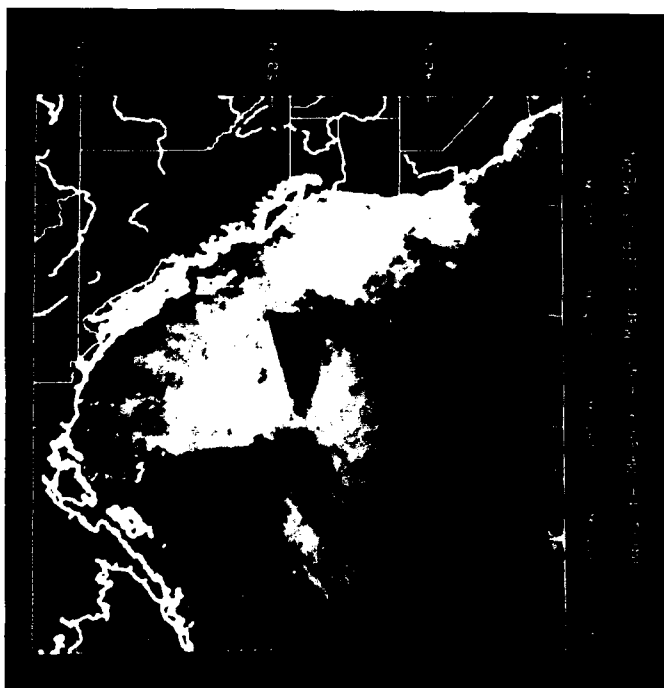
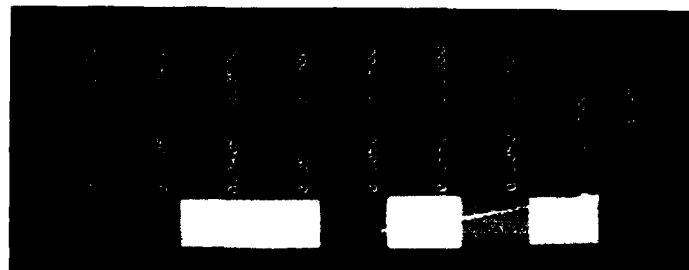


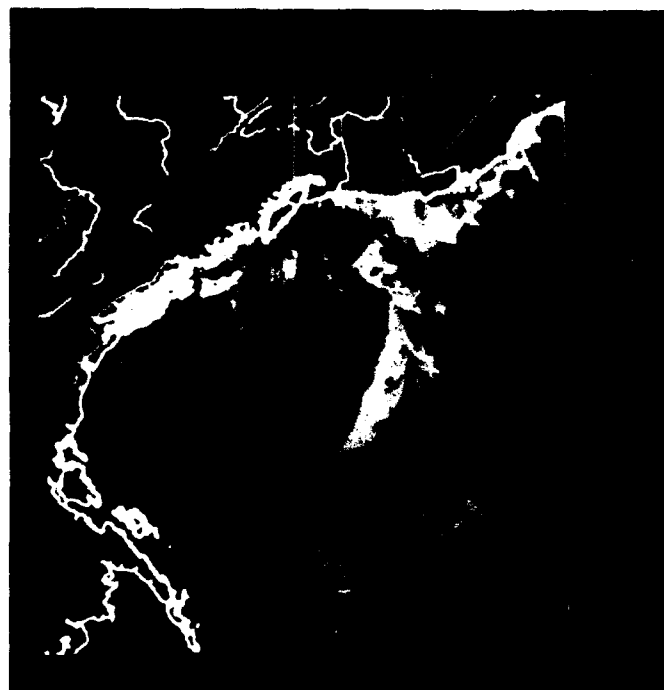
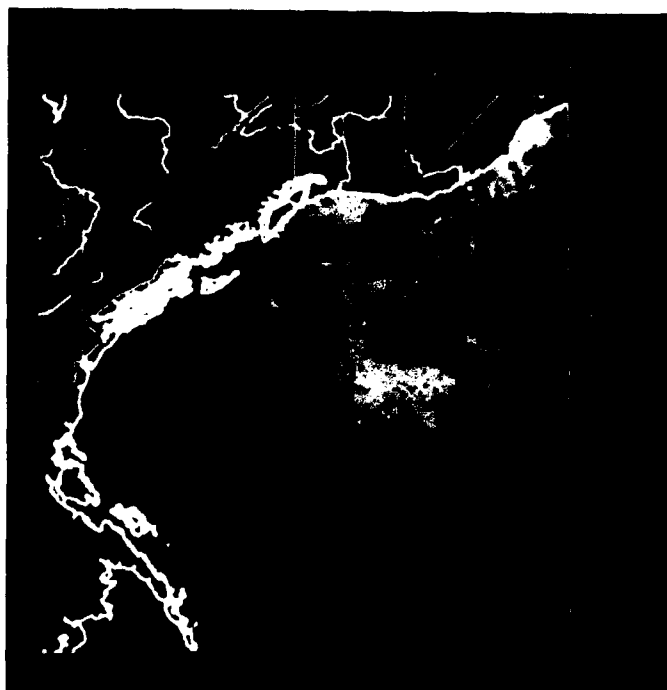
K(490)
Composite
Mean
May-Aug 1985



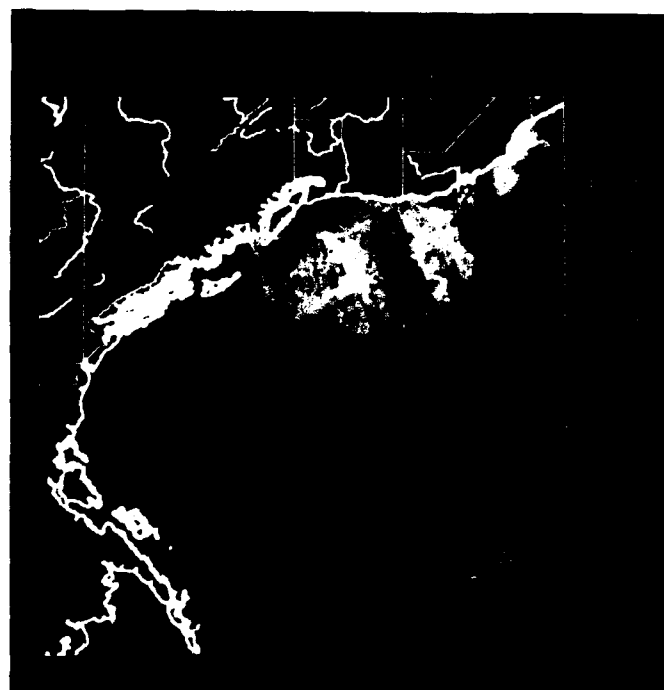
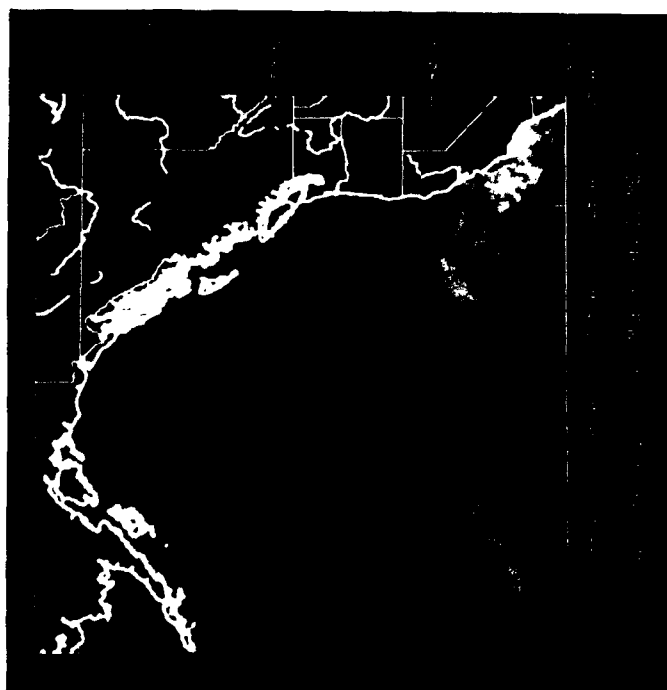
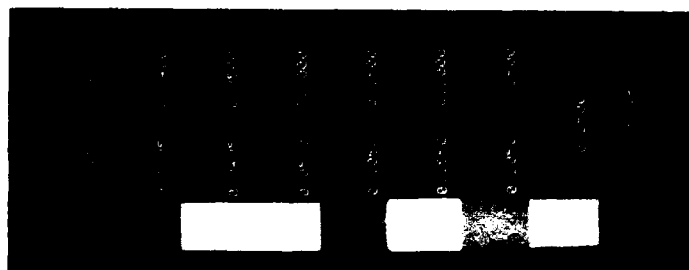


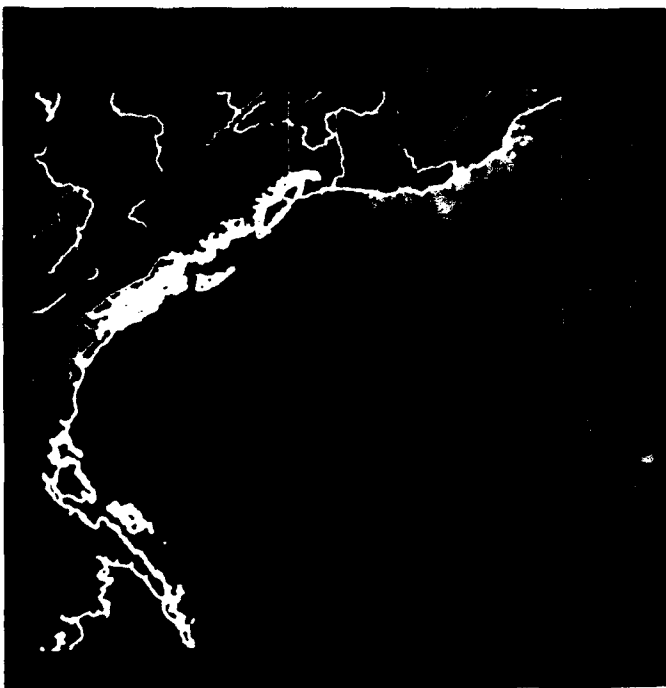
K(490)
Composite
Mean
Sep-Dec 1985



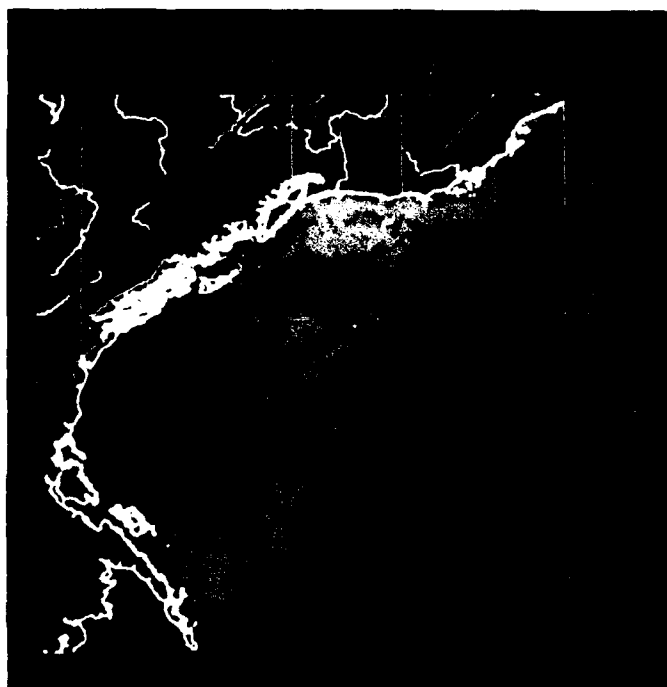
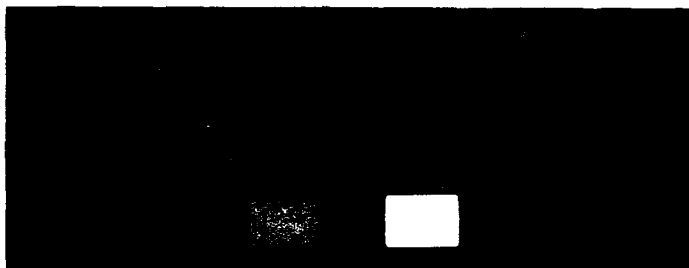


K(490)
Composite
Mean
Jan-Apr 1986





K(490)
Composite
Mean
May-Jun 1986



CZCS ceased operation in June 1986.

OPTICAL CLIMATOLOGY OF THE NORTHEAST PACIFIC OCEAN

APPENDIX B

Temporal Trends in CZCS K(490) Compared with *In Situ* Measurements

James L. Mueller

Center for Hydro-Optics & Remote Sensing
San Diego State University
6505 Alvarado Road, Suite 206
San Diego, CA 92120-5005

CHORS Technical Memorandum 001-93

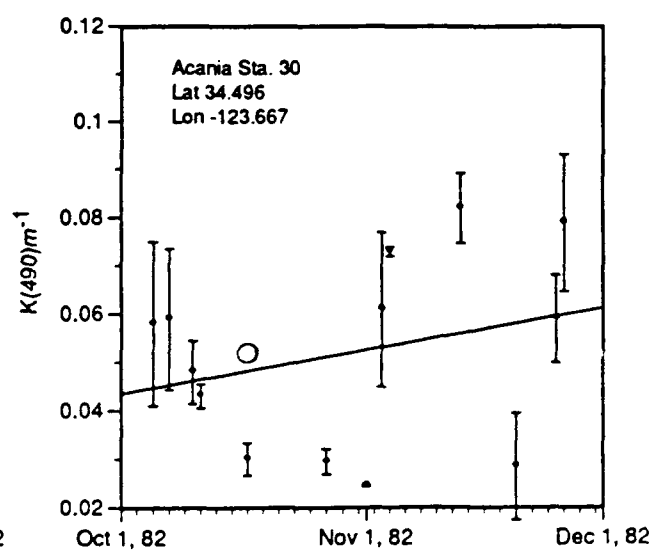
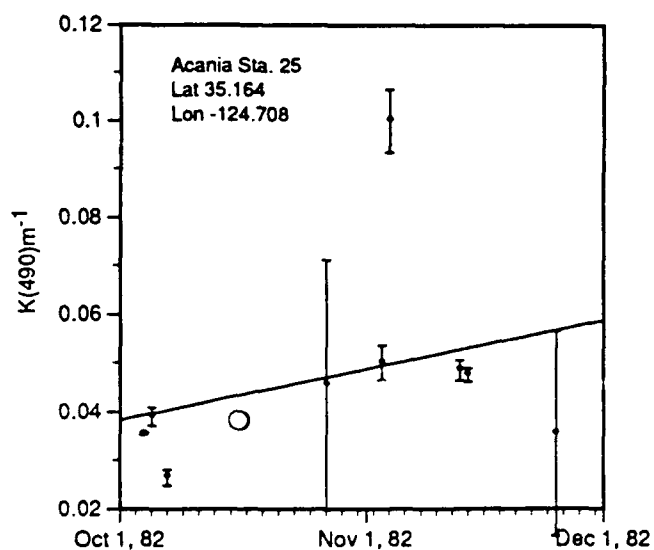
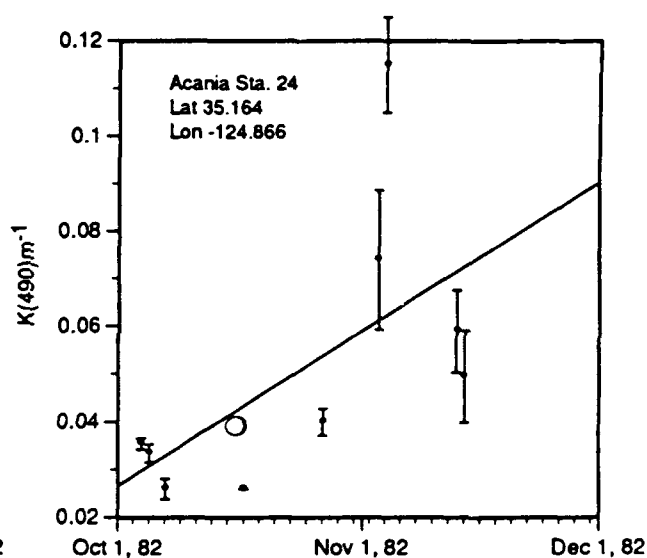
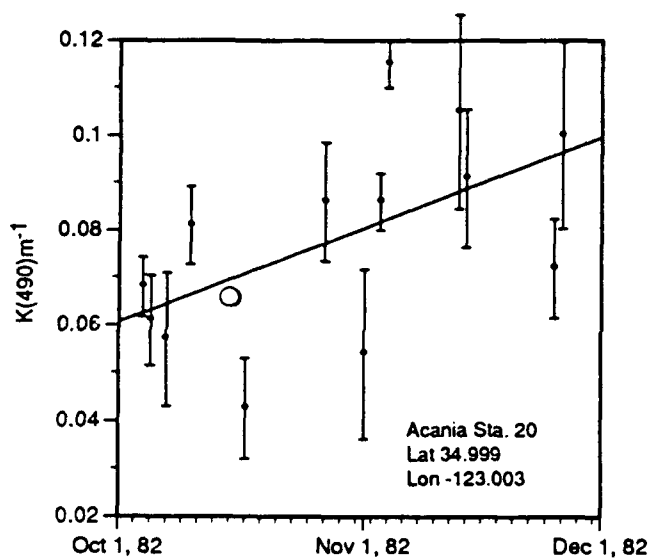
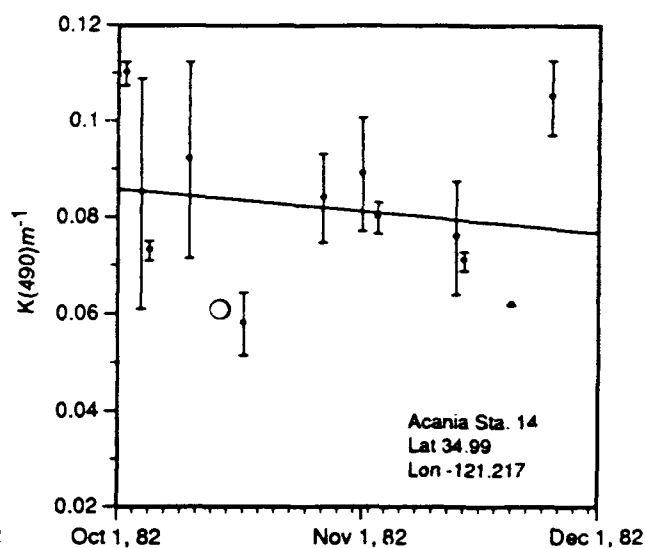
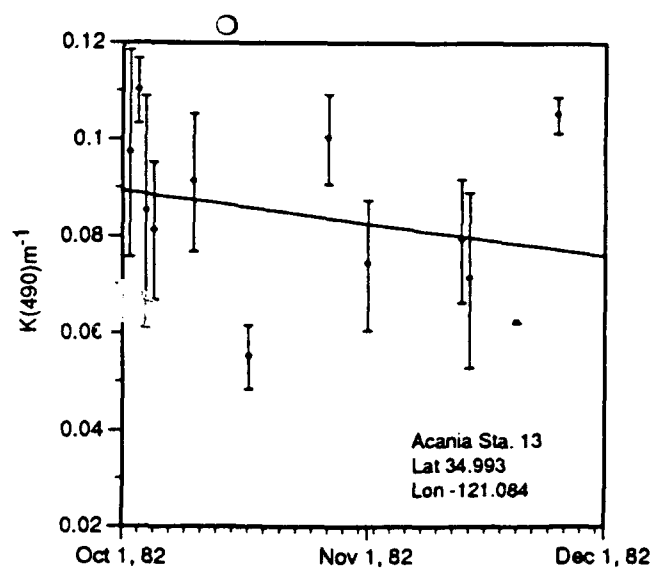
Prepared for the Naval Research Laboratory
(Stennis Space Center) Code 311
as part of the Final Report, NOARL Contract N00014-89-C-6007

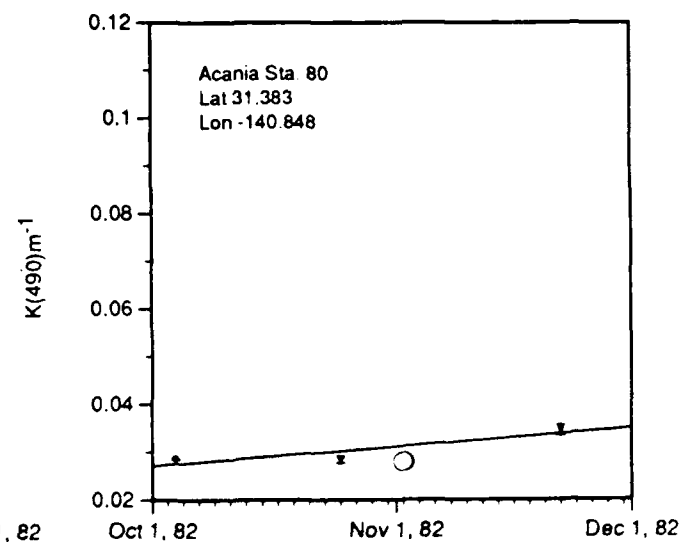
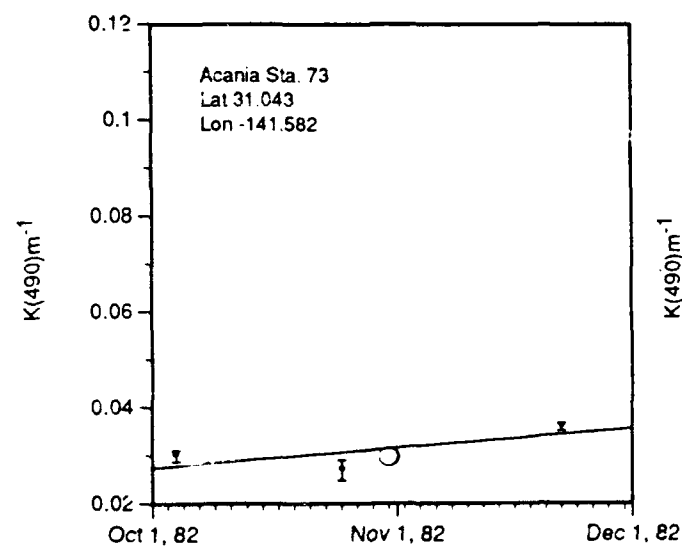
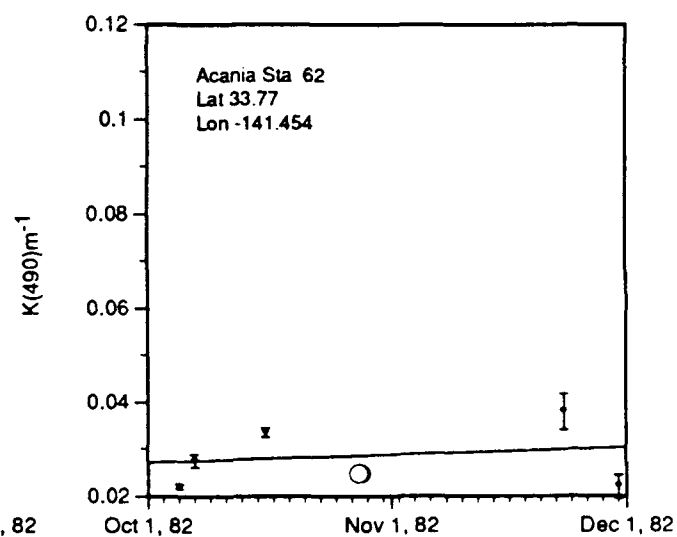
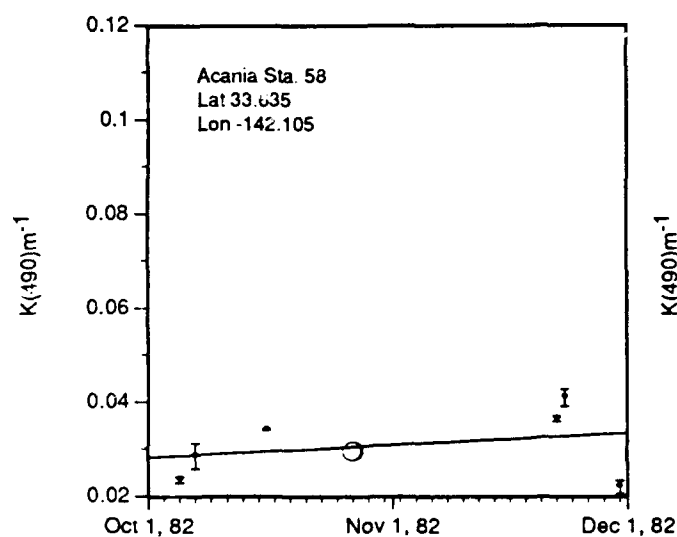
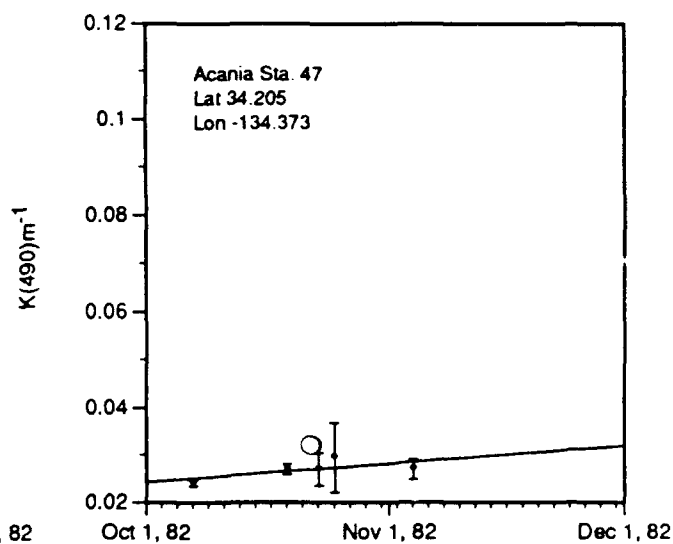
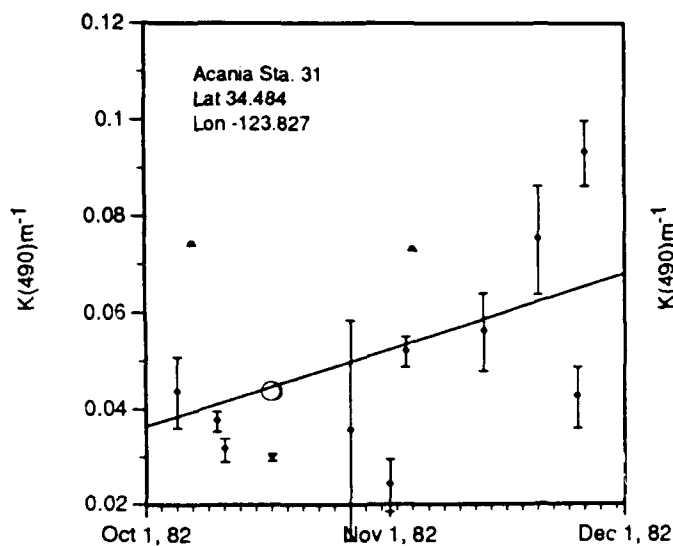
APPENDIX B

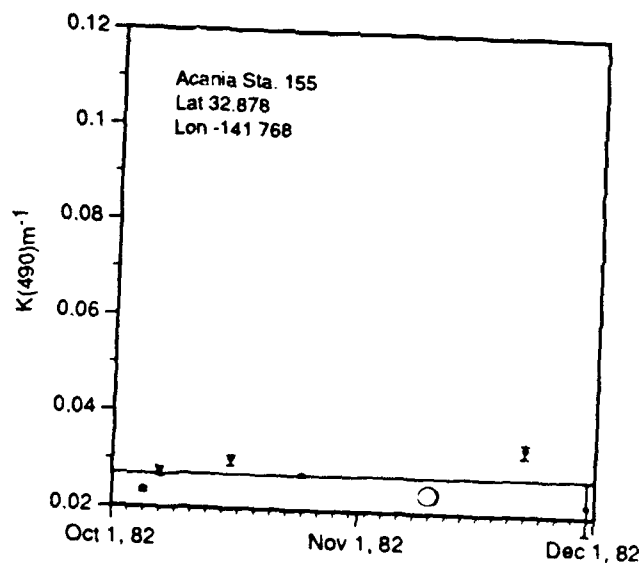
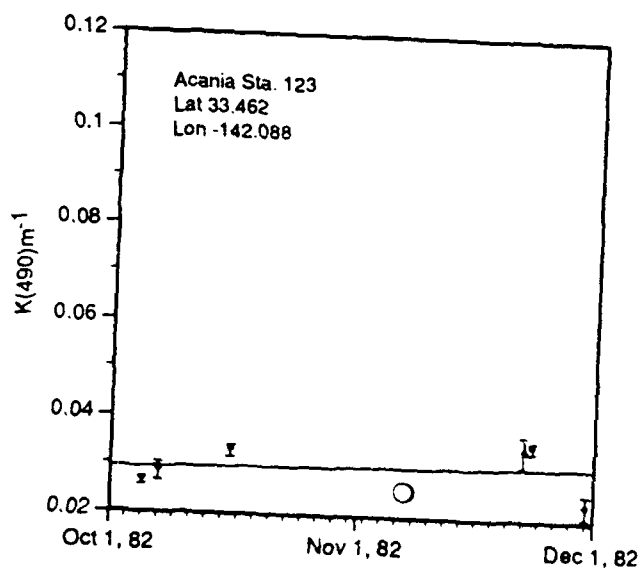
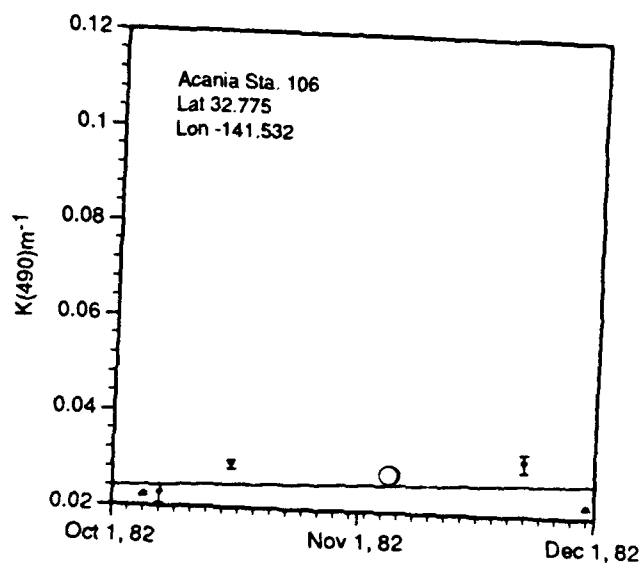
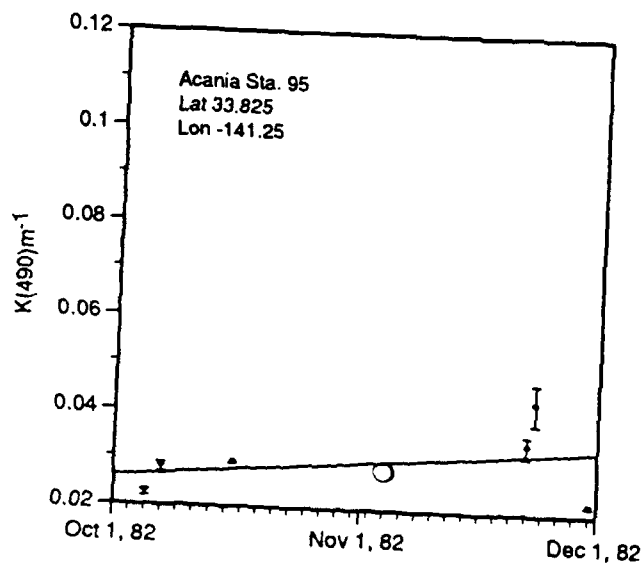
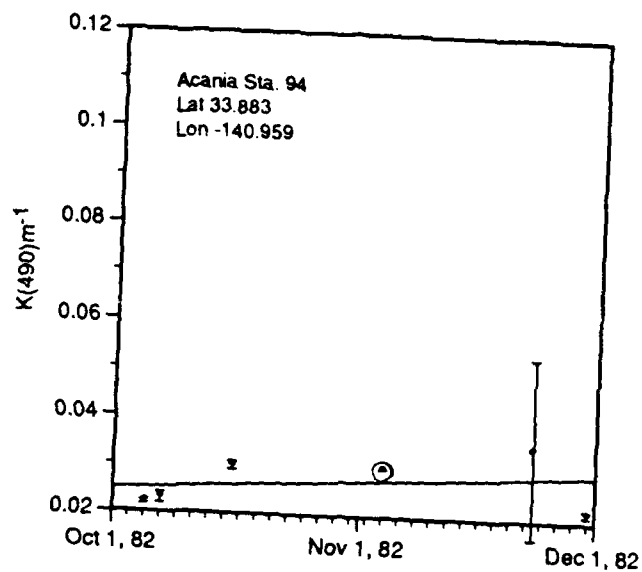
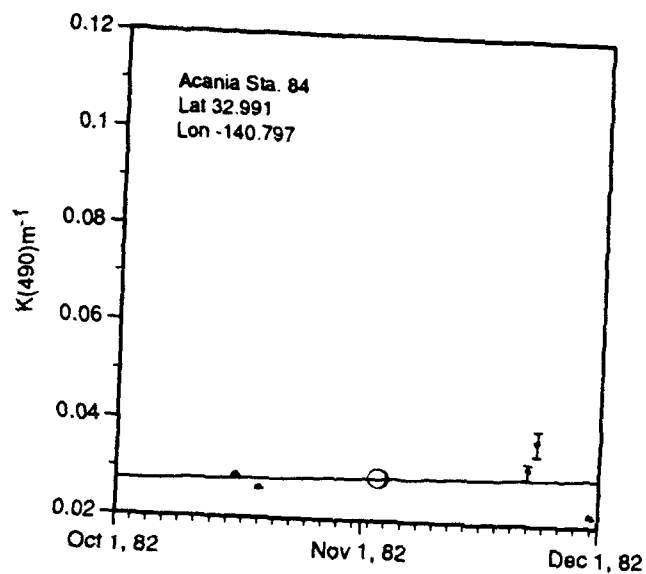
Temporal Trends in CZCS K(490) Compared with *In Situ* Measurements

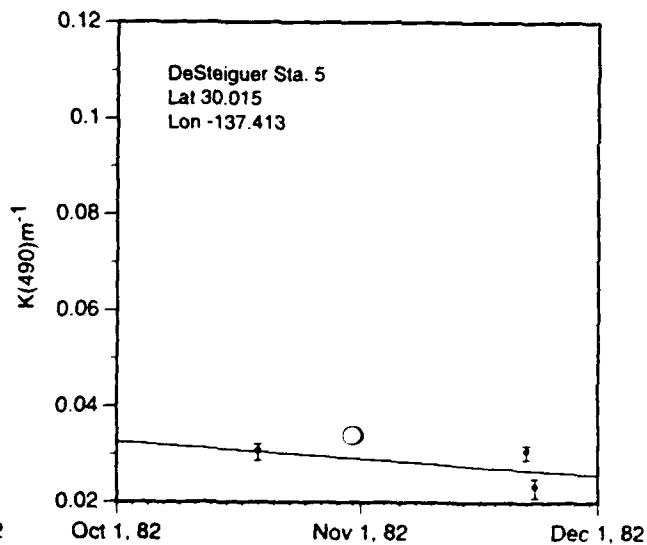
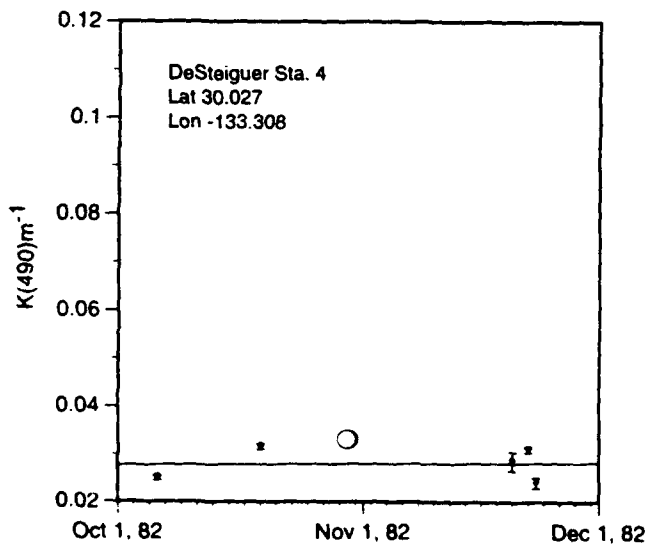
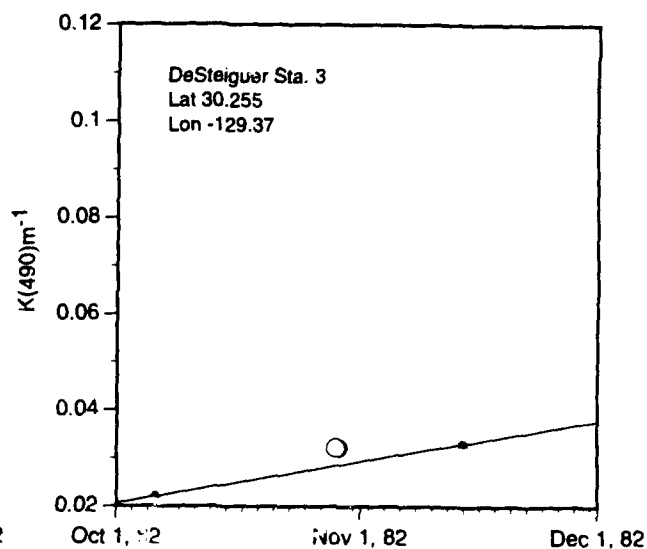
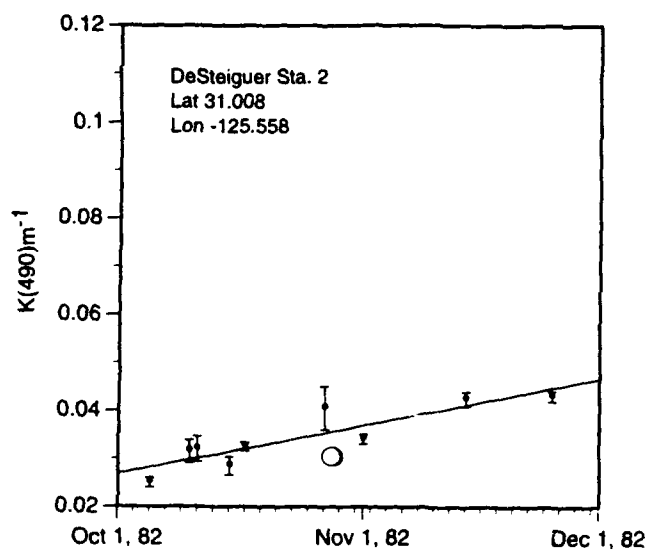
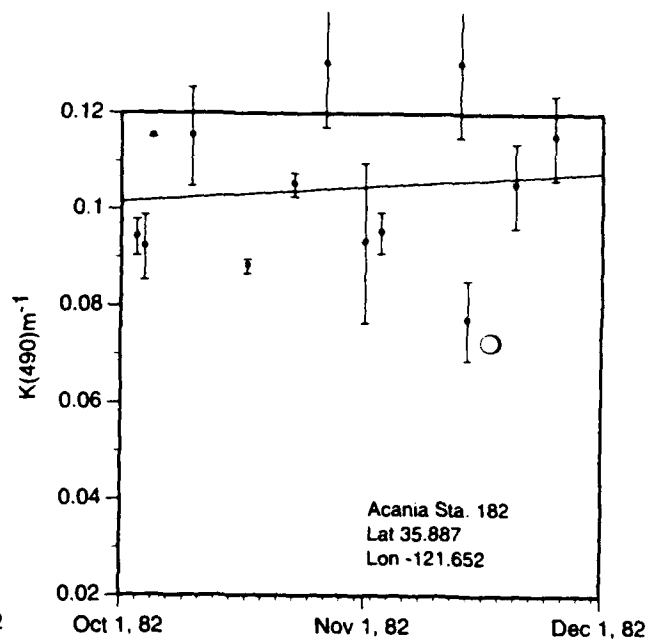
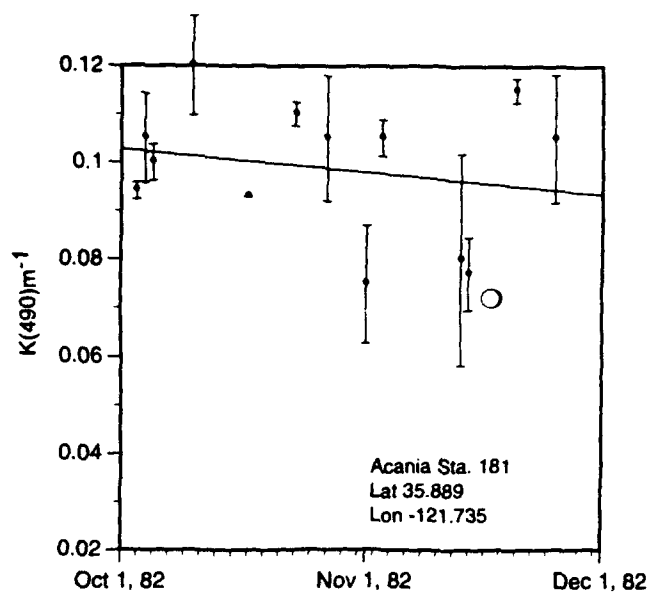
The graphs in this appendix to CHORS Technical Memorandum 001-93 (*Optical Climatology of the Northwest Pacific Ocean*) illustrate comparisons of CZCS K(490) m^{-1} estimates with $\bar{K}(490, z_{37}) \text{m}^{-1}$ values calculated from irradiance profiles $E_d(\lambda, z)$ measured *in situ* (CHORS TM 001-93, Sect. 4.1). Comparative graphs are presented for the locations of 39 stations at which $E_d(\lambda, z)$ profiles were measured during the 60-day period between 1 Oct. and 30 Nov. 1982 (CHORS TM 001-93: Sects. 2.3 and 4, Table 4.1, and Fig. 2.1). Latitude and longitude coordinates of each station are given in the legend of each graph.

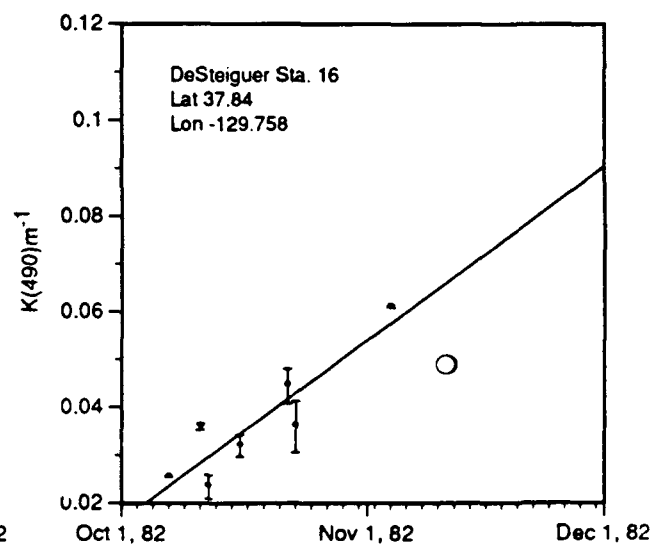
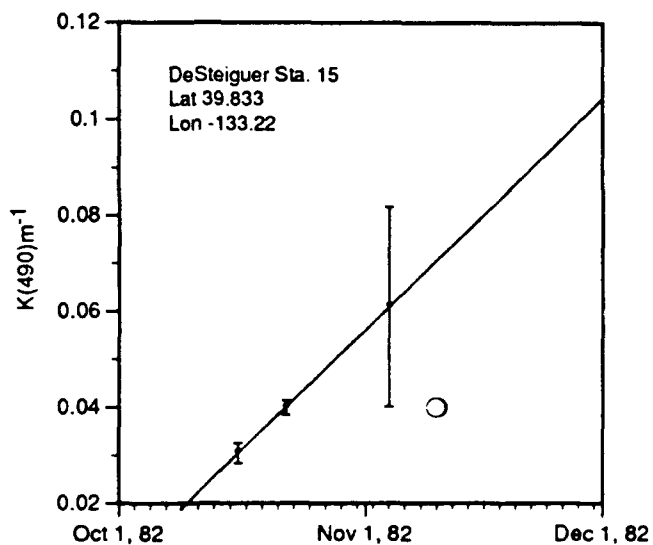
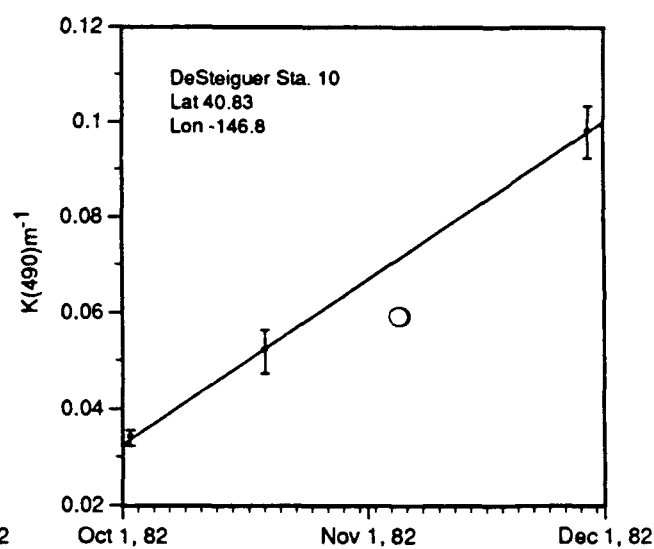
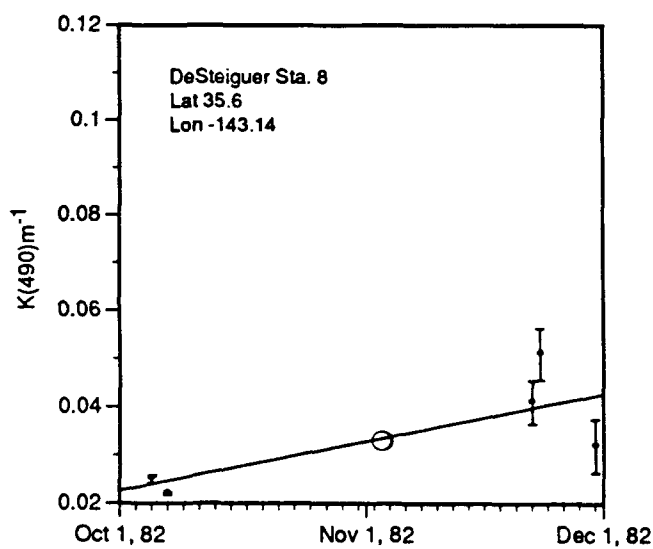
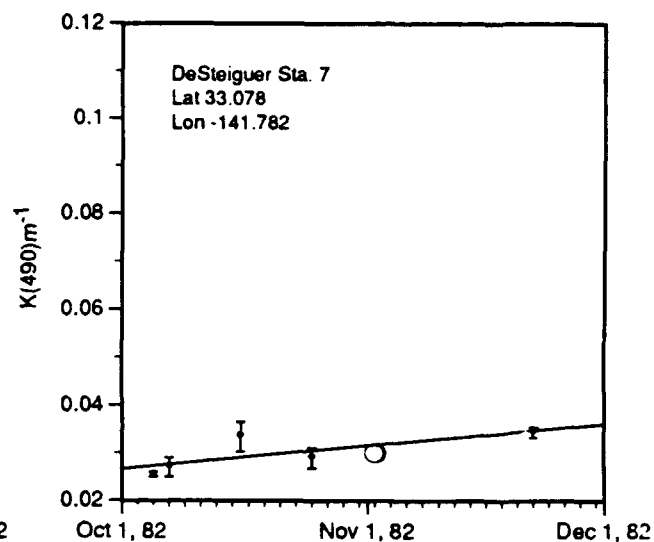
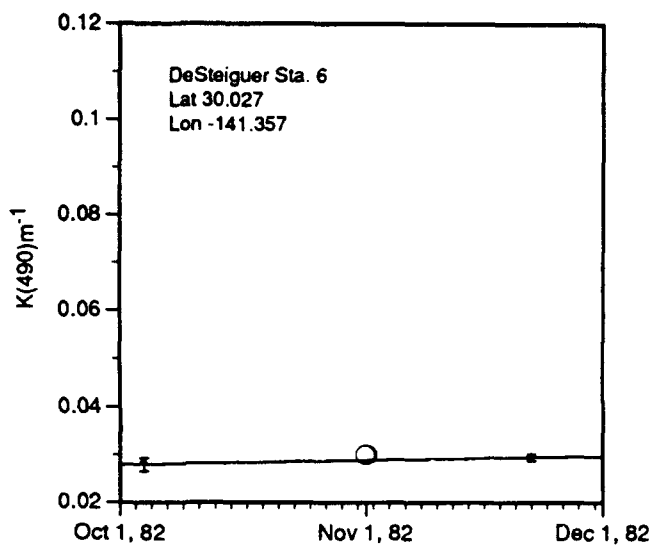
On each graph, *in situ* $\bar{K}(490, z_{37})$, and the day of its measurement, are plotted as an open circle. For each day on which valid CZCS observations were recorded at that location, CZCS K(490) is plotted as a solid dot, together with error bar representing the estimated standard deviation in each 3×3 grid cell block (CHORS TM 001-93: Sect. 4). The solid line plotted in each graph represents the 60-day least-squares trend fit to the median CZCS K(490) values; error is estimated as the difference between the least-squares trend fit and the *in situ* $\bar{K}(490, z_{37})$, on the day of the ship station (CHORS TM 001-93: Sect. 4 and Table 4.1).

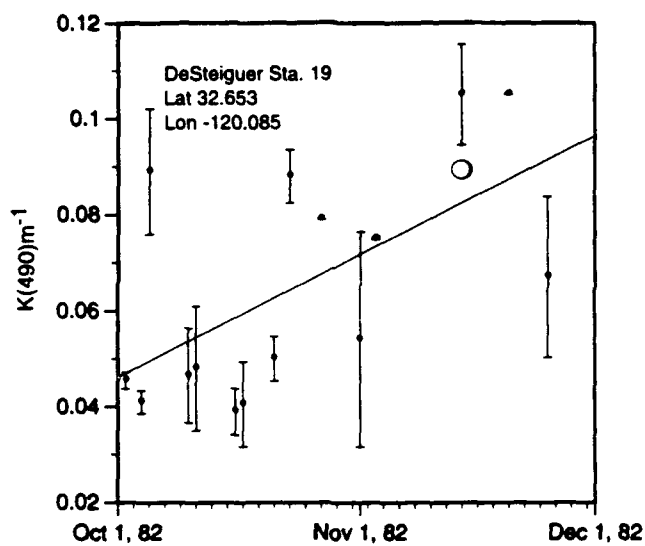
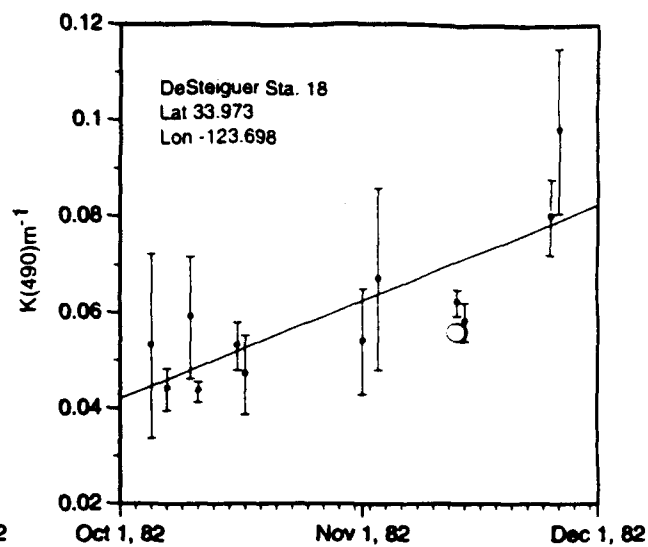
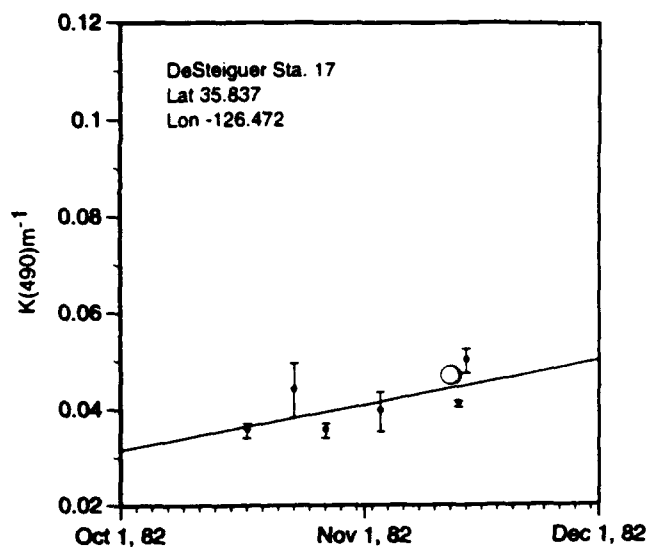












OPTICAL CLIMATOLOGY OF THE NORTHEAST PACIFIC OCEAN

APPENDIX C

Digital Data Directory

James L. Mueller

**Center for Hydro-Optics & Remote Sensing
San Diego State University
6505 Alvarado Road, Suite 206
San Diego, CA 92120-5005**

CHORS Technical Memorandum 001-93

**Prepared for the Naval Research Laboratory
(Stennis Space Center) Code 311
as part of the Final Report, NOARL Contract N00014-89-C-6007**

APPENDIX C

Digital Data Directory

Accompanying this Final Report are two sets of digital data, representing deliverable end products of this extensive CZCS data base analysis. These products are the 5° Latitude × 5° Longitude CZCS K(490) Time Series (Sects. 2.1.7, 3.1.4.5 and 3.3, together with Appendix D) and the time series of Monthly Composite Mean K(490) Maps of the Northeast Pacific Ocean (Sects. 2.1.6, 3.1.4.4 and 3.3, together with appendix A).

These data sets are delivered (in duplicate) on a single 9-track magnetic data tape. Density is 6250 bpi. The unlabeled tape contains 10 TAR (Tape Archive) files, recorded with a blocksize of 10,240 bytes. Each TAR file contains several separate data files, which are intended to be read into a single directory on disk; each TAR file also contains an ASCII "README" file which further identifies the content of the archived directory.

The contents, and approximate overall sizes of the 10 TAR files are:

File	Approximate Size	Data Contents
1	50 Kbytes	Time Series (1979-1986) of CZCS K(490) at 5° Latitude × 5° Longitude Grid Points
2	2.0 Mbytes	1978 Monthly Composite Mean K(490) Maps (Nov and Dec. only)
3	23.2 Mbytes	1979 Monthly Composite Mean K(490) Maps
4	23.2 Mbytes	1980 Monthly Composite Mean K(490) Maps
5	23.2 Mbytes	1981 Monthly Composite Mean K(490) Maps
6	23.2 Mbytes	1982 Monthly Composite Mean K(490) Maps
7	23.2 Mbytes	1983 Monthly Composite Mean K(490) Maps
8	23.2 Mbytes	1984 Monthly Composite Mean K(490) Maps
9	23.2 Mbytes	1985 Monthly Composite Mean K(490) Maps
10	11.6 Mbytes	1986 Monthly Composite Mean K(490) Maps (Jan through Jun. only)

(Note that approximately 180 Mbytes of disk storage would be required to keep the entire data base on line at once. Approximately one-half of this storage, however, would be taken up by the Sample Size *.n.K490 files in the Monthly Composite Mean K(490) Map directories. Since these files will not be needed for most applications, the complete Monthly Mean Climatology would require only 90 Mbytes of disk space.)

Refer to Sect 2.1.7 of the main report for a description of the internal format and data contents of the individual *.Ks data files in the 5° Latitude × 5° Longitude K(490) Time Series TAR directory (Archive File 1).

Refer to Sect. 2.1.6 of the main report for descriptions of the format, data content, and unpacking algorithms for the individual *.m.K490 (Mean Map) and *.n.K490 (Sample Size Map) data files in the Monthly Composite Mean K(490) Maps TAR directories (Archive Files 2-10).

OPTICAL CLIMATOLOGY OF THE NORTHEAST PACIFIC OCEAN

APPENDIX D

Time Series Graphs of CZCS K(490) at Selected Locations

James L. Mueller

**Center for Hydro-Optics & Remote Sensing
San Diego State University
6505 Alvarado Road, Suite 206
San Diego, CA 92120-5005**

CHORS Technical Memorandum 001-93

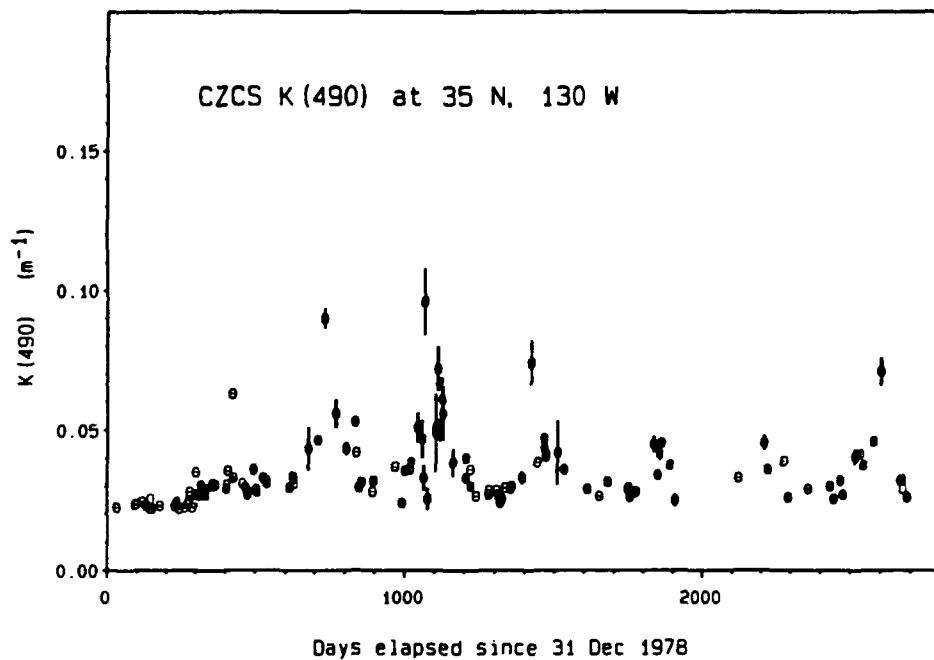
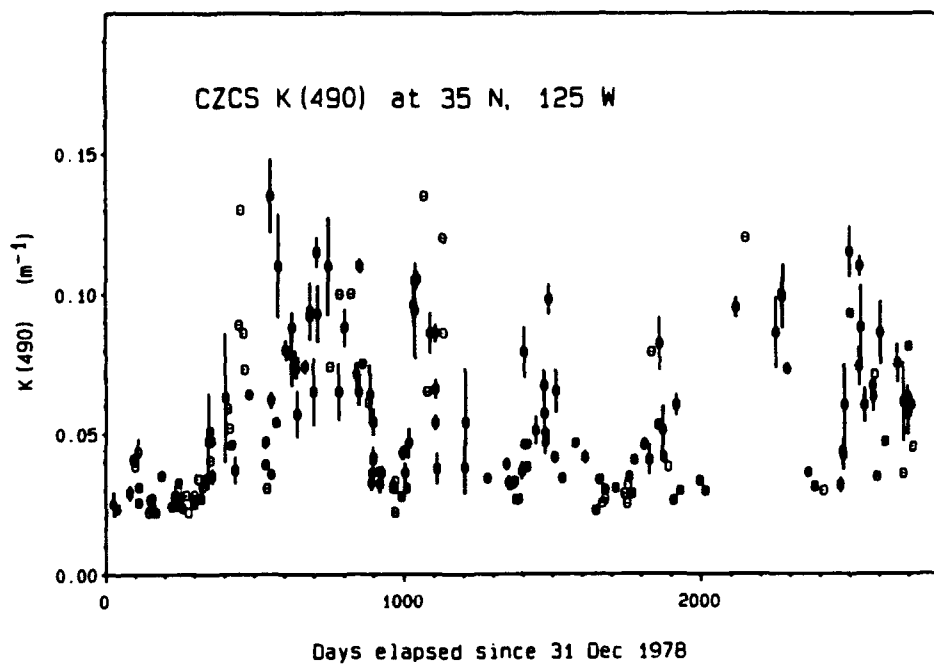
**Prepared for the Naval Research Laboratory
(Stennis Space Center) Code 311
as part of the Final Report, NOARL Contract N00014-89-C-6007**

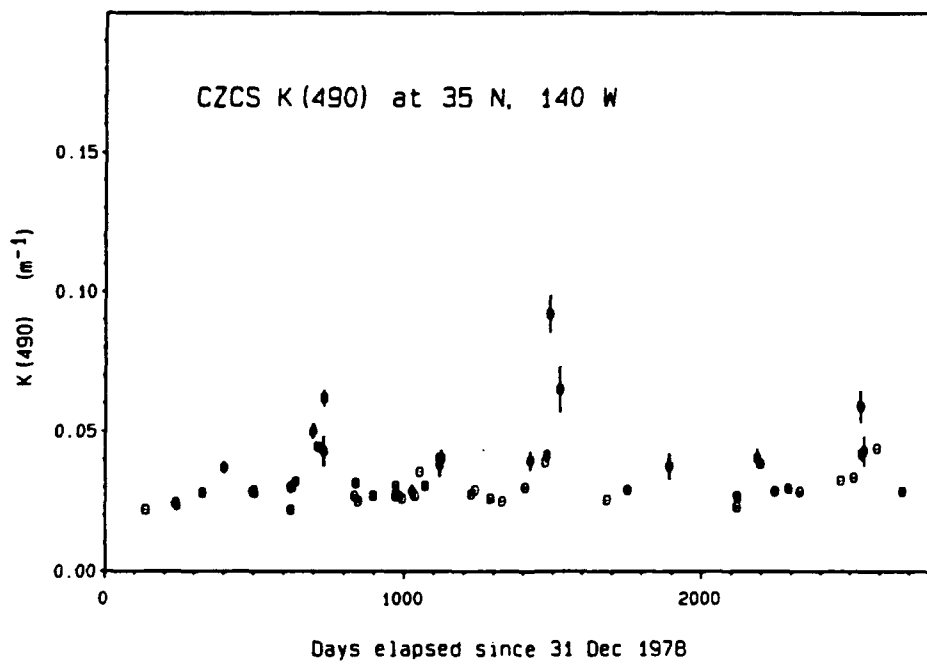
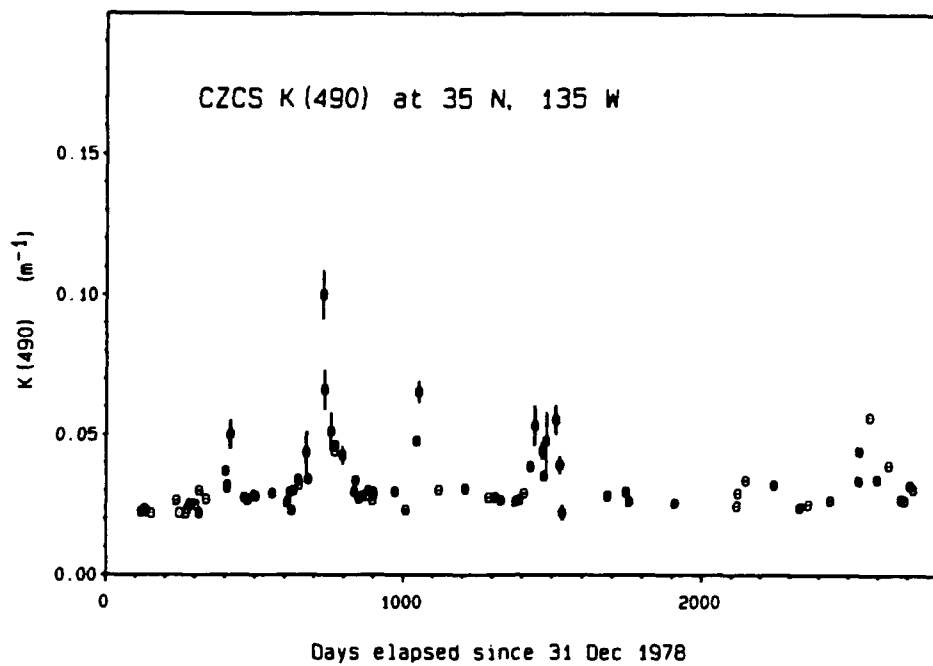
APPENDIX D

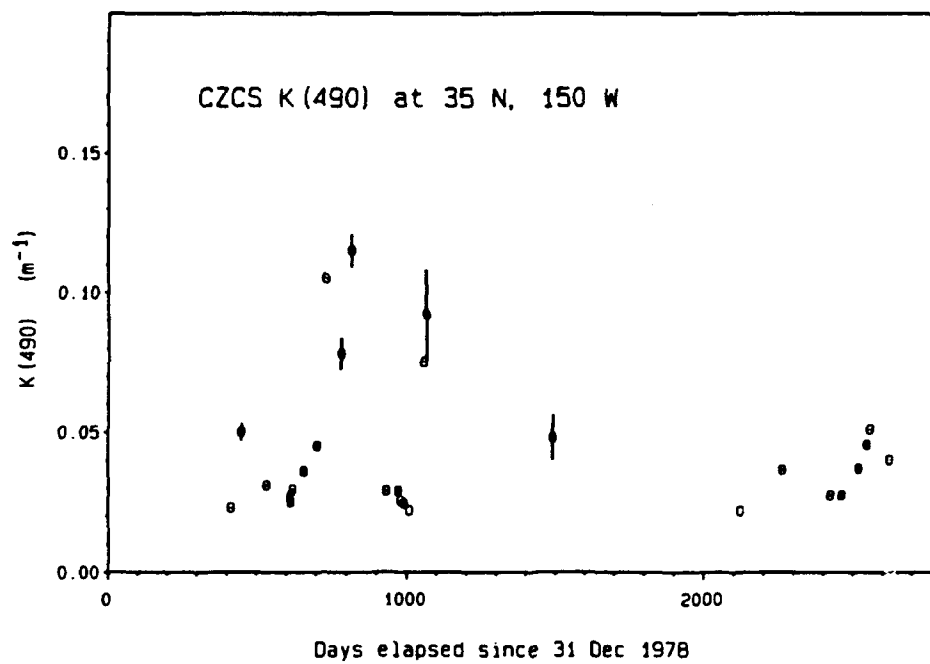
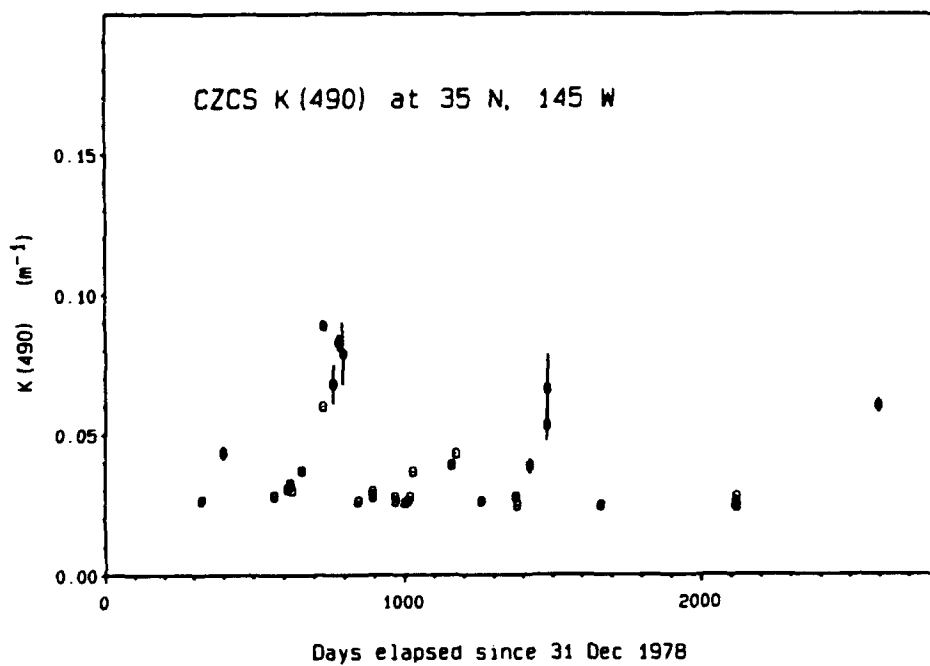
Time Series Graphs of CZCS K(490) at Selected Depths

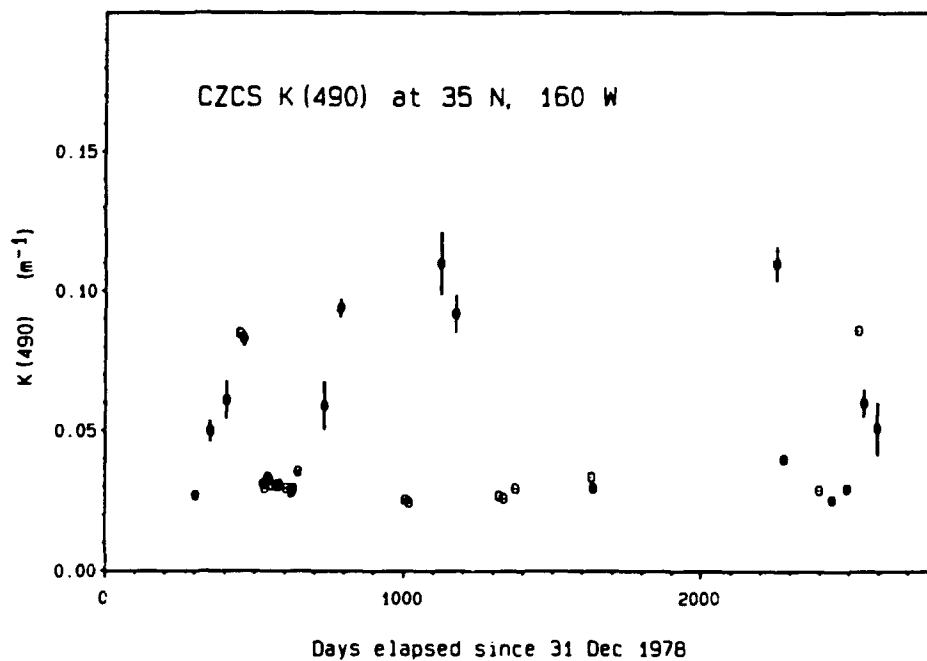
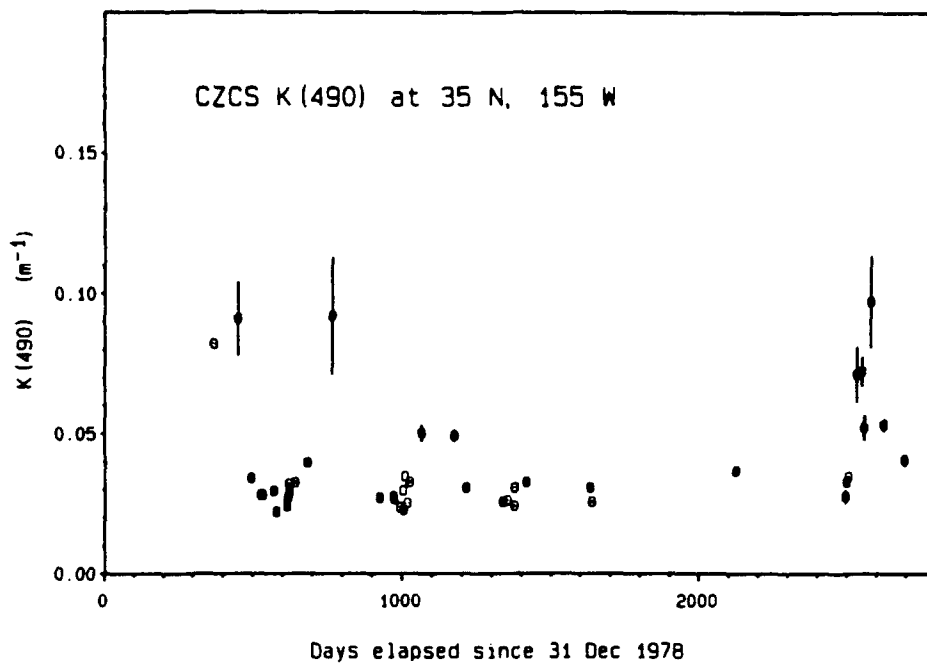
This appendix to CHORS Technical Memorandum 001-93 (*Optical Climatology of the Northeast Pacific Ocean*) presents graphs illustrating the scales and magnitude of temporal variability in CZCS K(490) estimates at geographic locations distributed widely over the Northeast Pacific Ocean (CHORS TM 001-93: Sect. 3.1.4.4 and 3.4, and Fig. 3.1.5); these locations are spaced at intervals of 5° latitude and 5° longitude and are listed in the legend of each figure.

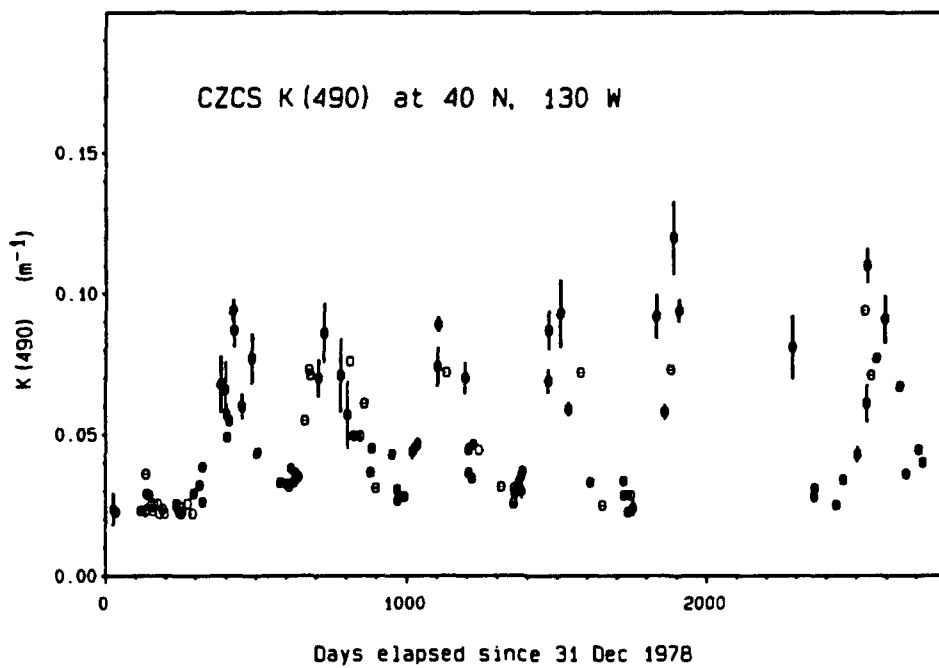
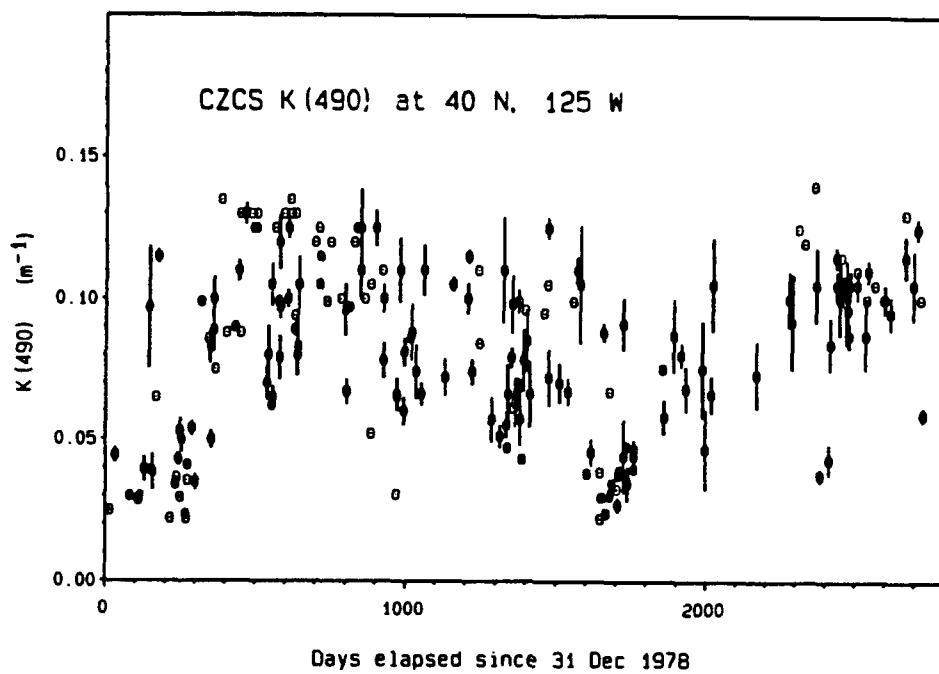
Each graph presents K(490) m^{-1} plotted against time, measured in days elapsed since 31 December 1978. At each data point, the open circle represents the median K(490), and the vertical line is the estimated standard deviation, from the CZCS K(490) data in the block of 5 line \times 5 pixel grid cells centered at that location on the day shown (CHORS TM 001-93: Sects. 3.1.4.1, 3.1.4.4, and 3.4); the effective spatial resolution of the individual K(490) estimates is, therefore, approximately 25 km. The preparation of these time series is described in Sect. 3.1.4.1, and their data content and significance are discussed Sect. 3.4, of CHORS TM 001-93.

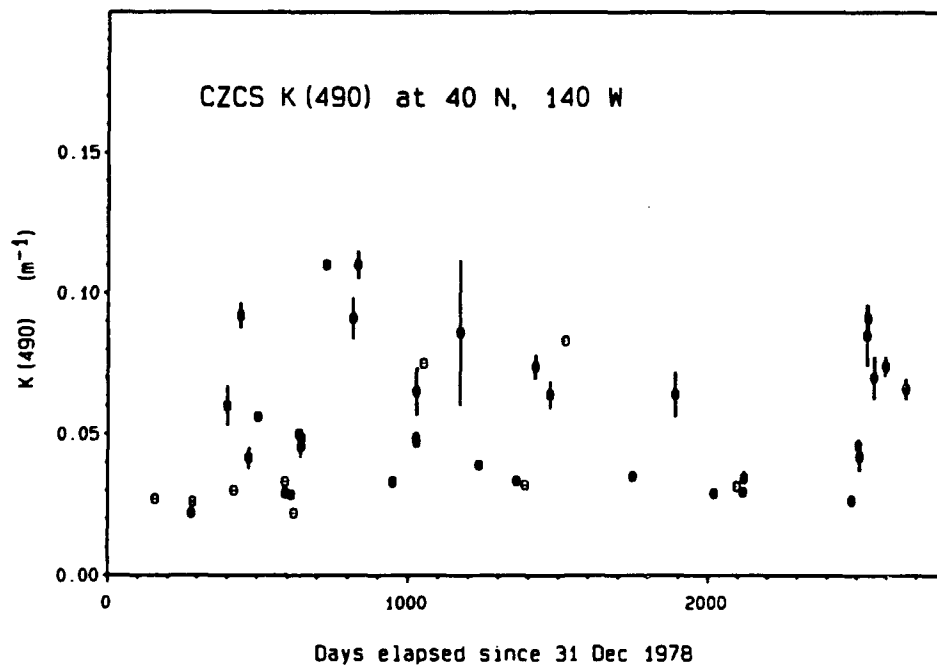
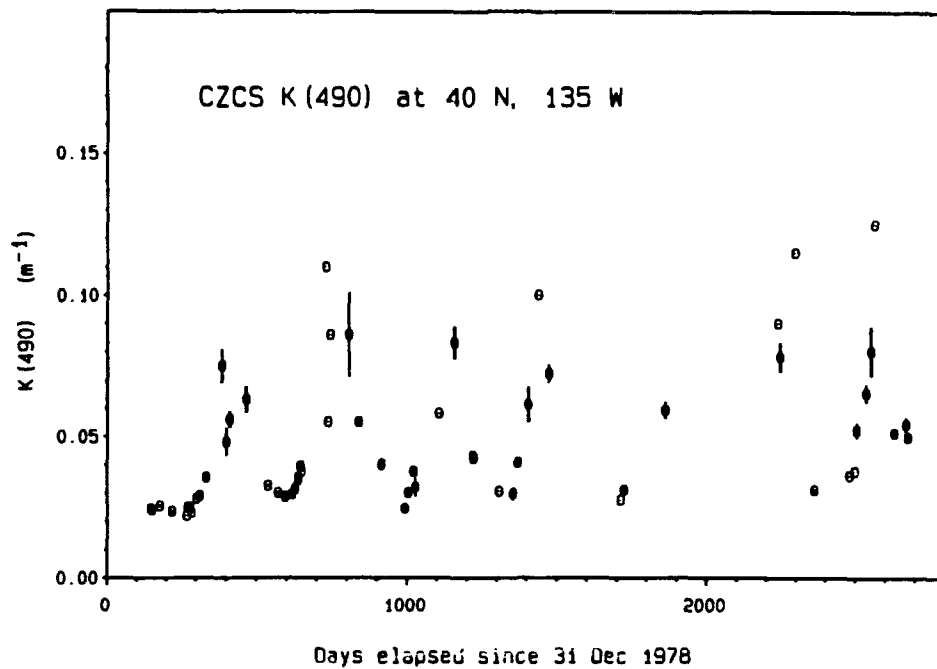


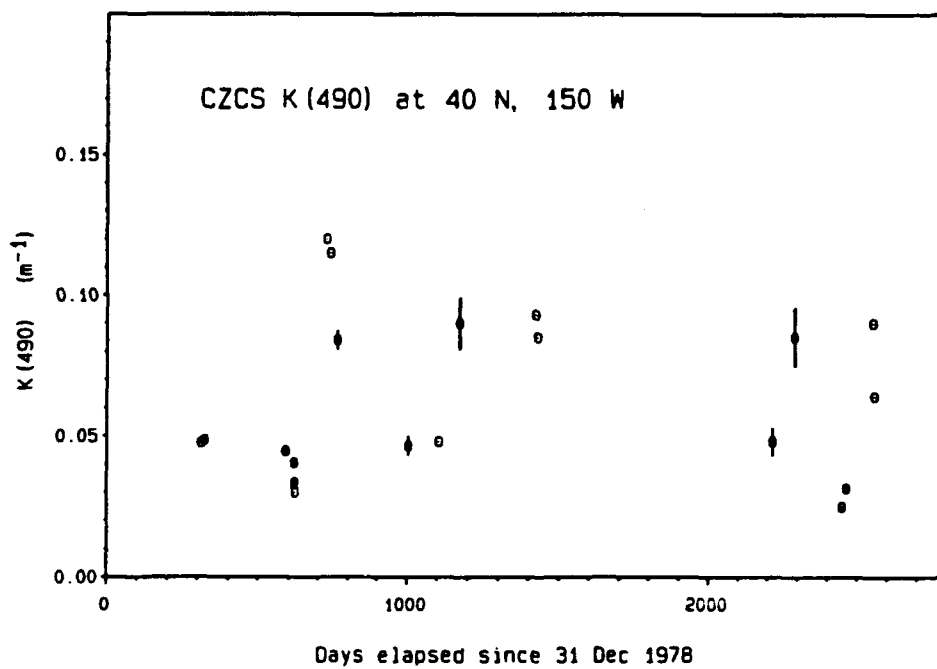
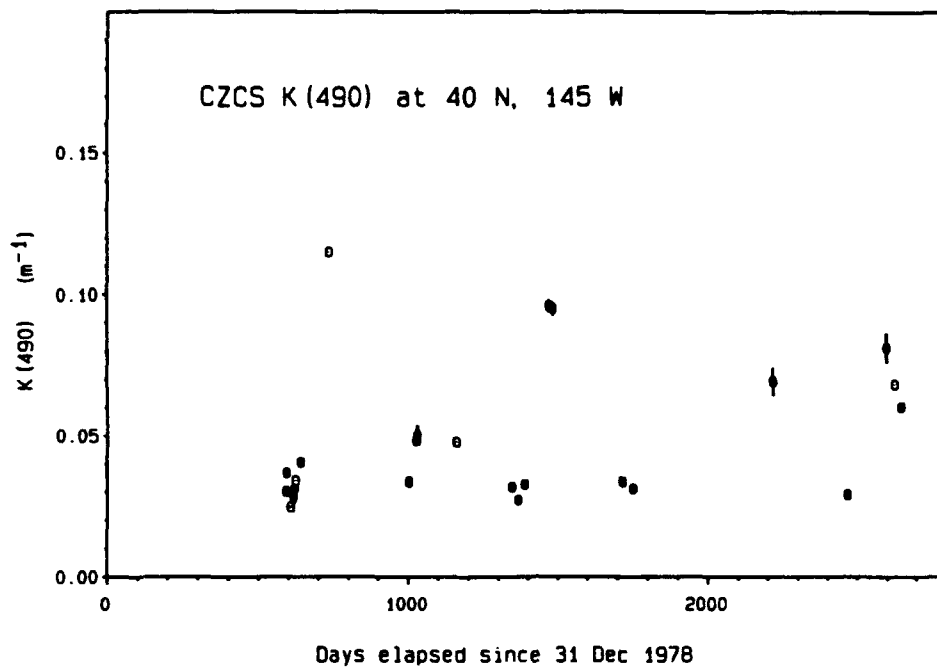


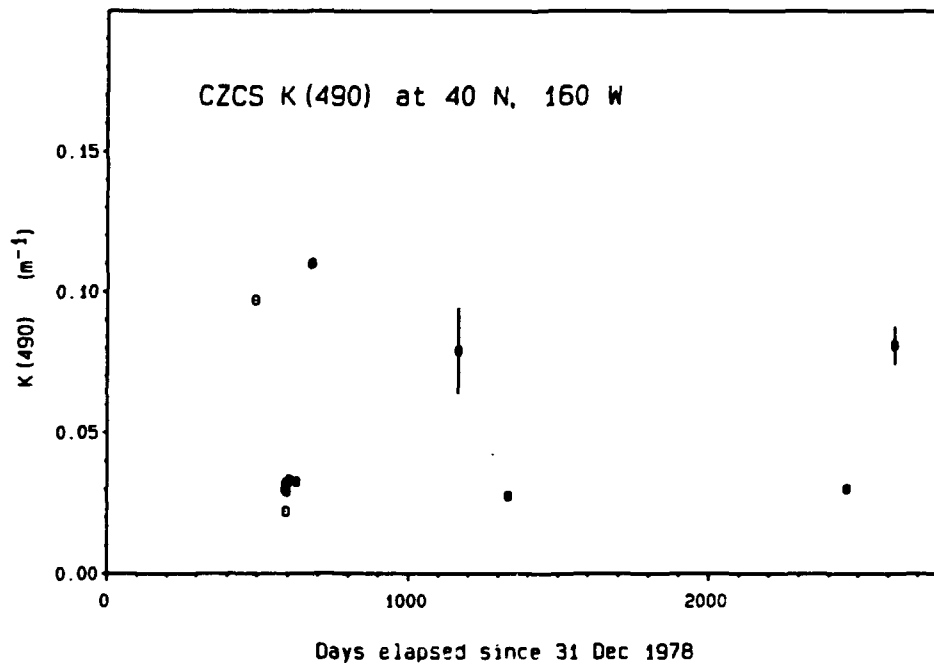
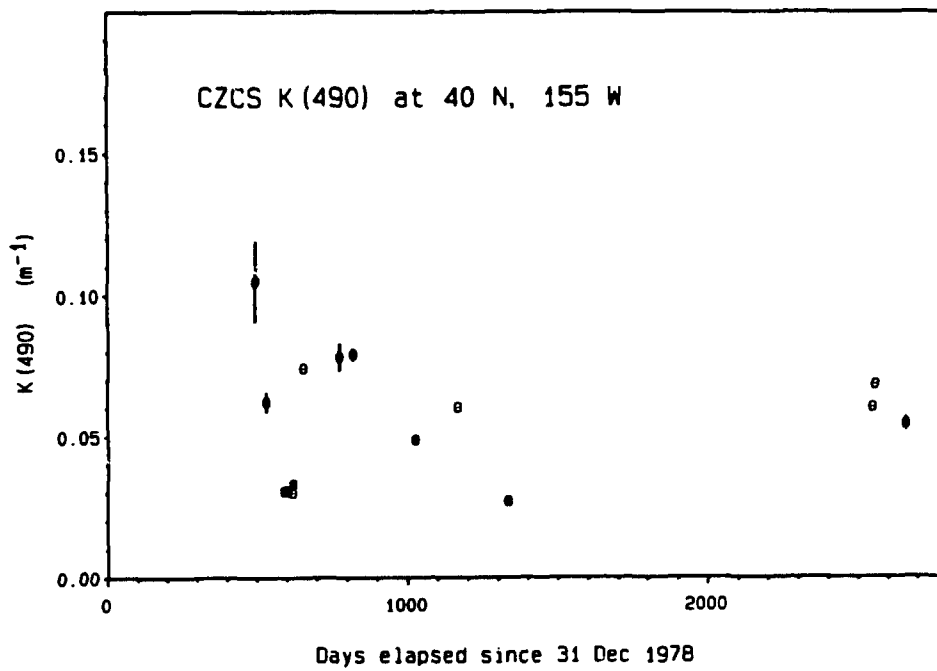


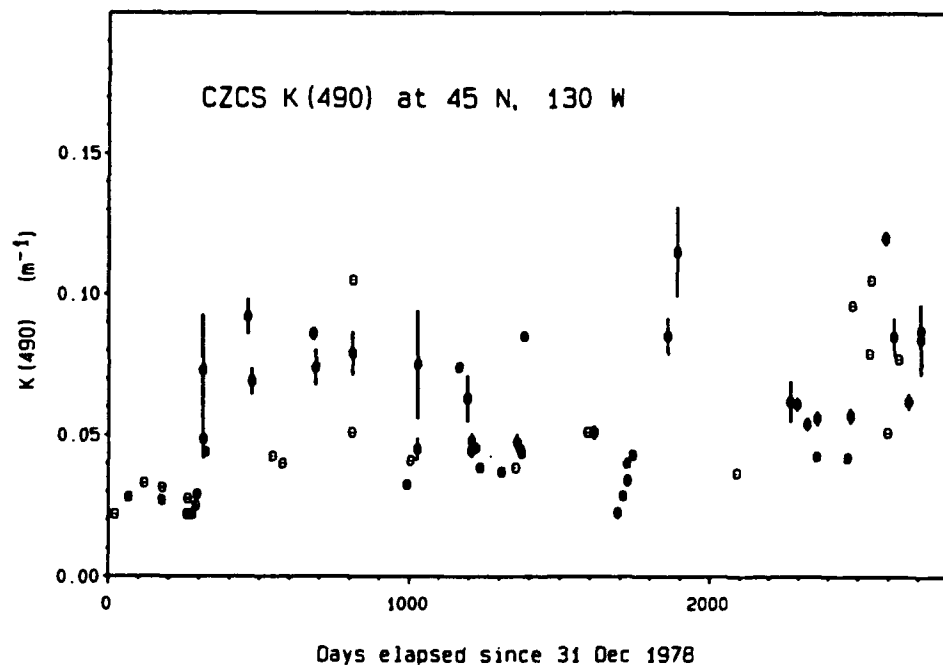
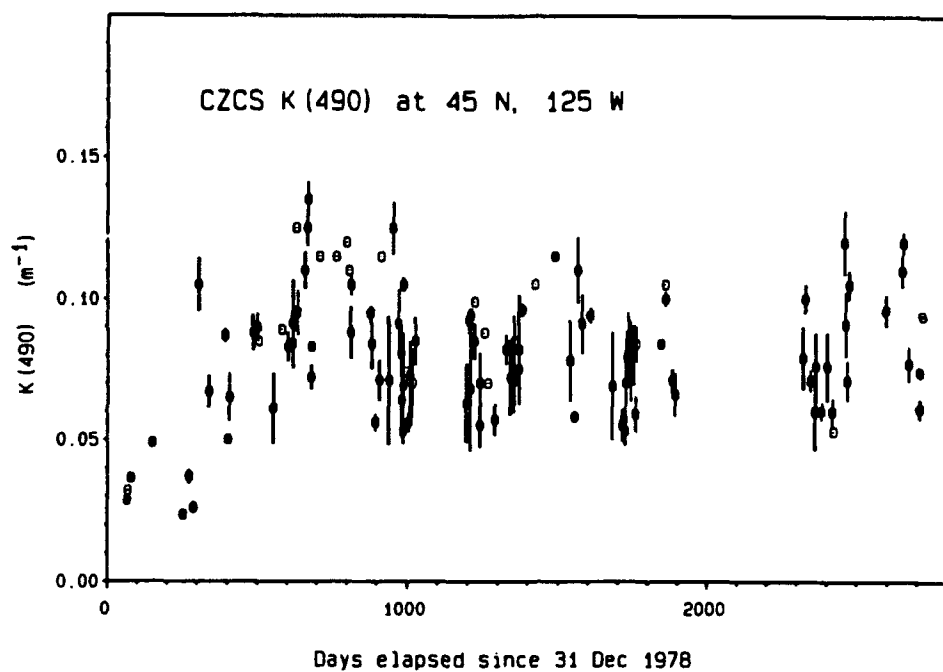


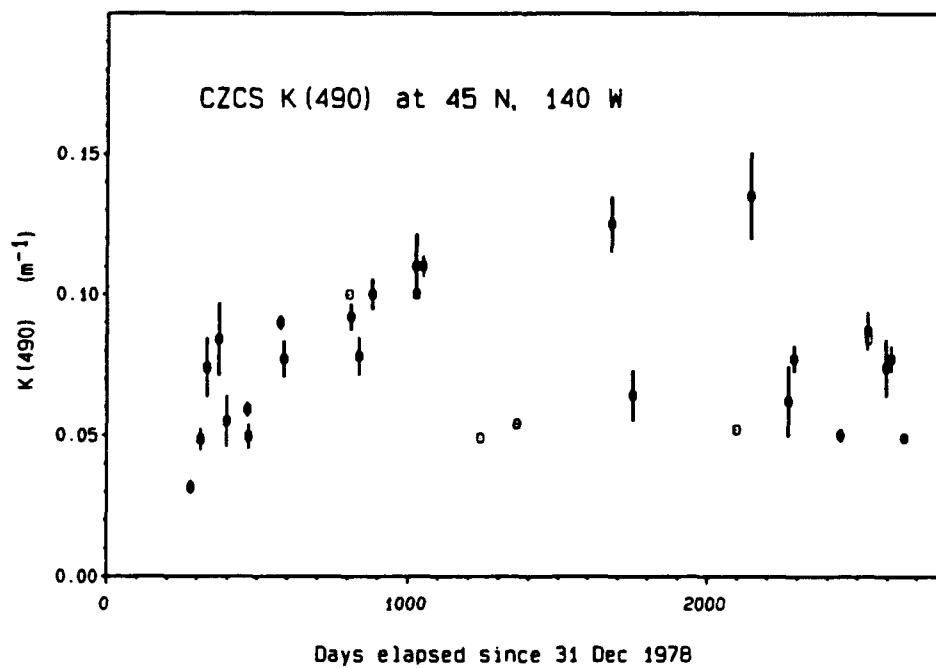
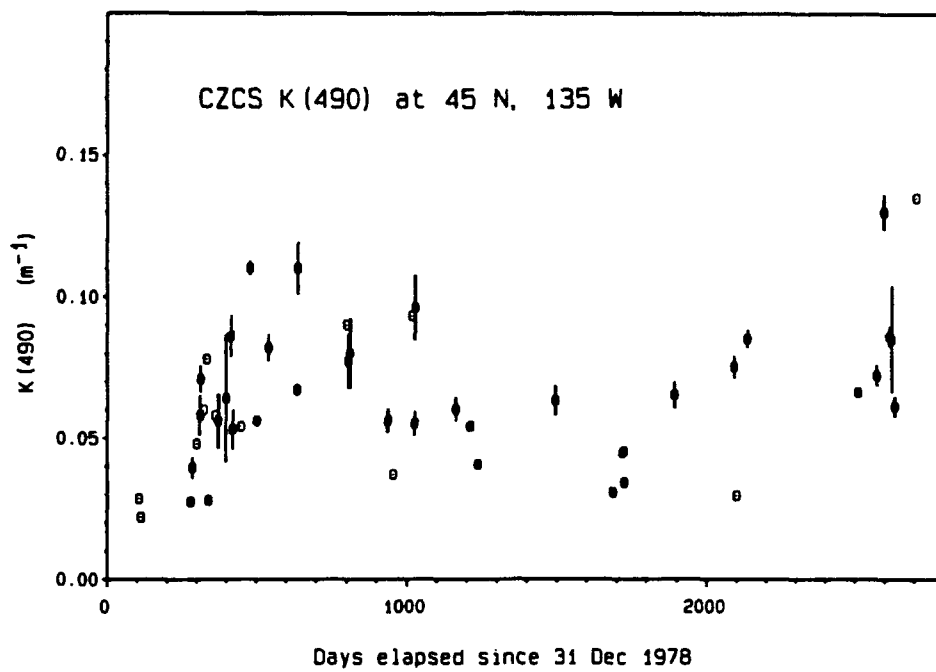


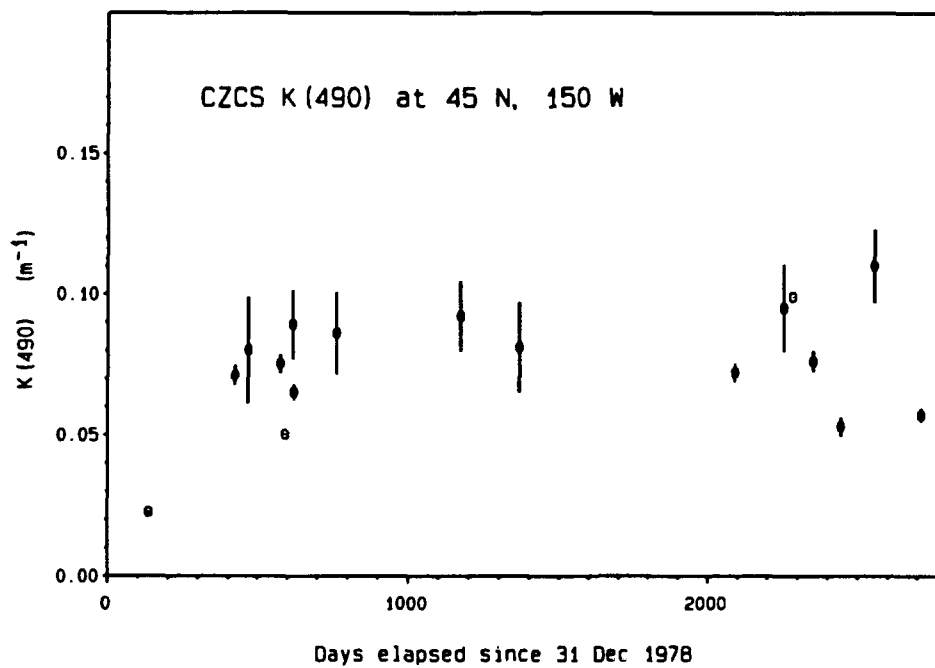
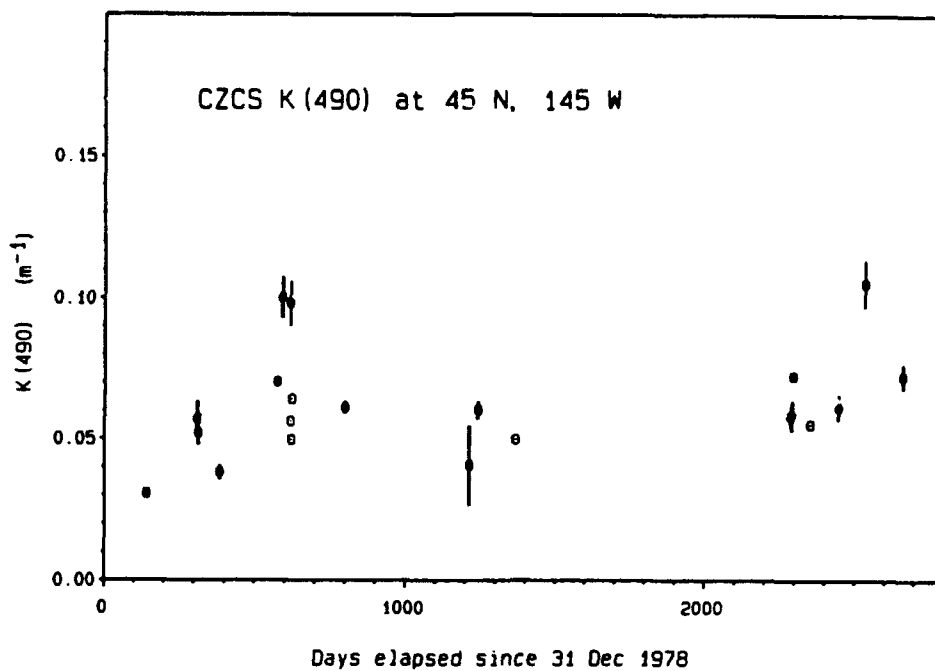


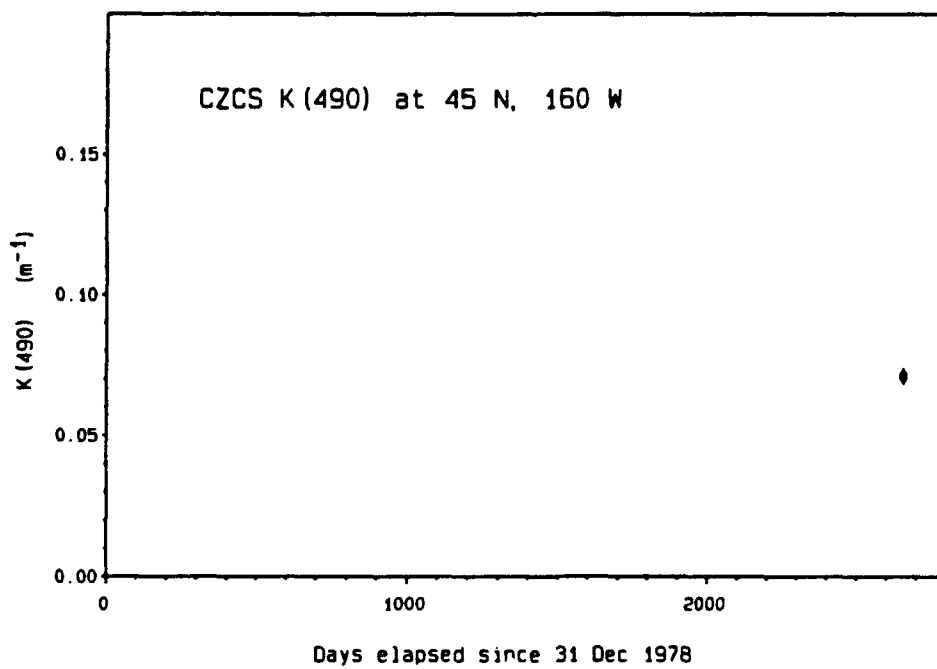
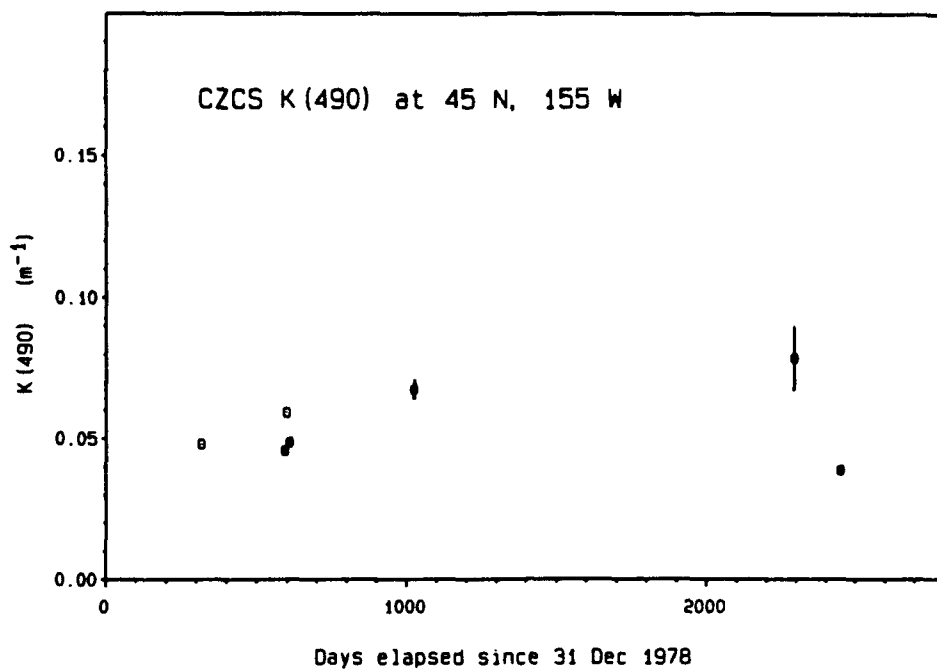


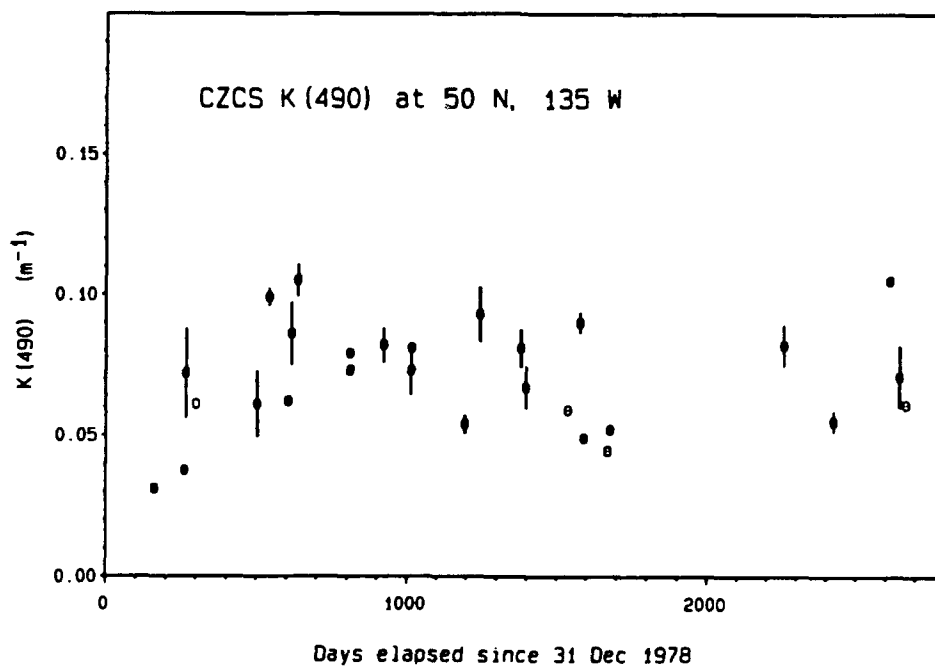
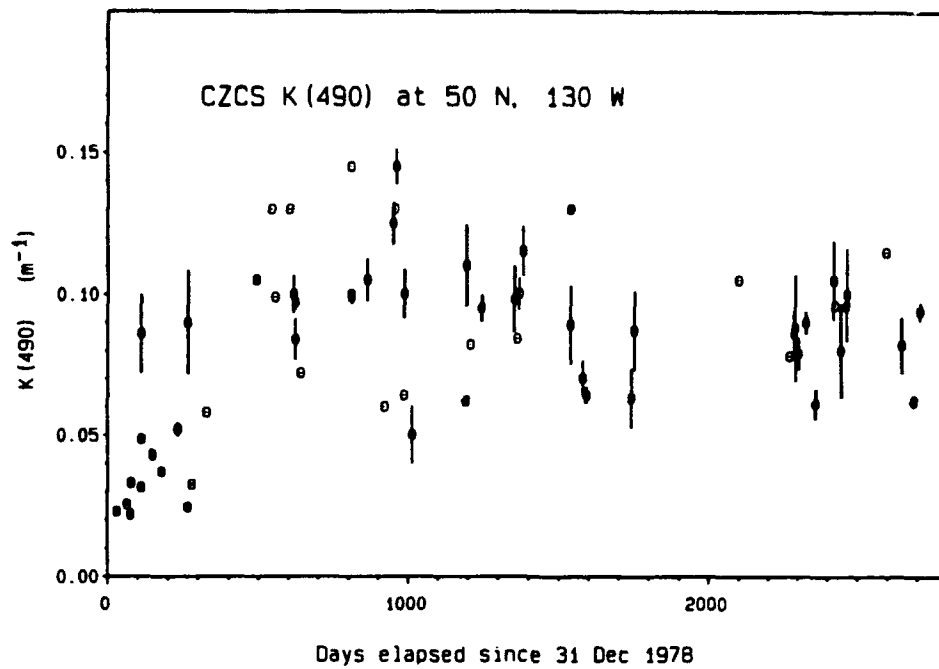


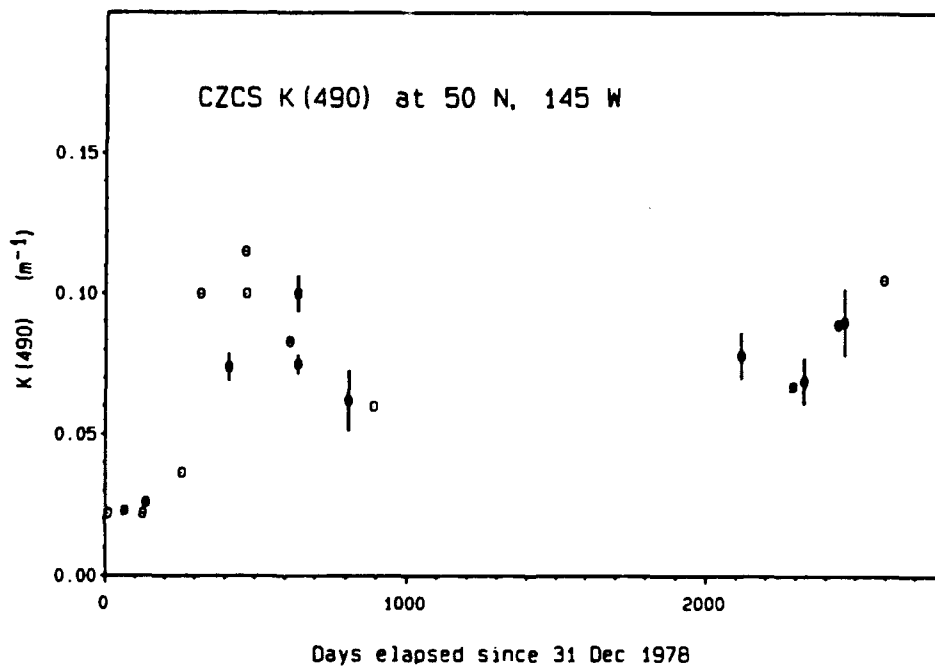
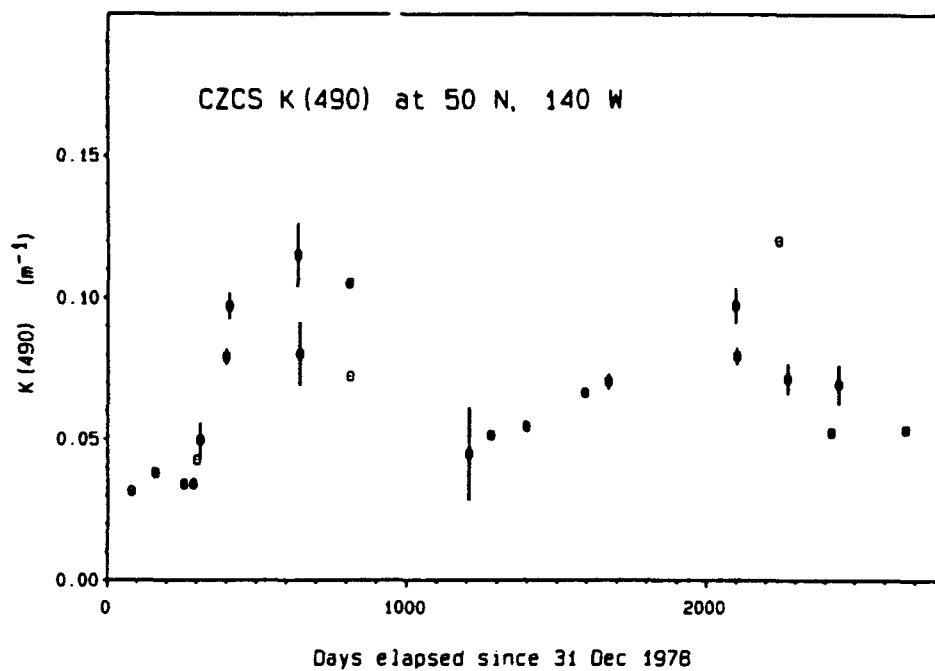


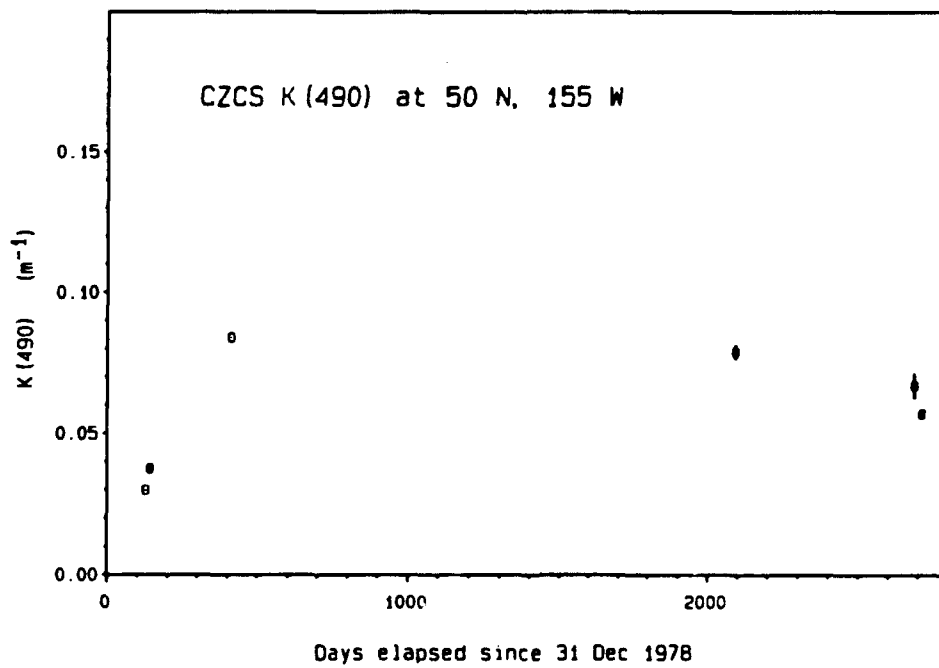
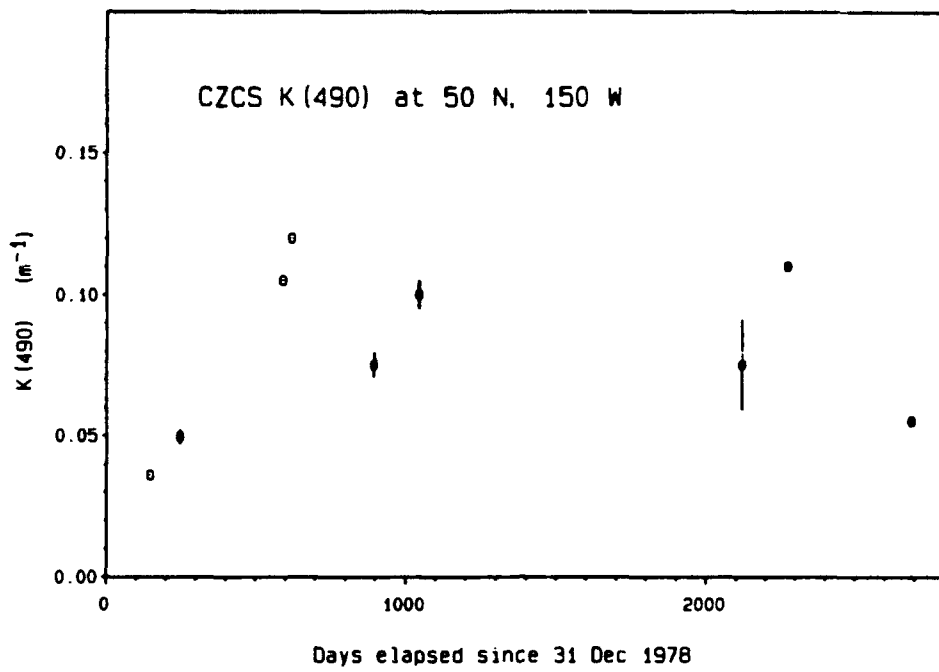


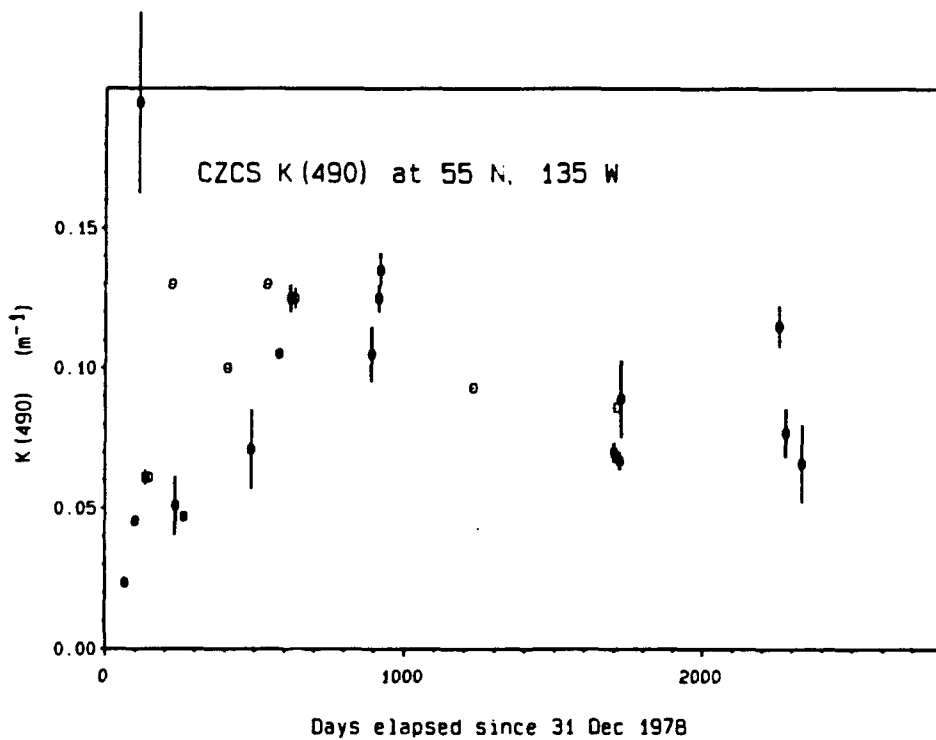
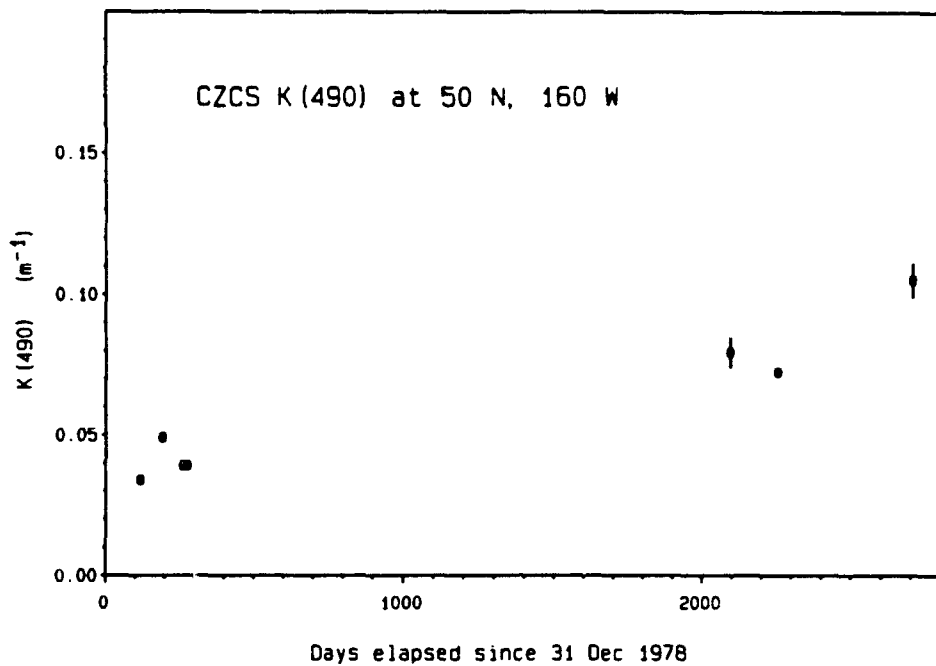


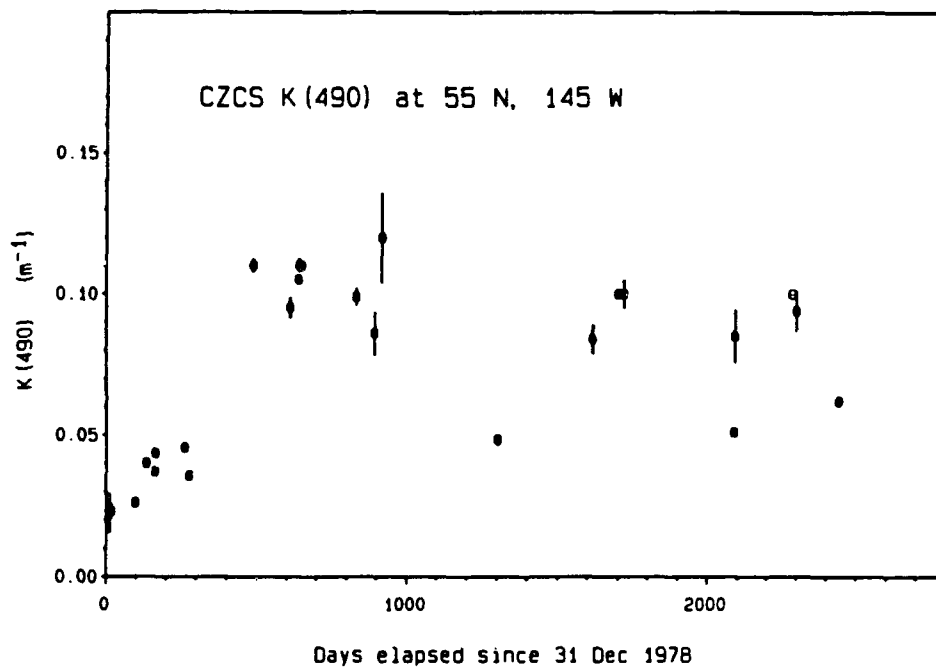
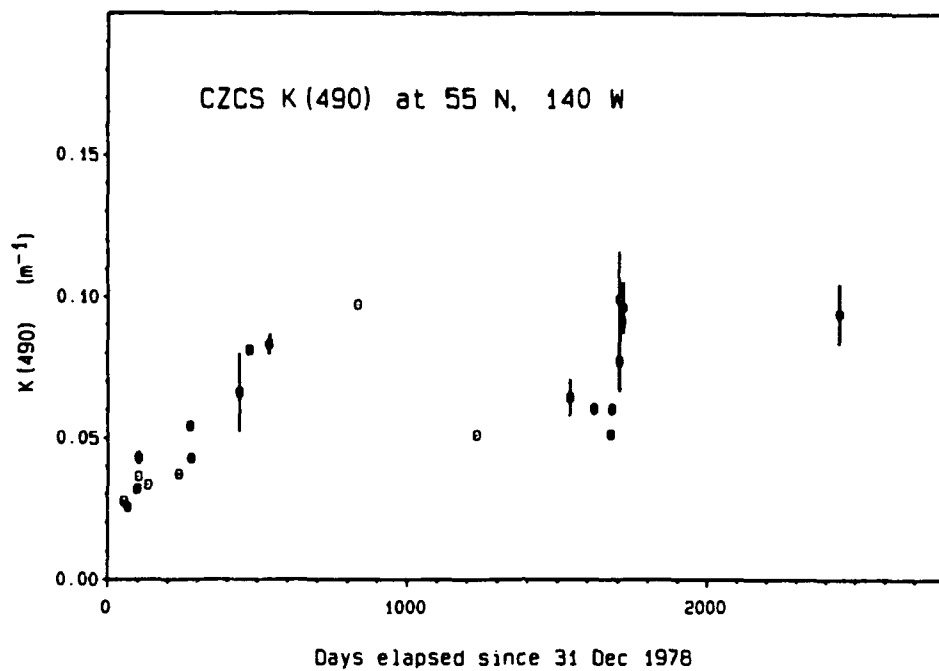


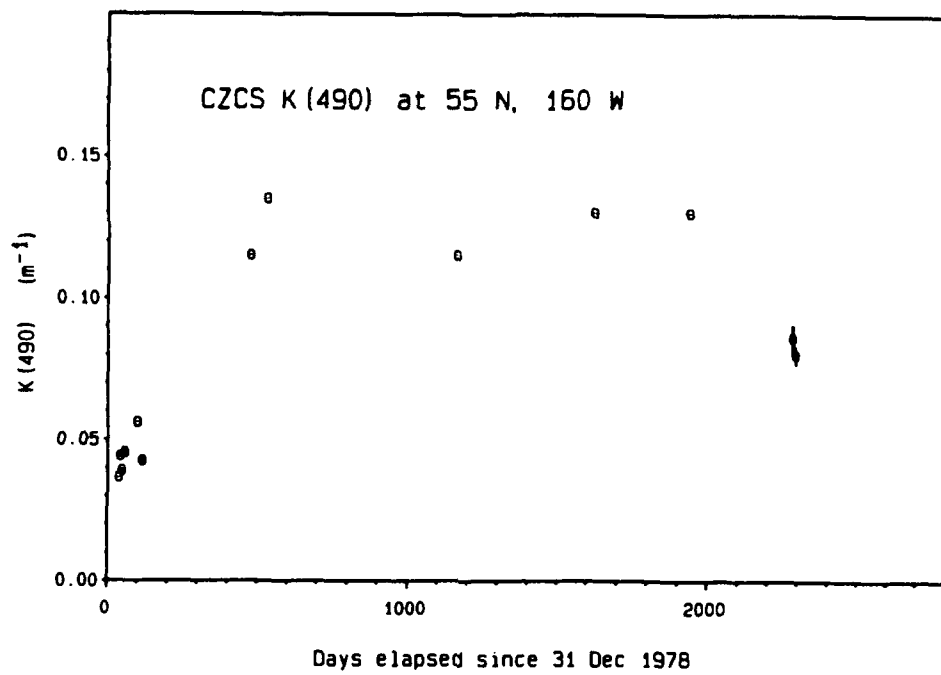


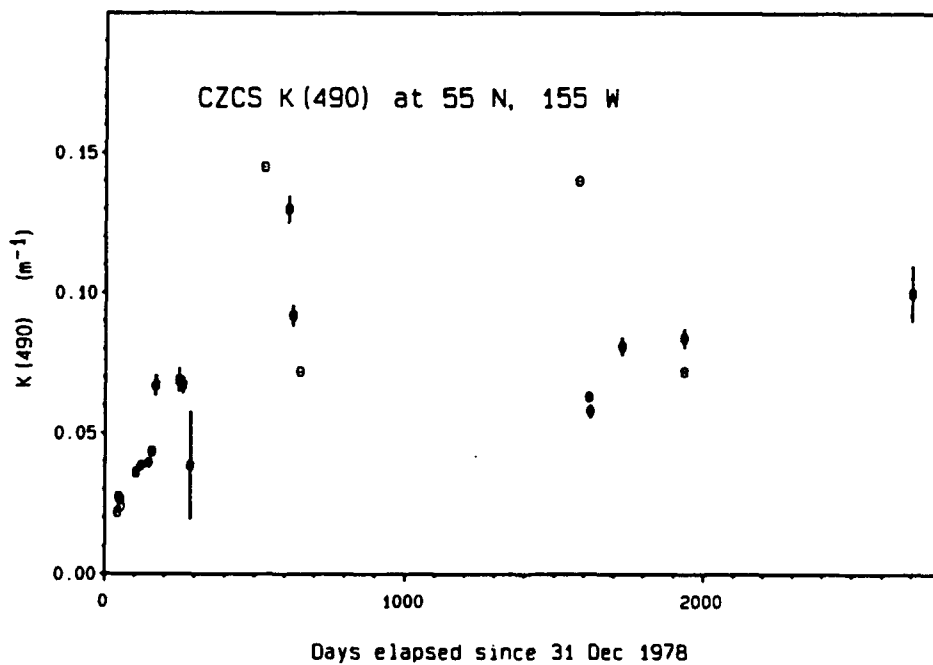
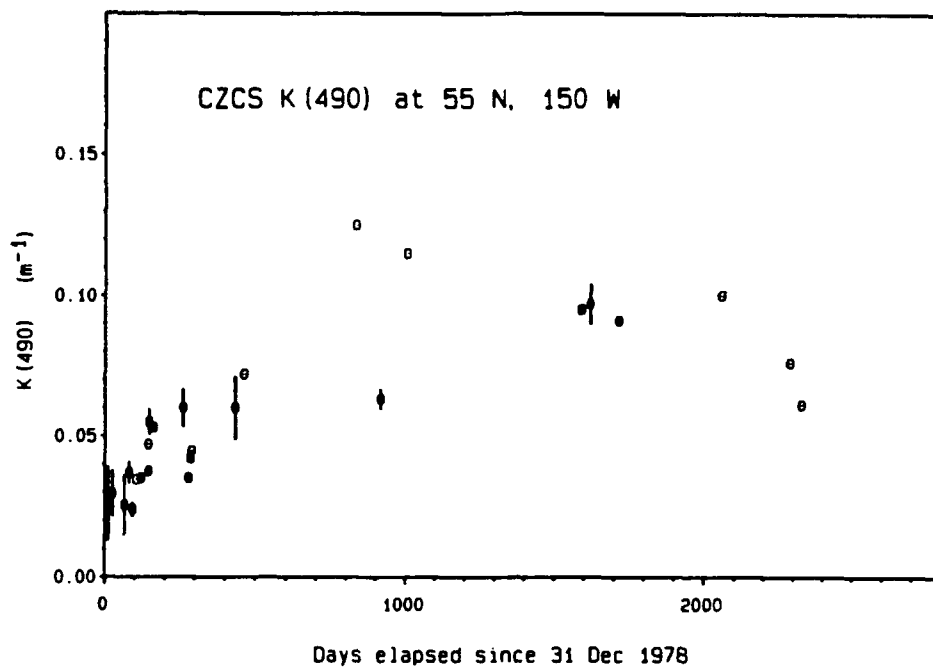












OPTICAL CLIMATOLOGY OF THE NORTHEAST PACIFIC OCEAN

APPENDIX E

**"Bio-Optical Provinces of the Northeast Pacific Ocean: A Provisional
Analysis" [Reprint of Mueller, J.L. and R.W. Lange, 1989, Limnol.
Oceanogr., 34(8): 1572-1586]**

James L. Mueller

Center for Hydro-Optics & Remote Sensing
San Diego State University
6505 Alvarado Road, Suite 206
San Diego, CA 92120-5005

CHORS Technical Memorandum 001-93

Prepared for the Naval Research Laboratory
(Stennis Space Center) Code 311
as part of the Final Report, NOARL Contract N00014-89-C-6007

Bio-optical provinces of the Northeast Pacific Ocean: A provisional analysis

James L. Mueller and R. Edward Lange

Center for Hydro-Optics and Remote Sensing, San Diego State University, San Diego, California 92182

Abstract

A provisional analysis of satellite ocean color imagery and in situ profiles of spectral irradiance and Chl *a* fluorescence partitions the Northeast Pacific Ocean into four geographically and bio-optically distinct provinces: the California Current system, the Alaskan gyre, the east central North Pacific central gyre, and the subarctic front. Within each province in a given 2-month period (June-July 1985 and October-November 1982), a family of regression equations was found to accurately predict the vertical profiles of irradiance attenuation and normalized Chl *a* fluorescence from *K*490—the surface diffuse attenuation coefficient which can be estimated from remotely sensed ocean color. The irradiance attenuation profile (to the depth where irradiance is 0.1% of the surface value) is predicted directly from the reciprocal of *K*490. Prediction of the Chl *a* fluorescence profile is based on a log-linear photoadaptive profile of fluorescence over diffuse optical depth—a conceptual model which robustly fit the entire sample analyzed. Given *K*490, the profile is determined from four regression models predicting the depth in meters of the fluorescence maximum, the optical depth of the deep background fluorescence minimum, the surface intercept of the profile, and the slope of the profile between the surface and maximum.

Remotely sensed ocean color can be used to determine phytoplankton pigment concentrations and optical diffuse attenuation coefficient *K*(490) (units given in list of symbols) in the near-surface layer of the ocean. A concern is that remotely sensed bio-optical properties represent only a shallow surface layer of the sea, while maxima in vertical profiles of Chl *a* concentrations (and Chl *a* fluorescence) are typically 2–3 times deeper, and values at the maxima may greatly exceed those near the surface. Because of this profile shape, past work found pigment biomass at the surface to be poorly correlated with that integrated through the euphotic zone in oligotrophic waters of the

east central North Pacific central gyre (Hayward and Venrick 1982) and in a persistent eddy off the California coast (Haury et al. 1986). On the other hand, analyses of *K*(490, *z*) profiles found statistically significant correlations between CZCS (Nimbus-7 Coastal Zone Color Scanner, a multispectral ocean color radiometer which measured images of spectral radiance upwelled from the ocean and atmosphere at wavelengths of 443, 520, 550 and 670 nm) *K*490 and the mean attenuation coefficient to 100 m (R. W. Austin pers. comm.).

We report a set of regression models, applicable to the Northeast Pacific Ocean, which predict the vertical profiles of both diffuse optical depth at 490 nm and normalized Chl *a* fluorescence from optical remote-sensing depth $1/K490$ (m) and which can be estimated from remotely sensed ocean color. Following an approach first suggested by Platt and Sathyendranath (1988), we organize our analysis within “bio-optical provinces,” which partition the study region geographically, and by time of year within each province. The in-water profile models are applied to a June–August composite mean CZCS *K*490 distribution to examine vertical bio-optical sections. The four bio-optical provinces (Fig. 1) are associated with well-known features of the regional ocean circulation.

Acknowledgments

We thank C. Trees, R. Zaneveld, and an anonymous reviewer for comments and suggestions which improved the manuscript. We also thank R. Smith and K. Baker for allowing us to use unpublished data from the *Acania* 1982 ODEX expedition, H. Pak for use of data from the 1985 *Discoverer* cruise, and R. Austin and J. Nollen for their help in analyzing data from the 1982 and 1985 *DeSteiguer* cruises. R. Wittenberg-Fay and J. C. Brown assisted with graphics and word processing.

This work was supported by Oceanographer of the Navy (NORDA) contracts N00014-87-C-6002 (SIO Visibility Lab, UCSD, La Jolla, Calif.) and N00014-89-C-6007 (SDSU CHORS, San Diego, Calif.), and NOSC contract N6601-86-D-0022 (SIO, UCSD, La Jolla).

Significant symbols

A_f	Surface intercept of log-linear photoadaptive fluorescence profile
B_f	Slope of log-linear photoadaptive fluorescence profile between the surface and fluorescence maximum
$E(z)$	Downwelling irradiance at depth z (wavelength is 490 nm unless specified), $\mu\text{W cm}^{-2} \text{ nm}^{-1}$
$Fl(z)$	Chl a fluorescence measured in situ at depth z , V
$Fl^*(z)$	Normalized fluorescence $= Fl(z)/Fl(z_{\text{max}})$
$K490$	Mean irradiance attenuation coefficient at 490 nm to depth $z = 1/(K(490, z))$, i.e. the mean value over the top optical depth $D(1/K490) = 1.0$, m^{-1} [symbol is used without parentheses to distinguish its reference to the value of "surface $K(490)$ " estimated from remotely sensed ocean color]
$\langle K(z) \rangle$	Mean irradiance attenuation coefficient from the surface to depth z for wavelength of 490 nm unless specified, m^{-1}
$K(z)$	Diffuse irradiance attenuation coefficient at depth z (wavelength is 490 nm unless specified), m^{-1}
$\tau(z)$	Diffuse optical depth at depth $\tau(z) = \langle K(z) \rangle z$ (wavelength is 490 nm unless specified)
z	Depth below the sea surface, m
z_{max}	Depth of the in situ Chl a fluorescence maximum, m
z_{min}	Depth of the deep background minimum in Chl a fluorescence, m
$Z_{\pi\%}$	Depth at which $E(Z_{\pi\%})$ is attenuated to $\pi\%$ of incident surface irradiance $E(0)$, m

- CCS—the California Current system. The western boundary of the CCS province is identified here with a transition from low salinity water masses (of subarctic origin) to higher salinity water masses of the ECNP central gyre near 130°W . CCS includes both eutrophic water masses over the continental slope and shelf, and mesotrophic water masses occupying the transition into the ECNP central gyre.
- ECNP—east central North Pacific central gyre water masses. The province is bounded on the north by the SAF and on the east by the CCS provinces and is used with reference to oligotrophic water masses of the central gyre. The zonal dotted line marked "STF" (Fig. 1) marks the approximate location of the subtropical

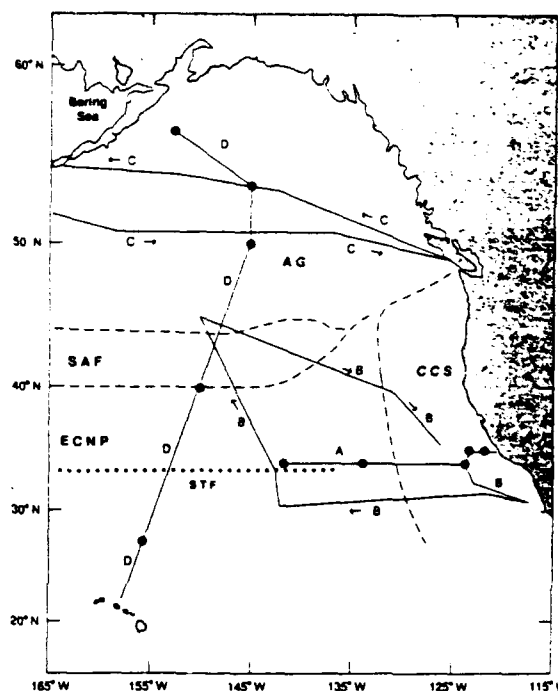


Fig. 1. Bio-optical provinces of the Northeast Pacific. Dashed lines represent provisional geographic boundaries of four bio-optically distinct provinces associated with features of the regional ocean circulation: the California Current system (CCS), the Alaskan gyre (AG), the North Pacific subarctic front (SAF), and the oligotrophic water masses of the east central North Pacific central gyre (ECNP). The dotted line at 33°N denotes the subtropical front (STF). Lines A–D show cruise tracks along which irradiance and fluorescence profiles were measured. Locations of example profiles shown in Figs. 10 and 11 —●.

front near 33°N , which corresponds to the southern limit of the climatological zone of convergence in Ekman transport extending southward from the SAF near 42°N (Roden 1975); the temperature/salinity curves of ECNP water masses on either side of the STF can be used to segregate north and south varieties of ECNP water (Niiler and Reynolds 1984).

- SAF—the eastern North Pacific subarctic front. This feature is usually found between 42°N and 45°N and is characterized by compensating horizontal gradients of temperature and salinity in the upper 100 m, and moderate horizontal density gradients below 100 m (Roden 1975, 1977). The surface layer in the front appears bio-optically as a ridge of high chlorophyll and particle concentration (and thus high $K490$), decreasing sharply into the ECNP

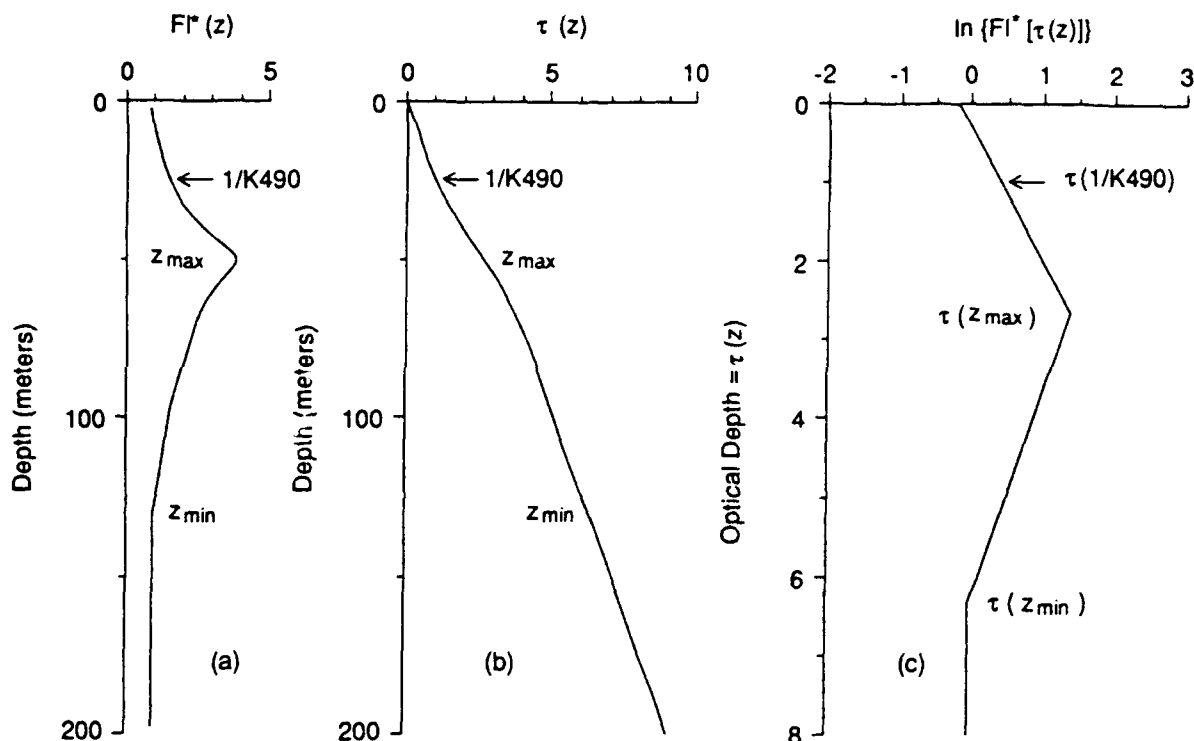


Fig. 2. Conceptual model relating vertical profiles of normalized Chl *a* fluorescence, $FI^*(z)$, and optical depth to optical remote-sensing depth $1/K490$ (m). Depths z_{max} of the Chl *a* fluorescence maximum, z_{min} of the deep background fluorescence minimum, and $1/K490$ are shown in panels a and b, and the corresponding optical depths $\tau(z_{max})$, $\tau(z_{min})$, and $\tau(1/K490)$ are marked on the log-linear photoadaptive profile of panel c.

province to the south and moderately to the north and east (Pak et al. 1988; and results below).

- AG—the Alaskan Gyre, comprising the currents and water masses in the Gulf of Alaska, but not including areas influenced by the SAF near $42^\circ N$ (which appear to be bio-optically distinct). This province is characterized by irregular patches of high *K490* and Chl *a* concentration, many of which are associated with seamounts and other bathymetric features.

The above association of bio-optical provinces with ocean current regimes differs slightly from the approach of Platt and Sathyendranath (1988), who organized the North Atlantic into nine regions based on depth and latitude, with the subtropical boundary fixed by inspection of satellite imagery. They assumed that within a province in a given season, the shape of the vertical profile of pigment biomass is stable and can be approximated by a "quasi-constant" Gaussian function.

The present approach adopts a concep-

tual photoadaptive model of optical depth and fluorescence (Fig. 2) which evolves from three assumptions: the deep minimum fluorescence $FI(z_{min})$ (Fig. 2a) is assumed to be a "background fluorescence," by which profiles measured with different fluorometers can be normalized and used as equivalent; within a province and period of several weeks, light adaptation by the phytoplankton population will tend to establish a log-linear photoadaptive profile of Chl *a* fluorescence over diffuse optical depth $\tau(z)$ (indexed at 490 nm), and an associated photoadaptive profile of $\tau(z)$ (Fig. 2b, c); and within a province and time period, geographic variability in the coupled photoadaptive profiles of fluorescence and diffuse optical depth is assumed to systematically covary with optical remote-sensing depth $1/K490$ (the upper "tail" of the optical depth profile).

The conceptual model of photoadaptive fluorescence profiles is illustrated by the three curves of Fig. 2. The vertical profile of in situ Chl fluorescence, $FI^*(z) = FI(z)/$

$Fl(z_{min})$, is shown in Fig. 2a, normalized to the deep background minimum fluorescence at depth z_{min} . A subtlety illustrated in Fig. 2a is that surface fluorescence may be $< Fl(z_{min})$. The curve in Fig. 2b illustrates the vertical profile of diffuse optical depth $\tau(z)$, which can be calculated directly from a measured profile of downwelling irradiance $E(z)$. To analyze data from a single station, we determine the log-linear photoadaptive profile (Fig. 2c) by a least-squares fit to the profile $\ln\{Fl^*[\tau(z)]\}$ calculated from measured $Fl(z)$ and $E(z)$ profiles. From samples of fitted station data representing a given bio-optical province and time, regression equations are determined relating $1/K490$ to characteristic parameters of $\tau(z)$ (Fig. 2b) and $\ln\{Fl^*[\tau(z)]\}$ profiles (Fig. 2c). To predict bio-optical profiles from $1/K490$, we use the regression equations for a province/time to predict curves 2b and c, which are then combined to construct profile 2a.

Data and methods of analysis

Vertical profiles of downwelling irradiance at 490 nm $E(z)$ and Chl *a* fluorescence $Fl(z)$ were extracted from the data reports of four cruises in the Northeast Pacific Ocean (Fig. 1 cruise tracks A through D). In October–November 1982, $E(z)$ and $Fl(z)$ data were acquired aboard the RV *Acania* along track A (Scripps Inst. Oceanogr., SIO Ref. 87-23). Also during October–November 1982, $E(z)$ profiles were measured aboard the RV *DeSteiguer* along track B (Scripps Inst. Oceanogr., SIO VisLab TM:DL-001-83t). In June 1985, $E(z)$ profiles were measured aboard the RV *DeSteiguer* along track C (Scripps Inst. Oceanogr., SIO VisLab TM:EN-009-85t). And in June–July 1985, $E(z)$ $Fl(z)$ profiles were measured aboard the RV *Discoverer* along track D (Oregon State Univ., OSU Opt. Oceanogr. Group Cruise Data Rep.), results of which have been reported by Pak et al. (1988).

The in situ profiles were first screened for quality. Data from stations were rejected if the local solar zenith angle exceeded 60° , if incident surface irradiance measured by a deck radiometer (when available) varied by more than a few percent during a cast, if temperature or salinity inversions in an accompanying CTD profile (when available)

suggested lateral mixing or interleaving of distinctly different water masses across fronts, or if a vertical profile $Fl(z)$ did not extend from the surface to a depth z_{min} where a background fluorescence minimum was observed.

The remaining irradiance and fluorescence profiles were organized into two subsamples of stations occupied in June–July 1985 and October–November 1982. We henceforth refer to these as “Jun/Jul” and “Oct/Nov” subsamples. Preliminary scattergrams were used to reveal visual correlations between optical remote-sensing depth $1/K490$ and characteristic parameters of the vertical irradiance and Chl *a* fluorescence profiles. These scattergrams were also examined to partition the data from each period into subsets associated with the geographically distinct bio-optical provinces (Fig. 1), with possible further partitioning by magnitude of $1/K490$.

Irradiance profile analysis—From each profile $E(z)$ (at 490 nm), the vertical profile of diffuse optical depth was calculated as

$$\tau(z) = \ln[E(0)/E(z)]. \quad (1)$$

From the $\tau(z)$ profile, the optical remote-sensing depth $1/K490$ was determined as the depth (m) where $\tau(1/K490) = 1.0$, i.e. the depth at which $E(z) = E(0)\exp(-1)$. Depths $Z_{n\%}$ (m) at which $E(Z_{n\%}) = 10, 3, 1, 0.3$, and 0.1% of $E(0)$ were extracted from each irradiance profile at optical depths $\tau(Z_{n\%}) = 2.30, 3.51, 4.61, 5.81$, and 6.91 respectively.

Covariation of each light attenuation depth $Z_{n\%}$ with $1/K490$ was examined within each subsample. At each $Z_{n\%}$, statistically significant regression relationships of the form

$$Z_{n\%} = A_n + B_n/K490 \quad (2)$$

were determined.

Chlorophyll *a* fluorescence profile analysis—Vertical profiles of in situ Chl *a* fluorescence $Fl(z)$ (in volts) were normalized as $Fl^*(z) = Fl(z)/Fl(z_{min})$, where $Fl(z_{min})$ is the deep background minimum (Fig. 2a). The measured values $\ln\{Fl^*(z)\}$ and $\tau(z)$ were then paired at each depth z (from the surface to z_{min}) to create a discrete representation of the log-linear photoadaptive fluorescence

profile $\ln\{F^*[\tau(z)]\}$ (Fig. 2c). Linear regression analysis was used to fit the upper segment of the measured data (0 to z_{\max}) to the log-linear photoadaptive profile as

$$\ln\{F^*[\tau(z)]\} = A_f + B_f \tau(z), \quad z < z_{\max}. \quad (3)$$

A second least-squares fit to the $\ln\{F^*[\tau(z)]\}$ profile between z_{\max} and z_{\min} was used to determine the lower intercept $\tau(z_{\min})$ such that

$$\begin{aligned} \ln\{F^*[\tau(z)]\} &= \ln\{F^*[\tau(z_{\max})]\} \\ &\times \frac{[\tau(z_{\min}) - \tau(z)]}{[\tau(z_{\min}) - \tau(z_{\max})]}, \\ z_{\max} &< z < z_{\min}. \end{aligned} \quad (4)$$

The photoadaptive fluorescence profile is characterized in Eq. 3 and 4 by four parameters: z_{\max} [depth (m) of the Chl *a* fluorescence maximum], A_f (surface intercept of fluorescence), B_f (least-squares slope of increasing fluorescence with optical depth between the surface and z_{\max}), and $\tau(z_{\min})$ (the diffuse optical depth of the minimum "background" fluorescence). $\tau(z_{\max})$ is determined from the accompanying $\tau(z)$ model given z_{\max} .

Another set of scatter diagrams was examined to identify exploitable correlations between remote-sensing *K490* and the above four characteristic parameters of the photoadaptive fluorescence profile. Separate relationships were identified within ECNP (central gyre Jun/Jul and Oct/Nov), AG (July 1985 only), and CCS (October 1982 only). The best predictions of z_{\max} , $\tau(z_{\min})$, A_f , and B_f were obtained with regression equations

$$\ln[z_{\max}] = A_c + B_c \ln[1/K490], \quad (5)$$

$$\ln[\tau(z_{\min})] = A_m + B_m \ln[K490 - 0.02], \quad (6)$$

$$A_f = A_o + B_o \ln[K490 - 0.02], \quad (7)$$

and

$$B_f = A_z + B_z \ln[K490 - 0.02]. \quad (8)$$

Nimbus-7 CZCS K490 analysis—In the early stages of this project, it became ap-

parent that a "first-guess" example of a CZCS seasonal mean was needed as a basis for organizing the research. In particular, a reasonably complete spatial coverage of mean patterns of *K490* was required to guide a geographic partition of the region into bio-optical provinces. An example of a seasonal CZCS *K490* mean would also allow preliminary comparisons to be made between the CZCS and in situ bio-optical data. We therefore proceeded with a provisional analysis of only the summer CZCS data, when atmospheric corrections using the single scattering Rayleigh radiance approximation (Gordon et al. 1983) are accurate within a few percent, rather than wait to complete the implementation of the multiple scattering Rayleigh model of Gordon et al. (1988).

A complete set of *Nimbus-7* CZCS level-1 (earth-located radiance) data files covering the Northeast Pacific was assembled to study the bio-optical climate of the region. The portion of this data set spanning June–August of 1979–1985 was processed to produce a composite mean remotely sensed *K490* distribution. Each individual image was screened to eliminate areas either contaminated by sun glint or totally covered by land or clouds and to determine the wavelength dependence of aerosol radiance when suitable "clear-water" pixels were present in a scene (Gordon and Clark 1981). Atmospheric corrections were effected with the algorithms described by Gordon et al. (1983). The Mueller (1985) model was used to reduce the CZCS calibration sensitivity over time. CZCS observations of open-water areas viewed immediately after viewing clouds may be contaminated by electronic overshoot and were eliminated from each scanline (Mueller 1988). *K490* was calculated at each valid open-water pixel with the algorithm of Austin and Petzold (1981).

CZCS *K490* estimates were inserted into daily map files, at the proper geographic locations in a Mercator grid, with a "nearest neighbor" resampling algorithm. Each daily *K490* map was displayed and inspected for quality. A small fraction (<5%) of the CZCS data were rejected at this stage, either due to obvious geolocation errors or to anomalies in *K490* patterns or magnitudes which

Table 1. Irradiance attenuation profile model coefficients.

$n(\%)$	$\tau(Z_n)$	A_n	B_n	r^2	s_{τ}
Jun/Jul 1/K490 < 20 m					
10.0	2.30	1.26(1.50)	2.193(0.072)	0.95	1.67
3.0	3.51	3.34(2.73)	3.144(0.131)	0.93	3.03
1.0	4.61	4.79(4.79)	4.373(0.230)	0.89	5.32
0.3	5.81	17.05(7.09)	5.243(0.341)	0.84	7.89
0.1	6.91	21.16(8.96)	6.668(0.417)	0.82	9.36
Jun/Jul 1/K490 > 20 m					
10.0	2.30	-0.10(4.34)	1.763(0.084)	0.94	4.56
3.0	3.51	10.11(6.24)	2.060(0.121)	0.90	6.56
1.0	4.61	34.59(6.21)	2.002(0.120)	0.90	6.53
0.3	5.81	70.79(6.85)	1.848(0.132)	0.86	7.21
0.1	6.91	92.69(7.74)	2.060(0.146)	0.87	7.60
Oct/Nov 1/K490 < 20 m					
10.0	2.30	1.69(1.49)	2.251(0.078)	0.97	1.46
3.0	3.51	10.17(3.32)	2.781(0.174)	0.90	3.27
1.0	4.61	23.08(3.90)	2.934(0.205)	0.87	3.84
0.3	5.81	33.00(3.77)	3.682(0.198)	0.92	3.70
0.1	6.91	46.70(5.72)	4.383(0.312)	0.88	5.19
Oct/Nov 1/K490 > 20 m					
10.0	2.30	12.96(1.76)	1.669(0.039)	0.87	3.70
3.0	3.51	19.60(3.14)	2.232(0.069)	0.79	6.60
1.0	4.61	28.45(4.51)	2.672(0.099)	0.78	8.75
0.3	5.81	25.71(5.91)	3.680(0.124)	0.79	10.38
0.1	6.91	49.96(7.40)	3.903(0.161)	0.78	10.88

suggested symptoms of possible discrepancies in radiometric or algorithmic performance. The remaining daily maps were combined to form monthly composite means for June, July, and August of each year. The monthly composite means (and associated sample sizes) were combined to form June, July, and August composite means over the 7 yr (1979–1985). And finally, these three 7-yr monthly means were combined to form the provisional summer composite mean CZCS K490 (see Fig. 12 below).

Results

Irradiance attenuation profile analyses—The results of regression analyses predicting light attenuation depths Z_n from optical remote-sensing depth 1/K490 are summarized in Table 1. Separate sets of regression coefficients A_n and B_n (with 90% C.L. in parentheses) are given for the Jun/Jul and Oct/Nov subsamples and for optical remote-sensing depth ranges 1/K490 < 20 m and 1/K490 > 20 m in each time period. Based on Fisher's F -distribution, all the regression results in Table 1 are significant

at the 0.995 level, and the data are well distributed over the range of the fit (Figs. 3, 4). Stations with 1/K490 < 4 m, and those in the Bering Sea and SAF were excluded from the regressions. The four families of regression lines and associated scatter of the $Z_{10\%}$, $Z_{1\%}$, and $Z_{0.1\%}$ measurements are illustrated in Fig. 3 for Jun/Jul (ECNP and AG) and in Fig. 4 for Oct/Nov (ECNP and CCS). The break in regression slope near 1/K490 = 20 m is strongly apparent in both time periods, although at and below $Z_{1\%}$ it is much weaker in Oct/Nov than in Jun/Jul.

To calculate a modeled optical depth profile $\tau(z)$ given 1/K490, we select the appropriate coefficients from Table 1 and substitute in Eq. 2 to calculate the sequence of seven attenuation depths 0, 1/K490, $Z_{10\%}$, ..., $Z_{0.1\%}$ m corresponding to the seven optical depths 0, 1.0, $\tau(Z_{10\%})$, ..., $\tau(Z_{0.1\%})$. For depths $z < Z_{0.1\%}$, $\tau(z)$ is determined by linear interpolation. Finally, $\langle K \rangle$ for the layer from $Z_{0.3\%}$ to $Z_{0.1\%}$ is used to extrapolate $\tau(z)$ for $z > Z_{0.1\%}$.

There were too few stations from either the Bering Sea or the SAF for separate

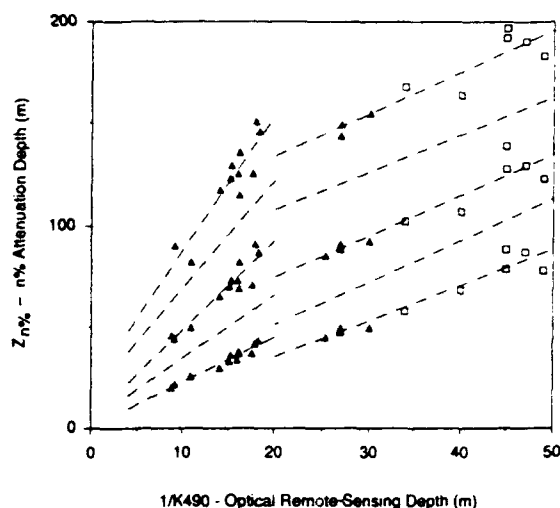


Fig. 3. Regression model predicting the vertical profile of irradiance attenuation from optical remote-sensing depth $1/K490$ in Jun/Jul ECNP (\square) and AG (\blacktriangle). The regression lines relate $1/K490$ (m) to the depths Z_n where $E(Z_n)$ is attenuated to 10, 3, 1, 0.3, and 0.1% of $E(0)$ (from bottom to top). Separate families of regression lines are given for $1/K490 < 20$ m and $1/K490 > 20$ m (Eq. 2 and Table 1). Scatter is shown for measured attenuation depths $Z_{10\%}$, $Z_{1\%}$, and $Z_{0.1\%}$ only.

regression analyses. Irradiance attenuation depths $Z_n\%$ measured in these provinces are compared in Fig. 5 with the Jun/Jul regression model (Fig. 3). The Bering Sea profiles agree with the model, suggesting that this region is not optically distinct from the AG province. The SAF profiles, however, are not in close agreement with either model at depths $> Z_{3\%}$ (although SAF stations from both time periods appear to follow the Jun/

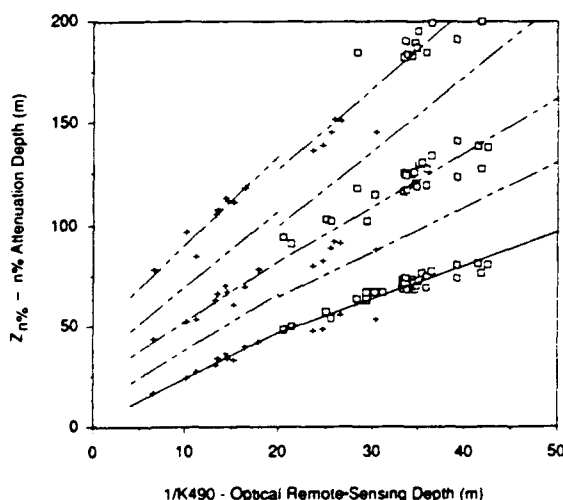


Fig. 4. As Fig. 3, but for Oct/Nov ECNP (\square) and CCS (+) near 34°N .

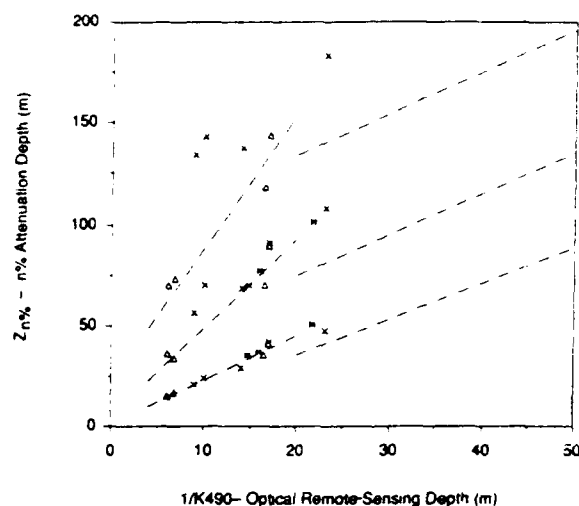


Fig. 5. Depths $Z_n\%$ (m) of 10, 1, and 0.1% light levels (from bottom to top) from irradiance profiles in the Bering Sea (June 1985— \triangle) and the SAF (November 1982 and June 1985— \times) compared with regression lines from Fig. 3.

Jul $1/K490 < 20$ -m models for $Z_{10\%}$ and $Z_{3\%}$). An ad hoc fit to the four deep optical profiles from SAF is used to model that region in the interpretation of CZCS-derived mean $K490$ (see Figs. 12 and 13): $Z_{10\%}$ and $Z_{3\%}$, and mean $\langle K \rangle$ for this depth layer, are calculated with the Jun/Jul [$1/K490 < 20$ m] model (extrapolated if necessary); it is assumed for $z > Z_{1\%}$ that $K(z) = 0.03 \text{ m}^{-1}$ (the average of four deep profiles); and $\langle K \rangle$ in the layer between $Z_{3\%}$ and $Z_{1\%}$ is assumed to be the average of $\langle K \rangle$ values for the two adjoining layers.

Chlorophyll *a* fluorescence profile analysis—The four characteristic parameters [z_{\max} , $\tau(z_{\min})$, A_f , and B_f] of the log-linear photoadaptive fluorescence profile (Fig. 2c; Eq. 3 and 4) were determined from pairs of $Fl^*(z)$ and $\tau(z)$ profiles (Jun/Jul, 19 sta., Fig. 1, track D; Oct/Nov, 33 sta., Fig. 1, track A). The fit of Eq. 3 and 4 to the measured $\ln\{Fl^*[(\tau(z))]\}$ profiles was remarkably robust, accounting for $>90\%$ of variance in 44 of 52 profiles and $>80\%$ in six of the remaining eight (the two poorly fit profiles were measured at a single nearshore station off California in November 1982).

Regression results relating z_{\max} to $1/K490$ and relating $\tau(z_{\min})$, A_f , and B_f to $\ln[K490 - 0.02]$ are collected in Table 2; scatter plots of measured values about regression lines are illustrated in Figs. 6–9. The number in

Table 2. Chlorophyll *a* fluorescence profile model coefficients.

Prov./monthst	A_i	B_i	r^2	s_m	P
Depth of fluorescence maximum, Eq. 5 $\ln[z_{\max}] = A_e + B_e \ln[1/K490]$					
A, E, G	0.367(0.091)	1.094(0.020)	0.95	0.134	0.995
B, C, F	1.017(0.073)	0.986(0.015)	0.91	0.136	0.995
Optical depth of minimum fluorescence, Eq. 6 $\ln[\tau(z_{\min})] = A_m + B_m \ln[K490 - 0.02]$					
A, E, G	1.666(0.056)	-0.046(0.009)	0.38	0.084	0.995
B, C, D, F	2.433(0.034)	0.114(0.006)	0.91	0.136	0.995
Intercept of $Fl^*(z)$ over $\tau(z)$, Eq. 7 $A_f = A_o + B_o \ln[K490 - 0.02]$					
G, E?, F?, D?	3.856(0.437)	0.692(0.079)	0.50	0.394	0.950
C, D?	3.577(0.212)	0.988(0.043)	0.31	0.208	0.995
A	-0.681(0.143)	-0.125(0.016)	0.62	0.071	‡
B	-0.775(0.035)	-0.115(0.005)	0.44	0.050	0.995
Slope of $Fl^*(z)$ over $\tau(z < z_{\max})$, Eq. 8 $B_f = A_z + B_z \ln[K490 - 0.02]$					
G, E?, F?, D?	-1.201(0.304)	-0.469(0.055)	0.490	0.274	0.950
C, D?	0.107(0.124)	-0.195(0.043)	0.618	0.121	0.990
A	0.570	0.000	—	0.143	—
B	0.430	0.000	—	0.043	—

† Key: A—ECNP/June–July 1985; B—ECNP/October–November 1982; C—CCS/October 1982; D—CCS/November 1982; E—SAF/July 1985; F—SAF/November 1982; G—Gulf of Alaska/July 1985.

‡ Not significant at the 0.90 level due to small sample size (five observations).

parentheses beside each regression coefficient is its 90% C.L. Data from the CCS–November subsample (four profiles from two closely spaced inshore stations) were excluded from the regression analyses, as were data from two stations that appear to be obvious outliers in Fig. 8b.

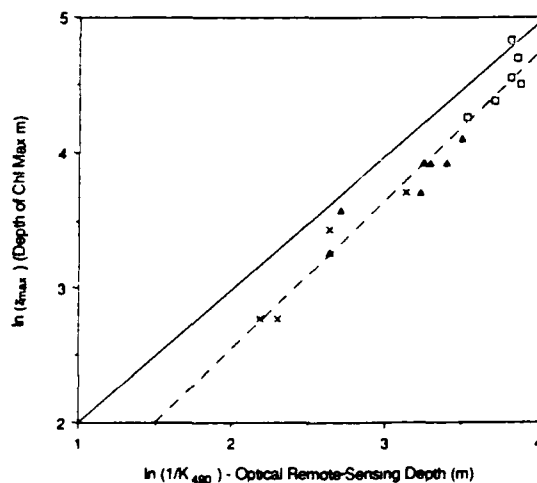


Fig. 6. Regression models predicting z_{\max} (depth of maximum Chl *a* fluorescence) from $1/K490$ for Jun/Jul ECNP and AG (dashed line) and Oct/Nov ECNP and CCS (solid line) (Eq. 5; Table 2). Scatter of the Jun/Jul observations from ECNP (\square), SAF (\times), and AG (\blacktriangle) stations is illustrated. Scatter of Oct/Nov ECNP and October CCS (not shown) is similar.

Statistically different regression equations were calculated from the Jun/Jul and Oct/Nov subsamples for z_{\max} and $\tau(z_{\min})$. The tendencies for z_{\max} and $\tau(z_{\min})$ to covary with remotely sensed $K490$ exhibit no apparent

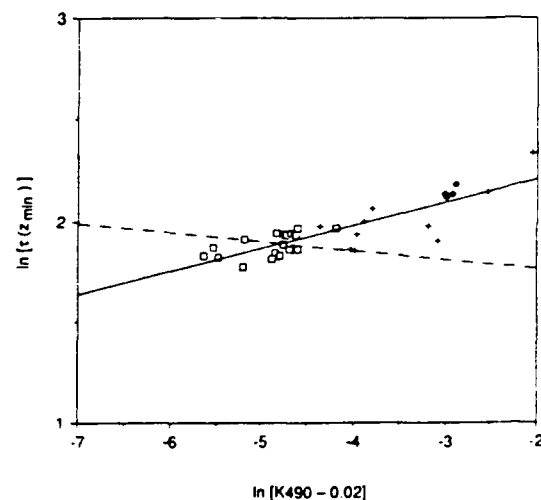


Fig. 7. Regression models predicting $\tau(z_{\min})$, optical depth of the deep background fluorescence minimum, from remotely sensed $[K490 - 0.02]$, where 0.02 is the approximate value of $K(490)$ for pure water, for Jun/Jul ECNP and AG (dashed line) and for Oct/Nov ECNP and CCS (solid line) (Eq. 6; Table 2). Scatter of Oct/Nov ECNP (\square), October CCS ($+$), and November CCS (\blacklozenge) data is illustrated. Scatter of Jun/Jul ECNP, SAF, and AG stations (not shown) is similar.

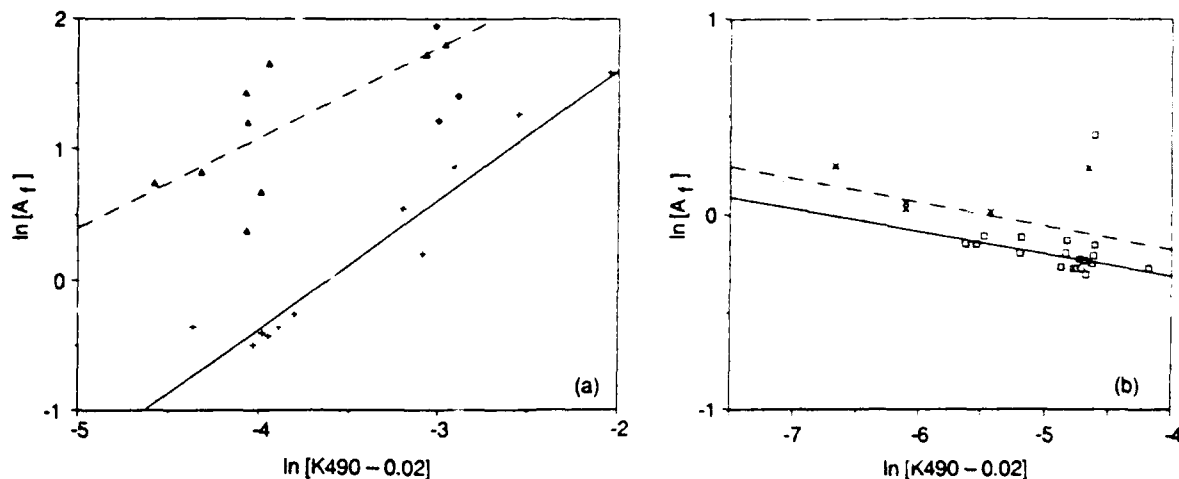


Fig. 8. Regression models predicting A_f , the surface intercept of the log-linear photoadaptive fluorescence profile, from remotely sensed $[K490 - 0.02]$ (Eq. 7; Table 2). Panel a compares Jun/Jul AG (Δ ; dashed line) and October CCS ($+$; solid line) scatter and regression lines. November CCS (\blacklozenge) data were excluded from the regression. Panel b compares Jun/Jul ECNP (\times ; dashed line) and Oct/Nov ECNP (\square ; solid line) scatter and regression lines.

dependence on geographic province (Figs. 6 and 7).

In contrast, the results pertaining to the surface intercept (A_f) and slope (B_f) of the upper segment of the log-linear photoadaptive fluorescence profile (Fig. 2c) depend both on time of year and geographic province (Table 1; Figs. 8 and 9). Significantly different regression lines were determined for ECNP(Jun/Jul), ECNP(Oct/Nov), CCS

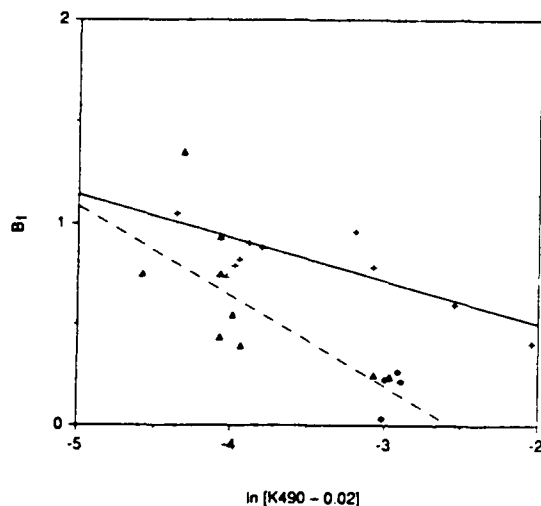


Fig. 9. Regression models for the slope B_f of the upper segment of the log-linear photoadaptive fluorescence profile (Fig. 2c) for Jun/Jul AG (Δ ; dashed line) and October CCS ($+$; solid line) (Eq. 8; Table 2). November CCS data (\blacklozenge) were excluded from the regression.

(October), and AG(July). Data from the SAF and CCS-November were excluded from this analysis (speculative associations of these "Province/Month" cases with regression models are therefore flagged by question marks in Table 2).

The separate Jun/Jul and Oct/Nov ECNP regression models for the surface intercept A_f (Fig. 8b; Table 2, footnote ‡) were selected in preference to a fit to the combined sample, because of superior performance in reconstructing $FI^*(z)$ profiles (Figs. 10 and 11).

The use of this model to generate a vertical profile of Chl *a* fluorescence, given remotely sensed $K490$, is straightforward. The optical depth model (Eq. 2 with coefficients from Table 1) is first applied to $1/K490$ to calculate a vertical profile of optical depth $\tau(z)$. Coefficients A_c , B_c , A_m , B_m , A_o , B_o , A_z , and B_z (appropriate to the bio-optical province and time period in question) are taken from Table 2 and substituted in Eq. 5–8 to calculate the profile parameters z_{max} , $\tau(z_{min})$, A_f , and B_f respectively. These four parameters are substituted, together with $\tau(z)$, in Eq. 3 [for $0 < \tau(z) < \tau(z_{max})$] or Eq. 4 [for $\tau(z_{max}) < \tau(z) < \tau(z_{min})$], to calculate $\ln[FI^*(z)]$ at each depth z . At depths where $\tau(z) > \tau(z_{min})$, $\ln[FI^*(z)] = 0$.

In Fig. 10, example profiles from the Jun/Jul samples are superimposed on profiles

calculated from a direct least-squares fit to the data (dashed curves) and from optical remote-sensing depth $1/K490$ (taken from the irradiance profile) using the combined models of the diffuse optical depth (Eq. 2 and Table 1) and log-linear photoadaptive fluorescence profiles (Eq. 3–8 and Table 2) (solid curves). The reconstructed profiles from CCS and ECNP Oct/Nov are of the same quality as those in Fig. 10.

The temporal change in ECNP bio-optical profile models between Jun/Jul (solid curves) and Oct/Nov (dashed curves) is illustrated in Fig. 11 for a typical $1/K490$ of 35 m. The vertical profiles $Fl^*(z)$, obtained by combining the modeled $\tau(z)$ and $\ln\{Fl^*[\tau(z)]\}$ profiles from panels a and b are compared in panel c.

Bio-optical variability estimates from CZCS data—Figure 12 is a photographic gray-shade display of the provisional summer mean (June–August) $K490$ distribution, calculated as a composite average of CZCS estimates in these months for 1979 through 1985. Light areas correspond to large $K490$ and dark gray shades to low $K490$ (or high and low phytoplankton pigment concentrations respectively). The relatively large patches of black centered near $48^\circ N$, $160^\circ W$ represent ocean areas that were not observed even once in all 7 yr during these months.

The $K490$ distribution in Fig. 12 provides a bio-optical visualization of many well-known features of the large-scale circulation in the Northeast Pacific Ocean. The ECNP central gyre water masses, characterized by $0.022 < K < 0.05 \text{ m}^{-1}$ ($45 \text{ m} > 1/K490 > 20 \text{ m}$), extend from $30^\circ N$ to the SAF near $42^\circ N$ and from $\sim 127^\circ W$ (at the base of the continental slope) to $165^\circ W$ in this map image. The zonal SAF near $42^\circ N$ appears in the map as a wavy bio-optical ridge extending from $165^\circ W$ to $\sim 135^\circ W$, where it appears to blend into the patchy bio-optical structure associated with the AG. A preliminary comparison with bathymetry indicates that many of the turbid, high $K490$ patches in the Gulf of Alaska are located over or near seamounts. The CCS appears as a region of high $K490$ due to rich biological production associated with coastal upwelling throughout each summer. It is in-

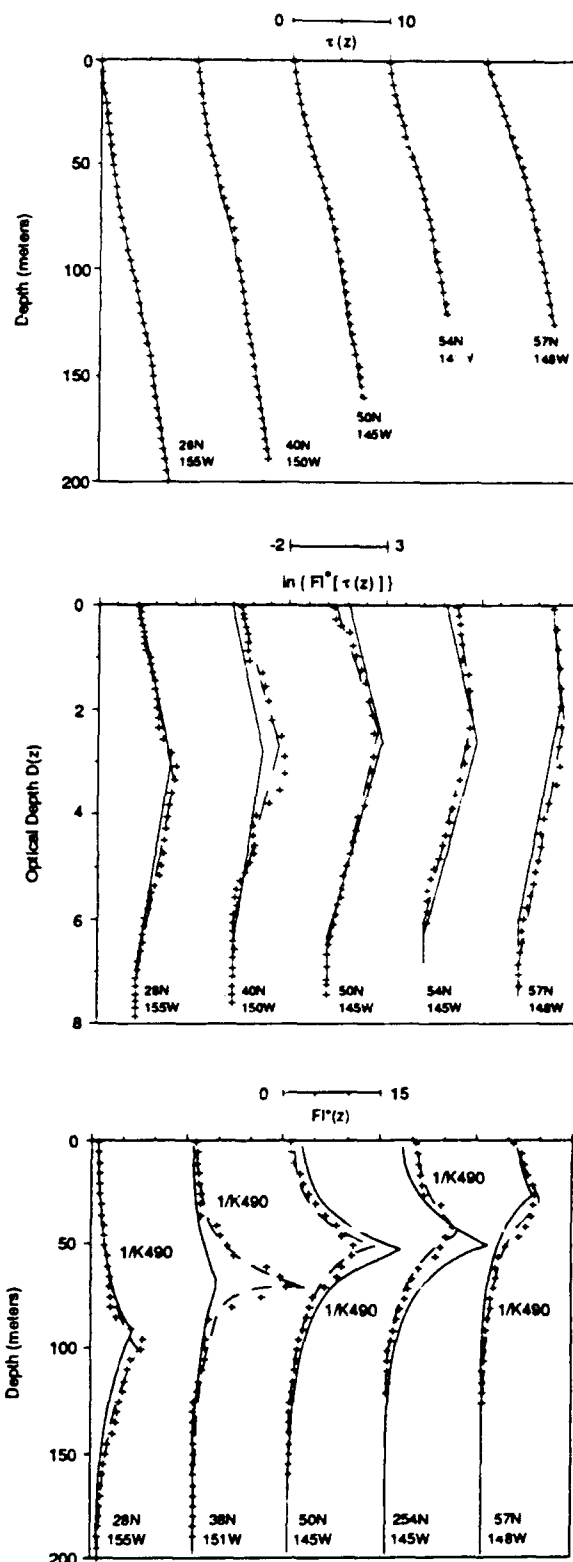


Fig. 10. Examples of measured (+), fitted (dashed lines), and modeled (solid lines) profiles of optical depth $\tau(z)$, photoadaptive fluorescence $\ln\{Fl^*[\tau(z)]\}$, and normalized fluorescence $Fl^*(z)$. Profiles were measured near $150^\circ W$ in the Jun/Jul ECNP and AG provinces (locations indicated on Fig. 1, track D).

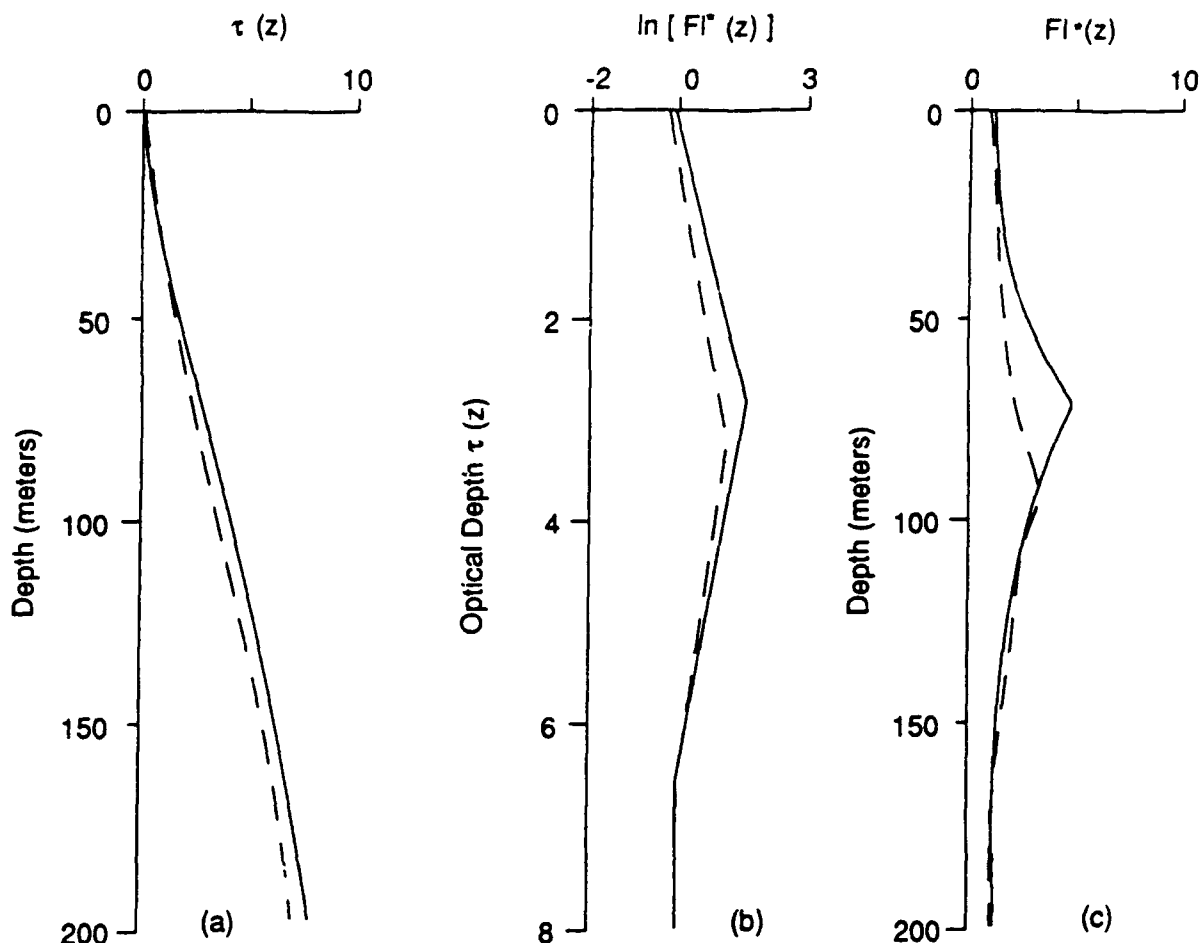


Fig. 11. Temporal change in modeled photoadaptive profiles of $\tau(z)$ and $FI^*(z)$ between Jun/Jul (solid lines) and Oct/Nov (dashed lines) in oligotrophic water masses of the ECNP. The profiles $\tau(z)$ and $\ln\{FI^*[\tau(z)]\}$ in panels a and b are modeled from Tables 1 and 2 for $1/K490 = 35$ m. The profile $FI^*(z)$ in panel c was determined by combining the curves from panels a and b.

interesting that in even this long-term average, CZCS K490 patterns show recognizable vestiges of mesoscale eddies and cross-shelf jets off Pt. Reyes and Pt. Conception, which are often observed in individual satellite images. These phenomena are clearly persistent features of the CCS circulation.

The meridional distribution of $1/K490$ extracted from Fig. 12 is profiled along the $150^\circ W$ meridian in Fig. 13, together with z_{max} and $FI^*(z_{max})$ calculated with the photoadaptive profile model. The CZCS composite mean $1/K490$ values (near $150^\circ W$) are systematically less than those measured aboard the RV *Discoverer* in 1985 (Pak et al. 1988; examples illustrated in Fig. 10) by an average factor of 0.67 at ECNP and 0.5 at SAF and AG station latitudes. A temporally coincident comparison was not pos-

sible, because there were no CZCS observations near $150^\circ W$ in July 1985. As a result of the apparent underestimation of $1/K490$ in the CZCS mean, the modeled z_{max} is significantly shallower than observed aboard *Discoverer* in 1985 (Pak et al. 1988), and $FI^*(z_{max})$ is also underestimated.

Geographic bio-optical provinces—The geographic boundaries of the SAF bio-optical province (Fig. 1) were determined by comparing Fig. 12 with published physical and bio-optical descriptions of the frontal region (Roden 1975, 1977; Pak et al. 1988). The zonal boundary separating the CCS and AG was extended to the coast based on a subjective interpretation of Fig. 12. The western boundary of the CCS province was placed at about $34^\circ N$, $130^\circ W$ at a transition from low salinity water masses (of subarctic

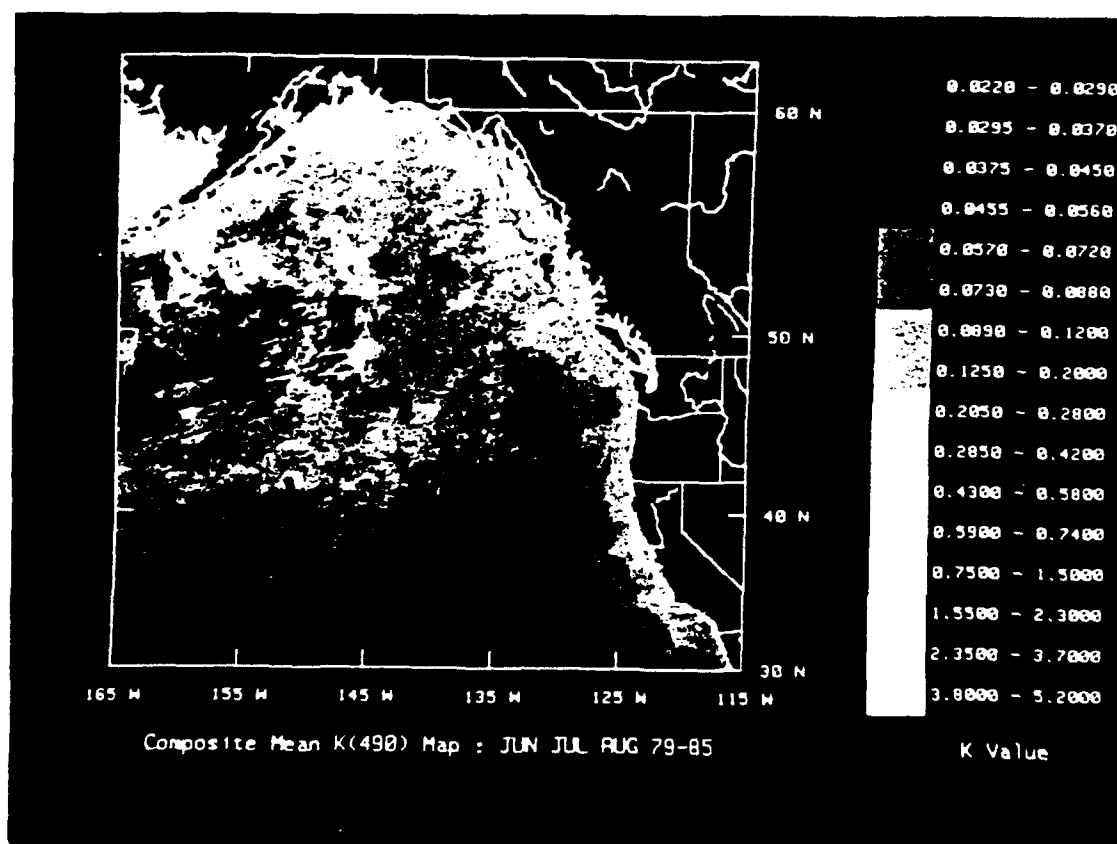


Fig. 12. Provisional summer composite mean K_{490} in the Northeast Pacific Ocean, using all available CZCS data for the months of June, July, and August 1979–1985. The data are presented on a Mercator projection, resolving 3 arc-min of longitude (which yields a spatial resolution < 5 km over the entire grid). Lighter (darker) gray shades indicate higher (lower) K_{490} values. Black denotes areas not observed by CZCS.

origin) to higher salinity water masses within ECNP, in temperature and salinity sections along track A of Fig. 1 (Naval Postgraduate School Data Rep. NPS-68-86-013, and unpubl. data from RV *Acania* cruises in October 1983 and April 1984). The CCS–ECNP boundary (Fig. 1) was then sketched through this location to generally parallel the coastline and the trend in offshore K_{490} gradients (Fig. 12).

Discussion and conclusions

Tables 1 and 2 comprise an internally consistent characterization of geographically distinct bio-optical provinces (Fig. 1) of the Northeast Pacific Ocean. Within each province at a particular time of year, characteristic parameters of the vertical profiles of irradiance attenuation (diffuse optical depth) and normalized Chl *a* fluorescence are quantitatively estimated from consistent values of optical remote-sensing depth

$1/K_{490}$ (derived directly from the measured irradiance profiles).

The vertical profile of irradiance attenuation [and therefore $\tau(z)$] may be predicted from $1/K_{490}$ to depths well below the euphotic zone. With the exception of the SAF, profiles from all provinces follow a common regression model within each time period. A distinct break in the slopes of the regression equations at each depth appears near $1/K_{490} = 20$ m in both Jun/Jul and Oct/Nov data sets; we can offer no explanation of why the 20-m optical remote-sensing depth is apparently critical and pragmatically report separate equations for the ranges of $1/K_{490}$ above and below it (Figs. 3 and 4).

The profiles $\tau(z)$ and $Fl^*(z)$ are related by a log-linear photoadaptive profile $\ln(Fl^*[\tau(z)])$ (Fig. 2c). Close inspection of example profiles (Fig. 10b) suggests that a small, but systematic, residual curvature may exist.

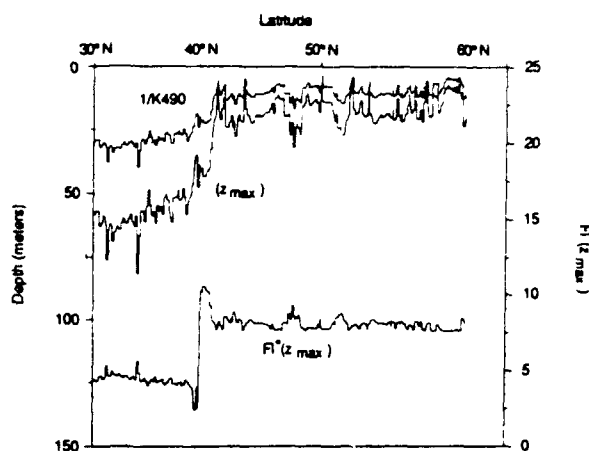


Fig. 13. Distribution with latitude of 1/K490 (uppermost curve) from Fig. 12 at 150°W, together with modeled values (Table 2) of the depth z_{\max} (m) and amplitude $FI^*(z_{\max})$ of the normalized Chl *a* fluorescence maximum (scale at right). (The CZCS K490 curve has been smoothed with a 5-point median filter.)

Nevertheless, the log-linear profile form yielded a robust first-order approximation to the data considered here.

To our knowledge, the present work is the first published demonstration that individual fluorescence profiles can usually be fit to the simple two-layer form of Fig. 2c. However, previously published results address the causes underlying the exponential nature of each layer. The log-linear tendency for $FI^*(z)$ to increase with optical depth to $\tau(z_{\max})$ is consistent with the model of Kiefer and Kremer (1981) (see also Kiefer 1984), which predicts a log-linear relationship between scalar irradiance and the ratio of chlorophyll to particulate organic nitrogen. It is also consistent with laboratory culture data showing log-linear increases in chlorophyll per cell with decreasing growth irradiance (Falkowski 1980; Falkowski et al. 1985). These models and results were cited by Pak et al. (1988) in their interpretative analyses of observed profiles of suspended particle concentration, Chl *a* biomass, and irradiance. This earlier work offers a first-order explanation for the robustness of the upper segment of the log-linear photoadaptive fluorescence profile. Although factors other than Chl *a* biomass affect $FI(z)$, a strong correlation can usually be found between fluorescence and pigment biomass within a given geographic region, time of year, and depth interval (e.g. Pak et al. 1988).

Platt and Sathyendranath (1988) and Platt et al. (1988) adopted an exponential (Gaussian) profile of pigment biomass over depth that is symmetrical above and below z_{\max} ; although they described the sensitivity of productivity estimates to the profile form beneath the maximum, they did not discuss possible causes for its exponential nature. Pak et al. (1988) noted that growth rates below z_{\max} are light limited and therefore decrease exponentially with depth. The log-linear decrease of Chl *a* fluorescence between $\tau(z_{\max})$ and $\tau(z_{\min})$ implies that Chl *a* per cell either remains constant or also varies exponentially with depth in this layer.

Predictions of z_{\max} and $\tau(z_{\min})$ from K490 each follow a single regression trend spanning all provinces (except November CCS) in each time period. Prediction models for A_f and B_f , on the other hand, vary strongly between provinces. The quality of fit to the A_f and B_f models is generally very good in the ECNP (both periods) and CCS (October only), and fair in the AG (Figs. 8 and 9). The relatively large scatter in the AG may result, in part, from effects of complex three-dimensional flow over seamounts and other bathymetric features colocated with many of the high turbidity patches seen in Fig. 12. Bio-optical profiles from the SAF and the November CCS were clearly anomalous, indicating the need for separate treatments, but there were too few observations from either province/time to explore possible covariability of photoadaptive fluorescence profiles with K490.

During summer and the early stages of the fall transition in Oct/Nov, a seasonal pycnocline exists in ECNP at a depth 40–50 m above the nutricline, which has been observed to coincide approximately with z_{\max} (Pak et al. 1988). This stratification isolates the nutricline from turbulent energy needed to entrain new nutrients into the euphotic zone and thus permits a progressive depletion of nutrients that are lost with sinking organic particles. Pak et al. (1988) discussed the effects of nutrient limitation and reduced self-shading in producing a deep, relatively weak maximum in a typical pigment biomass profile in the central gyre. The difference between the Jun/Jul and Oct/Nov regression models for $\tau(z)$ (Figs. 3 and

4) and $Fl^*(z)$ (Fig. 11) provides a provisional quantitative description of these effects (assuming data from two different years can be combined in this way). For example when $1/K490 = 35$ m, $Z_{1\%}$ (at 490 nm) increases from 105 to 120 m, z_{max} increases from 70 to 90 m, and $Fl^*(z_{max})$ decreases from ~ 5 to 3.5 during this 4-month period (Fig. 11).

In ECNP at either time, the surface fluorescence intercept A_f of the photoadaptive profile decreases with increasing remote sensing $[K490 - 0.02]$ (which varies directly with pigment biomass) (Fig. 8b). This seeming paradox occurs because A_f is a characteristic parameter of the entire upper segment of the profile from the surface to $\tau(z_{max})$ and is sensitive to both z_{max} and $Fl^*(z_{max})$. It is not directly equatable to surface pigment biomass or fluorescence. Because A_f , z_{max} (Fig. 6), and $Fl^*(z_{max})$ (Fig. 11) all decrease with increasing K490, it follows that $\ln\{Fl^*[\tau(z_{max})]\}$ changes at a faster rate than does $\tau(z_{max})$.

The provisional CZCS-derived estimates of $1/K490$, and resulting three-dimensional estimates of photoadaptive profiles $\tau(z)$ and $Fl^*(z)$ (Figs. 12, 13) agree qualitatively with the geographic patterns of the in situ measurements. There is also good agreement between Fig. 12 and patterns of Secchi disk transparency analyzed by Lewis et al. (1988), who discussed the implications of this geographic distribution on regional productivity.

The June–August composite mean CZCS $1/K490$ values extracted from Fig. 12 along $150^\circ W$ (Fig. 1) significantly underestimate $1/K490$ measured in Jun/Jul along track D (Fig. 1). Mueller (1984) reported a better agreement between CZCS and in situ $1/K490$ along track A (Fig. 1) in October 1982, using a CZCS sensitivity degradation model which was weighted heavily by data from October–November 1979–1982 (Mueller 1985). The Mueller (1985) CZCS sensitivity model was probably biased by systematic errors in the single scattering Rayleigh radiance algorithm at the large solar zenith angles prevailing in Oct/Nov. Furthermore, there is evidence that the CZCS may have changed sensitivity at an irregular rate through its operating lifetime (R. Evans pers. comm.).

The primary source of apparent positive bias in CZCS K490 estimates (Figs. 12, 13) is, therefore, suspected to be an inaccurate history of the instrument's radiometric sensitivity. Without other supporting evidence, a systematic factor of 1.5–2.0 bias in K490 is too large to be attributed intuitively to interannual variability. Furthermore, the CZCS in-water K490 algorithm (Austin and Petzold 1981) has been recently demonstrated to be robust, based on analysis of in situ optical profiles from widely distributed stations in the North Pacific, North Atlantic, and Greenland Sea (R. W. Austin pers. comm.) and is unlikely to contribute bias errors of this magnitude. In an attempt to resolve this issue, a radiometric consistency analysis of the full 7-yr CZCS time series is now in progress; it makes use of the Gordon et al. (1988) multiple-scattering Rayleigh radiance algorithm.

Our chief conclusion here is that vertical profiles of irradiance attenuation and Chl *a* fluorescence are related to remotely sensed ocean color in a predictable way at a given time in a geographic province. Bio-optical provinces in the Northeast Pacific Ocean are related to well-known features of the regional ocean circulation. Models within each province are provisional, for the data underlying Tables 1 and 2 do not resolve annual (let alone interannual) variability. Nevertheless, in a worst-case scenario, regional bio-optical distributions could be estimated with this method, using satellite remotely sensed ocean color supported by monthly (or bimonthly) cruises to determine new in-water profile relationships. In a more optimistic projection, additional data may reveal systematic temporal trends related to biogeochemical processes and thereby reduce reliance on in situ profiles for bio-optical prediction.

References

- AUSTIN, R. W., AND T. J. PETZOLD. 1981. The determination of the diffuse attenuation coefficient of sea water using the Coastal Zone Color Scanner, p. 239–256. In J. F. R. Gower [ed.], *Oceanography from space*. Plenum.
- FALKOWSKI, P. G. 1980. Light-shade adaptation in marine phytoplankton, p. 99–119. In *Primary productivity in the sea*. Brookhaven Symp. Biol. 31. Plenum.

- , Z. DUBINSKY, AND K. WYMAN. 1985. Growth-irradiance relationships in phytoplankton. *Limnol. Oceanogr.* 30: 311–321.
- GORDON, H. R., J. W. BROWN, AND R. H. EVANS. 1988. Exact Rayleigh scattering calculations for use with the Nimbus-7 Coastal Zone Color Scanner. *Appl. Opt.* 27: 862–871.
- , AND D. K. CLARK. 1981. Clear water radiances for atmospheric correction of Coastal Zone Color Scanner imagery. *Appl. Opt.* 20: 4175–4180.
- , AND OTHERS. 1983. Phytoplankton pigment concentrations in the Middle Atlantic Bight: Comparison of ship determinations and CZCS estimates. *Appl. Opt.* 22: 20–36.
- HAURY, L. R., AND OTHERS. 1986. Biological consequences of a recurrent eddy off Point Conception, California. *J. Geophys. Res.* 91: 12,937–12,956.
- HAYWARD, T. L., AND E. L. VENTRICK. 1982. Relation between surface chlorophyll, integrated chlorophyll and integrated primary production. *Mar. Biol.* 69: 247–252.
- KIEFER, D. A. 1984. Microplankton and optical variability in the sea: Fundamental relationships, p. 42–48. *In* Ocean Optics 7, Proc. SPIE 489.
- , AND J. N. KREMER. 1981. Origins of vertical patterns of phytoplankton and nutrients in the temperate, open ocean: A stratigraphic hypothesis. *Deep-Sea Res.* 28: 1087–1105.
- LEWIS, M. R., N. KURING, AND C. YENTSCH. 1988. Global patterns of ocean transparency: Implications for the new production of the open ocean. *J. Geophys. Res.* 93: 6847–6856.
- MUELLER, J. L. 1984. Effects of water reflectance at 670 nm on Coastal Zone Color Scanner (CZCS) aerosol radiance estimates off the coast of central California, p. 179–186. *In* Ocean Optics 7, Proc. SPIE 489.
- . 1985. Nimbus-7 CZCS: Confirmation of its radiometric sensitivity decay rate through 1982. *Appl. Opt.* 24: 1043–1047.
- . 1988. Nimbus-7 CZCS: Electronic overshoot due to cloud reflectance. *Appl. Opt.* 27: 438–440.
- NIILER, P. P., AND R. W. REYNOLDS. 1984. The three-dimensional circulation near the eastern North Pacific subtropical front. *J. Phys. Oceanogr.* 14: 217–230.
- PAK, H., D. A. KIEFER, AND J. C. KITCHEN. 1988. Meridional variations in the concentration of chlorophyll and microparticles in the North Pacific Ocean. *Deep-Sea Res.* 35: 1151–1171.
- PLATT, T., AND S. SATHYENDRANATH. 1988. Oceanic primary production: Estimation by remote sensing at local and regional scales. *Science* 241: 1613–1620.
- , ———, C. M. CAVERHILL, AND M. R. LEWIS. 1988. Oceanic primary production and available light: Further algorithms for remote sensing. *Deep-Sea Res.* 35: 855–879.
- RODEN, G. I. 1975. On North Pacific temperature, salinity, sound velocity and density fronts and their relation to the wind and energy flux fields. *J. Phys. Oceanogr.* 5: 557–571.
- . 1977. Oceanic subarctic fronts of the central Pacific; structure of and response to atmospheric forcing. *J. Phys. Oceanogr.* 7: 761–778.

DISTRIBUTION LIST

Chief of Naval Operations
NO96
U.S. Naval Observatory
3450 Massachusetts Avenue, NW
Washington, DC 20392-5421
(1) OP-021T2B E. Hashimoto

Director
Office of Naval Research
800 North Quincy Street
Arlington, VA 22217
Ocean Sciences
(1) Code 1123 Dr. R. Spinrad

Commanding Officer
Naval Research Laboratory Detachment
SSC, MS 39529-5004
(3) Code 7410 K.M. Ferer
(5) Code 7035.3
(1) Code 7240 Dr. A. Pressman

Commanding Officer
Naval Oceanographic Office
SSC, MS 39529-5001
(1) Code OP V. Sprague

Commanding Officer
Naval Research Laboratory
4555 Overlook Avenue, SW
Washington, DC 20375-5000
(1) Code 7600 Dr. K. Johnston

Commander Submarine Force
U.S. Pacific Fleet
Pearl Harbor, HI 96860-6550
(1) Code OOT Mr. Kittredge

Commander
Submarine Group NINE
Bremerton, WA 98315-5100
(1) LCDR B. Williams